



**SAPIENZA**  
UNIVERSITÀ DI ROMA  
DIPARTIMENTO DI SCIENZE DELLA TERRA



DOTTORATO DI RICERCA  
IN SCIENZE DELLA TERRA

**SAPIENZA UNIVERSITY OF ROME**  
**DEPARTMENT OF EARTH SCIENCES**

DOCTORAL SCHOOL *VITO VOLTERRA* IN ASTRONOMICAL,  
CHEMICAL, EARTH, MATHEMATICAL AND PHYSICAL SCIENCES

PH.D. THESIS

---

**NONLINEAR STRAIN EFFECTS INDUCED  
BY THERMAL FORCING ON JOINTED  
ROCK MASSES**

---

**PH.D. CANDIDATE:** GUGLIELMO GRECHI

**ADVISOR:** PROF. SALVATORE MARTINO<sup>1</sup>

<sup>1</sup>*SAPIENZA UNIVERSITY OF ROME – DEPARTMENT OF EARTH SCIENCES*

**PH.D. CYCLE:** XXXIV

**PH.D. COORDINATOR:** PROF. SILVIO MOLLO

**ACADEMIC YEARS:** 2018/2019, 2019/2020, 2020/2021

**SCIENTIFIC DISCIPLINARY SECTOR:** GEO/05









**SAPIENZA**  
UNIVERSITÀ DI ROMA

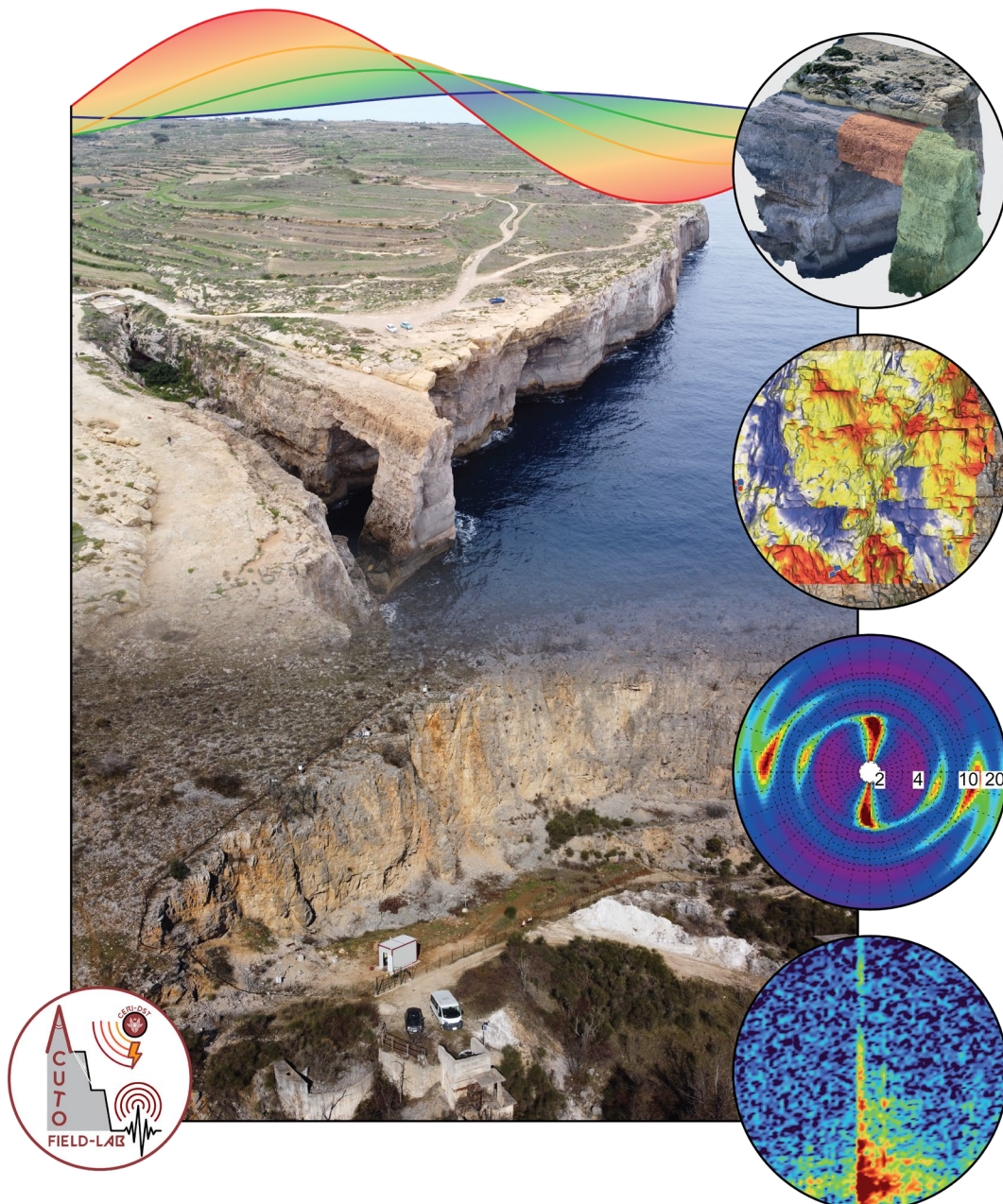
Dipartimento di Scienze della Terra



DOTTORATO DI RICERCA  
IN SCIENZE DELLA TERRA

PH.D. THESIS

**NONLINEAR STRAIN EFFECTS INDUCED BY THERMAL FORCING  
ON JOINTED ROCK MASSES**



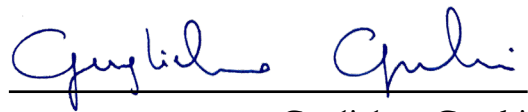
**PH.D. CANDIDATE:** GUGLIELMO GRECHI

**ADVISOR:** PROF. SALVATORE MARTINO



*Author's Declaration:*

This dissertation is submitted for the degree of Doctor of Philosophy at the Sapienza University of Rome (Doctoral School "Vito Volterra"). The manuscript is an original contribution by the Author and contains published and unpublished works produced during the three-year Ph.D. programme in Earth Sciences. All literature sources (both printed and electronic sources) are clearly referenced in the text in accordance with international requirements of copyright.

A handwritten signature in blue ink, reading "Guglielmo Grechi", is positioned above a horizontal line.

Guglielmo Grechi

*Revised by:*

Dr. Chiara Colombero, Ph.D.

Department of Environment, Land and Infrastructure Engineering (DIATI)

Politecnico di Torino

Turin (Italy)

Dr. Jan Burjánek, Ph.D.

Institute of Geophysics

Czech Academy of Science

Prague (Czech Republic)





The Road goes ever on and on  
Down from the door where it began.  
Now far ahead the Road has gone,  
And I must follow, if I can,  
Pursuing it with eager feet,  
Until it joins some larger way  
Where many paths and errands meet.  
And whither then? I cannot say.

—*J.R.R. Tolkien, The Fellowship of the Ring*



---

# Table of contents

<b>List of tables .....</b>	<b>III</b>
<b>List of figures .....</b>	<b>IV</b>
<b>Abstract.....</b>	<b>1</b>
<b>Chapter 1 – Introduction.....</b>	<b>3</b>
<b>Chapter 2 – State of Art .....</b>	<b>8</b>
2.1 Near-surface temperature fluctuations as a preparatory factor for rock slope instabilities .....	8
2.2 Thermomechanical damaging on jointed rock masses.....	16
<b>Chapter 3 – Materials and Methods .....</b>	<b>27</b>
3.1 Case studies.....	27
3.1.1 The Wied Il-Mielah sea arch.....	27
3.1.2 The Acuto field laboratory .....	38
3.2 Ambient seismic noise and microseismic monitoring .....	49
3.2.1 Ambient vibration monitoring system .....	55
3.2.2 Data acquisition .....	58
3.2.3 Microseismic event detection and analysis.....	65
3.2.4 Ambient seismic noise analysis .....	73
3.3 Infrared thermography surveys.....	79
3.3.1 The infrared thermography technique .....	79
3.3.2 Infrared thermography applications for jointed rock mass characterization..	82
3.3.3 Data acquisition and processing.....	84

---

<b>Chapter 4 – Results</b> .....	<b>96</b>
4.1 Results of microseismic monitoring.....	96
4.2 Results of ambient seismic noise analysis.....	121
4.3 Results of infrared thermography surveys at the Wied Il-Mielaň sea arch.....	147
4.4 Results of 3D thermal point cloud reconstruction.....	160
<b>Chapter 5 – Discussion</b> .....	<b>172</b>
<b>Chapter 6 – Conclusion</b> .....	<b>186</b>
<b>References</b> .....	<b>189</b>

---

# List of tables

<b>Table 3.1.</b> Summary of the geomechanical properties of the intact rock mass, considering both GL (Globigerina Limestone Formation) and LCL (Lower Coralline Limestone Formation) in all its members; $\rho$ – density; $\gamma_n$ – natural specific gravity; UCS – uniaxial compressive strength. ....	35
<b>Table 3.2.</b> Synthesis of the geomechanical characteristics of the identified joint sets at the Wied Il-Mielah sea arch. For JRC and JCS only average values are presented. ....	36
<b>Table 3.3.</b> Geomechanical characteristics of the discontinuity sets identified on the rock block and the adjacent rock wall through field surveys, and physical–mechanical properties of the intact rock matrix derived from laboratory analyses; $\gamma_n$ – natural specific gravity, $\gamma_s$ – solid specific gravity, $k$ – thermal conductivity, $\alpha$ – linear thermal expansion coefficient, UCS – uniaxial compressive strength, $E$ – Young elastic modulus. ....	45
<b>Table 3.4.</b> Summary of the technical characteristics (physical, environmental and dynamic) of the Bruel & Kjaer type-8433 microaccelerometers composing the microseismic monitoring system (from D’Angiò, 2019). ....	57
<b>Table 3.5.</b> Summary of the main features of the two monitoring campaigns conducted at the Acuto field laboratory between 2018 and 2019. ....	60
<b>Table 3.6.</b> Synthesis of ambient vibration monitoring activities at the Wied Il-Mielah sea arch between 2019 and 2020. T = triaxial array configuration, L = linear array configuration. ....	63
<b>Table 3.7.</b> Synthesis of the selected parameters for the analysis of the Acuto (ACT) and Wied Il-Mielah (WIM) datasets through the STA/LTA algorithm. ....	71
<b>Table 3.8.</b> Synthesis of IRT surveys at the Wied Il-Mielah sea arch. ....	85
<b>Table 3.9.</b> Main technical specification of the employed IR camera; FPA – Focal Plane Array, NETD – Noise Equivalent Temperature Difference, FOV – Field of View. ....	86
<b>Table 3.10.</b> Example of the relation between the number of acquired photos during one seasonal survey and number of points characterizing TIR sparse and dense point clouds (modified from Grechi et al., 2021). ....	93

# List of figures

## Chapter 2

- Figure 2.1.** Landslide–sequencing model explaining the short- to long-term evolution of a landslide through the consideration of triggering and preparatory factors (from Julian and Anthony, 1996 and adapted by Gunzburger et al., 2005; modified)..... 9
- Figure 2.2.** Evolution of uniaxial compressive strength (UCS) and Young’s elastic modulus under cyclic thermal loading **(a)**. Variation of UCS vs P-wave velocity **(b)** (from Villarraga et al., 2018)..... 11
- Figure 2.3.** Theoretical heat propagation in depth as a function of time (herein represented as different wave phases) according to Carslaw and Jaeger (1959) semi-infinite solid model **(a)**. At different distances from the heat exchange interface, the rock matrix experience temperature fluctuations which amplitude not only exponentially decay with depth due to its thermal inertia, but it also shows a clear delay between maximum thermal peaks **(b)** (from Fiorucci et al., 2018; modified)..... 14
- Figure 2.4.** Conceptual model of the interaction between open fractures and the heat propagation deriving from near-surface temperature fluctuations in a jointed rock mass (from Fiorucci et al., 2018)..... 15
- Figure 2.5.** Synoptic plot of the mean daily temperature (red line) and the number of microseismic events per day recorded at the Matterhorn Peak, which clearly highlight the correlation between event clusters and the abrupt drop of temperatures (from Occhiena and Pirulli, 2012)..... 20
- Figure 2.6.** Long-term evolution of seismic noise parameters due to temperature fluctuations are well–described by the synoptic plot of almost 3 years of monitoring activities at the Madonna del Sasso cliff (from Colombero et al., 2018a). Each panel describes: rainfall amount **(a)**, air temperature and rock temperature fluctuations at 20 m depth **(b)**, fundamental frequency and azimuth values derived from H/V spectral ratios **(c)**, seismic velocity changes obtained from cross-correlations between two monitoring stations **(d)**, normalized H/V spectral ratio zoomed on the first resonance frequency of the unstable rock mass **(e)**..... 23
- Figure 2.7.** Simplified sketches representative of thermally-driven mechanisms responsible for fluctuations of resonance frequency ( $f_i$ ) and seismic velocity ( $dV/V$ ) values within a potentially unstable rock mass compartment, separated by the stable sector by a rear subvertical fracture: Fracture-effect (FE) **(a)**, Surface-effect (SE) **(b)**, Bulk-effect (BE) **(c)**. Inner graphs describe the evolution of the most significant mechanical and dynamic parameters due to thermal cyclicity, namely: **T** – air temperature, **fw** – fracture width, **K<sub>c</sub>** –

contact stiffness,  $\mathbf{K}_b$  – bulk stiffness,  $\mathbf{E}_b$  – bulk Young’s elastic modulus,  $\mathbf{G}_b$  – bulk shear modulus,  $\sigma_i$  – internal stresses,  $t$  – time (daily and/or seasonal scale) (from Colombero et al., 2021b)..... 26

## Chapter 3

**Figure 3.1.** Geographic and geodynamic setting of the Maltese Archipelago in the Central area of the Mediterranean Sea (**a**) and main structural elements of the region (**b**) (from Prampolini et al., 2018, modified). Geology of the island of Gozo and localization of the Wied Il-Mielaħ sea arch (**c**). ..... 28

**Figure 3.2.** Thermo-pluviometric plot for the Maltese region based on the 30-year climatic period 1961-1990. Data collected by the Malta Airport MetOffice (Galdies, 2011). ..... 29

**Figure 3.3.** Different views of the Wied Il-Mielaħ sea arch, located in the northwestern sector of Gozo (Malta). Front and bottom view of the arch (**a**, **b**), from which it is possible to observe the regular and block-like morphology of this natural structure; aerial views of the arch (**c**, **d**). ..... 31

**Figure 3.4.** Geology of the northwestern sector of Gozo, where the Wied Il-Mielaħ sea arch is located (**a**). 3D model of the arch where the detailed stratigraphic sequence of the LCL members is represented (**b**). ..... 33

**Figure 3.5.** Simplified sketch model of the evolution and lifecycle of a sea arch (modified from Gatt, 2013). The first stages of a sea arch are characterized by the formation of a small sea tunnel (young sea arch) along the traces of major joints (**a**); the evolution of the sea cliff by slab failures determines not only the retreat of the coastline, but also the widening of the window (mature sea arch) (**b**); collapse of the sea arch and generation of an isolated stack (**c**). ..... 34

**Figure 3.6.** Aerial orthophoto of the Wied Il-Mielaħ sea arch where major fracture traces of the four discontinuity sets are mapped (**a**). Synthetic stereographic projection (equal-angle lower hemisphere) representing pole density distributions and planes of the four main discontinuity sets (**b**). The coexistence of several major discontinuities affecting the integrity of the arch results in a peculiar block-like morphology. .... 35

**Figure 3.7.** Due to its morphology and jointing conditions the Wied Il-Mielaħ structure can be simplified by considering three different compartments partially isolated by major fractures (**a**). The rock bridge is bounded and intersected by five highly persistent discontinuities (**b–d**) characterized by opening values in the range 0.2–0.3 m. This sector of the arch also shows a higher tendency toward gravitational instabilities as witnessed by the presence of (i) a potentially unstable rock volumes in its central part (light blue area, **e**), (ii) a partially isolated rock slab (orange area, **c–e**), and (iii) multiple detachment areas of small rockfalls (yellow areas, **d**, **e**). ..... 37

**Figure 3.8.** Panoramic view of the abandoned Prenestina quarry located within the municipality of Acuto (central Italy) (a). Aerial orthophoto of the western sector of the quarry where the Acuto field laboratory was implemented in 2015 (b). The 20 m<sup>3</sup> rock block selected as the main target of the permanent multiparametric monitoring system..... 38

**Figure 3.9.** Geological sketch of the Central Appenine region: (A) Marine and continental Plio–Quaternary deposits, (B) Pliocene–Pleistocene volcanic deposits, (C) Pliocene conglomerates, (D) Messinian conglomerates, (E) Tortonian flysch units, (F) Meso-Cenozoic carbonates of the Umbrian domain, (G) Meso-Cenozoic carbonates of the Latium-Abruzzi domain, (H) Triassic carbonate succession, (I) main normal faults, (L) main thrusts (from Billi and Tiberti, 2009; modified)..... 40

**Figure 3.10.** Geological map of Acuto (scale 1:10.000). The location of the quarry area where the field laboratory was implemented is highlighted by the blue box (courtesy of Dr. Geol. Paolo Sarandrea; modified)..... 41

**Figure 3.11.** Thermo-pluviometric plot for the Piglio-Acuto area based on the 15-year climatic period 2000-2015 (source: Regione Lazio)..... 42

**Figure 3.12.** Front view of the potentially unstable rock block selected as the main target of the multiparametric monitoring system of the Acuto field laboratory, along with the fault line that laterally bounds its volume (a); Back view of the rock block and of the open joint that determines the its partial detachment from the rock wall behind..... 44

**Figure 3.13.** Representation of the main joint traces dissecting the monitored rock block and the adjacent quarry wall sector (a); Synthetic stereographic projection (equal-angle lower hemisphere) representing pole density distributions and planes of the four main discontinuity sets, along with the direction of the slope face (SF) (b); open joint acting as the release system that separates the rock block from the rock mass (c); monoaxial microaccelerometer installed on the rock block surface during one of the performed long-term microseismic monitoring campaigns (d); fully-equipped weather station (e); temperature probe (f); extensometer installed on an open fracture along with a strain gauge placed on a microcrack and covered with aluminum tape for thermal insulation (g). ..... 47

**Figure 3.14.** Seismic motion wave frequency spectrum and field of application of microseismic monitoring (from Cai et al., 2007)..... 50

**Figure 3.15.** Interpolated map of mean site-to-reference spectral ratios for the horizontal components of ground motion — 125 °N in the upper row, normally oriented to the slope, and 35 °N in the lower row, parallelly oriented to the slope — (from Burjáněk et al.,2010). ..... 54

**Figure 3.16.** Technical drawings of the Bruel & Kjaer type-8344 microaccelerometer (a) and relative calibration chart describing the dynamic range of flat frequency response (b).

---



---

Complementary modules composing the acquisition system (c): data logger — SomatXR CX23-R (on the left); signal amplifier — SomatXR MX1601B-R (on the right). ..... 56

**Figure 3.17.** Front view of the monitored jointed rock block at the Acuto field laboratory (a). The two boxes help to better visualize the different volumes involved by the configurations adopted during the first (I, red box) and the second monitoring campaign (II, green box). Between February and May 2018, six microaccelerometers were deployed along a linear alignment which was specifically designed to mark the transition from the stable rock mass to the unstable rock block (b). The second monitoring campaign (November 2018 - October 2019) was conducted by installing six microaccelerometers in a “composite” double triaxial configuration (c). ..... 59

**Figure 3.18.** Schematic view of sensors positioning during ambient vibration monitoring at the Wied Il-Mielah sea arch: horizontal alignment along the entire length of the arch (a) and composite triaxial arrays installed on the three compartments of the arch (b). Panels c–e show the different installation stages of the microseismic array. .... 62

**Figure 3.19.** Aerial view of the Wied Il-Mielah sea arch where the location of active and reference seismometers is reported (a). Active seismometer placed on the rock pillar of the arch (b) and reference sensor placed on horizontal bedrock (c). ..... 64

**Figure 3.20.** Flow chart summarizing the adopted workflow for the automatic detection and preliminary classification of microseismic events from ambient seismic noise continuous recordings. .... 67

**Figure 3.21.** Example of one event automatically detected and classified as microseismic event through visual screening of its time and frequency domain features (left: signal waveform; center: power spectral density estimate; right: spectrogram). ..... 69

**Figure 3.22.** Example of one event automatically detected and classified as false event through visual screening of its time and frequency domain features (left: signal waveform; center: power spectral density estimate; right: spectrogram). ..... 69

**Figure 3.23.** Fourier amplitude spectrum (FAS) of a 3-hour long recording affected by the presence of periodically recurrent narrow spectral peaks (a). The working principle of the used Hampel filter is described by the plot in panel b:  $M$  – median value,  $3MAD$  – threshold value equals to three times the median absolute deviation. Example of FAS before (blue line) and after (green line) the application of the designed filter (c). The efficiency of this approach is witnessed by the perfect similarity between the original and the filtered signal (d). ..... 75

**Figure 3.24.** Polarization ellipse showing the three parameters previously described (strike, dip and ellipticity) (a). Example of the histogram representing the relative occurrence of strike –  $\varphi$  – (azimuth) of ambient vibrations for a single frequency and polar plot representation of histograms for different frequencies, where the color-scale indicated the relative frequency of occurrence (b) (modified from Burjánek et al., 2012). ..... 78

---

---

<b>Figure 3.25.</b> Partial representation of the EM radiation spectrum. Infrared (IR) and adjacent spectral regions and expanded view of the so-called thermal infrared. This is the region where IR imaging systems for short-wave (SW), mid-wave (MW), or long-wave (LW) cameras exist (from Vollmer and Möllmann, 2013). .....	79
<b>Figure 3.26.</b> Aerial view of the Wied II-Mielah sea arch in which the location of the weather station and the acquisition point of IR images (i.e., where the tripod was located) are shown (a, b). Simplified sketch of the georeferencing process of IR images for reconstructing a panoramic view of surface temperature of the arch (c): $d$ – acquisition distance, $\beta$ – horizontal angle of view of the IR camera, $\theta$ – total angle of view of the panoramic image obtained by mosaicking overlapped thermograms. ....	87
<b>Figure 3.27.</b> Front view of the arch where the location of control points for the extraction of temperatures is indicated by colored circles (a). Example of TIR imagery processing and analysis (b): 1D and 2D analyses were performed by extracting temperature time series from the abovementioned control points (c) and through the computation of distributed daily mean temperatures and thermal ranges (d). ....	89
<b>Figure 3.28.</b> Acquisition method used for the reconstruction of 3D point clouds of the rock block from IRT surveys (a, b). Front view of the rock block from which the cold signatures of the employed highly reflective aluminum GCPs are evident (c) (modified from Grechi et al., 2021). ....	91
<b>Figure 3.29.</b> Adopted workflow for the generation of TIR point clouds (from Grechi et al., 2021). ....	95

## Chapter 4

<b>Figure 4.1.</b> Results of the sensitivity analysis performed on the $N_{Th}$ (i.e., number of channels simultaneously triggered by the same event) considering the microseismic dataset collected during the monitoring campaign of February 2020: number of detected events per hour (a) and cumulative number of events (b). ....	97
<b>Figure 4.2.</b> Example of two unclassified events recorded by the microseismic monitoring system at the Wied II-Mielah sea arch during the campaign of February 2020: waveforms (a, d), power spectra (b, e) and spectrograms (c, f). ....	98
<b>Figure 4.3.</b> Temporal evolution of maximum frequency – $f_{max}$ – (a), normalized amplitude – $A_{max}/A_{mean}$ – (b), and uniform duration (c) of the events composing the manually classified dataset for the monitoring campaign of February 2020. ....	99
<b>Figure 4.4.</b> Microseismic dataset collected at the Acuto field laboratory during the two monitoring campaigns conducted between February 2018 and October 2019. Number of	

---

events per day (a), cumulative number of events (b), number of events detected per accelerometers during the first (c) and second monitoring campaign (d). ..... 101

**Figure 4.5.** Distributions of the detected events (a) and of the 1-hour recorded files (b) during both monitoring campaigns as a function of the hour of the day..... 102

**Figure 4.6.** Examples of electrical disturbances recorded at the Acuto field laboratory and manually classified as false events: waveforms (a, d), power spectra (b, e) and spectrograms (c, f)..... 103

**Figure 4.7.** Examples of two typical events recorded at the Acuto field laboratory and manually classified as microseismic events: waveforms (a, d), power spectra (b, e) and spectrograms (c, f)..... 104

**Figure 4.8.** Examples of two event sequences recorded at the Acuto field laboratory and manually classified as microseismic events: waveforms (a, d), power spectra (b, e) and spectrograms (c, f)..... 105

**Figure 4.9.** Results of the comparison between manually classified false and microseismic events based on time and frequency domain features. The following plots are presented: kurtosis vs bracketed duration (a), kurtosis vs uniform duration (b), maximum amplitude normalized to the mean of the envelope of the signal ( $A_{\max}/A_{\text{mean}}$ ) vs Arias Intensity ( $I_A$ ) (c),  $A_{\max}/A_{\text{mean}}$  vs the frequency peak of power spectra ( $f_{\max}$ ) (d) and the 10-Hz frequency band with the maximum spectral content ( $f_{\text{band}}$ ) (e). ..... 107

**Figure 4.10.** Synthesis of results obtained from the statistical comparison the two manually identified classes of detected events at the Acuto field laboratory for the period February 2018 – October 2019. For each class, the extension of the blue boxes represents the interquartile range (IQR, defined as the difference between the upper (Q3) and lower (Q1) quartiles), red lines are median values, black whiskers extend to extreme values and red crosses are the not considered outliers. The parameters considered for this analysis are: PGA (a), normalized amplitude (b), kurtosis (c), Arias Intensity (d), bracketed (e) and uniform duration (f), peak frequency (g) and most energized frequency band (h). ..... 108

**Figure 4.11.** Comparison between the logarithm of Arias Intensity ( $I_A$ ) and the logarithm of the cumulative number of occurrences (N) for microseismic events (a) and false events (b), following the modified Gutenberg & Richter (1954) power-law relation. .... 109

**Figure 4.12.** Cumulative number of microseismic and false events computed over the entire monitoring period (a). 1-hour air temperatures and daily rainfall recorded by the weather station installed inside the quarry area (b). Four time intervals (P<sub>1</sub>–P<sub>2</sub>–P<sub>3</sub>–P<sub>4</sub>) are highlighted in both plots representing the periods in which the highest increments in the event occurrence were observed. Gray areas in panel d–e represent periods in which the microseismic monitoring network was not working due to power supply interruptions. .... 110

**Figure 4.13.** Comparison between the temporal evolution of MS events and environmental factors at the Acuto field laboratory: daily and cumulative number of events (a), daily maximum and minimum rock temperatures (b), daily and cumulative rainfall (c). Dashed lines highlight a 10-day period in which rock mass temperatures experienced a sharp decrease due to an extreme meteorological event. Gray areas in panel d–e represent periods in which the microseismic monitoring network was not working due to power supply interruptions. .... 111

**Figure 4.14.** Comparison between the distribution of MS events (a), daily thermal ranges (b) and mean daily temperature rates (c). In each plot, the distinction between heating (in red) and cooling (blue) phases of the rock mass is proposed with a view to investigating the response of the jointed rock block to different thermal regimes of increasing (heating) or decreasing (cooling) temperatures. Gray areas in panel d–e represent periods in which the microseismic monitoring network was not working due to power supply interruptions. . 113

**Figure 4.15.** Comparison between environmental factors and the occurrence of MS events for the period comprised between 23/02/2018 and 13/03/2018, when the quarry area was interested by an intense winter storm: 10-minute air (blue line) and rock mass temperature (red line) (a), daily temperature range (i.e., thermal excursion) (black line) and 1-hour rock temperature rate (blue line) (b), 1-hour cumulated rainfalls (blue bars) and relative 1-hour cumulative curve (blue line) (c), 1-hour cumulated MS events (red bars) and relative 1-hour cumulative curve (red line) (d), daily distribution of MS events occurred during the heating phase (red bars) and cooling phase (blue bars) of the rock mass (e), temporal evolution of Arias Intensity ( $I_A$ ) of the MS events occurred during the heating phase (in red) and cooling phase (in blue) of the rock mass (f). Gray areas in panel d–f represent periods in which the microseismic monitoring network was not working due to power supply interruptions. . 117

**Figure 4.16.** Comparison between environmental factors and the occurrence of MS events for the period comprised between 08/04/2018 and 25/04/2018: 10-minute air (blue line) and rock mass temperature (red line) (a), daily temperature range (i.e., thermal excursion) (black line) and 1-hour rock temperature rate (blue line) (b), 1-hour cumulated rainfalls (blue bars) and relative 1-hour cumulative curve (blue line) (c), 1-hour cumulated MS events (red bars) and relative 1-hour cumulative curve (red line) (d), daily distribution of MS events occurred during the heating phase (red bars) and cooling phase (blue bars) of the rock mass (e), temporal evolution of Arias Intensity ( $I_A$ ) of the MS events occurred during the heating phase (in red) and cooling phase (in blue) of the rock mass (f). Gray areas in panel d–f represent periods in which the microseismic monitoring network was not working due to power supply interruptions. .... 118

**Figure 4.17.** Comparison between environmental factors and the occurrence of MS events for the period comprised between 10/06/2019 and 24/06/2019: 10-minute air (blue line) and rock mass temperature (red line) (a), daily temperature range (i.e., thermal excursion) (black line) and 1-hour rock temperature rate (blue line) (b), 1-hour cumulated rainfalls (blue bars) and relative 1-hour cumulative curve (blue line) (c), 1-hour cumulated MS events (red bars) and relative 1-hour cumulative curve (red line) (d), daily distribution of MS events occurred during the heating phase (red bars) and cooling phase (blue bars) of the rock mass (e), temporal evolution of Arias Intensity ( $I_A$ ) of the MS events occurred during the heating

phase (in red) and cooling phase (in blue) of the rock mass (f). Gray areas in panel d–f represent periods in which the microseismic monitoring network was not working due to power supply interruptions. .... 119

**Figure 4.18.** Percentage distribution of MS events during heating (in red) and cooling phases (in blue) for the whole monitoring period (a), the only winter storm of February 2018 (b), and for the entire monitoring period excluding the winter storm (c). .... 120

**Figure 4.19.** Synthesis of the results obtained from the analysis of ambient seismic noise at the Acuto field laboratory: example of 1-hour time history (a); mean and standard deviation of background noise levels recorded during the second monitoring campaign (November 2018 – October 2019) by each microaccelerometer (b); power spectral density (PSD) and residual spectral noise of the employed Bruel & Kjaer Type 8344 microaccelerometers (c); evolutionary power spectral density (EPSD) for a 12-day period (d). .... 122

**Figure 4.20.** Comparison between ambient seismic noise recordings at the two case studies (MIE – Wied Il-Mielah; ACT – Acuto): 1-hour acceleration time histories (a); mean and standard deviation of background noise levels (b); power spectral densities (PSD) and the level of spectral residual noise of microaccelerometers derived from calibration charts (SRN) (c). .... 123

**Figure 4.21.** Results of spectral analysis for the reference station (MIE-2, in blue) and the active station (MIE-1, in red) located on the arch (a, c, e) and SRSR (site-to-reference spectral ratio, in green) computed for each component of ground motion (b, d, f): EW component (a, b), NS component (c, d), UD component (e, f). Gray bands highlight the three spectral peaks ( $f_1, f_2, f_3$ ) interpreted as resonance frequencies of the Wied Il-Mielah arch. .... 125

**Figure 4.22.** Results of polarization analysis for the reference station (MIE-2) and the active station (MIE-1) located on the arch; colormaps are indicative of the relative frequency of occurrence of a specific frequency in the noise recording; plot of ellipticity vs. frequency (a, b); plot of strike vs. frequency – frequencies are represented along the log-scaled radius – (c, d); plot of dip vs. frequency – frequencies are represented along the log-scaled radius (e, f). .... 126

**Figure 4.23.** Stereographic projection (equal-angle, lower hemisphere) representing the comparison between the orientations of the three resonance frequencies ( $f_1, f_2, f_3$ ) and the main discontinuity sets (J1, J2, J3, J4). The black dashed line indicates the orientation of the major axis of the arch. .... 127

**Figure 4.24.** Summary of the two array configurations employed for ambient seismic noise recordings at the study site. The linear array is composed of six microaccelerometers recording only the EW component of ground motion (a); the triaxial array is composed of 8 microaccelerometers deployed to record all components of ground motion on the pillar (EW – ch1<sub>T</sub>, NS – ch2<sub>T</sub>, UD – ch3<sub>T</sub>) and bridge compartments (EW – ch4<sub>T</sub>, NS – ch5<sub>T</sub>, UD –

ch6<sub>T</sub>). Differently, the bedrock sector was instrumented with only two microaccelerometers (EW – ch7<sub>T</sub>, UD – ch8<sub>T</sub>)..... 128

**Figure 4.25.** Results of spectral analysis for each channel of the linear array: hourly power spectral densities (PSDs) for channels located in correspondence of the pillar (**a, b** – in green), of the bridge (**c, d** – in red) and of the bedrock (**e, f** – in blue) compartments. Gray bands highlight the three spectral peaks ( $f_1, f_2, f_3$ ) interpreted as resonance frequencies of the arch..... 130

**Figure 4.26.** Results of spectral analysis for each channel of the triaxial array: hourly power spectral densities (PSD) for channels located in correspondence of the pillar (**a, b, c** – in green), of the bridge (**d, e, f** – in red) and of the bedrock (**g, i** – in blue) compartments. The NS component of ground motion was not recorded in correspondence of the bedrock sector. Gray bands highlight the three spectral peaks ( $f_1, f_2, f_3$ ) interpreted as resonance frequencies of the arch. .... 131

**Figure 4.27.** Results of SRSR (site-to-reference spectral ratio) analysis considering the linear array of one-component microaccelerometers deployed on the Wied Il-Mielaħ arch (see **Figure 4.24**). Normalized amplitude spectra (**a**), and spectral ratios computed between ch1–ch5 and the reference sensor ch6 (**b**). Gray bands highlight two of the three resonance frequencies of the arch ( $f_2$  and  $f_3$ ). Spatial distribution of spectral ratios at  $f_2 = 5.4$  Hz (**c, e**) and  $f_3 = 10.8$  Hz (**d, f**) (black arrows describe the direction of maximum polarization of  $f_2$  and  $f_3$ ). The size and color of each point varies according to the relative amplification factor. In panel **e** and **f**, the amplification factor at each measuring channel is plotted against the progressive distance between ch6 ( $x = 0$  m) and the external boundary of the arch ( $x = 40$  m), where the relative position of main discontinuities (F1–F4) is also reported. The distinction between the three sectors of the arch is defined by the three colored areas: anchored bedrock – blue, rock bridge – red, rock pillar – green. .... 133

**Figure 4.28.** Temporal evolution of the 54 hourly normalized power spectral densities (PSDs) recorded at the MIE-1 station during the monitoring campaign of February 2020 for the NS (**a**), EW (**b**) and UD (**c**) components. PSDs were hourly normalized to their maximum value to better follow their temporal evolution. Two 12-hour gaps are present in the recording and are highlighted by gray bands..... 136

**Figure 4.29.** Temporal evolution of hourly normalized power spectral densities (PSDs) centered on the three identified resonance frequencies of the arch –  $f_1$  (**a**),  $f_2$  (**b**) and  $f_3$  (**c**). 10-minute averaged rock temperatures recorded at the surface of the arch (**d**). 10-minute average relative humidity (yellow line) and wind speed (green line) recorded by the weather station located in proximity of the arch. PSDs were normalized to their maximum value in each frequency band to better follow their temporal evolution. Two 12-hour gaps are present in the recording and are highlighted by gray bands. .... 137

**Figure 4.30.** Results of cross-correlation between the three resonance frequencies of the arch and rock surface temperatures at the daily scale. Comparison between the temporal evolution of  $f_1, f_2$  and  $f_3$  and rock surface temperatures (**a–c**). Results of the sine curves

---

fitting on raw data (e–f). Normalized cross-correlograms for each resonance frequency (g–i). ..... 139

**Figure 4.31.** Temporal evolution of hourly normalized power spectral densities (PSDs) (a) and site-to-reference spectral ratios (SRSRs) (b), centered around  $f_2$ , during the four monitoring campaigns conducted from February 2019 and February 2020. Evolution of rock surface temperatures recorded at the site, where blue dashed lines indicate the mean value computed over the considered monitoring period (c). PSDs in panel a were computed for ch1 of the linear array, located on the pillar sector of the arch, and SRSRs in panel b were compiled considering ch6 of the same array as the reference station. Gray bands highlight time gaps in the recordings due to instrumental malfunctioning. .... 141

**Figure 4.32.** Temporal evolution of hourly normalized power spectral densities (PSDs) (a) centered around  $f_1$ , during the four monitoring campaigns conducted from February 2019 and February 2020. Evolution of rock surface temperatures recorded at the site, where blue dashed lines indicate the mean value computed over the considered monitoring period (b). PSDs were computed for ch2 (NS component) of the triaxial array installed on the pillar sector of the arch. The PSDs of all monitoring campaigns are bandpass filtered around  $f_1$  to enhance the recognition of its temporal evolution, with the exception of February 2020, because several spectral disturbances influenced lower and higher frequencies. Gray bands highlight time gaps in the recordings due to malfunctioning of the monitoring systems. 142

**Figure 4.33.** Results of cross-correlation of  $f_1$  and  $f_2$  with air temperature at the seasonal scale. The temporal evolution of  $f_1$  (a) and  $f_2$  (b) from June 2018 to February 2020 was compared to mean monthly air temperature time series (c) extracted from the database of the permanent weather station of the International Luqa Airport (Malta). Results of the sine curves fitting on raw data (e–f). Normalized cross-correlograms for each resonance frequency (g–i). The red bands in panels a–c highlight the monitoring campaign during which during which a violent storm invested the entire Maltese Archipelago. .... 144

**Figure 4.34.** Results of the IRT monitoring performed in April 2019 showing the 2D evolution of surface temperature distributions from 07:00 (at sunrise – a) to 18:00 (after sunset – n). Thermograms are overlapped to visible images of the arch to enhance the comparison between near-surface temperatures and morphological features of the monitored cliff. Color scales are normalized to daily maximum and minimum values to highlight the temporal evolution of distributed thermal fields throughout the analyzed daily thermal cycle. .... 148

**Figure 4.35.** Visible (a) and thermal (b) images of the monitored surface where the traces of main fractures (i.e., white dashed lines), as well as oriented surfaces and scar areas (i.e., green dashed areas) are reported. It is evident that such elements, along with minor morphological irregularities, are responsible for the heterogeneity of surface temperature distributions since they cause marked thermal contrasts to rise. .... 149

**Figure 4.36.** Surface temperature distributions computed for the IRT survey of April 2019 (a). In each chart, the median (M, red line) and interquartile range (IQR, blue box) values

are plotted to enhance the great variability affecting surface temperature distributions during different hours of the day. Synthesis of the results obtained for every hour of IRT monitoring (b). For each hour, the extension of the blue boxes represents the interquartile range (IQR, defined as the difference between the upper (Q3) and lower (Q1) quartiles), red lines are median values, and black whiskers extend to extreme values. The light blue area in panel b highlights the amplitude of the observed thermal excursion. .... 151

**Figure 4.37.** Daily and seasonal variability of temperatures derived from the 1D analysis of thermograms performed on Autumn (a), Winter (b), Spring (c) and Summer (d) surveys. In each plot, the evolution of temperatures extracted from clusters of points in correspondence of the rock surface ( $T_R$ ), a fracture zone ( $T_F$ ) and a hollow area ( $T_H$ ) is compared to the evolution of air temperature ( $T_A$ ). Gray bands highlight time gaps in IRT acquisitions... 153

**Figure 4.38.** Comparison of hourly computed differences between temperature timeseries derived from IRT and air temperatures recorded by the weather station during the Autumn (a), Winter (b), Spring (c) and Summer (d) IRT surveys. In these bar charts, yellow boxes highlight time intervals in which IRT-derived temperatures were higher than air temperature ( $\Delta T > 0$ ), while blue boxes indicate the opposite condition ( $\Delta T < 0$ ). .... 154

**Figure 4.39.** Results of the comparison between quantitative descriptors of heating and cooling ramps of the monitored arch during different seasons: Heating Thermal Rate (HTR) (a), Cooling Thermal Rate (CTR) (b), Heating Thermal Excursion (HTE) (c), Cooling Thermal Excursion (CTE) (d). The amplitude and time duration of heating ramps were calculated considering the first measurement and the positive temperature peak (generally found around 10:00–12:00), while cooling ramps characteristics were derived after the stages of maximum insolation, thus when the effect of the incident solar radiation can be neglected (14:00–18:00). .... 156

**Figure 4.40.** 2D color-scaled visualization of daily mean temperature distributions computed for the Autumn (a), Winter (b), Spring (c) and Summer (d) surveys. The respective histograms, where bars are colored according to the same color-scale of thermograms, show how the amplitude and distribution of mean temperatures strongly vary under different climatic conditions. In each chart, the median (M, red line) and interquartile range (IQR, blue box) values are also plotted. Synthesis of the results obtained for every seasonal survey (e). For each season, the extension of the blue boxes represents the interquartile range (IQR, defined as the difference between the upper (Q3) and lower (Q1) quartiles), red lines are median values, and black whiskers extend to extreme values. .... 158

**Figure 4.41.** 2D color-scaled visualization of daily temperature range distributions computed for the Autumn (a), Winter (b), Spring (c) and Summer (d) surveys. The respective histograms, where bars are colored according to the same color-scale of thermograms, show how the amplitude and distribution of temperature ranges strongly vary under different climatic conditions. In each chart, the median (M, red line) and interquartile range (IQR, blue box) values are also plotted. Synthesis of the results obtained for every seasonal survey (e). For each season, the extension of the blue boxes represents the interquartile range (IQR, defined as the difference between the upper (Q3) and lower (Q1) quartiles), red lines are median values, and black whiskers extend to extreme values. .... 159

---



**Figure 4.42.** 3D TIR merged point clouds of the Spring survey at four different acquisition times; (a-d) The front view (i.e., eastward) and (e-h) back view (i.e., southward) of the rock block are shown for each point cloud in order to demonstrate the great enhancement in the visualization of surface temperature distributions and evolution in time (modified from Grechi et al., 2021)..... 161

**Figure 4.43.** Color-scale maps of residual distances between TIR point clouds, acquired at 11:30 (a), 13:00 (b), 16:00 (c) and 17:00 (d) during the spring survey, and the reference high-resolution RGB optical point cloud. For each map, the distribution of residual distances is plotted along with their statistical descriptors: M – median value, IDR – interdecile range (from Grechi et al., 2021). ..... 162

**Figure 4.44.** Temperature distributions derived from original (red bars) and merged point clouds (blue bars) (a). Comparison between mean temperature values and standard deviations of original and merged point clouds (b). The high grade of correspondence between derived values is also highlighted, both in terms of central tendency and dispersion values, by the computation of the absolute difference in mean ( $\Delta\mu$ ) and standard deviation ( $\Delta\sigma$ ) values for each original and merged point cloud (c) (modified from Grechi et al., 2021). ..... 163

**Figure 4.45.** Results of the comparative analysis between temperatures extracted from 2D thermograms (a-b) and 3D TIR point clouds (c) for the Spring survey. Surface profiles from which temperatures were extracted (AB and CD) are marked both in 2D thermograms and for an example of a 3D point cloud visualization (d-e). None of the two profiles intercept any instrumental device of the monitoring system. Absolute temperature values are plotted against the length of the respective section for 3D and 2D data (f-g). For each analyzed section and for every acquisition, the difference between absolute temperature values ( $\Delta T$ ) was computed (h - section AB, i - section CD). A  $\pm 2$  °C buffer zone, representing the calibrated temperature accuracy of the IR camera, is also highlighted (yellow box) (from Grechi et al., 2021)..... 165

**Figure 4.46.** 3D color-scale visualization of daily temperature ranges of the investigated rock block computed for the Autumn (a), Winter (b), Spring (c) and Summer (d) survey. The respective histograms show how the amplitude and distribution of temperature ranges strongly vary under different climatic conditions. Three percentiles (P25, P50 and P75), along with the i-th percentile corresponding to a temperature range equal or greater than 8 °C, are also presented to highlight the main differences between the four distributions of temperature range (modified from Grechi et al., 2021). ..... 168

**Figure 4.47.** Color-scale representation of the 3D point cloud dip angle values (a) along with the relative frequency distribution of dip angle classes (b). Dip angle values corresponding to the 27th and 50th percentiles are marked in the histogram (from Grechi et al., 2021). 169

**Figure 4.48.** 3D plot showing the eight dip direction classes from two different perspectives, clearly enhancing the existence of differently oriented surfaces of the rock block (a-b). Polar plots of the eight dip direction classes representing temperature ranges as derived for the four

performed surveys (c). Every colored area describes, according to its color band and radial extension, the mean ( $\mu$  - thick black line) and standard deviation values ( $\mu \pm \sigma$ ) of the temperature range recorded during each seasonal survey for every class of dip direction (from Grechi et al., 2021). .....171

## Chapter 5

**Figure 5.1.** Comparison between the cumulative number of days in which more than 1 MS event was recorded (in red) and the number of days characterized by no MS events (in blue) at the Acuto field laboratory. The longest time intervals in which microseismic activity was absent are highlighted within the entire monitoring period (February 2018–October 2019). Gray areas represent periods in which the microseismic monitoring network was not working due to power supply interruptions. ....173

**Figure 5.2.** Temporal evolution of displacement and rock temperature monitoring timeseries recorded by the permanent multiparametric monitoring system at the Acuto field laboratory. ....177

**Figure 5.3.** From the preliminary identification of potentially unstable subvolumes (Sv) the reconstruction of merged thermal and optical point clouds could allow to assess their thermal behavior. On such elements, the analysis of temperature distributions and evolution in time, as well as their geomechanical conditions, can provide useful information to constrain the role near-surface temperature fluctuations in controlling their stability (from Grechi *et al.*, 2021, modified). ....180

**Figure 5.4.** Exemplary sketch that summarizes the logic behind the need for investigating thermomechanical effects on jointed rock structures at different dimensional scales: **a)** rock block ( $10^1 \text{ m}^3$ ), **b)** rock column ( $10^2 \text{ m}^3$ ), **c)** rock arch ( $10^3 \text{ m}^3$ ). From a theoretical perspective, the comprehension of the interaction mechanisms between near-surface daily and seasonal temperature fluctuations and rock masses at progressively increasing dimensional scales might lead to the identification of the contribution of single elements in the dynamics of thermomechanical effect on jointed rock masses. ....182

**Figure 5.5.** 3D models of the jointed rock block (**a**), main target of multiparametric monitoring activities at the Acuto field laboratory since 2016, and the jointed rock column (**b**) that will be instrumented with multiple geotechnical and geophysical devices. Low- and high-frequency geophones already installed inside the Acuto field laboratory (**c**, **d**). .....184





## Abstract

The study of the deformative response to cyclical thermal stresses of rock masses is considered crucial in geological risk mitigation relative to those instabilities that can configure high hazard slope instability scenarios due to their impulsiveness and high frequency of occurrence. Under specific climatic conditions, the superposition of heating and cooling cycles can influence the mechanical behavior of rock masses. Temperature fluctuations can exert slight yet repeated perturbations of stress fields resulting in a day-to-day cumulative effect, contributing to lead rock slopes toward prone-to-failure conditions over wide time scales. As a direct consequence of the thermal expansion-contraction cycles, the stress field of rock masses undergoes such perturbations capable of inducing both the genesis of new cracks and the growth of preexisting ones (i.e., subcritical crack-growth). These processes can induce inelastic deformations that can trigger shallow slope instabilities, such as rockfalls and rock topples. A multimethodological approach based on environmental, thermal, microseismic, and ambient seismic noise monitoring was designed for the purpose of identifying and characterizing nonlinearity of thermally-induced deformation on jointed rock masses at different dimensional scales. Two different case studies—a massive 10.000 m<sup>3</sup> natural rock arch and a 20 m<sup>3</sup> intensely jointed rock block—were selected to investigate the influence of repeated thermal cycles on their stability. In particular, their complex 3D geometries, different volume sizes and jointing conditions were considered to be of great interest to better comprehend the effectiveness of shallow thermal stresses interacting with different rock mass dimensional scales.

Passive seismic monitoring techniques (i.e., ambient seismic noise and microseismic monitoring) allowed to obtain interesting insights on the interaction between the investigated rock masses and the periodic fluctuations of their temperature fields. The analysis of ambient seismic noise was aimed at investigating the possible wandering of resonance frequencies within short- to long-duration monitoring surveys, and highlighted the existence of thermally-driven, in-phase daily and seasonal fluctuations, but no irreversible modifications in their values—potentially related to a progressive damaging process and acceleration toward failure of the structure—were observed. For what concerns the analysis of local microseismicity, a semi-automatic approach was implemented to

---

identify possible irreversible clusters of fracture-related microseismic events over long-term monitoring windows. Based on the collected data, the here presented analyses highlighted not trivial insights on the role played by continuous near-surface temperature fluctuations and extreme thermal transients in influencing the stability of rock masses. In particular, the comparison of monitoring periods characterized by the most intense microseismic activity pointed out a peculiar distribution of microseismic events during heating and cooling phases of the rock mass in relation to different environmental conditions. These behaviors can be interpreted as the consequence of different driving mechanisms at the base of local failures.

Along with the study of the seismic response of these jointed rock systems, Infrared thermography surveys were carried out at both sites for the characterization of their thermal behavior through different methodological approaches (i.e., 2D and 3D). The multitemporal acquisition of thermograms at Wied Il-Mielah allowed to achieve a preliminary characterization of the thermal behavior of the rock arch in response to the continuous fluctuation of near-surface temperatures at the daily and seasonal scale, highlighting the importance of considering the effect solar radiation and its interaction with complex morphological settings. Besides, a simplified method integrating Structure from Motion and Infrared thermography techniques was adopted at the Acuto field laboratory. The obtained results revealed that through the generation and co-registration of thermal and optical point clouds, the transfer of temperature attributes from low- to high-density point clouds can provide a detailed 3D representation of geometric features and surface temperature distributions and evolutions. The accurate reconstruction of 3D temperature fields will allow to obtain further insights for the assessment of the role played by thermal stresses in the concentration of elastic and plastic deformations in jointed rock masses, giving the possibility to weight the contribution of lighting and shadowing effects on entire slopes or isolated block volumes characterized by variable exposures and hence differentially heated by the solar radiation.

The combination of different approaches can provide new insights on the effects related to near-surface thermal stresses fluctuations by allowing the investigation of the mechanical behavior of rock masses from fracture-scale to joint-isolated rock blocks, and the characterization of the spatio-temporal evolution of near-surface thermal fields.

---

# Chapter 1

## Introduction

In the last few decades, the scientific interest has increased with regards to the analysis of thermally-induced strain and progressive mechanical weathering of rock masses caused by the daily and seasonal fluctuation of near-surface temperatures. The study of the deformative response to cyclical thermal stresses of rock masses is considered crucial in the field of geological risk mitigation especially with respect to high hazard slope instability scenarios with rapid movement and high frequency of occurrence.

It is well known that the continuous action of thermal cycles can be regarded as a non-secondary factor (i.e., preparatory factor) of progressive damaging processes, since it can lead already unstable rock masses toward even more evident unstable conditions, especially in the absence of main triggering factors. In this framework, the investigation of rock mass damaging (RMD) processes commonly requires the definition of monitoring systems and strategies capable of dealing with the timescale of such mechanisms and the dimensional scale of volumes involved in rock mass instabilities. Therefore, it is good practice to collect vast and multiparametric datasets to consider all possible variables that could contribute to potential reversible and irreversible variations of mechanical and dynamic parameters over short- to long-term monitoring windows. However, even year-long monitoring datasets might not show significant changes in the investigated parameters, since fracturing processes at the base of the progressive deterioration of stability conditions of rock masses, such as subcritical crack-growth or the propagation of preexisting discontinuities, tend to become effective over unpredictable and usually wider time scales. On the contrary, when considering fast-evolving instability contexts, irreversible trends of deformations compatible with incipient failures can be identified even in the short-term.

Based on these considerations, and to better constrain the role of temperature fluctuations in driving reversible and irreversible deformations of jointed rock masses, a multimethodological approach was tested, encompassing passive seismic monitoring techniques and infrared thermography surveys, with the aim of analyzing the role played by fracture and microfracture networks in the dynamic of thermally-induced deformative

---

processes in rock masses at the rock block scale or meso-scale. Two different case studies were selected to test this experimental approach. The first one is the Wied Il-Mielaħ sea arch, located in the northwestern sector of Gozo (Malta), which is an outstanding example of coastal landforms and a continuously and fast-evolving 10.000 m<sup>3</sup> jointed rock structure under the pressure of multiple environmental stressors. The second case study is instead represented by a prone-to-fall 20 m<sup>3</sup> rock block that is the main target of an experimental field laboratory located within an abandoned quarry in central Italy (Acuto, FR).

These case studies were selected at the very first stages of this Ph.D. project by following a non-casual logic, as they were considered to be representative of strongly different, or even opposite, geomechanical and environmental boundary conditions. In particular, from a geomechanical perspective, while the Acuto rock block is characterized by a severe fracturing degree, resulting from a dense discontinuity network, the Wied Il-Mielaħ arch outcrops as a massive rock structure dissected in major compartments by few and highly persistent discontinuities.

In virtue of these contrasts in fracturing conditions and volumes, these two elements were considered suitable for evaluating the interaction of thermally-induced processes with different volumes potentially involved in gravitational instabilities, since they range from micro- (< 1 m<sup>3</sup>) to mesoscale (> 10 m<sup>3</sup>) at the two case studies. Several monitoring campaigns at both case studies were carried out by employing a microseismic monitoring array composed of several one-component microaccelerometers, acquiring short- and long-term seismic recordings, with a view of performing a complementary analysis of ambient vibrations and microseismic activity to identify potential evidence of irreversible deformations related to periodic daily and seasonal temperature fluctuations at different dimensional scales. Moreover, multitemporal IRT monitoring campaigns were carried out at the two selected case studies to characterize the 2D and 3D thermal behavior of the outcropping rock masses. The objective of these remote thermal surveys was to investigate the role of jointing and surface conditions in modifying near-surface temperature distributions and evolutions in time. As a matter of fact, the analysis of the role played by near-surface temperatures and the extent to which their fluctuations can influence the dynamic and mechanical behavior of rock masses, constraining their spatial and temporal characteristics, might help in better comprehending thermomechanical processes. It must be stated that the experimental activities discussed in this dissertation did not find completeness

---



during the three years of this Ph.D. project. The outbreak of the Covid-19 pandemic determined the impossibility to pursue the already scheduled plan of experimental activities, among which the data collection at the Wied Il-Mielah case study had to be completely interrupted in February 2020. For this reason, and also considering the impossibility to modify the already employed experimental monitoring setup at both case studies, the here presented activities and relative results must be regarded as a preliminary attempt to shed light on the preparatory role of near-surface temperature fluctuations in controlling the stability conditions of jointed rock masses.

This dissertation is divided into different chapters and for the ease of the reader they can be summarized as follows:

- [Chapter 2](#) provides a brief review of literature sources with the twofold objective of (i) highlighting the preparatory role of near-surface temperature fluctuations for rock slope instabilities, and (ii) presenting several case studies from literature in which integrated geotechnical and geophysical monitoring approaches successfully detected the contribution of thermomechanical effects to progressive rock mass damaging processes;
- [Chapter 3](#) introduces experimental materials and the adopted experimental approach for the study of thermomechanical effects at the two selected case studies. At first, the preliminary description of the geological and geomorphological contexts of the Wied Il-Mielah sea arch and the Acuto field laboratory is provided. Then, focusing on the experimental layout of this work, each monitoring technique is presented with particular attention to the adopted strategies for data acquisition and analysis;
- [Chapter 4](#) presents the results obtained at each case study maintaining the same subdivision of monitoring approaches used in [Chapter 3](#). The results of short- and long-term ambient vibration monitoring campaigns are treated in order to highlight the outcomes of microseismic activity and ambient seismic noise, mainly focusing on their correlation with temperature fluctuations. Then the results obtained from 2D IRT surveys at the Wied Il-Mielah arch and the 3D thermal mapping of the rock block inside the Acuto field laboratory are presented;

- **Chapter 5** illustrates the main inferences derived from the conducted experimental activities, highlighting the outcomes of vibrational and thermal monitoring in the perspective of assessing the influence of thermally-induced effects on jointed rock masses characterized by complex 3D geometries, different dimensional scales and fracturing degrees;
- **Chapter 6** provides conclusive remarks of this work.

Part of the preliminary results obtained in the framework of this research and herein presented has already been published in the following journal papers or conference proceedings:

- Grechi, G., & Martino, S. (2019). Preliminary results from multitemporal infrared thermography surveys at the Wied Il-Mielah rock arch (island of Gozo). *Italian Journal of Engineering Geology and Environment*, 1(1), 41–46. <https://doi.org/10.4408/IJEGE.2019-01.S-07>.
- Marmoni, G. M., Fiorucci, M., Grechi, G., & Martino, S. (2020). Modelling of thermo-mechanical effects in a rock quarry wall induced by near-surface temperature fluctuations. *International Journal of Rock Mechanics and Mining Sciences*, 134(March), 104440. <https://doi.org/10.1016/j.ijrmms.2020.104440>.
- D’Angiò, D., Fantini, A., Fiorucci, M., Grechi, G., Iannucci, R., Marmoni, G. M., Martino, S., & Lenti, L. (2020). Multisensor monitoring for detecting rock wall instabilities from precursors to failures: The Acuto test-site (central Italy). *ISRM International Symposium - EUROCK 2020*.
- Grechi, G., & Martino, S. (2021). Multimethodological Study of Non-linear Strain Effects Induced by Thermal Stresses on Jointed Rock Masses. In *Understanding and reducing landslide disaster risk. Catastrophic landslides and frontiers of landslide Science* (pp. 315–321). [https://doi.org/10.1007/978-3-030-60319-9\\_35](https://doi.org/10.1007/978-3-030-60319-9_35).
- Grechi, G., Fiorucci, M., Marmoni, G. M., & Martino, S. (2021). 3D Thermal Monitoring of Jointed Rock Masses through Infrared Thermography and Photogrammetry. *Remote Sensing*, 13(5). <https://doi.org/10.3390/rs13050957>.

- Grechi, G., D'Angiò, D., Fiorucci, M., Iannucci, R., Lenti, L., Marmoni, G. M., and Martino, S. (2021). Integrated geophysical and geotechnical monitoring for multiscale rock mass damaging investigation at the Acuto Field-Lab (Italy), EGU General Assembly 2021, online, 19–30 Apr 2021, EGU21-9403, <https://doi.org/10.5194/egusphere-egu21-9403>, 2021.
- Grechi, G., D'Angiò, D., Martino, S., Lenti, L. (2021). Thermomechanical effects in jointed rock masses inferred through microseismic signals analysis. VII AIGA National Congress, Lecco 2021.

## Chapter 2

### State of Art

#### 2.1 Near-surface temperature fluctuations as a preparatory factor for rock slope instabilities

Over the last decades, the study of thermally-induced strain effects caused by daily and seasonal near-surface temperature fluctuations of rock slopes has gathered growing interest from engineering geology researchers. The study of the deformative response to cyclical thermal stresses of rock masses is nowadays considered crucial in the field of geological risk mitigation relative to those instabilities that, due to their impulsiveness and high frequency of occurrence, can configure high hazard slope instability scenarios. Under specific climatic conditions, where temperature ranges can exceed the tens of degrees, the effects of the superimposition of heating and cooling cycles, negligible if considered in short time intervals, can influence the mechanical behavior of rock masses acting as a thermal fatigue process (Collins and Stock, 2016; Gischig et al., 2011a, 2011b; Gunzburger et al., 2005). From a more general perspective, rock slope failures can be triggered by several mechanisms, which are in turn controlled by factors constraining their frequencies of occurrence and involved volumes. These factors can be classified into three main groups:

- Triggering factors, such as strong earthquakes and heavy rainfalls that are considered as the most immediate causes of rock mass instabilities due to their intensity and impulsiveness;
- Predisposing factors that permanently characterize rock masses stability and correspond to the main geological, topographical, and geomorphological features. Then, predisposing factors must be considered as the necessary conditions for a slope to evolve toward instability, which can be eventually reached through destabilizing actions of external stresses;
- Preparatory factors that include all those factors controlling medium- to long-term changes in either the internal resistance of natural systems or disturbing forces acting on them.

While predisposing factors show no evolution in time, permanently affecting the stability of rock masses (Fischer and Huggel, 2008), triggering and preparatory factors evolve in time and space, eventually determining generalized or localized failure events. The role played by triggering and preparatory factors in controlling the stability of rock masses can be better understood through the landslide–sequencing model proposed by Finlayson and Statham (1980) and modified by Julian and Anthony (1996) (Figure 2.1). This model highlights the great distinction between immediate and progressive failure causes, provided that the former act directly on rock masses by provoking sudden decreases of internal resistance or the abrupt increase in the magnitude of disturbing forces, while the latter exert a continuous and cumulative effect which requires longer time intervals to produce irreversible consequences (Gunzburger et al., 2005).

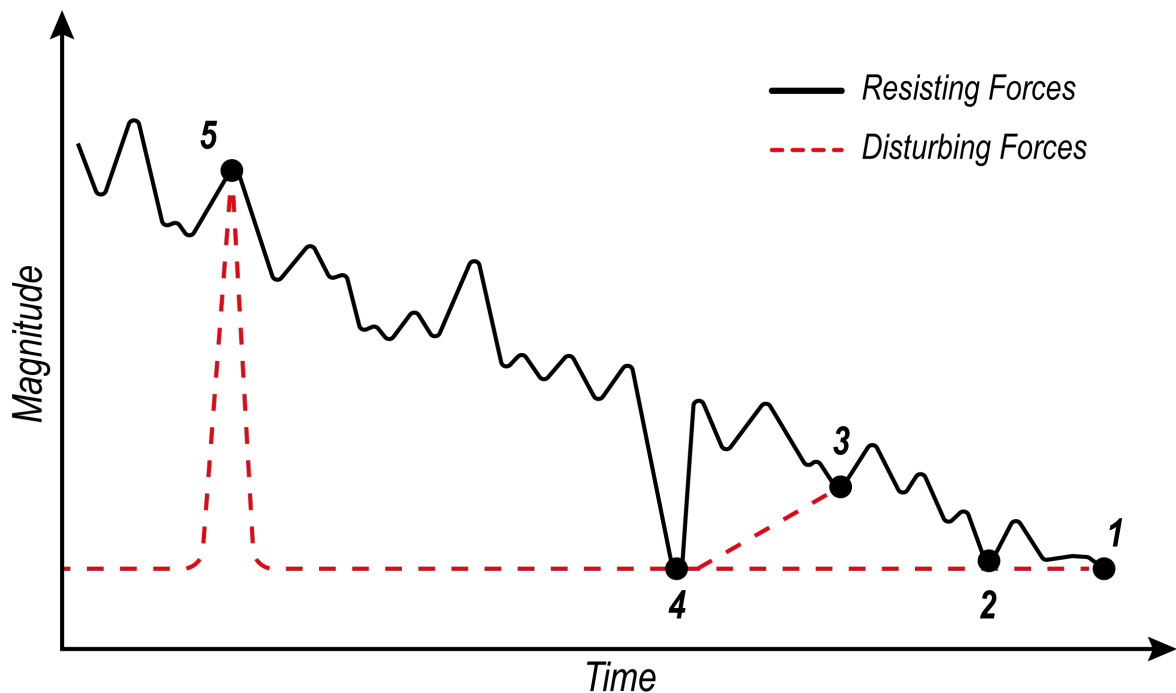


**Figure 2.1.** Landslide–sequencing model explaining the short- to long-term evolution of a landslide through the consideration of triggering and preparatory factors (from Julian and Anthony, 1996 and adapted by Gunzburger et al., 2005; modified).

Since the stability of slopes is controlled by the equilibrium between resisting and disturbing forces, the integrity of rock masses is granted until the overall internal resistance of the natural system is greater than the sum of all destabilizing external forcing. Rock mass failure occurs when disturbing forces equal resisting forces, as described by points 1 to 5. Points 4 and 5 describe failures that are the direct consequence of brief and violent phenomena which are concurrently responsible for lowering the level of resistance (point 4) and increasing the

intensity of external stresses (point 5). These are the cases of strong earthquakes, heavy rainfalls, or storms, which action can lead to slope failures in very short time intervals. Point 3 represents the case of the progressive increase of disturbing forces (e.g., slope steepening due to toe erosion) that can lead to failure over medium to long time spans ( $10^2$ – $10^4$  years). Failures at points 1 and 2 can instead be considered as the result of the long-term gradual decrease of resistance levels due to rock weathering and progressive damaging that can ultimately determine the reaching of failure thresholds, even in the absence of major triggering factors (Gunzburger et al., 2005; Villarraga et al., 2018). Among all factors that can be considered responsible for rock mass damaging and weathering, near-surface temperature fluctuations play an important role, even though the ability of thermal stresses to produce irreversible deformations is still debated (Hall and Thorn, 2014). Daily and seasonal temperature fluctuations are well represented by the schematic landslide–sequencing model of [Figure 2.1](#)—especially for what concerns failure at points 1 and 2—as their continuous and periodical action can determine a not negligible decrease in resistance levels over wide timescales, driving permanent deformations which may trigger gravitational instabilities of jointed rock masses (Do Amaral Vargas et al., 2013; Taboada et al., 2017).

The majority of the studies investigating thermomechanical effects on jointed rock masses are focused on high–mountain alpine regions, where thermally-induced deformations mainly derive from freezing and thawing cycles of water fillings within discontinuity networks (Frayssines and Hantz, 2006; Matsuoka, 2001; Matsuoka and Murton, 2008; Matsuoka and Sakai, 1999; Mufundirwa et al., 2011). This mechanism occurs when temperatures fall below the freezing point causing the propagation or the genesis of fractures due to the stress increase related to the phase–transition from water to ice (Arosio et al., 2013; Deprez et al., 2020). Where temperature fields are above the freezing point of water, and generally dry conditions exist, the interaction between rock materials and near-surface temperature fluctuation results in a progressive degradation of mechanical properties. Although it was assumed that thermal stresses can induce only elastic strains, since the magnitude of thermal fluctuations related to climatic factors are moderate and exert their influence in a subcritical regime (Harrison and Herbst, 1977), several experimental studies proved that low magnitude thermal cycles—representative of the surface climatic conditions of rock masses—can drive the accumulation of plastic deformations, promoting the genesis of microfractures (Gasc-Barbier et al., 2014; Hall, 1999; Hall and André, 2001). This

---

phenomenon, defined as thermal ratcheting or thermal fatigue, is related to the superposition of thermal expansion-contraction cycles between minerals, and it is responsible for the development of compressive and tensile intergranular stresses (Hall, 1999; Siegesmund et al., 2000; Villarraga et al., 2018).

Furthermore, the existence of contrasts in thermophysical properties of minerals (i.e., thermal expansion coefficients, specific heat capacity, and thermal conductivity) can increase the stress intensity at grain boundaries, causing grain disaggregation and microcracking (Eppes et al., 2016). This fatigue mechanism is considered to be the main trigger of the progressive degradation of rock mechanical properties, such as shear and tensile strength (Franzoni et al., 2013; Mahmutoglu, 1998), uniaxial compressive strength (Chen et al., 2014) and elastic moduli (Gasc-Barbier et al., 2014; Villarraga et al., 2018; Yavuz et al., 2010). For example, Villarraga et al. (2018) analyzed the effect of cyclic thermal stresses on cylindrical limestone specimens sampled at the monitoring site of La Roque Gageac (France). Laboratory tests were carried out employing a climatic chamber which allowed for the simulation of a target number of thermal cycles (up to 900) in the range 10–50 °C and characterized by a variation rate of 0.35 °C/min. They found that the accumulation of plastic deformations and the progressive degradation of mechanical properties can be observed from the evolution of P- and S-wave velocities, uniaxial compressive strength, and elastic moduli, which showed a linear decrease of up to 10%. (Figure 2.2).

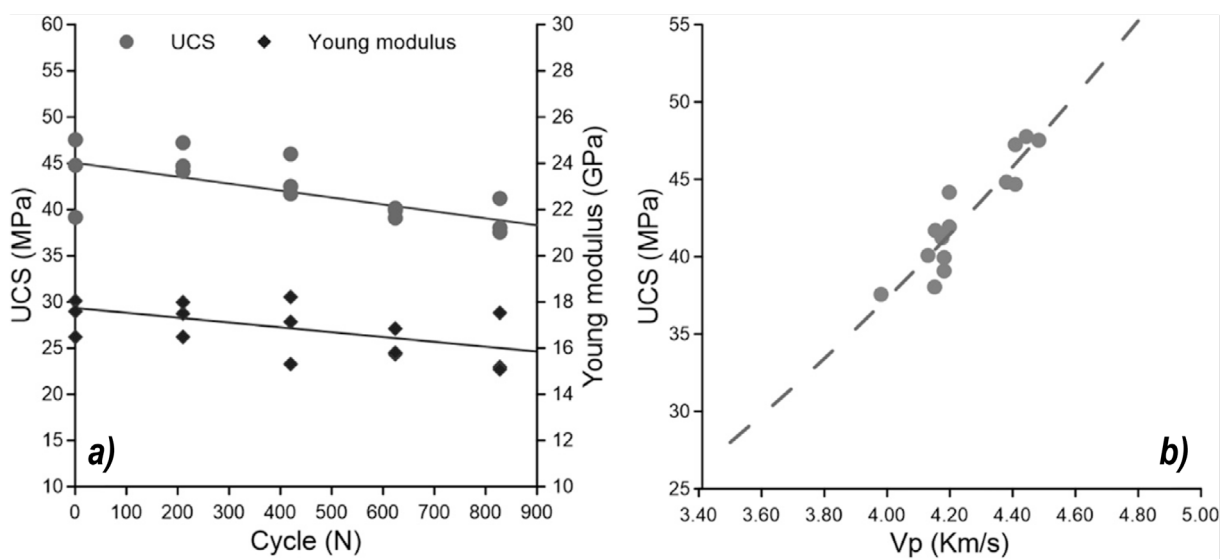


**Figure 2.2.** Evolution of uniaxial compressive strength (UCS) and Young's elastic modulus under cyclic thermal loading (a). Variation of UCS vs P-wave velocity (b) (from Villarraga et al., 2018).

In specific climatic contexts, where thermal regimes are generally far from freezing conditions, temperature fluctuations interact with rock masses by exerting slight, yet repeated, perturbations of local stress fields that can result in a day-to-day cumulative effect (Gunzburger et al., 2005). The repetition of surface thermal cycles determines the periodic alternation of thermal expansions and contractions of the rock matrix, potentially driving joint shear movements that can ultimately provoke a global and progressive deterioration of the mechanical properties of rock masses (Marmoni et al., 2020), thus leading these complex systems toward prone-to-failure conditions over wide timescales. As a direct consequence of the superposition of thermal expansion-contraction cycles, stress fields undergo such perturbations capable of inducing both the genesis of new cracks and the growth of preexisting ones in subcritical regimes (i.e., subcritical crack-growth) (Aldred et al., 2016; Eppes et al., 2016). In particular, subcritical crack-growth mechanisms foster the concentration of plastic deformations at the tip of fractures until internal strain thresholds are met and macroscopic creep-like effects become evident (Voigtländer et al., 2018). These mechanisms can eventually induce inelastic strains consisting of triggering thresholds of shallow slope instabilities, such as rockfalls and rock topples (Do Amaral Vargas et al., 2013; Gischig et al., 2011a, 2011b). Rock masses are continuously exposed to near-surface temperature fluctuations (i.e., daily and seasonal), and thermally-induced deformations are generally considered to be localized within their shallowest layers (Collins et al., 2018; Collins and Stock, 2016).

The propagation in depth of the incoming heat wave—resulting from the radiative, conductive, and convective heat balance with the outer environment—can be described according to the 1D semi-infinite solid model proposed by Carslaw and Jaeger (1959) (eq. 1.1), which allows for the quantitative evaluation of the Temperature profile ( $T$ ) in depth ( $x$ ) in the case of a periodic thermal forcing:

$$T(x, t) = T_0 + Ae^{-x/\delta} \sin\left(\omega t - \frac{x}{\delta}\right) \quad (\text{eq. 1.1})$$

Where  $T_0$  is the initial temperature condition,  $A$  is the amplitude of the temperature fluctuation,  $\omega$  is the angular frequency of the periodic temperature variation and  $-x/\delta$  represents the decay factor of the exponential decrease of the temperature amplitude with

---



depth ( $x$ ). In particular,  $\delta$  is the typical penetration depth (TPD) of the conductive heat front, and can be expressed as:

$$\delta = \sqrt{\frac{2a}{\omega}} \quad (\text{eq. 1.2})$$

This factor is dependent on the thermal diffusivity of the rock matrix ( $a$ ), which is in turn a function of density ( $\rho$ ), thermal conductivity ( $k$ ), specific heat capacity ( $C_p$ ), and the angular frequency ( $\omega$ ) of the periodical temperature fluctuation:

$$a = \frac{k}{\rho C_p} \quad (\text{eq. 1.3})$$

The TPD thus represents the distance from the heat exchange interface at which the amplitude of temperature fluctuations decays of a factor  $1/e$  relative to the magnitude of the periodical thermal forcing at surface (Figure 2.3).

The volume of rock mass internally bounded by the TPD is defined as the thermal active layer (TAL) and represents the most superficial portion of rock volume experiencing the greatest thermal excursions. Since the TPD is proportional to the period of the temperature fluctuation (eq. 1.2), its location varies with seasonal and daily thermal cycles. While for daily thermal cycles (24-hour period), average values of TPDs for different lithologies are estimated in the range 0.1–0.2 m (Fiorucci et al., 2018; Gunzburger et al., 2005), annual temperature fluctuations (365 days period) cause the deepening of this physical boundary up to 3–4 m (Gischig et al., 2011a, 2011b), resulting in a net increase of the volume of rock mass affected by significant temperature variations. In this framework, discontinuity networks can significantly affect the propagation of heat fronts and thermal fields inside jointed rock masses, thus actively contributing to all those external factors (i.e., triggering and preparatory factors) that control the evolution of these natural systems. For example, the role of fracture networks in perturbing the thermal behavior of rock masses was approached by Pappalardo et al. (2016). They analyzed the influence of different climatic conditions on rock masses characterized by intense degrees of fracturing and found that jointing conditions (i.e., density and orientation) can constrain the thermal behavior of rock masses, mainly exerting a direct control on the rate of cooling phases. More in detail, they proposed a

cooling rate index (CRTm), which describes the role of discontinuity traces in controlling the velocity of cooling phases, also pointing out linear relationships between common quantitative fracturing indexes and this parameter.

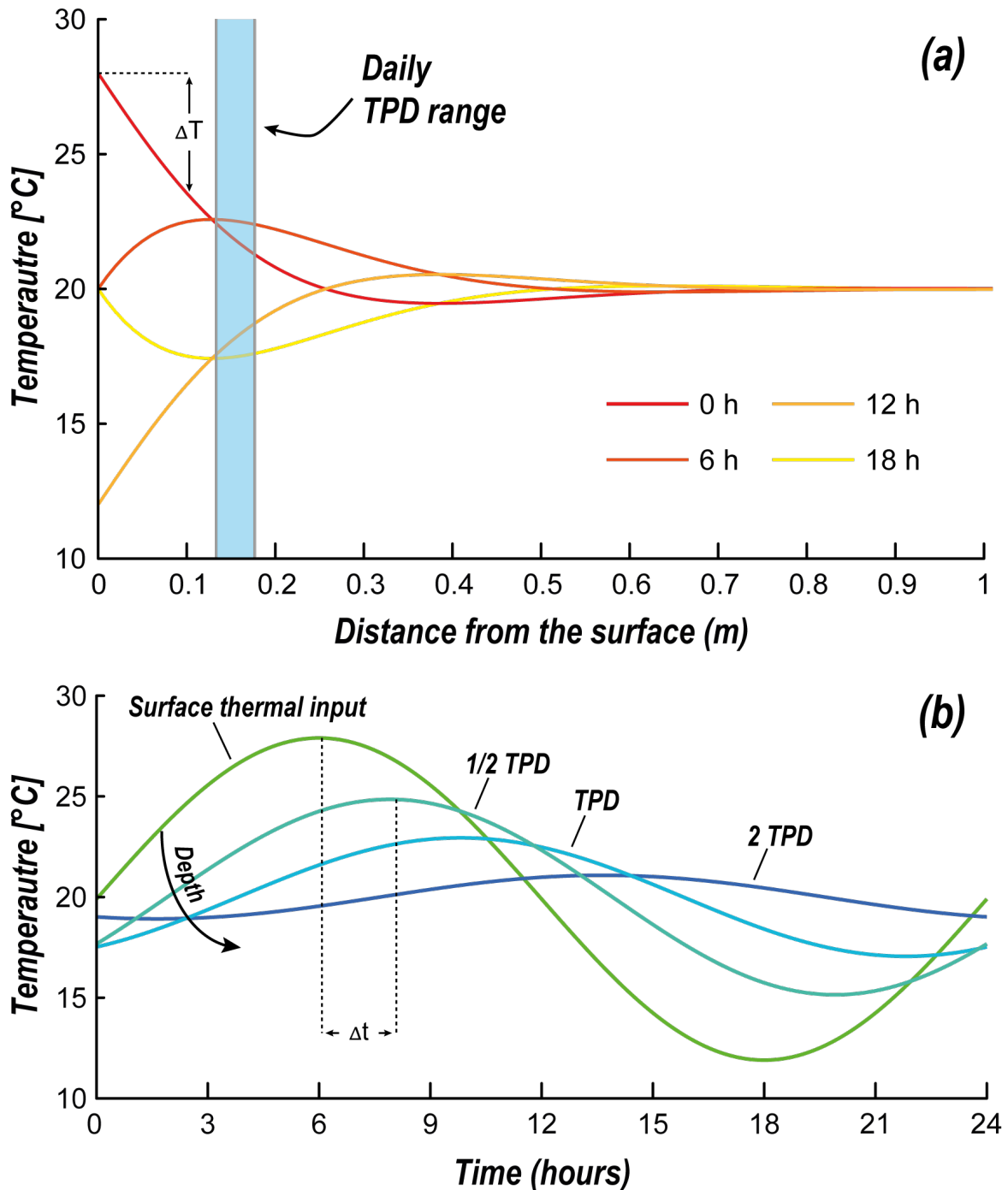


**Figure 2.3.** Theoretical heat propagation in depth as a function of time (herein represented as different wave phases) according to Carslaw and Jaeger (1959) semi-infinite solid model (a). At different distances from the heat exchange interface, the rock matrix experience temperature fluctuations which amplitude not only exponentially decay with depth to its thermal inertia, but it also shows a clear delay between maximum thermal peaks (b) (from Fiorucci et al., 2018; modified).

Similarly, Fiorucci et al. (2018) studied the thermal response of a jointed rock block through multitemporal infrared thermography surveys, highlighting the role of persistent fractures in perturbing near-surface thermal fields. They observed that where open joints fall within the TAL, the heat front propagation in depth can be markedly affected by the contrast in thermal properties between the rock matrix and air-filled discontinuities. This difference in thermal properties can determine the fragmentation of thermal fields and the genesis of high temperature contrasts across fractures, ultimately resulting in a differential heating of adjacent rock blocks (Figure 2.4). This mechanism can be regarded as a factor potentially driving the progressive accumulation of thermally-induced plastic deformations along fractures (Marmoni et al., 2020). In fact, the intensity of heating-cooling cycles can vary in correspondence of open joints resulting in differential thermomechanical strains that could contribute, over wide timescales, to generate unstable conditions. Discontinuity sets can act as physical boundaries that lead to the concentration of thermomechanical effects within the most superficial layers of rock masses. However, surficial thermally-induced deformations can extend far below the daily and annual TAL due to the convective airflow that can be hosted within very persistent cracks, which can provide the mechanism for heat transportation at considerable depths (Moore et al., 2011b). As a consequence of the heat propagation at depth, cyclic thermal stresses within the shallowest volumes of the rock mass can be responsible for stress changes along weak planes at depths greater than 100 m and may induce slip in correspondence of already critically stressed discontinuities (Gischig et al., 2011a, 2011b).

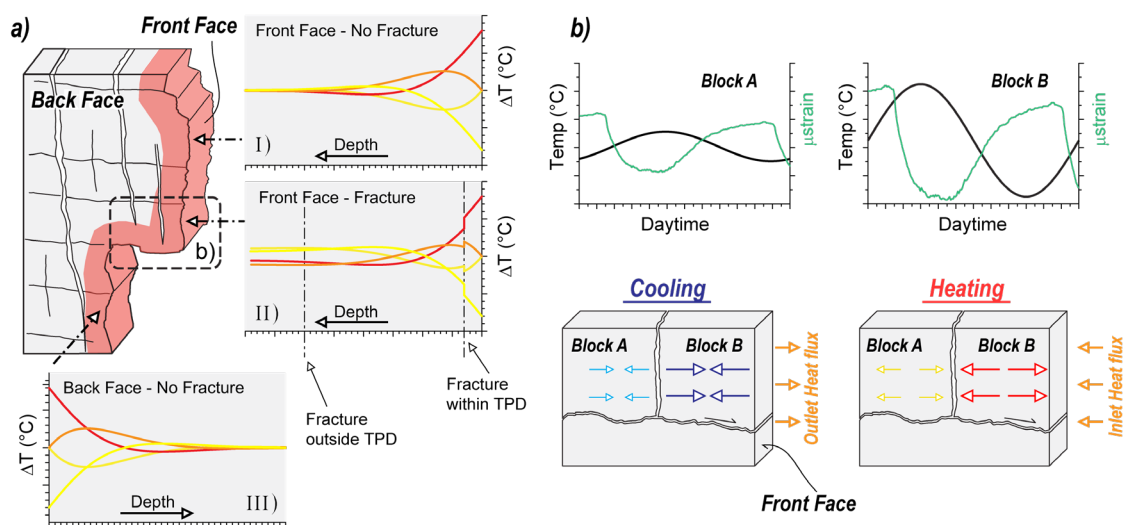


**Figure 2.4.** Conceptual model of the interaction between open fractures and the heat propagation deriving from near-surface temperature fluctuations in a jointed rock mass (from Fiorucci et al., 2018).

## **2.2 Thermomechanical damaging on jointed rock masses**

The last decades have seen a significantly increasing academic interest in studying thermomechanical effects on jointed rock masses caused by near-surface temperature fluctuations.

The in-situ monitoring and quantification of thermally-induced damaging processes on jointed rock masses constitutes a frontier nowadays in the field of landslide risk mitigation of natural and anthropized rock slopes. Although the effect of thermal cycles has been extensively studied at the microscale, inferring how temperature fluctuations induced by climatic actions can produce plastic deformations at mineral boundaries via thermal shock and thermal fatigue mechanisms (Hall, 1999), laboratory tests cannot completely replicate the discontinuous nature of jointed rock masses. Indeed, one of the primary shortcomings of thermomechanical laboratory-scale experimental programs is their failure to account for the dualistic role of fractures in controlling the mechanical behavior of rock masses and in perturbing the spatial-temporal evolution of near-surface thermal fields. Consequently, they are limited to the characterization of the thermomechanical behavior of intact rock matrix samples.

As a matter of fact, while thermal fatigue and crack-growth are associated with microscopic scale mechanisms (Aldred et al., 2016; Eppes et al., 2016; Gasc-Barbier et al., 2014; Hall and André, 2001), it could be stated that discontinuity networks are responsible for the macroscopic thermal and mechanical anisotropy of rock masses, the effects of which can be investigated both at the meso- and macroscale.

In natural contexts, the contribution of thermomechanical processes to the preparation of rock slope instabilities is not easy to discern since rock masses are constantly subjected to a broad spectrum of external processes, and complex physical interactions must be taken into consideration. Several studies, however, have demonstrated that daily and seasonal temperature fluctuations can be primary factors in inducing fracture propagation and rock slope instabilities when favorable climatic conditions exist. For example, Hatzor (2003) and Bakun-Mazor et al. (2013) investigated the stability of two rock slopes at the Masada archaeological site in Israel, where several unstable rock blocks are separated from the rock mass by subvertical rear tension cracks. They were able to compare the expected seismic and thermally-induced displacements of the monitored prone-to-fall rock blocks by

---

implementing a multimethodological approach that included multiparametric monitoring systems, physical and mechanical laboratory tests, and numerical modeling. The analysis of monitoring data highlighted that the observed unrecoverable displacements within a two-year time window were primarily caused by local seismicity, while temperature fluctuations tend to produce elastic deformations. Nonetheless, by invoking a thermally-induced wedging-mechanism, the amplitude of seasonal temperature fluctuations can be considered sufficient to induce permanent, irreversible strain. Additionally, their numerical modeling analyses, which simulated seismic and thermal actions over a 5000-year time span, allowed them to demonstrate that the observed in-situ displacements were most likely caused by thermal loadings rather than local earthquakes.

The analysis of thermomechanical effects on jointed rock masses has been widely approached through comparative analyses (statistical and observational-based approaches) of temperature and stress-strain long-term monitoring timeseries. Numerous studies established a strong correlation between near-surface temperature fluctuations and rock masses deformations (Aldred et al., 2016; Bakun-Mazor et al., 2020, 2013; Collins et al., 2019; Collins and Stock, 2016; Gunzburger et al., 2005; Hall, 1999; Hall and Thorn, 2014; Marmoni et al., 2020; Merrien-Soukatchoff et al., 2010), demonstrating the existence of inelastic trends even in the absence of transient and violent phenomena such as heavy rainfalls, strong winds, or local seismicity, which are frequently considered to be the primary triggering factors of plastic strain.

Gunzburger et al. (2005) and Merrien-Soukatchoff et al. (2010) analyzed the case of a large rockfall that occurred in southern France when no significant triggering factors were identified. Based on numerical modeling and monitoring results, the authors hypothesized that the 2000 m<sup>3</sup> rockfall was triggered by the continuous superposition of thermally-driven expansion and contraction cycles, which could cause macroscopic evidence of irreversible displacements along specific stability-controlling discontinuities. Similarly, Do Amaral Vargas et al. (2013) investigated various rock slope collapses within the Rio de Janeiro area (Brazil) during winter, that at those latitudes represents the season marked by the highest daily thermal ranges and the lack of significant rainfalls. Through the collection of field data and the implementation of numerical modeling analyses, their experimental results indicated that, even in the absence of evident triggers, ambient temperature variations might produce thermal strains capable of propagating already existing fractures and causing slope

---

instabilities. Other examples of critically stressed jointed rock masses were provided by Collins et al. (2018, 2019), who analyzed the long-term evolution of an exfoliated granitic rock dome in California that suffered extremely rapid surficial fracturing events between 2014 and 2016. Borehole extensometers, stress-strain monitoring devices, near-surface air and rock temperature loggers, and acoustic emission sensors were employed to instrument the test-site. This monitoring setup enabled the investigation of short- to long-term trends in the contraction and relaxation stages of rock slabs, revealing a strong control of deformation magnitude and spatial patterns operated by temperature fluctuations, similarly to the results obtained by Collins and Stock (2016) at an exfoliating cliff in the Yosemite National Park. Indeed, they conducted a thermodynamic analysis of a rock slab based on over three years of direct monitoring data and found that daily and annual thermal cycles can drive the cumulative opening and growth of fractures determining the possible detachment of rock volumes.

Multiparametric monitoring systems focusing on the analysis of temperature cyclicity on the mechanical response and progressive damaging of rock masses have also been applied to the preservation of natural and cultural heritage sites (Alcaino-olivares and Perras, 2019; Greif et al., 2017; Vlcko et al., 2009). The main purpose of these systems was to shed light on the existing relationship between near-surface temperature fields and thermomechanical processes, unveiling to which extent thermally-induced deformations can contribute to the overall stability of natural and anthropic rock structures. For example, Greif et al. (2017) monitored crack displacements and surficial thermal variations at the Pravcicka Brana sandstone arch in Czech Republic. Numerous thermocouples were installed at progressively increasing depths, allowing to quantify the heat flux inside the rock mass and to determine rock mass thermophysical parameters. Together with long-term strain monitoring timeseries, these findings were used to calibrate coupled thermal and mechanical numerical modeling of the rock arch. Numerical modeling revealed the existence of thermally-driven deformation, which included both thermoelastic and plastic deformations, confirming the hypothesis that temperature fluctuations are the most contributing factor to the total displacement observed at this heritage site.

The studies discussed above, which are only a part of a vast literature in this thematical area, investigated thermomechanical effects on jointed rock masses using multiparametric monitoring data and numerical modeling methods in order to demonstrate the non-

---

negligible influence of cyclic thermal stresses on the stability of fractured rock slopes and structures.

Passive seismic monitoring techniques have been widely exploited to identify and study thermally-driven deformations in rock masses. Ambient seismic noise, microseismic activity and acoustic emissions monitoring techniques showed the greatest potential in providing new insights on incipient fracturing processes affecting rock masses, enabling to infer how daily and annual oscillations of near-surface temperatures can cause evident changes in the mechanical and dynamic behavior of jointed rock masses, ultimately impacting the evolution in time of already recognized and studied slope instabilities at various dimensional scales (Amitrano et al., 2010; Arosio et al., 2018; Bottelin et al., 2017, 2013b, 2013a; Burjánek et al., 2018; Colombero et al., 2021b, 2021a, 2018b, 2018a; Coviello et al., 2015; D'Angiò et al., 2021b, 2021a; Dietze et al., 2021; Kleinbrod et al., 2017; Larose et al., 2015; Lévy et al., 2011, 2010; Occhiena et al., 2012; Occhiena and Pirulli, 2012; Starr et al., 2015; Valentin et al., 2017).

During the last decade, the exploitation of high-sensitivity seismic sensors for studying gravitational instabilities affecting jointed rock masses has well-constrained the existence of cause-to-effect relationships between growing instability conditions and microseismic activity (Arosio et al., 2018, 2015, 2009; Got et al., 2010; Lévy et al., 2010), also showing their potential in providing precursory patterns of failure events (Amitrano et al., 2010, 2005; Senfaute et al., 2009).

Correlations between microseismic activity and environmental factors (e.g., rainfalls, snowfalls, air temperature, and wind) were studied by several authors, since microseismic monitoring networks have proven to be valuable tools for the identification of fracturing processes in jointed rock masses. Most of these studies are focused on high-mountainous regions, where thermal regimes are characterized by the continuous fluctuations of temperatures around freezing conditions.

(Lévy et al., 2011) investigated the evolution of the dynamic behavior of a 21,000 m<sup>3</sup> rock column in the French Alps before its collapse. The site was instrumented with a seismic array that recorded ambient vibrations during a 4-month period, and almost 200 events were identified within the seismic traces. By comparing rainfall and temperature data, they discovered that most microseismic events were genetically related to severe temperature

---

drops, while almost no correlation was found with rainfalls, suggesting a stronger thermal control on progressive damaging and failure events.

Amitrano et al. (2010) and Occhiena and Pirulli (2012) investigated potential correlations between air temperature fluctuations and microseismicity at the Matterhorn Peak. By comparing microseismic event rates and air temperature records, the authors identified clusters of events and an evident increase in microseismic activity when significant and rapid temperature drops occurred (Figure 2.5), especially during cooling stages of the rock mass.

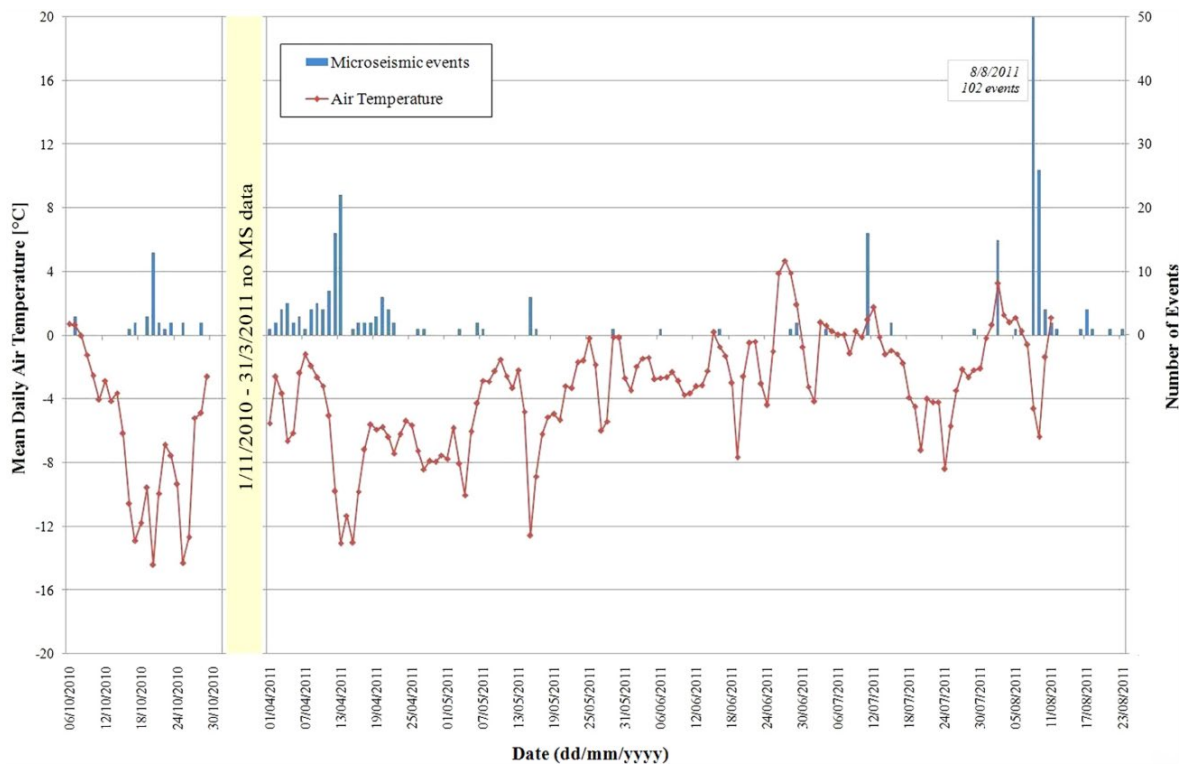


**Figure 2.5.** Synoptic plot of the mean daily temperature (red line) and the number of microseismic events per day recorded at the Matterhorn Peak, which clearly highlight the correlation between event clusters and the abrupt drop of temperatures (from Occhiena and Pirulli, 2012).

Another interesting study focused on the role played the thermal variations in controlling microseismic activity was provided by Colombo et al. (2018b), who analyzed a 3-year long monitoring dataset recorded at the Madonna del Sasso cliff in the Italian Alps. They showed that the long-term evolution of microseismicity revealed cyclic reversible seasonal oscillations characterized by the highest daily occurrence rates clustered during summer months. On the contrary, by taking into consideration the short-term evolution of microseismic activity, the authors demonstrated that rapid and abrupt temperature variations, resulting in both temporal and spatial gradients, can be regarded as the main



causes of differential thermal dilatation–contraction cycles that can induce thermal strains able to generate and propagate microfractures inside the rock mass.

In addition to microseismic monitoring techniques, the application of ambient seismic noise measurements to various geological contexts proved to be a useful tool for local seismic hazard assessments and the characterization of the dynamic behavior of complex rock slopes and rock structures. The ambient seismic noise wavefield results from a complex superposition of a wide spectrum of seismic signals produced by numerous natural and anthropic sources, such as sea waves, wind, industrial machineries, or man–related signals in general. It is due to this multiplicity of sources that ambient seismic noise covers a broad range of frequencies.

Over the last decades, several approaches of seismic noise analysis have been tested to investigate and monitor slopes affected by gravitational instabilities (Burjánek et al., 2010; Häusler et al., 2021; Iannucci et al., 2020a, 2020b; Kleinbrod et al., 2017; Martino et al., 2016; Moore et al., 2011a), potentially unstable rock columns and cliffs (Got et al. 2010; Lévy et al. 2010; Bottelin et al. 2013a, b; Valentin et al. 2017; Colombero et al. 2018a; Taruselli et al. 2021) and natural rock arches (Geimer et al., 2020; Moore et al., 2018, 2016; Starr et al., 2015) by applying different methodologies, such as spectral and polarization analysis of surface waves, HVSR analyses, site-to-reference spectral ratios and cross-correlation analyses.

Most of these studies pointed out the capability of ambient noise measurements to identify short- to long-term modifications—both reversible and irreversible—of the dynamic behavior of jointed rock masses. Seismic noise data may be helpful for monitoring purposes since different processes, such as the drop in natural resonance frequencies, seismic velocity changes, and the evolution of peculiar amplification and polarization attributes of surface waves, have been interpreted as direct descriptors of an overall growing instability of potentially unstable rock masses (Burjánek et al., 2018; Colombero et al., 2018a; Häusler et al., 2021; Iannucci et al., 2020b; Valentin et al., 2017) and rock blocks (Bottelin et al., 2017; Colombero et al., 2021a; Got et al., 2010; Taruselli et al., 2021). It is also worth noting that the analysis of ambient noise parameters highlighted the not negligible role of meteorological factors on the seismic response of rock slopes. Among all climatic factors constantly acting on rock masses, temperature fluctuations were found to be of particular interest with ambient

---

seismic noise data since different authors interpreted near-surface thermal loadings as capable of inducing significant daily and seasonal changes in dynamic properties of jointed rock masses.

At the Vercors Massif site in French Alps, Bottelin et al. (2013a) analyzed the spectral content of ambient noise recordings acquired during a two-year long monitoring campaign and recognized several spectral peaks attributable to resonance frequencies of the unstable limestone cliff. They observed that the first resonance frequency of the monitored rock column was affected by daily and seasonal fluctuations strongly correlated to temperature variations, even though no irreversible trends were detected. Daily variations of the fundamental frequency ( $f_1$ ), generally in the range  $\pm 0.1$  Hz, were found to be in phase with air temperature and characterized by a delay of few hours, suggesting that this thermal control was mainly exerted within the shallowest layers of the rock column at this timescale. On the contrary, by considering longer time windows, a negative correlation between air temperature and  $f_1$  was observed and interpreted as the result of the long-term and more pervasive temperature variation of the rock column which, due to its thermal inertia, caused a 3-month delayed modification of bulk properties of the rock column. Furthermore, temperature fluctuations determined a dramatic drop of  $f_1$  with a net increase from 5 Hz to more than 25 Hz during freezing periods. This significant increment was interpreted as the result of a mechanism of ice-growth within a rear fracture separating this rock volume from the stable rock cliff, which determined the overall stiffening of contacts and rock bridges between these two compartments. Similar results were obtained by Burjánek et al. (2018) at the Preonzo study site (Switzerland), and by Colombero et al. (2018a) at the abovementioned case study of Madonna del Sasso (Italian Alps). In particular, Colombero et al. (2018a) observed significant daily and annual changes both in resonance frequency ( $f_1$ ) values and seismic velocities ( $dV/V$ ) of the unstable rock mass volume under investigation. The same evidence was retrieved through the computation of H/V and H/H spectral ratios. Differently to Bottelin et al. (2013a) the wandering resonance frequencies was found to be in phase with air temperature at both daily and seasonal scales, with almost no delay in time (Figure 2.6). This rapid response to thermal fluctuations was attributed to a site-specific condition where discontinuity sets control the rock cliff's stability. Thus, the effect of fracture stiffening due to thermal dilation and contraction is more perturbing than the modification of bulk properties due to long-term temperature fluctuations.

---

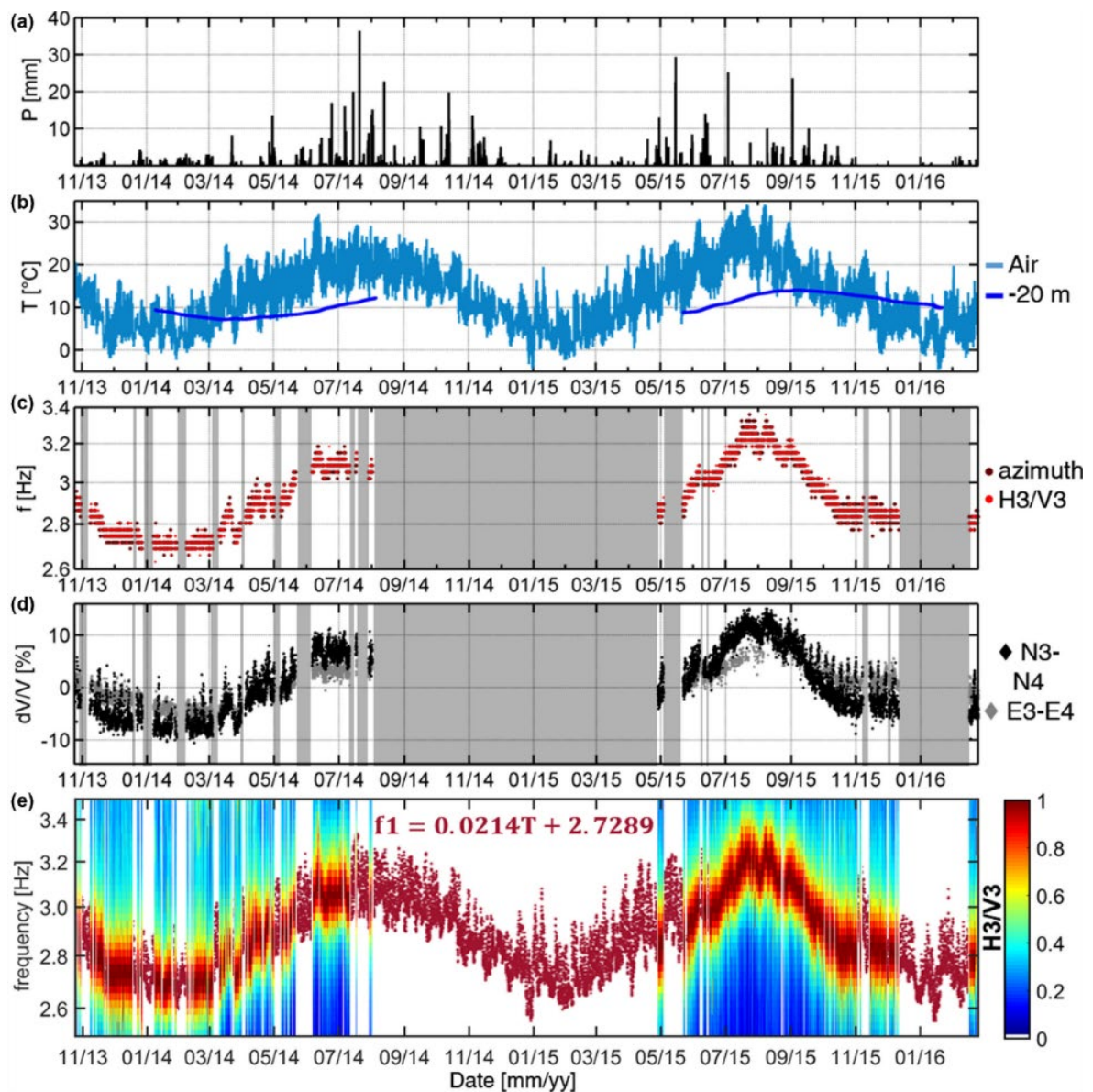


**Figure 2.6.** Long-term evolution of seismic noise parameters due to temperature fluctuations are well-described by the synoptic plot of almost 3 years of monitoring activities at the Madonna del Sasso cliff (from Colombero et al., 2018a). Each panel describes: rainfall amount (a), air temperature and rock temperature fluctuations at 20 m depth (b), fundamental frequency and azimuth values derived from H/V spectral ratios (c), seismic velocity changes obtained from cross-correlations between two monitoring stations (d), normalized H/V spectral ratio zoomed on the first resonance frequency of the unstable rock mass (e).

A great effort was made by Colombero et al. (2021b) to produce an extensive review of several case studies from literature in which ambient seismic noise monitoring techniques were adopted to investigate reversible and irreversible changes of seismic noise parameters in landslide-involved slopes. Through the analysis and the comparison of the results obtained at different sites, most of which are characterized by different and complex geological settings, the authors proposed a classification of the identified mechanisms

driving variations in seismic noise parameters, especially resonance frequency and seismic velocity changes, of potentially unstable rock masses. In the framework of this Ph.D. thesis, three of these mechanisms are of particular interest since resulting from the only influence of near-surface temperature fluctuations at the daily and seasonal scale.

The Fracture-effect (FE – [Figure 2.7a](#)) is widely considered the most frequent mechanism at the base of the periodic change in seismic noise parameters of potentially unstable jointed rock masses. This mechanism can be explained as the result of the superposition of opening–closing phases of joints caused by thermal dilation and contraction cycles involving the rock mass. Indeed, many authors observed that fracture closures due to thermal dilation of the rock mass (i.e., when temperatures increase) might result in a relative increase in fracture contact stiffness, which can be indirectly detected through the resultant rise in fundamental frequency values. When temperatures decrease, the opposite occurs, and fundamental frequencies are expected to decrease as well. The magnitude of thermally-driven resonance frequency wandering has been measured in the range 1% to 7% and 4% to 12% from the average reference values at the daily and seasonal scales, respectively. Additionally, the temporal response to temperature changes showed a not negligible variability among different sites, with delay values ranging from less than 1 hour at the daily scale and up to one month at the seasonal scale. As Colombero et al. (2021b) suggested, this variability in the percentage changes of seismic parameters and their delayed response to thermal fluctuations can be regarded as strictly dependent on the jointing conditions of the unstable rock mass (i.e., joint density, opening, spacing and persistence).

The Surface-effect (SE – [Figure 2.7b](#)) is mainly linked to the quasi–immediate response of rock masses to daily heating and cooling cycles in terms of resonance frequencies and seismic velocity changes. This mechanism, also defined as stress–stiffening by Starr et al. (2015), is the result of a thermally-driven stiffening and softening of the most superficial layers of the rock mass due to daily thermal cycles, which cause oscillations of elastic moduli values and, as a consequence of that, fluctuations of fundamental frequencies and seismic velocity changes.

The Bulk-effect (BE – [Figure 2.7c](#)) is the driving mechanism of the anti–phase correlation between long-term temperature variations and seismic noise parameters wandering, as observed by Bottelin et al. (2013a) From a thermomechanical point of view, when the heat

---

front propagates in depth and reaches the most internal part of a rock volume, it causes a bulk stiffness modification that is expected to be inversely proportional to the temperature variation (e.g., if temperature increases, bulk stiffness decreases), according to the linear relationship between Young's elastic modulus ( $E$ ) and temperature proposed for concrete materials by Xia et al. (2011) (eq. 1.4):

$$E(T) = E(T_0)[1 - \theta_E(T - T_0)] \quad (\text{eq. 1.4})$$

where  $T_0$  is the reference temperature,  $T$  is the actual temperature, and  $\theta$  is a positive material-dependent coefficient of the elastic modulus. Then, when thermal changes involve an entire rock mass or structure, thus penetrating at depth and generating perceptible temperature variations, Young's elastic modulus is expected to vary as well, therefore determining consequent modifications in resonance frequency values. This temperature-driven mechanism tends to produce significant delays between thermal variations and seismic responses due to the decreasing amplitude of temperature variations with depth that is strictly related to both the period of thermal cycles and thermophysical properties of the rock medium, as described by eq. 1.1 and 1.2 in Section 2.1.

Basing on the here presented literature examples, the comprehension of the thermomechanical behavior of rock masses is not straightforward. In fact, several internal and external factors actively contribute to the genesis of complex interactions between rock masses and near-surface temperature fluctuations. Among these factors, discontinuity networks play a significant role in constraining the thermal attitude of rock masses, and thus also their mechanical and dynamic behavior. For this reason, the definition of a multimethodological approach is required to identify micro- and macroscale thermally-driven effects, such as subcritical crack-growth, resonance frequencies wandering, and microseismic event rate drifts.

In this framework, the integration of widespread geotechnical and geophysical monitoring techniques could provide a significant enhancement in recognition of nonlinear strain in intensely stressed systems such as jointed rock masses.

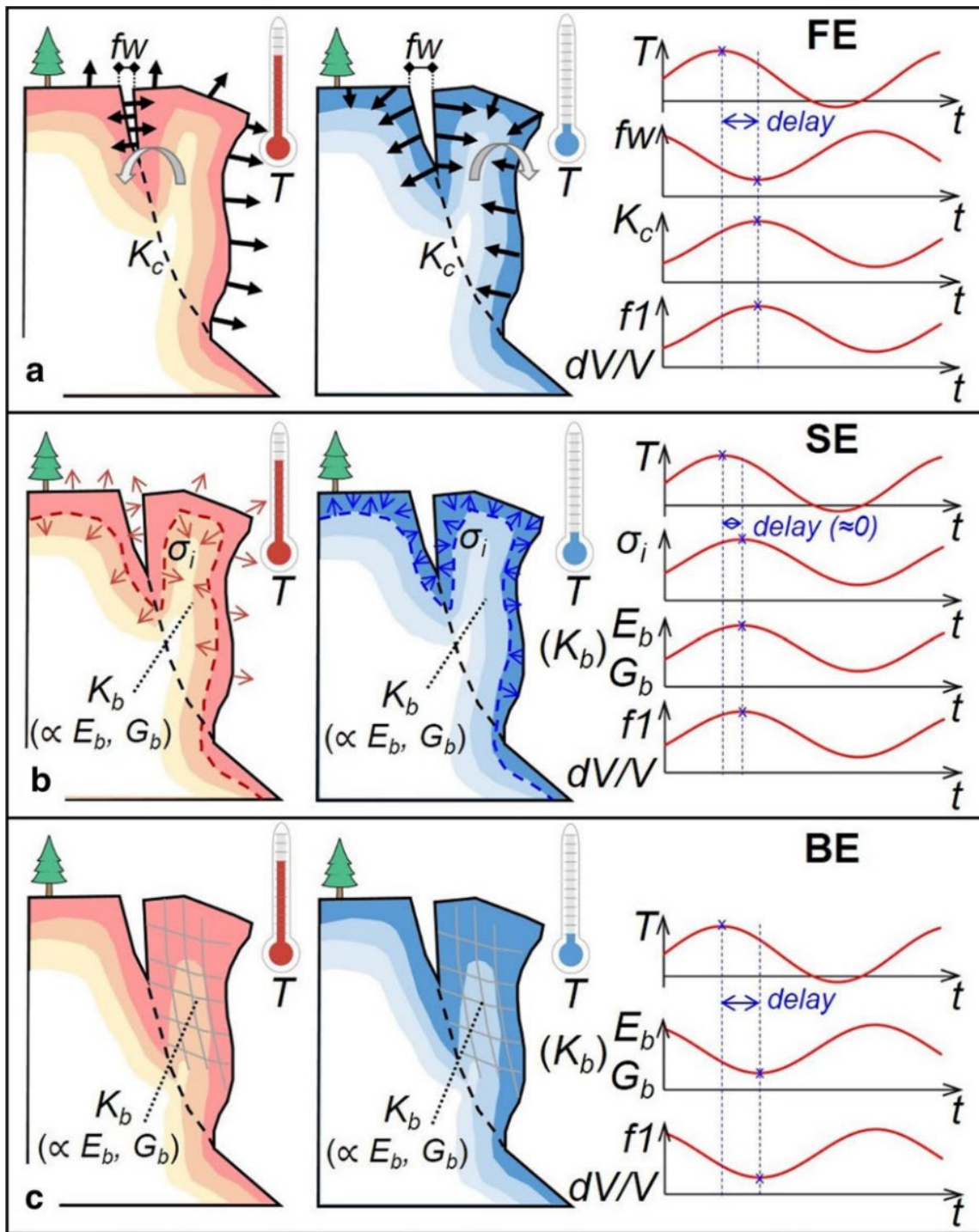


**Figure 2.7.** Simplified sketches representative of thermally-driven mechanisms responsible for fluctuations of resonance frequency ( $f_i$ ) and seismic velocity ( $dV/V$ ) values within a potentially unstable rock mass compartment, separated by the stable sector by a rear subvertical fracture: Fracture-effect (FE) (a), Surface-effect (SE) (b), Bulk-effect (BE) (c). Inner graphs describe the evolution of the most significant mechanical and dynamic parameters due to thermal cyclicity, namely:  $T$  – air temperature,  $fw$  – fracture width,  $K_c$  – contact stiffness,  $K_b$  – bulk stiffness,  $E_b$  – bulk Young’s elastic modulus,  $G_b$  – bulk shear modulus,  $\sigma_i$  – internal stresses,  $t$  – time (daily and/or seasonal scale) (from Colombero et al., 2021b).

# Chapter 3

## Materials and Methods

### 3.1 Case studies

#### 3.1.1 The Wied II-Mielaħ sea arch

##### 3.1.1.1 Regional geological setting

The Maltese Archipelago is located in the central area of the Mediterranean Sea ([Figure 3.1a](#)), about 100 km south of Sicily and 300 km northeast of Tunisia, and it is composed of three main islands (Malta, Comino and Gozo). The Archipelago stands on a shallow submarine elevation, the Malta Plateau, which is part of the Pelagian Platform, and represents the currently emergent part of an extensive shallow-water shelf extending from eastern Sicily to the Malta Graben (Gigli et al., 2012; Pedley, 2011) ([Figure 3.1b](#)). The island of Gozo is the second largest island of the Maltese Archipelago with an area of 67 km<sup>2</sup> (Prampolini et al., 2018). The exposed sedimentary succession on the island comprises Late Oligocene to Miocene marine deposits, mainly composed of limestones and marls, and classified in five geological formations (Baldassini and di Stefano, 2017; Bialik et al., 2021; Gigli et al., 2012; Hyde, 1955; Pedley et al., 1976) ([Figure 3.1c](#)):

- Lower Coralline Limestone (LCL), a compact and hard gray Oligocene limestone (Late Chattian) whose thickness varies between 100 and 140 m;
- Globigerina Limestone Formation (GL), a soft fine-grained yellow limestone of Lower Miocene (Langhian–Acquitanian) with thickness from 20 up to 200 m;
- Blue Clay Formation (BC), a very soft pelagic blue to greenish gray marl and limey clay of Middle Miocene (Serravallian) with thickness varying between 20 and 75m;
- Greensand Formation (GS), massive brown to dark green bioclastic limestone of Upper Miocene (Tortonian), with thickness up to 10 m in the central sectors of Gozo;
- Upper Coralline Limestone (UCL), a gray and fossiliferous coarse-grained limestone of Upper Miocene (Tortonian–Messinian), up to 160 m thick.

These formations are almost horizontal across the islands and are dislocated by two different normal fault systems: the oldest one is oriented WSW-ENE, while the most recent is oriented NW-SE, then parallel to the Pantelleria Rift (Foglini et al., 2016).

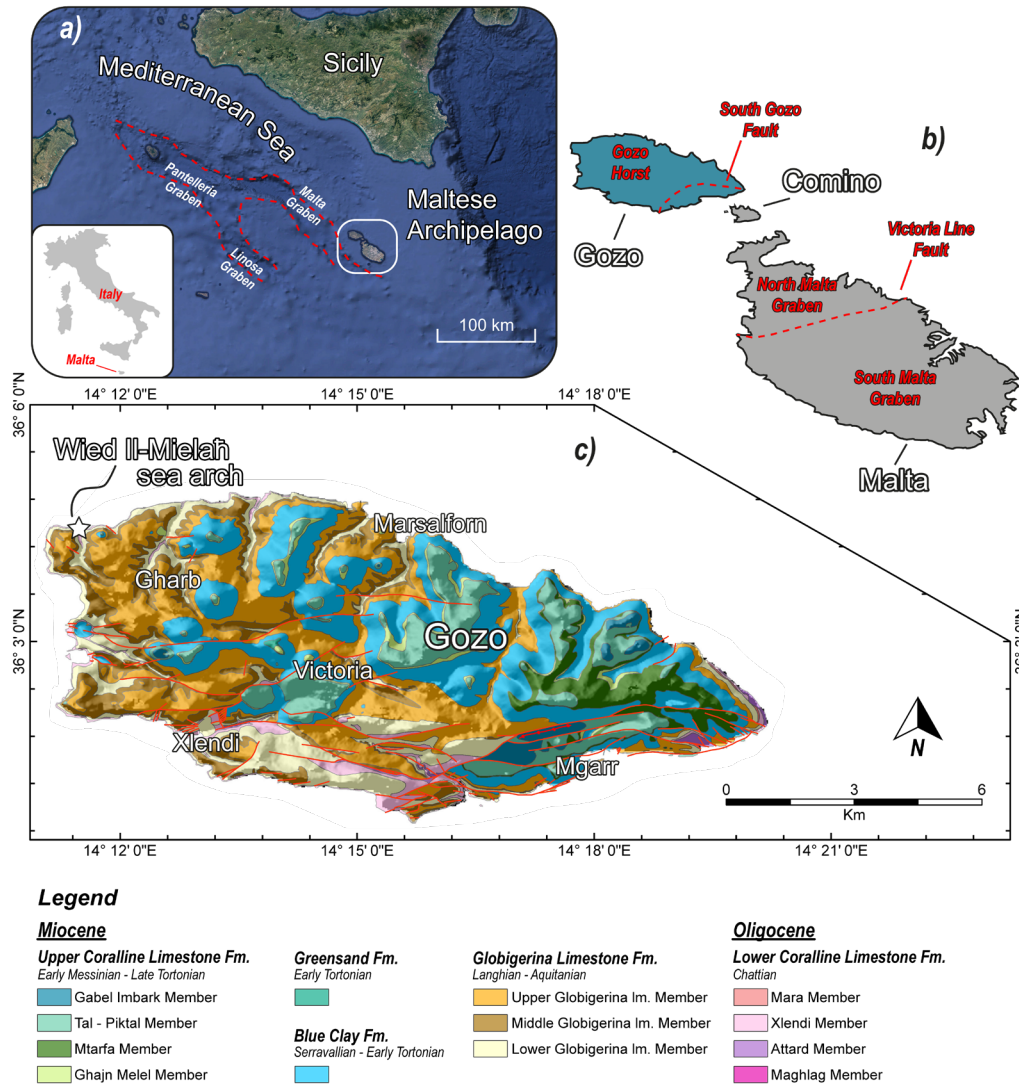


**Figure 3.1.** Geographic and geodynamic setting of the Maltese Archipelago in the Central area of the Mediterranean Sea (a) and main structural elements of the region (b) (from Prampolini et al., 2018, modified). Geology of the island of Gozo and localization of the Wied Il-Mielah sea arch (c).

The island of Gozo is characterized by a regional dip toward north, which caused the LCL to develop into vertical cliffs up to 120 m height in the southern coast, whereas they only reach 20 to 40 m a.s.l. in the northern sectors (Gauci and Scerri, 2019; Pedley, 2011). Even though Gozo covers a small area with respect to Malta, it hosts the complete sedimentary sequence and, as a consequence of that, the general geomorphological setting is characterized by a great variety of morphotypes which genesis is strongly correlated to the



mutual interaction between such geotechnically different geological formations (Gauci and Scerri, 2019; Magri, 2006; Prampolini et al., 2018). The central and eastern sectors of Gozo mainly consist of hills and fragmented mesas of UCL plateaus lying on BC slopes with low steepness ( $\sim 30^\circ$ ). The northern and western areas of the island are dominated by the presence of GL and LCL, which form extensive low-lying hills and plains and vertical plunging cliffs (Alexander, 1988; Biolchi et al., 2016). In particular, steep sea cliffs are one of the most diffuse coastal landforms of the Gozitan island, covering almost half of the Maltese coastline. These cliffs are vertical to subvertical and descend into a considerable depth far below low-tide level without any development of shore platforms (Biolchi et al., 2016; Sunamura, 1992). They are generally cut in the LCL and are characterized by heights ranging from 20 up to 200 m (Magri, 2006). The climate of the Maltese Archipelago is typically Mediterranean with short, mild-humid winters and long, hot-dry summers. The average minimum air temperature of the coldest months is always above  $3^\circ\text{C}$ , and for this reason freezing conditions are sporadic. The lowest ever recorded temperature occurred during winter 1981 when the temperature fell to  $1.4^\circ\text{C}$  (Galdies, 2011). During the summer months, air temperature can reach very high values, with mean maximum temperatures ranging between  $33$  and  $36^\circ\text{C}$  (Figure 3.2). The highest ever recorded temperature (i.e.,  $43.8^\circ\text{C}$ ) was reached during summer 1999. The average annual precipitation is  $530\text{ mm}$ , even though rainfalls show a very high variability every year. From the seasonal distribution of rainfalls, it is possible to observe that the wet period is comprised between October and March, when almost 90% of the expected rainfalls occur, while the dry period covers the months between April and September.

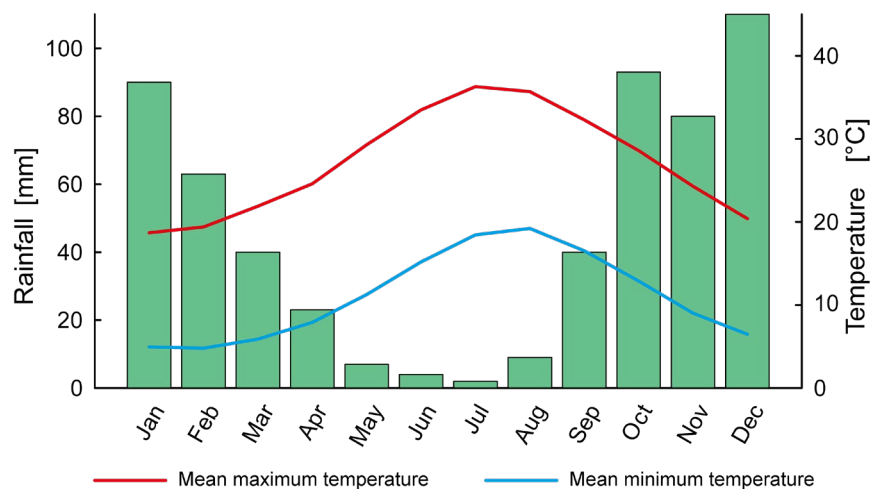


**Figure 3.2.** Thermo-pluviometric plot for the Maltese region based on the 30-year climatic period 1961-1990. Data collected by the Malta Airport MetOffice (Galdies, 2011).

### 3.1.1.2 Geological setting of the Wied Il-Mielaħ sea arch

The Wied Il-Mielaħ sea arch is located in the northwestern sector of Gozo (Figure 3.1c), and since the collapse of the famous Azure Window in March 2017, it has become one of the major touristic attractions of the island (Figure 3.3). The sea arch represents the culmination of the left flank of a 30 m deep gorge where temporary streambeds (*wied* or *wieden* in Maltese) can occur after intense rainfall episodes. Water courses occupied these morphological elements during the warm and humid stages of the Quaternary. Major *wied* valleys were found to be continuous below the sea level and interpreted as relict fluvial valleys, thus witnessing a paleo-drainage network developed during sea level lowstands (Prampolini et al., 2018).

The arch is ~25 m high with a span of 15 m, an average thickness of ~4 m in its central part, a N10°E orientation of its major axis and, even though it is protruded with respect to the coastline, it is in continuity with the adjacent vertical cliff. Moreover, this structure is anchored both to the seafloor and to the right flank of the gorge through a partially submerged shelf that bounds a submerged cavity. From a geological point of view, the arch is entirely found within the LCL upper levels, overlaid on its left side by a continuous plateau of GL (Figure 3.4a). The outcropping rock mass appears well-bedded, with sub-horizontal strata and several pervasive joints that determine the partial isolation of different rock compartments.

The cliff is characterized by a succession of different lithologies, resulting in evident differential erosion morphologies (Figure 3.3) and different rheological behavior when the rock mass is subjected to stress and tension (Gatt, 2013). The complete site stratigraphy of the arch is represented in Figure 3.4b, and two different principal members can be recognized according to Pedley et al. (1976) and Gatt (2013):

- A Member, divided into four submembers or facies (A1-A2-A3-A4) and representing the equivalent to the Attard Member, is characterized by almost 20 m of horizontal strata of micritic to fine-grained limestone dominated by calcareous coralline red algae. These bioclastic elements occur in different morphologies, from pebble-sized *rhodolites* to coarse-grained algal debris. The depositional environment was deeper than 30 m, in fact the moderate current activity sorted the fines and let *rhodolites* to be overturned.



**Figure 3.3.** Different views of the Wied Il-Mielah sea arch, located in the northwestern sector of Gozo (Malta). Front and bottom view of the arch (**a**, **b**), from which it is possible to observe the regular and block-like morphology of this natural structure; aerial views of the arch (**c**, **d**).

- B Member, divided into five submembers or facies (B1-B2-B3-B4-B5) and representing the equivalent to the Xlendi and Mara Members respectively, is characterized by a 7–10 m sequence of horizontal to cross-bedded grainstone to packstone limestones (B2-B3) overlaid by packstone to wackestone limestones (B4-B5) with frequent fragments of *Scutella Subrotonda* and echinoid spines. At the top of the B Member, the transition between LCL and GL is marked by a 1 m thick hybrid facies (H), characterized by a lighter orange tint with respect to B5 submember.

The geological features of the arch strongly constrain its stability since the presence of alternating units characterized by different sedimentological and geomechanical properties can represent a predisposing factor of gravitational instabilities. Also, rock mass-water interactions, mainly expressed through the mechanical and chemical weathering of sea waves and marine aerosols, represent one of the most important geomorphological agents controlling the evolution and integrity of the sea arch.

The sea cliffs along all the western coastline of Gozo are the result of both the geostructural setting of the island and the continuous geomorphological processes acting on these exposed vertical rock walls. Within this framework, chemical and mechanical weathering, driven by the dissolution of limestones and the impacts of sea waves, are undoubtedly the most active processes controlling surface erosion rates and thus the evolution of these morphostructures (Coratza et al., 2016; Gatt, 2013). The evolutionary stages of coastal or sea arches generally follow a typical pattern (Figure 3.5). The genesis of the Wied Il-Mielah sea arch, similarly to the Azure Window, is no exception and it is strictly related to the mechanical erosion of sea waves and to the different mechanical properties of the outcropping lithological members (Satariano and Gauci, 2019)

The development of the arch is the result of sea wave deflections toward the coastline which determined a concentrated erosion along weak elements and eventually an evolution by slab failure.

This process starts with the formation of a notch at the interface with the sea level and, consequently, the continuous increase in lateral tensile stresses is responsible for the progressive growth of vertical joints along the headland (Figure 3.5a). Slab failures occur mainly by toppling and, as the cliff retreats, this mechanism leads to a progressive joint widening and a consequent worsening of stability conditions, also determining the complete formation of a mature arch characterized by a rectangular span (Figure 3.5b) (Gatt, 2013; Satariano and Gauci, 2019). Repetitive slab failures along vertical joints can contribute to the general collapse of the sea arch (Figure 3.5c).

By considering its morphology, especially with respect to the conditions of the Azure Window prior to its collapse in 2017, the Wied Il-Mielah sea arch can be considered to be in an early-mature stage of its lifecycle.

Starting from 2017, detailed engineering geological field surveys were carried out at the Wied Il-Mielah site to define the geomechanical properties of the jointed rock mass outcropping in correspondence of the cliff slope and the sea arch (Regina, 2018). Firstly, the recognized joints affecting the rock mass were mapped and represented on an aerial orthophoto by combining information derived by GPS devices, field and remote observations, such as direction and length of joint traces (with centimetric resolution) (Figure 3.6a).

---

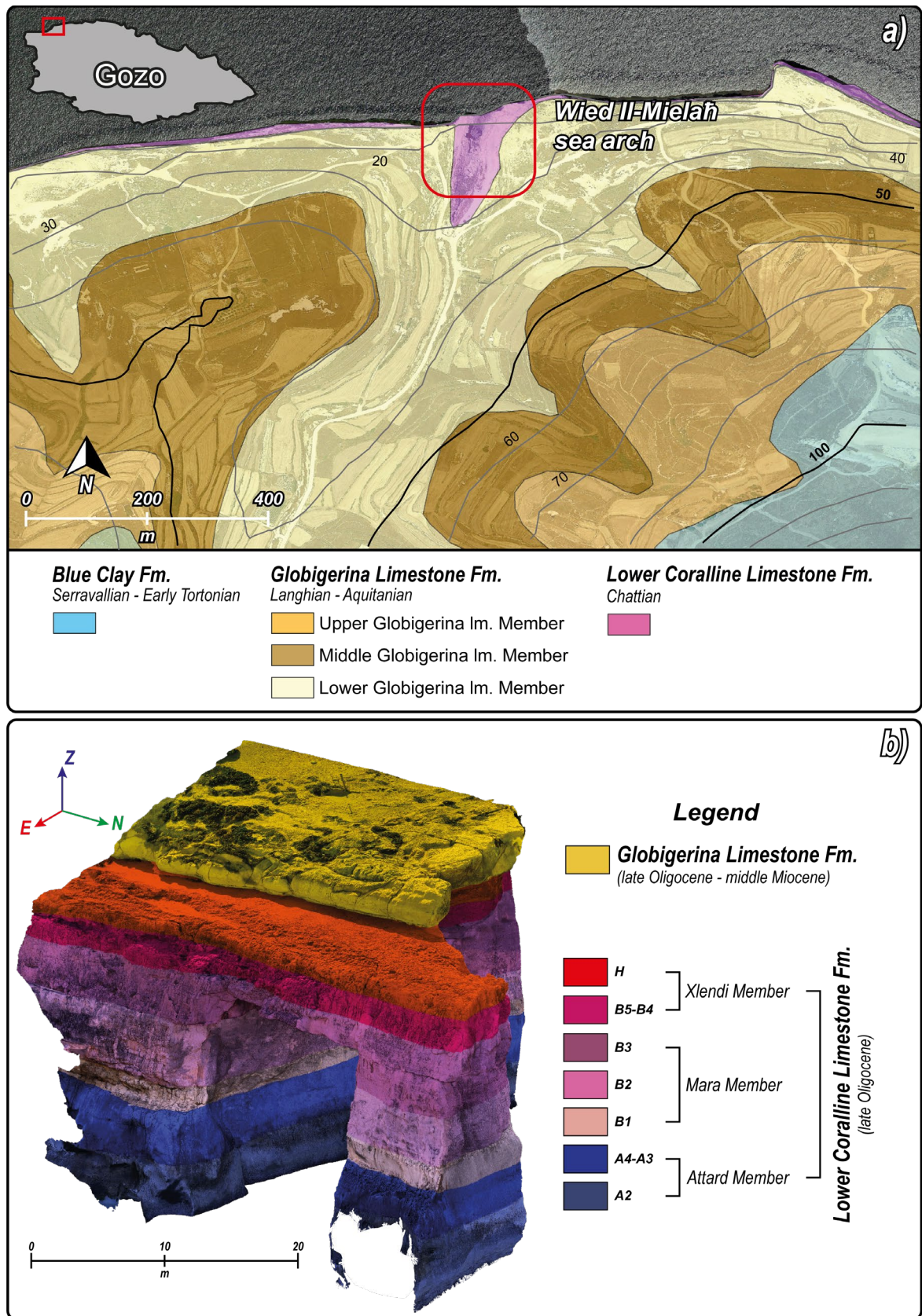


**Figure 3.4.** Geology of the northwestern sector of Gozo, where the Wied Il-Mielah sea arch is located (a). 3D model of the arch where the detailed stratigraphic sequence of the LCL members is represented (b).

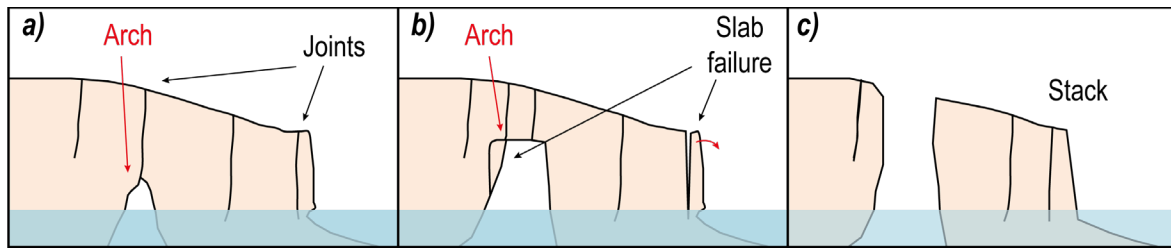


**Figure 3.5.** Simplified sketch model of the evolution and lifecycle of a sea arch (modified from Gatt, 2013). The first stages of a sea arch are characterized by the formation of a small sea tunnel (young sea arch) along the traces of major joints (a); the evolution of the sea cliff by slab failures determines not only the retreat of the coastline, but also the widening of the window (mature sea arch) (b); collapse of the sea arch and generation of an isolated stack (c).

Then, according to the ISRM standard (Ulusay, 2014), each joint was characterized by defining its attitude (dip direction and dip), spacing, persistence, opening, infilling, JCS (Joint Compressive Strength coefficient, representative of the joint surface compressive strength and derived using the Schmidt hammer) and JRC (Joint Roughness Coefficient, indicating the joint wall roughness and obtained by the Barton comb).

All collected data were inventoried within a GIS-based geodatabase. The geomechanical properties of the intact rock matrix (GL and LCL) were investigated through laboratory analyses performed at the Laboratory of Engineering Geology of the Earth Sciences Department of Sapienza University of Rome.

Multiple samples from all the geological units of the arch were collected and analyzed to retrieve key information. Rock matrix density ( $\rho$ ) and natural specific gravity ( $\gamma_n$ ) were derived through the hydrostatic weighting procedure (Ulusay, 2014), while the uniaxial compressive strength (UCS) was obtained by point load tests (D5731-08, 2008). The results of laboratory tests are briefly presented in [Table 3.1](#).

Due to the inaccessibility of the vertical faces of the arch, the investigation of jointing conditions was carried out by implementing a direct-remote approach.

Field surveys were conducted by performing several geomechanical scanlines on top and in the proximity of the arch, allowing to estimate the main properties of discontinuity sets directly, while remote surveys, performed on orthophotos and 3D photogrammetric models, allowed to enrich the dataset by acquiring information concerning spacing and orientation of the remotely recognized joint sets.

Unit		$\rho$ (kg/m <sup>3</sup> )	$\gamma_n$ (kN/m <sup>3</sup> )	UCS (MPa)
GL		1720	16.88	25.31
LCL	H	1950	19.19	14.42
	B4-B5	2250	22.15	25.19
	B3-B2	2080	20.41	37.19
	B1	2480	24.33	27.15
	A2-A3-A4	2390	23.44	36.7

**Table 3.1.** Summary of the geomechanical properties of the intact rock mass, considering both GL (Globigerina Limestone Formation) and LCL (Lower Coralline Limestone Formation) in all its members;  $\rho$  – density;  $\gamma_n$  – natural specific gravity; UCS – uniaxial compressive strength.

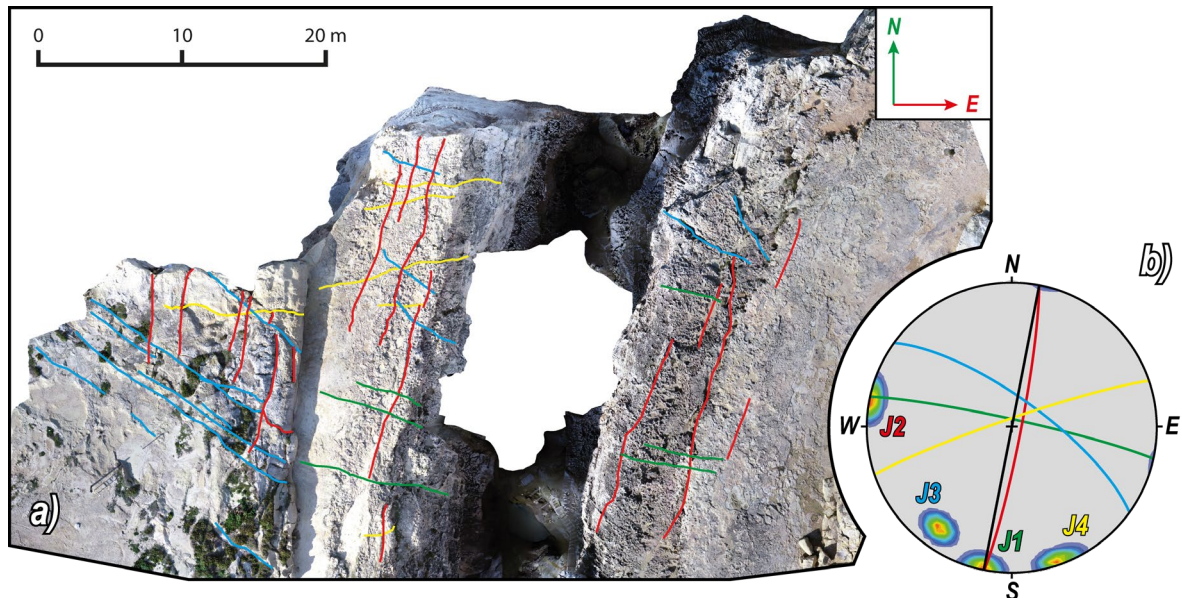


**Figure 3.6.** Aerial orthophoto of the Wied II-Mielah sea arch where major fracture traces of the four discontinuity sets are mapped (a). Synthetic stereographic projection (equal-angle lower hemisphere) representing pole density distributions and planes of the four main discontinuity sets (b). The coexistence of several major discontinuities affecting the integrity of the arch results in a peculiar block-like morphology.

From field and remote surveys four main joint systems were identified both on the LCL members composing the arch structure and on the GL layer at the top of it: J1 (12/85; dip direction/dip), J2 (100/83), J3 (37/72) and J4 (338/83) (Figure 3.6a, b). The principal characteristics of discontinuity sets are described in Table 3.2. Geomechanical measurements allowed to reconstruct the discontinuity network of the sea arch, highlighting how the most persistent and open fractures are clustered within the central sector of the

structure. These elements are characterized by the widest opening (0.2–0.3 m), rare to none filling materials, and deeply intersect the rock mass, bounding the bridge area and delimiting three dislodged compartments (Figure 3.7a):

- The anchored bedrock, which is the non-protruded sector with respect to the coastline. This sector is slightly fractured and affected by subvertical, widely-spaced and tight discontinuities, and represents the most stable unit from a geomechanical perspective;
- The rock pillar, a massive and prism-shaped rock volume directly exposed the mechanical action of sea waves. This sector presents a higher fracture density respect to the bedrock, but the main intersecting joints are tight bedding planes and superficial fractures with low-persistence;
- The rock bridge is the most fractured compartment of the sea arch, and it is affected by five primary fractures dislodging its integrity. The higher number of persistent and wide discontinuities (Figure 3.7b–d) is probably related to the local stress field acting at the center and boundaries of this suspended beam, where shear and tensile stresses determine the continuous accumulation of strain that can eventually lead to the genesis or progressive growth of rock mass joints.

Set	Orientation	Spacing (m)	Opening (m)	JRC	JCS (MPa)
<b>J1</b>	12/85	2.2 ± 1.25	0.15 ± 0.04	14-16	58.2
<b>J2</b>	100/83	1.2 ± 0.41	0.16 ± 0.12	14-16	67.6
<b>J3</b>	37/72	1.21 ± 0.6	0.08 ± 0.03	12-14	55.4
<b>J4</b>	338/83	2.13 ± 0.34	0.25 ± 0.11	12-14	62.3

**Table 3.2.** Synthesis of the geomechanical characteristics of the identified joint sets at the Wied Il-Mielah sea arch. For JRC and JCS only average values are presented.

The higher degree of instability of the rock bridge with respect to the anchored bedrock and pillar sectors is witnessed by the presence of multiple rockfall detachment areas and two evident unstable rock volumes, isolated by decimetric-wide open fractures (Figure 3.7c-e). The proposed zonation, based on the engineering geological setting of the arch and focused on the characterization of the possible instability processes involving this natural structure,



was adopted to design passive seismic measurements and to define the position where to locate the microseismic monitoring array. A detailed description of acquisition methods and processing steps of the collected seismic dataset will be given in [Section 3.2.2.2](#), [3.2.3](#) and [3.2.4](#).

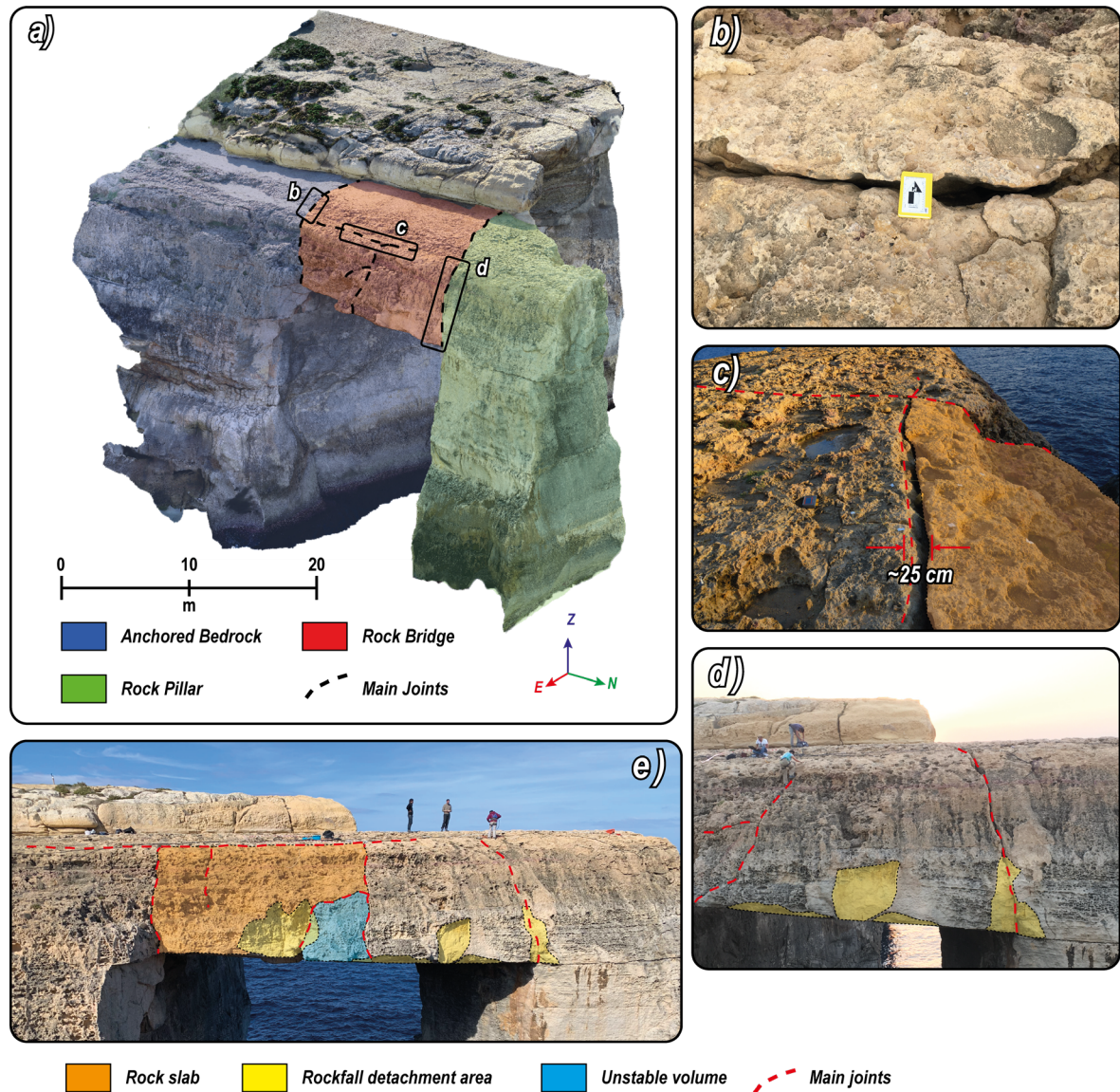


**Figure 3.7.** Due to its morphology and jointing conditions the Wied Il-Mielah structure can be simplified by considering three different compartments partially isolated by major fractures (a). The rock bridge is bounded and intersected by five highly persistent discontinuities (b–d) characterized by opening values in the range 0.2–0.3 m. This sector of the arch also shows a higher tendency toward gravitational instabilities as witnessed by the presence of (i) a potentially unstable rock volumes in its central part (light blue area, e), (ii) a partially isolated rock slab (orange area, c–e), and (iii) multiple detachment areas of small rockfalls (yellow areas, d, e).

### 3.1.2 The Acuto field laboratory

#### 3.1.2.1 Regional geological setting

The Acuto field laboratory is situated in the westernmost sector of an abandoned limestone quarry (Prenestina quarry) within the municipality of Acuto (central Italy) (Figure 3.8). It was designed and instrumented starting from november 2015 in the framework of multiple experimental activities managed by the Research Center for Geological Risks (CERI) of Sapienza University of Rome. This natural test-site aims to investigate rock mass damaging processes deriving from natural and anthropic external stressors through the implementation of a permanent multiparametric monitoring system composed of several geophysical and geotechnical devices.

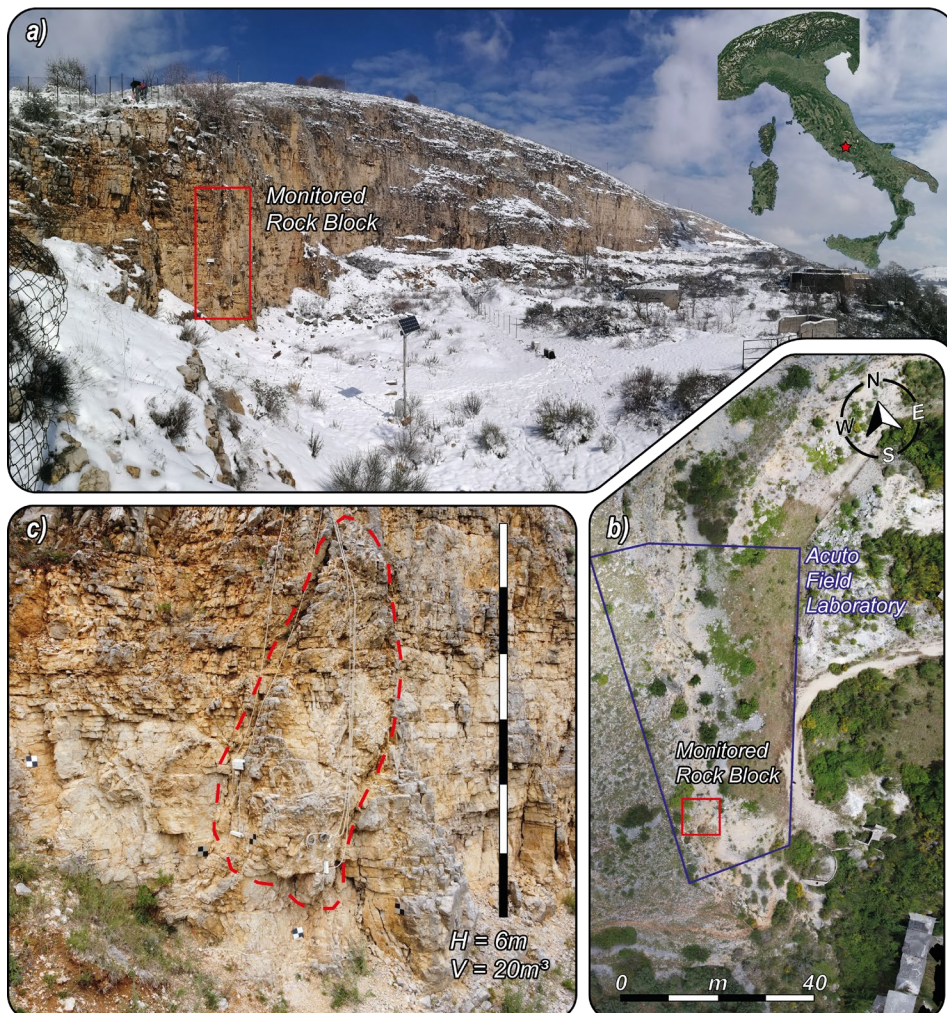


**Figure 3.8.** Panoramic view of the abandoned Prenestina quarry located within the municipality of Acuto (central Italy) (a). Aerial orthophoto of the western sector of the quarry where the Acuto field laboratory was implemented in 2015 (b). The 20 m<sup>3</sup> rock block selected as the main target of the permanent multiparametric monitoring system.

The Acuto municipality is located 100 km SE from Rome, in the western region of the Mts. Simbruini-Ernici ridge (central Apennines), which represents a portion of the Latium-Abruzzi platform sedimentary domain. This geological structure is longitudinally limited by the Latina Valley to SW and by the Roveto Valley to NE, and it is mainly characterized by a powerful succession of Meso-Cenozoic deposits (Devoto, 1970). This sector of the Apennine was involved in the NE migration of the thrust belt during lower Messinian, leading to the development of several ridges (e.g., Sibillini Mts., Reatini Mts., Simbruini Mts., Ernici Mts., Sabini Mts.) (Cosentino et al., 2010).

The general geological setting of central Apennines, especially within the Latium region, is characterized by the coexistence of extensional and compressive tectonic structures, which witness the superposition of different deformational styles that alternated starting from Early Miocene (Figure 3.9). In this context, the Simbruini Mts. Ridge represents a principal fold-and-thrust unit that developed with the typical Apennine orogeny NW-SE trending and NE verging, and it is characterized by a sedimentary succession of Triassic-Upper Cretaceous limestones (Devoto, 1970). The existence of syn-orogenic and thrust-top deposits enabled to date the age of compressional episodes in the Simbruini ridge in the Messinian-Early Pliocene age, when multiple thrusting events interested these structural units (Delchiaro et al., 2021; Fabbi, 2018). Furthermore, among all main thrusts dissecting this region, the Olevano–Antrodoco thrust probably represents the most significant tectonic element since it marks an important transition between different geological domains. At its hangingwall, Meso-Cenozoic transitional carbonates and marls belonging to the Umbria-Marche pelagic domain dominate the sedimentary succession, while Mesozoic carbonates ascribable to the Latium-Abruzzi carbonate platform outcrop at its footwall (Billi and Tiberti, 2009; Civitelli and Brandano, 2005).

The present structural setting of central Apennines is undoubtedly the result of a complex geodynamic transition between the general northeastward migration of the orogenic system and the superimposed post-orogenic extensional and strike-slip tectonics (Billi and Tiberti, 2009; Mattei et al., 2008). In fact, in the Late Miocene-Pleistocene age, the extensional tectonic regime related to the development of the Tyrrhenian basin and the migration of thrust fronts toward E-NE determined the formation of multiple normal fault systems bounding intermontane sedimentary basins, whose age becomes progressively younger from the Tyrrhenian coast toward the hinterland of the chain (Delchiaro et al., 2021).

---

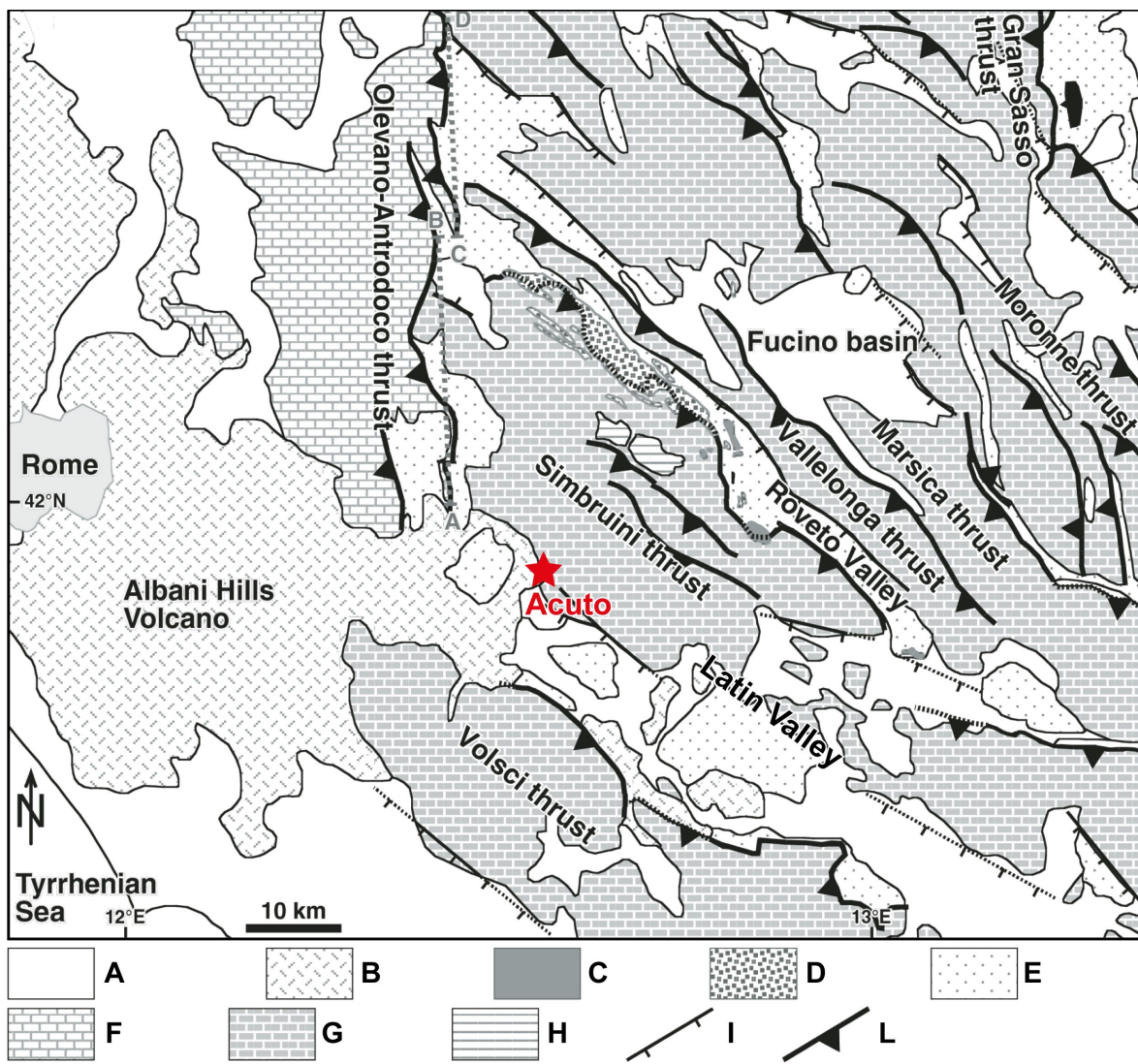
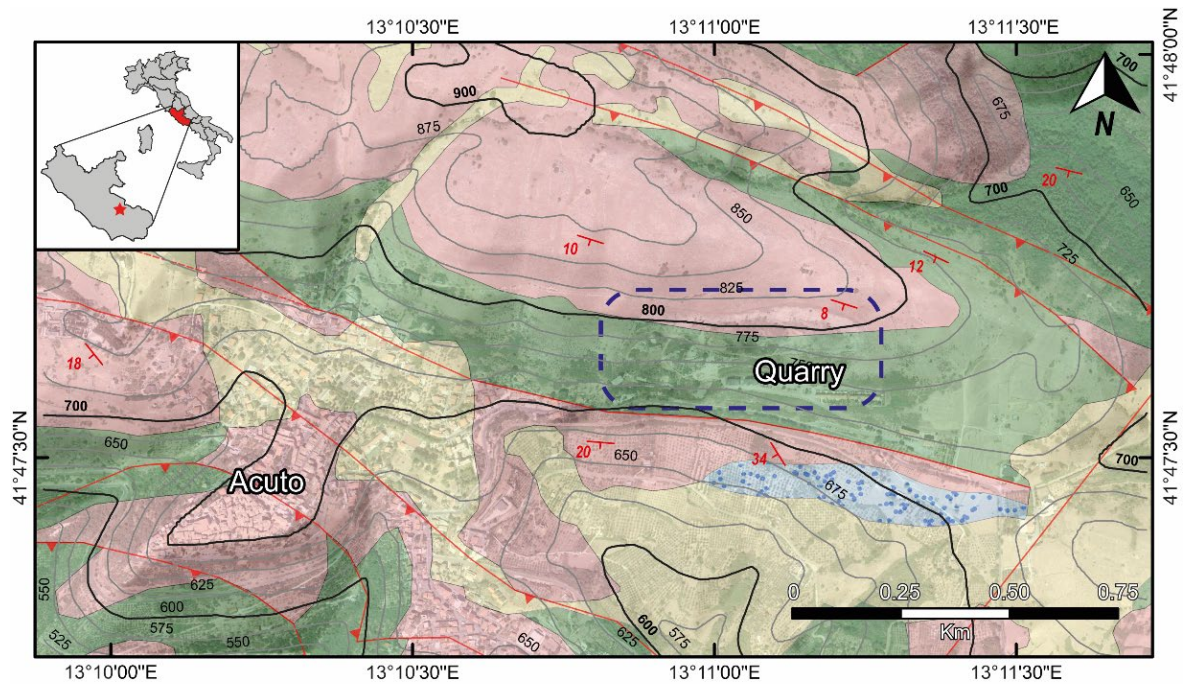


**Figure 3.9.** Geological sketch of the Central Apennines region: (A) Marine and continental Plio-Quaternary deposits, (B) Pliocene–Pleistocene volcanic deposits, (C) Pliocene conglomerates, (D) Messinian conglomerates, (E) Tortonian flysch units, (F) Meso-Cenozoic carbonates of the Umbrian domain, (G) Meso-Cenozoic carbonates of the Latium-Abruzzi domain, (H) Triassic carbonate succession, (I) main normal faults, (L) main thrusts (from Billi and Tiberti, 2009; modified).

An NW-SE orientation is the prevailing tectonic trend for extensional features in the central Apennines. However, normal faults with an anti-Apennine trend (NE-SW) are also present in the area (Vignaroli et al., 2020). The municipality of Acuto is located at an altitude of 750 m a.s.l. on the southwestern flank of the Simbruini ridge which bound the Latin Valley to NE. This valley divides the Lepini Mts. ridge from the Simbruini-Ernici ridge and represents a clear example of an extensional fault-bounded sedimentary basin, which developed during the Pliocene-Pleistocene age (Cosentino et al., 2010). The abandoned Prenestina quarry, which is few hundred meters NE far from Acuto, is found on a monoclinic SW-dipping

carbonate slope, where a powerful succession of Meso-Cenozoic limestone outcrops and is affected by steeply-dipping NW-SE striking normal faults, which are characterized by offsets up to 10 m (Accordi et al., 1986). In correspondence of the quarry area Mesozoic calcilitites with *rudists* are overlaid by Cenozoic calcarenitic limestones (Figure 3.10). The field laboratory was implemented on a vertical rock wall located in the western sector of the abandoned quarry, which is characterized by an overall N20°E trend and variable heights ranging from 15 to 50 m.



### Legend

#### Cretaceous

Mesozoic calcilitites  
with rudists  
Campanian - Coniacian

#### Miocene

Cenozoic yellowish  
calcarenitic limestone  
Serravallian - Langhian

#### Holocene

Slope Debris  
Eluvial-Colluvial

Attitudes

Tectonic Elements

**Figure 3.10.** Geological map of Acuto (scale 1:10.000). The location of the quarry area where the field laboratory was implemented is highlighted by the blue box (courtesy of Dr. Geol. Paolo Sarandrea; modified).

The climatic setting of this area is characteristic of pedemountain regions of central Apennine. According to the phytoclimatic classification of Latium region proposed by Blasi (1994) and based on the analysis of thermo-pluviometric data collected during the period 1955-1985, the climate of this area of interest is typically temperate and characterized by a

submountain thermotype. In order to provide a more detailed and accurate description of the climatic and meteorological conditions of this case study, temperature and rainfall timeseries referring to the period 2000-2015 and collected from the closest weather station of the Piglio municipality (800 m a.s.l.) are also presented. Even though Piglio is located outside the area where the field laboratory is found, these data can be considered representative for the meteo-climatic conditions of Acuto due to the short distance separating the two municipalities (5 km ca.) and their almost coincident elevation above sea level.

Mean temperature values highlight an evident maximum peak in correspondence of summer months, with values in the range 32–34 °C, while winter months are characterized by average minimum temperatures generally close to 0 °C. The average monthly rainfall presents a maximum of 130–140 mm during the autumn-winter transition and a minimum of 40–50 mm in correspondence of summer months, thus together with maximum air temperature values (Figure 3.11).

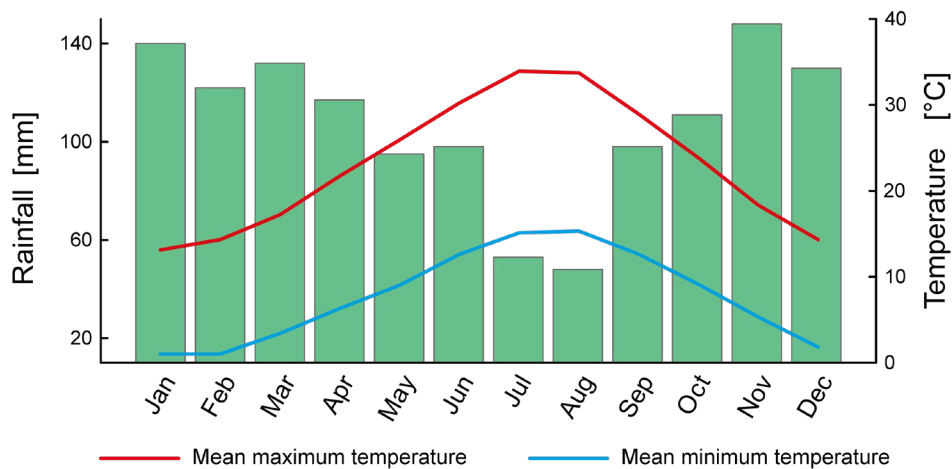


**Figure 3.11.** Thermo-pluviometric plot for the Piglio-Acuto area based on the 15-year climatic period 2000-2015 (source: Regione Lazio).

### 3.1.2.2 The field laboratory

The Acuto field laboratory was designed and implemented in 2015 inside the abandoned Prenestina quarry located in the municipality of Acuto. The main objective of this natural laboratory was to test the ability of an integrated multiparametric monitoring system to decipher the role of environmental and anthropic external stresses in determining the worsening of rock mass stability conditions. Several experimental activities were carried out since its foundation, providing novel insights both in terms of data analysis and methodologies for the comprehension of rock mass damaging processes and the definition of early-warning strategies for the management of landslide-related geological risks.

The permanent monitoring system, consisting of several geotechnical and geophysical devices, was installed on the vertical rock wall outcropping in the western sector of the abandoned quarry. More specifically, after a preliminary surveying stage, a potentially unstable 20 m<sup>3</sup> rock block was identified as the main target of monitoring activities (Figure 3.12a). This element was selected due to its severe fracturing degree—which allowed the instrumentation of numerous fractures and microcracks—and the presence of a rear and subvertical discontinuity that partially detaches the rock block from the quarry wall behind, thus predisposing this volume to instability (Figure 3.12b). These conditions were considered optimal for testing and evaluating different multiparametric monitoring strategies for inferring the role of continuous and transient stresses in leading jointed rock mass toward localized or generalized failure events. A peculiar geometry also characterizes this intensely jointed and protruded rock block: it is directly exposed to the outer environment on two free surfaces exposed toward E-SE (front face) and S-SW (back face). On its northern face, it is anchored to the contiguous quarry wall even though this contact is marked by the presence of a small-scale fault line. This slab configuration, comprising two exposed surfaces and a subvertical open joint acting as a backward release system, limited the installation of monitoring devices on those elements that are mostly subjected to exogenous stresses (front and back face) and potentially controlling the stability of the rock block (main joints and microfractures). In order to provide a quantitative description of jointing conditions and to reconstruct an engineering geological model of the quarry wall where the target rock block is located, several direct and remote geomechanical surveys were performed starting from 2015 (Fantini et al., 2016; Fiorucci, 2017; Modanesi, 2015).

---



**Figure 3.12.** Front view of the potentially unstable rock block selected as the main target of the multiparametric monitoring system of the Acuto field laboratory, along with the fault line that laterally bounds its volume (a); Back view of the rock block and of the open joint that determines the its partial detachment from the rock wall behind.

Traditional geomechanical surveys were carried out on the outcropping rock mass according to the ISRM standard (Ulusay, 2014) to identify major discontinuity sets and quantify their mechanical properties. Multiple scanlines were performed both on the rock block and the adjacent rock wall to better frame the general fracturing condition of this quarry sector. Each recognized discontinuity set was characterized by defining its attitude (dip direction and dip), spacing, persistence, opening, presence of infilling, hydraulic conditions, joint compressive strength (JCS), and joint roughness coefficient (JRC) employing a Schmidt hammer sclerometer and a Barton comb profilometer. Moreover, peak friction angle values ( $\varphi_{\text{peak}}$ ) were derived according to the Barton and Choubey failure criterion (Barton and Choubey, 1977). Field surveys allowed the identification of four main discontinuity sets (Figure 3.13a, b): J0 — bedding planes — (93/4; dip direction/dip), J1 (4/80), J2 (198/86) and J3 (91/64). Furthermore, the intact rock matrix's physical, thermal and mechanical properties were investigated through laboratory analyses performed at the Laboratory of



Engineering Geology of the Earth Sciences Department of Sapienza University of Rome and EcamRicert laboratories. The main characteristics of discontinuity sets derived from field activities and the results of laboratory tests are synthetically presented in [Table 3.3](#).

Along with direct geomechanical surveys, remote surveys were also carried out to reconstruct the dense point cloud of the investigated rock block to enrich the information concerning minor rock subvolumes isolated by the discontinuity network. (Modanesi, 2015) and Fiorucci (2017) identified 18 potentially unstable blocks and performed susceptibility and stability analyses which highlighted that the only failure mechanisms able to satisfy the kinematic and dynamic compatibility criteria concurrently are wedge and planar sliding.

#### Discontinuity sets

Set	Orientation	JRC	JCS (MPa)	$\phi$ ( $^{\circ}$ v)
<b>J0</b>	93/4	3–4	180	53
<b>J1</b>	4/80	8–9	120	54
<b>J2</b>	198/86	3–4	130	49
<b>J3</b>	91/64	4–5	110	49

#### Intact rock matrix

$\gamma_n$ (kN/m <sup>3</sup> )	$\gamma_s$ (kN/m <sup>3</sup> )	k (W/mK)	$\alpha$ ( $^{\circ}$ C <sup>-1</sup> )	UCS (MPa)	E (MPa)
26.44	26.72	2.09	3.8E-6	130	6E+4

**Table 3.3.** Geomechanical characteristics of the discontinuity sets identified on the rock block and the adjacent rock wall through field surveys, and physical–mechanical properties of the intact rock matrix derived from laboratory analyses;  $\gamma_n$  – natural specific gravity,  $\gamma_s$  – solid specific gravity, k – thermal conductivity,  $\alpha$  – linear thermal expansion coefficient, UCS – uniaxial compressive strength, E – Young elastic modulus.

Given this geological context and the peculiar configuration of the investigated rock block, an integrated multiparametric monitoring system was designed and the two exposed surfaces (front and back faces) were instrumented with numerous geotechnical and geophysical devices starting from winter 2015, aiming at understanding the deformational and dynamic behavior of this prone-to-fall element under natural and forced actions. The permanent multiparametric monitoring system consists of:

- One temperature probe for rock mass temperature monitoring, installed at a depth of 8 cm on the front face of the rock block ([Figure 3.13f](#));

- Six strain gauges installed in correspondence of microcracks and intact rock matrix (Figure 3.13g);
- Four extensometers installed on open fractures (Figure 3.13g);
- One fully-equipped weather station comprising air-thermometer, hygrometer, pluviometer, and anemometer, that was installed at the top of the quarry wall (Figure 3.13e);

The whole system is cable-connected to a Campbell Scientific CR1000 data logger, which has 24 acquisition channels and is configured to collect data with 1-minute sampling rate. The data logger is also provided with a GPRS wireless communication system that allows the automatic data transfer to a local server. Apart from the permanently installed devices on the rock block, which are continuously collecting deformational and environmental data since 2015, the spectrum of monitoring activities at the Acuto field laboratory was enriched by several experimental activities carried out through the years. Most of these activities were planned to study the effect of preparatory factors of slope instabilities and test novel methodologies for the investigation of progressive damaging processes in jointed rock masses.

Starting from 2016, an artificial intelligence camera prototype (AiCP) was installed inside the field laboratory to monitor a one meter long railway track located at the bottom of the rock block to simulate a risk scenario for major infrastructures. By implementing a specific change-detection algorithm, the capability of the AiCP in detecting the presence of debris deriving from rock slope failures along railway lines such as was successfully tested (Fantini et al., 2017).

In 2017, a multitemporal infrared thermography monitoring campaign targeting the rock block started with the objective of investigating the thermal behavior of this potentially unstable rock volume, mainly focusing on the influence of discontinuities in controlling near-surface temperature fields (Fiorucci et al., 2018). Temperature and strain data deriving from both the multiparametric monitoring system and infrared thermography surveys were also employed to calibrate coupled thermomechanical models to simulate the effect of daily and annual thermal cycles in influencing the near-surface strain response of the jointed rock block (Marmoni et al., 2020).

---



**Figure 3.13.** Representation of the main joint traces dissecting the monitored rock block and the adjacent quarry wall sector (a); Synthetic stereographic projection (equal-angle lower hemisphere) representing pole density distributions and planes of the four main discontinuity sets, along with the direction of the slope face (SF) (b); open joint acting as the release system that separates the rock block from the rock mass (c); monoaxial microaccelerometer installed on the rock block surface during one of the performed long-term microseismic monitoring campaigns (d); fully-equipped weather station (e); temperature probe (f); extensometer installed on an open fracture along with a strain gauge placed on a microcrack and covered with aluminum tape for thermal insulation (g).

Furthermore, in 2018 and 2019, a microseismic monitoring array composed of several monoaxial microaccelerometers ([Figure 3.13d](#)) was installed on the rock block and the contiguous rock mass. This system perfectly integrated with the already existing one, since it provided interesting insights on the dynamic and deformational response of the studied rock block in response to environmental continuous and transient forcings (D'Angiò, 2019; D'Angiò et al., 2021b, 2021a).

In the framework of this Ph.D. thesis, the microseismic monitoring dataset collected at the Acuto field laboratory during two different campaigns was considered to be of particular interest because it represented a valuable starting point for the investigation of nonlinear strain effects related to near-surface daily and seasonal temperature fluctuations at the dimensional scale of a jointed rock block. Besides, this field laboratory offered the not negligible advantage of its great accessibility and remote position, far from anthropic disturbances, thus representing a very suitable location for analyzing the evolution of thermally-induced deformations through the analysis of long-term ambient vibrations timeseries. A detailed description of acquisition methods and processing steps of the collected microseismic dataset will be given in [Section 3.2.2.1](#).

Along with the analysis of a vast microseismic monitoring dataset, the abovementioned accessibility of the rock block also allowed testing a novel approach consisting for the integration of multitemporal infrared thermography surveys with close-range digital photogrammetry for the reconstruction of 3D thermal point clouds. Acquisition protocols and processing steps will be described in [Section 3.3.3.2](#).

## 3.2 Ambient seismic noise and microseismic monitoring

Over the last decades, passive seismic techniques have drawn the attention of engineering geology researchers since they were recognized to represent a valuable tool for short- to long-term monitoring activities of unstable or landslide-involved rock masses. Among these methods, the most exploited approaches deal with the collection of seismic signals for the identification of energetic seismic events of interest and their evolution in time (i.e., microseismic activity) and the characterization of the dynamic parameters of anthropic or natural structures under investigation from the analysis of site-specific ambient vibrations (i.e., ambient seismic noise).

In the framework of seismic structural health monitoring activities of natural and anthropic structures, microseismic signals analysis represents nowadays one of the most widespread and affirmed diagnostic tool in several different fields of investigation, since it allows to retrieve useful information on the acceleration of progressive damaging processes (Colombero, 2017; Colombero et al., 2018b; D'Angiò, 2019; D'Angiò et al., 2021b, 2021a).

As previously described in [Section 2.2](#), microseismic events are low-energy seismic signals genetically related to the occurrence of plastic deformations within a medium. It is well known that, if for example considering a rock mass, when internal relative slips or the propagation of fractures occur due to the reaching of a certain strain threshold, the energy stored in the rock mass is rapidly released in the form of elastic waves, leading to infrasonic, sonic, or microseismic signals (Tang et al., 2015).

Microseismic monitoring mainly focuses on analyzing signals characterized by a wide range of frequency contents, spanning from  $10^1$  to  $10^3$  Hz, thus ranking between traditional earthquake and seismological scale studies and the acoustic emission domain ([Figure 3.14](#)) (Cai et al., 2007). The energy released from fracturing sources in the form of seismic waves radiates away and may be detected by employing specifically designed seismic devices, such as accelerometers and geophones.

Depending on the characteristics of the site under investigation, microseismic sensors can be arranged in several different array configurations (i.e., varying their location, distance, and density) to properly surround the target of monitoring activities (Xiao et al., 2016). Several issues must be considered when dealing with microseismic arrays installation since

---

adverse conditions generally characterize the environments where sensors are deployed. Particular attention needs to be devoted to the choice of sensor locations and installation techniques. Moreover, a sufficient data storage capacity and the availability of power supply have to be guaranteed to allow for continuous data recording.

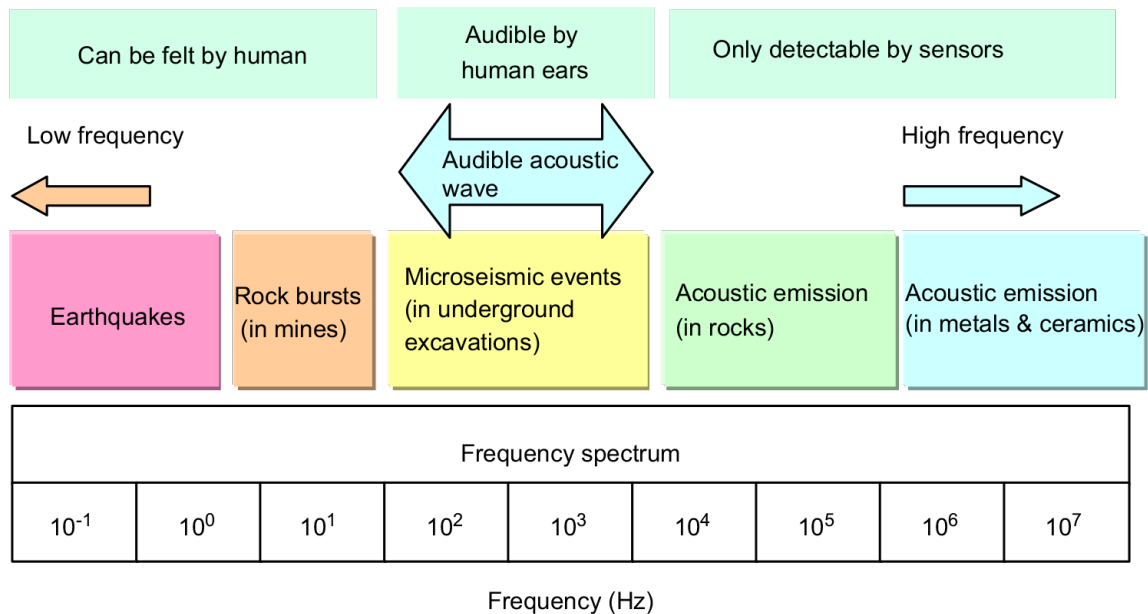


**Figure 3.14.** Seismic motion wave frequency spectrum and field of application of microseismic monitoring (from Cai et al., 2007).

Microseismic data processing generally starts with the identification and the subsequent extraction of signals of interest embedded in ambient vibration recordings. The recognition of microseismic waveforms related to fracturing processes is crucial because it can strongly influence the size and accuracy of collected datasets to be analyzed. This task is nowadays performed through automatic event detection algorithms that enable the identification of weak transient signals within continuous seismic data recordings. There exists a great variety of techniques for the recognition of microseismic events that are based on the analysis of the amplitude or the power of signals in frequency and time domain (Vaezi and van der Baan, 2014), but the Short-Time-Average/Long-Time-Average (STA/LTA) triggering algorithm indeed represents the most widespread and extensively applied method for seismic monitoring purposes (Trnkoczy, 2012). After microseismic events are identified, they can be analyzed, classified, and located to investigate source parameters and mechanisms related to fracturing processes (Xiao et al., 2016). In particular, microseismic event classification is a critical step in data processing since it represents a mandatory practice to guarantee that

no suspicious or artificial waveforms are contained in the dataset and enable the recognition of different microseismic event typologies (Provost et al., 2018). This task is generally accomplished by means of manual or automatic analyses of a great variety of parameters, such as envelope shape, event duration, frequency content, and energetic characteristics of signals. In this framework, there are several examples in literature that proposed the semi-automatic and automatic classification of microseismic events through the implementation of novel methodologies, mainly comprising supervised and unsupervised machine learning techniques (Colombero, 2017; Hibert et al., 2014; Peng et al., 2019; Provost et al., 2018; Spillmann et al., 2007).

During the last decades, the development of high-sensitivity sensors able to detect very low amplitude seismic signals paved the way to innovative applications of microseismic monitoring methods in several research contexts. A vast literature exists and encompasses numerous examples of microseismic monitoring applications in civil engineering (Dai et al., 2017, 2016; Liu et al., 2020; Tang et al., 2015; Xu et al., 2016), mining and quarrying activities (Carlà et al., 2017; Hudyma and Potvin, 2010; Peng et al., 2019; Tang et al., 2015; Wesseloo and Sweby, 2008), tunneling excavation (Liu et al., 2020; Ma et al., 2021), and slope stability analysis (Amitrano et al., 2005; Arosio et al., 2018; Colombero et al., 2021a, 2018b; Iannucci et al., 2020a; Lévy et al., 2011; Senfaute et al., 2009; Spillmann et al., 2007).

Concerning the application of microseismic monitoring techniques for rock slope stability purposes, several case studies are present in literature where high-sensitivity microseismic networks were deployed to test their performance in deciphering the evolution of slopes (i.e., both in soil and rock) affected by gravitational instabilities (Amitrano et al., 2007; Got et al., 2010; Helmstetter and Garambois, 2010). When dealing with the study of microseismic events in jointed rock masses, the analysis of temporal rates, as well as their characterization in terms of relative or absolute amplitude (i.e., peak ground acceleration and moment magnitude), energy and frequency content, are among the most employed strategies to study the time and space evolution of potentially unstable rock masses.

Besides microseismic monitoring strategies, the analysis of ambient seismic noise to investigate jointed rock masses and potentially unstable slopes represents another valuable tool for characterizing their dynamic behavior and evolution due to progressive damaging processes. The ambient seismic noise wavefield results from the superposition of various and

---

different ground vibrations that can be randomly generated by natural sources (e.g., sea waves, wind, trees) or anthropic activities (e.g., industrial machineries, road traffic, train transits). All these sources actively contribute to enrich the ambient noise with their own vibrations and, as a consequence of that seismic noise can cover a very broad frequency range. According to Bonnefoy-Claudet et al. (2006), who proposed a review of the several literature sources dealing with the study of the origin of ambient seismic noise, lower frequency contents (i.e., in the range  $10^{-3}$ – $10^{-1}$  Hz) are prevalently correlated to natural sources, while at frequencies higher than 1 Hz noise the influence of anthropic activities can be dominant.

Similarly to microseismic monitoring, ambient seismic noise monitoring strategies have been applied to a broad spectrum of research fields, especially in civil engineering and engineering geological contexts, as they proved to be adequate for short- to long-term monitoring of dynamic properties of buildings and major infrastructures (Clinton et al., 2006; Kaya and Ventura, 2019), as well as landslide bodies (del Gaudio et al., 2014; Mainsant et al., 2012) and prone-to-fall rock slopes and blocks (Bottelin et al., 2013a; Burjánek et al., 2018; Colombero et al., 2018a; Häusler et al., 2021; Kleinbrod et al., 2019; Valentin et al., 2017). Within these various contexts, it was observed how the spectral analysis of ambient vibrations could reveal both reversible and irreversible changes in seismic properties of the structures under investigation, especially in their resonance frequency values. These studies based their analysis on the assumption that the dynamic behavior of complex structures (both natural and anthropic) can be approximated to a simple oscillator (Bottelin et al., 2013a; Colombero, 2017), which natural resonance frequency ( $f_n$ ) is described by the equation:

$$f_n = \frac{1}{2\pi} \sqrt{\frac{K}{M}} \quad (\text{eq. 3.1})$$

with K and M that are the respectively the stiffness and mass of the oscillating system. Considering [equation 3.1](#), the resonance frequency of a structure is expected to increase with stiffness and decrease with volume. In particular, the term natural is used to emphasize that this is a natural property of a system when it is allowed to vibrate freely without any external excitation (Chopra, 2013).

---



In natural environments, especially when unstable slopes are concerned, resonance frequencies can represent a useful and easy-to-monitor descriptor of their stability conditions. Numerous studies focused on the investigation of prone-to-fall rock masses through spectral analysis of ambient seismic noise and demonstrated not only that resonance frequencies can be identified by prominent peaks in frequency spectra, but also that their modifications might be directly dependent on the progressive development of more unstable conditions (Bottelin et al., 2013a; Colombero et al., 2018a; Lévy et al., 2010). For example, Lévy et al. (2010) studied the dynamic response of 21.000 m<sup>3</sup> rock column at the Chamousset site (French Alps) by implementing an approach based on ambient seismic noise analysis. Monitoring activities were carried out by deploying several sensors on the stable rock mass and the unstable rock volume, enabling the identification of different resonance frequencies of the unstable compartment (which were absent on the stable rock cliff) and the evaluation of their variations in time. Their results showed a significant drop in the values of resonance frequencies of the rock column before its collapse, witnessing the progressive decoupling of the column from the stable rock cliff due to a stiffness decrease deriving from the failure of rock bridges. However, resonance frequencies were also affected by low magnitude and reversible fluctuations due to the continuous action of environmental factors, such as thermal cycles and meteorological events (Bottelin et al., 2013a; Colombero et al., 2018a; Larose et al., 2015). Other applications of ambient seismic noise monitoring in unstable rock masses comprise the extraction of polarization attributes of particle motion (Burjánek et al., 2018; Galea et al., 2014; Häusler et al., 2021; Iannucci et al., 2020b) and the analysis of spectral ratios in both single station and site-to-reference configurations (Burjánek et al., 2010; Colombero et al., 2018a; Moore et al., 2011a). The effectiveness of these two techniques in providing information about the dynamic behavior of unstable rock masses is well-described by the extensive investigation of the Randa landslide case study carried out by Burjánek et al. (2010) and Moore et al. (2011a). In particular, Burjánek et al. (2010) designed a method (WAVEPOL analysis code) to perform the time-frequency dependent polarization analysis (TFPA) of particle motion from ambient seismic noise measurements. By applying this technique, they observed a consistent polarization of resonance frequencies toward the direction of maximum slope displacement, normally oriented with respect to the strike of main fractures in the unstable rock mass compartment. Similarly, through the computation of site-to-reference spectral ratios (SRSR) for several manually identified

---

seismic events, the authors observed high amplification factors, up to 10 at 5 Hz, that were completely absent in the stable rock mass (Figure 3.15) (Moore et al., 2011a)

In the framework of this Ph.D. thesis, ambient seismic noise and microseismic activity monitoring activities were carried out at two different case studies. The objective of this brief introduction, along with the results obtained by several authors and presented in Section 2.2, is to introduce the most exploited methods and analysis techniques to investigate gravitational instabilities and progressive damaging processes affecting jointed rock masses. The description of the monitoring system used for ambient vibrations monitoring, as well as the main stages of data acquisition and processing, will be presented in the following sections.

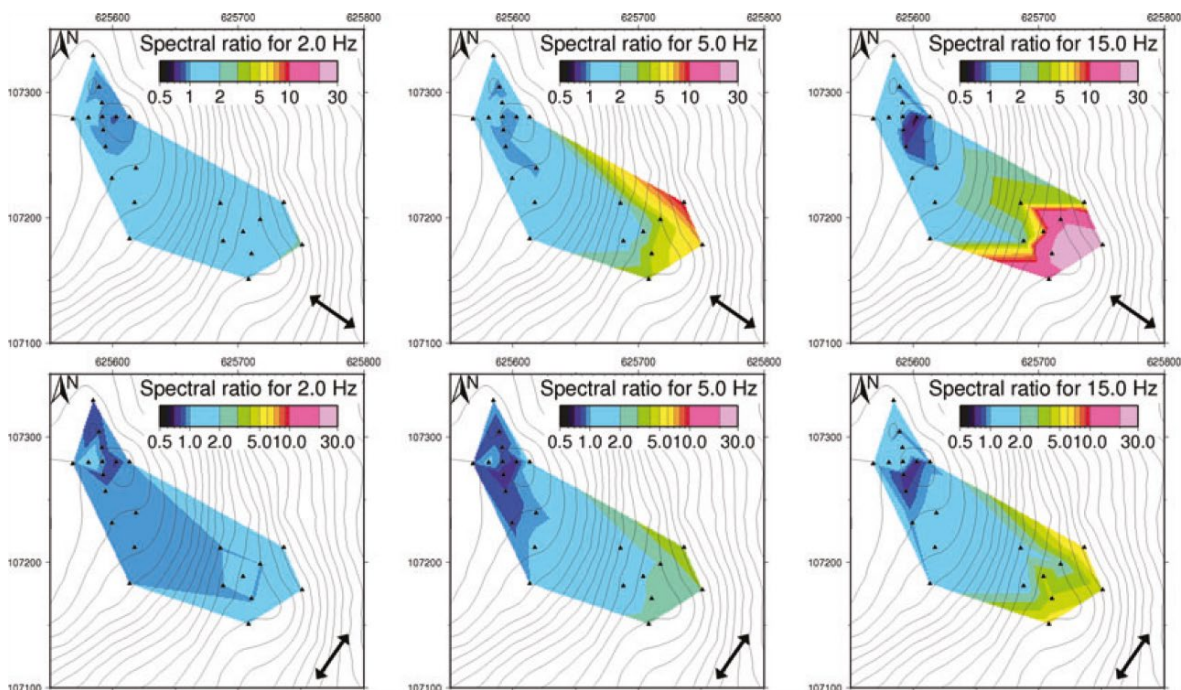


**Figure 3.15.** Interpolated map of mean site-to-reference spectral ratios for the horizontal components of ground motion— $125^\circ\text{N}$  in the upper row, normally oriented to the slope, and  $35^\circ\text{N}$  in the lower row, parallelly oriented to the slope—(from Burjáněk et al., 2010).

### 3.2.1 Ambient vibration monitoring system

With a view of acquiring continuous ambient vibration recordings to analyze ambient seismic noise and extract microseismic events at the Acuto field laboratory and the Wied Il-Mielah sea arch, a high-sensitivity microseismic monitoring network was employed. The monitoring system is composed of multiple (up to nine) one-component piezoelectric microaccelerometers (Bruel & Kjaer type 8344) (Figure 3.16a) connected with 20 meter long low-noise cables to an HBM SomatXR MX1601B-R signal amplifier coupled with a SomatXR CX23-R digital data controller (Figure 3.16c).

These piezoelectric microaccelerometers were primarily selected due to their optimized design for low-frequency and low-level vibration measurements, as witnessed by their high sensitivity (2500 mV/g) and flat frequency response from 5 to 2kHz (Figure 3.16b) which allow these devices to detect very low amplitude signals. The main physical and dynamic characteristics of the employed microaccelerometers are synthetically described in Table 3.4.

Microaccelerometers were directly installed on the surface of both monitored rock masses. Specific holes were drilled in correspondence of locations of interest on the rock block of the Acuto field laboratory, and chemical grout was used to ensure the optimal coupling of sensors on 5 mm steel studs. Instead, at the Wied Il-Mielah case study, preexisting holes and surface irregularities were selected to install steel studs to avoid inconvenient drilling operations.

The data logger can simultaneously record up to 16 channels with a maximum sampling frequency of 20 kHz until the internal storage capacity is reached (64 GB). Depending on the number of recording channels and sampling frequency, which was set to 2400 Hz for both study sites, the internal storage can continuously collect ambient vibration data from several days to months. Furthermore, this acquisition system (i.e., digital amplifier and acquisition module) is characterized by a rugged and insulated case that protects it from dust or water intrusions, thus allowing its use even in harsh environments.

The alimentation of the monitoring system was guaranteed by means external power supply deriving from batteries and a solar panel since both case studies were not served with electricity. At the Acuto field laboratory, power supply was obtained through a 105 W solar panel coupled to a voltage regulator and a backup battery that allowed continuous data

---

acquisition. Notwithstanding this configuration, several gaps exist in the dataset due to some issues related to the exposition of the solar panel and the absence of optimal weather conditions. At the Wied II-Mielah sea arch, installing a solar panel was not possible and, since only short-term monitoring campaigns were conducted, a 12V battery guaranteed power supply.

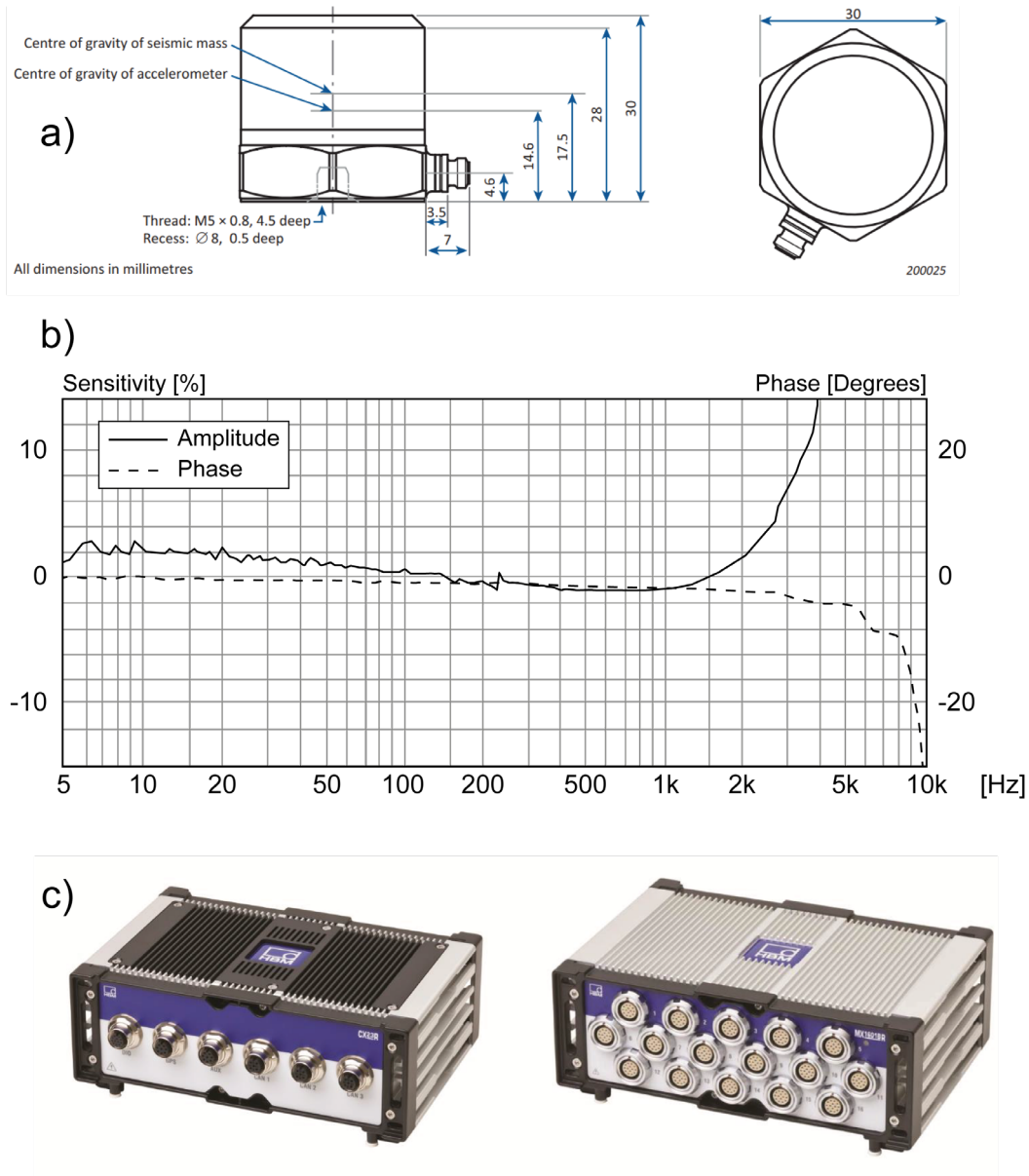


**Figure 3.16.** Technical drawings of the Bruel & Kjaer type-8344 microaccelerometer (a) and relative calibration chart describing the dynamic range of flat frequency response (b). Complementary modules composing the acquisition system (c): data logger — SomatXR CX23-R (on the left); signal amplifier — SomatXR MX1601B-R (on the right).

Dynamic Characteristics	Voltage Sensitivity (@ 159.2 Hz and 4 mA supply current)	$mV/ms^{-2}$ (mV/g)	$250 \pm 20\%$ (2500 $\pm$ 20%)
	Measuring Range	$ms^{-2}$ peak (g peak)	$\pm 26$ (2.6)
	Frequency Range ( $\pm 10\%$ limit) Amplitude Response	Hz	0.2– 3000
	Frequency Response		Individual Frequency Response on calibration chart
	Mounted Resonance Frequency	kHz	>10
	Transverse Sensitivity (@ 30 Hz, 100 $ms^{-2}$ )	%	< 5 of the sensitivity of the axis in question
	Transverse Resonance Frequency	kHz	3.5
Environmental Characteristics	Operating Temperature Range	$^{\circ}C$ ( $^{\circ}F$ )	– 50 to + 100 (– 58 to + 212)
	Temperature Coefficient of Sensitivity	%/ $^{\circ}C$	+ 0.05
	Temperature Transient Sensitivity (3 Hz LLF, 20 dB/decade)	$ms^{-2}/^{\circ}C$	0.001
	Base Strain Sensitivity (at 250 $\mu\epsilon$ in base plane)	Equiv. $ms^{-2}/\mu\epsilon$ (g/ $\mu\epsilon$ )	0.002 (0.0002)
	Magnetic Sensitivity (50 Hz, 0.038 T)	$ms^{-2}/T$ (g/T)	0.5 (0.05)
	Max. Non-destructive Shock	$ms^{-2}$ peak (g peak)	3500 (350)
	Humidity		100% RH non-condensing
Physical Characteristics	Case Material		Stainless steel AISI 316– L
	Sensing Element		Piezoelectric, Type PZ 27
	Sealing		Hermetically sealed
	Weight (excluding cable)	gram (oz.)	176 (6.2)

**Table 3.4.** Summary of the technical characteristics (physical, environmental and dynamic) of the Bruel & Kjaer type-8433 microaccelerometers composing the microseismic monitoring system (from D’Angiò, 2019).

## 3.2.2 Data acquisition

### 3.2.2.1 The Acuto field laboratory

The prone-to-fall rock block at the Acuto field laboratory was instrumented with the high-sensitivity microseismic array during two different monitoring campaigns that were carried on from February 2018 to November 2019. In particular, these campaigns mainly differentiate because two distinct array configurations were designed and implemented (Figure 3.17a). However, the acquisition was set in continuous mode, with a 2400 Hz sampling frequency, and data were stored in 3-hour files to reduce the amount of data to be processed. The acquisition system was placed on top of the quarry wall inside a plastic shielded and sealed box for optimal thermal and water insulation. The same setting was also applied to the Wied Il-Mielah study site.

The first monitoring campaign was conducted from February 23th to May 31st 2018, covering a 3-month time window during the transition from winter to the end of spring. Six one-component micro accelerometers were installed and organized in a linear array characterized by an almost regular 15 cm spacing on the back face of the rock block, where a subvertical open joint partially detaches this unstable rock volume from the stable rock wall. This configuration was designed to characterize the dynamic behavior and microseismic activity of three different portions of the rock mass under investigation (Figure 3.17b). To this aim, three sensors were installed on the rock block (1-2-3), two on the stable rock wall (5-6) and one in the transition zone bounded by major discontinuities (4).

The second monitoring campaign took place from November 28th 2018 to October 23rd 2019, covering a full year of vibration monitoring. The time gap between these two campaigns derives from the long-term employment of this microseismic system to study induced vibrations on a jointed rock mass in correspondence with a railway site (D'Angiò, 2019).

A different array configuration was designed for the second monitoring campaign, and microaccelerometers were deployed in a “composite” triaxial setting in order to investigate potential differences in the 3D dynamic behavior of both the stable rock mass and unstable rock block. This configuration was specifically designed following a site-to-reference logic to highlight any amplification or polarization effects of ambient vibrations potentially

---

associated with the supposed greater mobility of the rock block with respect to the stable rock mass.

In order to effectively measure all three components of ground motion (i.e., NS, EW and Z) microaccelerometers were normally installed in different spots on either the rock wall (ID: 1-2-3) and the rock block (ID: 4-5-6), according to the scheme proposed in [Figure 3.17b](#).

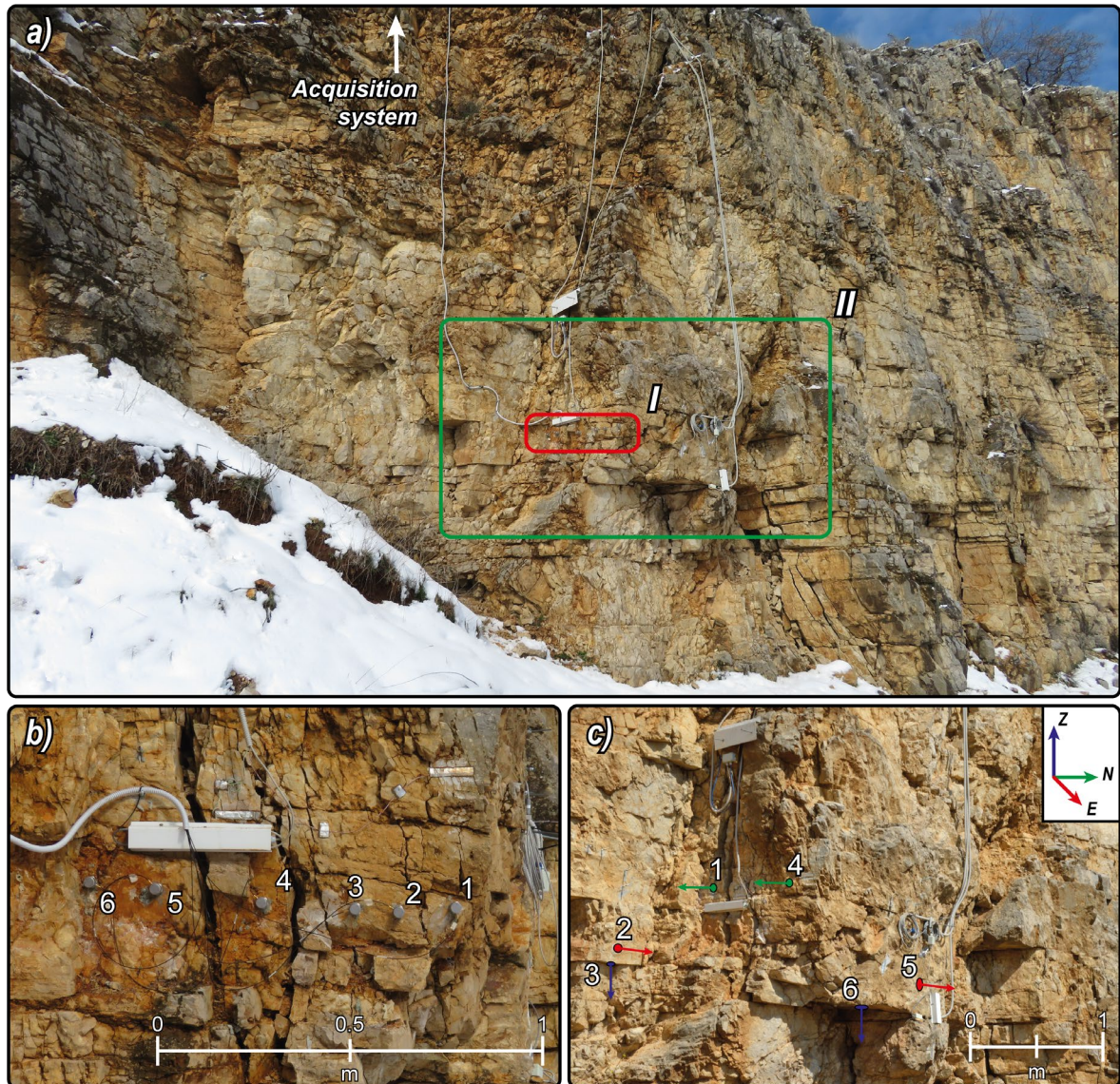


**Figure 3.17.** Front view of the monitored jointed rock block at the Acuto field laboratory (a). The two boxes help to better visualize the different volumes involved by the configurations adopted during the first (I, red box) and the second monitoring campaign (II, green box). Between February and May 2018, six microaccelerometers were deployed along a linear alignment which was specifically designed to mark the transition from the stable rock mass to the unstable rock block (b). The second monitoring campaign (November 2018 - October 2019) was conducted by installing six microaccelerometers in a “composite” double triaxial configuration (c).

It is worth underlying that several time gaps affect the continuity of data acquisition in both monitoring periods. Even though routine maintenance activities were performed with monthly recurrence in order to test the efficiency of the system and to troubleshoot possible issues with backup batteries, recurrent nighttime interruptions of power supply could not be avoided. Furthermore, several weeks-long gaps are present in the dataset collected during the second monitoring campaign due to extraordinary maintenance operations and field activities at different case studies.

A synthesis of the adopted array configurations of microaccelerometers for the two monitoring campaigns is presented in [Table 3.5](#).

Monitoring campaign			N° of sensors	ID Rock wall	ID Rock block	Measured component
N°	Start	End				
I	Feb-2018	May-2018	6	5-6	1-2-3-4	NS
II	Nov-2018	Oct-2019	6	1-2-3	4-5-6	NS-EW-UD

**Table 3.5.** Summary of the main features of the two monitoring campaigns conducted at the Acuto field laboratory between 2018 and 2019.

### 3.2.2.2 The Wied II-Mielah sea arch

At the Wied II-Mielah sea arch ambient seismic noise and microseismic monitoring activities started in February 2019 and were periodically scheduled with seasonal recurrence to acquire a dataset able to describe and characterize the dynamic behavior of the sea arch under different climatic and environmental boundary conditions.

During four seasonal surveys, monitoring activities were carried on through the continuous acquisition of ambient vibrations at 2400 Hz sampling frequency in four- to five-day monitoring time windows. In addition to seismic noise acquisition, a portable weather station and multiple thermocouples connected to a datalogger were employed during every survey to monitor air and rock mass temperature, relative humidity, wind speed and direction.

The microseismic system was supplied by a 12V battery that, considered the high sampling frequency and the number of employed microaccelerometers, guaranteed up to two days of continuous data collection, after which it had to be recharged for several hours.



The deployment of microaccelerometers was designed following a criterion based on the arch's preliminary engineering geological zonation (Section 3.1.1.2), and two different array configurations were adopted during each seasonal survey. The first configuration has seen the deployment of six microaccelerometers along an almost 30-meter long linear alignment on the eastward surface of the arch (Figure 3.18a), and since these sensors are one-component, they only recorded the E-W component of the ground motion. This dense setting was designed to investigate the dynamic behavior of the arch for its entire length and to evaluate the seismic response of the partially dislodged rock compartments.

To this aim, two microaccelerometers were installed on each previously identified structural compartment of the arch with a relative spacing variable in the range 2–5 m (Figure 3.18a): two sensors were installed on the subvertical cliff where the arch is anchored (ID: 5-6), on the central sector of the arch (ID: 3-4) and on the freestanding rock pillar (ID: 1-2).

For what concerns the second configuration, eight microaccelerometers were installed on the three compartments of the arch in order to reconstruct composite triaxial arrays recording all components of ground motion (i.e., NS, EW and Z) (Figure 3.18b). This setting was designed to frame better the 3D dynamic behavior of the three compartments of the arch. More in detail, this configuration followed the same site-to-reference logic adopted for the Acuto rock block, thus aiming at identifying potential amplification or polarization effects within the dislodged sectors of the arch, which were considered to be characterized by a greater mobility with respect to the stable cliff.

Unfortunately, since only eight sensors were available during the performed monitoring campaigns, it was decided to adopt a specific setting more focused on the reconstruction of 3D mobility of the potentially unstable compartments of the arch (i.e., the bridge and the pillar): two three-component arrays were installed on the rock surface of both the rock pillar (ID: 1-2-3) and the rock bridge (ID: 4-5-6), while only two sensors, measuring E-W and vertical components of vibrations, were placed on the stable bedrock sector (ID: 7-8).

As previously introduced, four seasonal monitoring campaigns were conducted (i.e., February 2019, May 2019, September 2019 and February 2020) and a synthesis of the collected data and adopted array configurations is reported in Table 3.6. In particular, during the first monitoring campaign of February 2019, the entire Maltese Archipelago was invested by a violent Mediterranean storm. This extreme event not only caused the rapid

---

temperature decrease toward near-freezing conditions, but was also characterized by heavy rainfalls (45 mm/day), hurricane-force winds (130 km/h), and tidal surges that determined environmental conditions even more severe than those related to the winter storm that caused the collapse of the Azure Window in 2017.

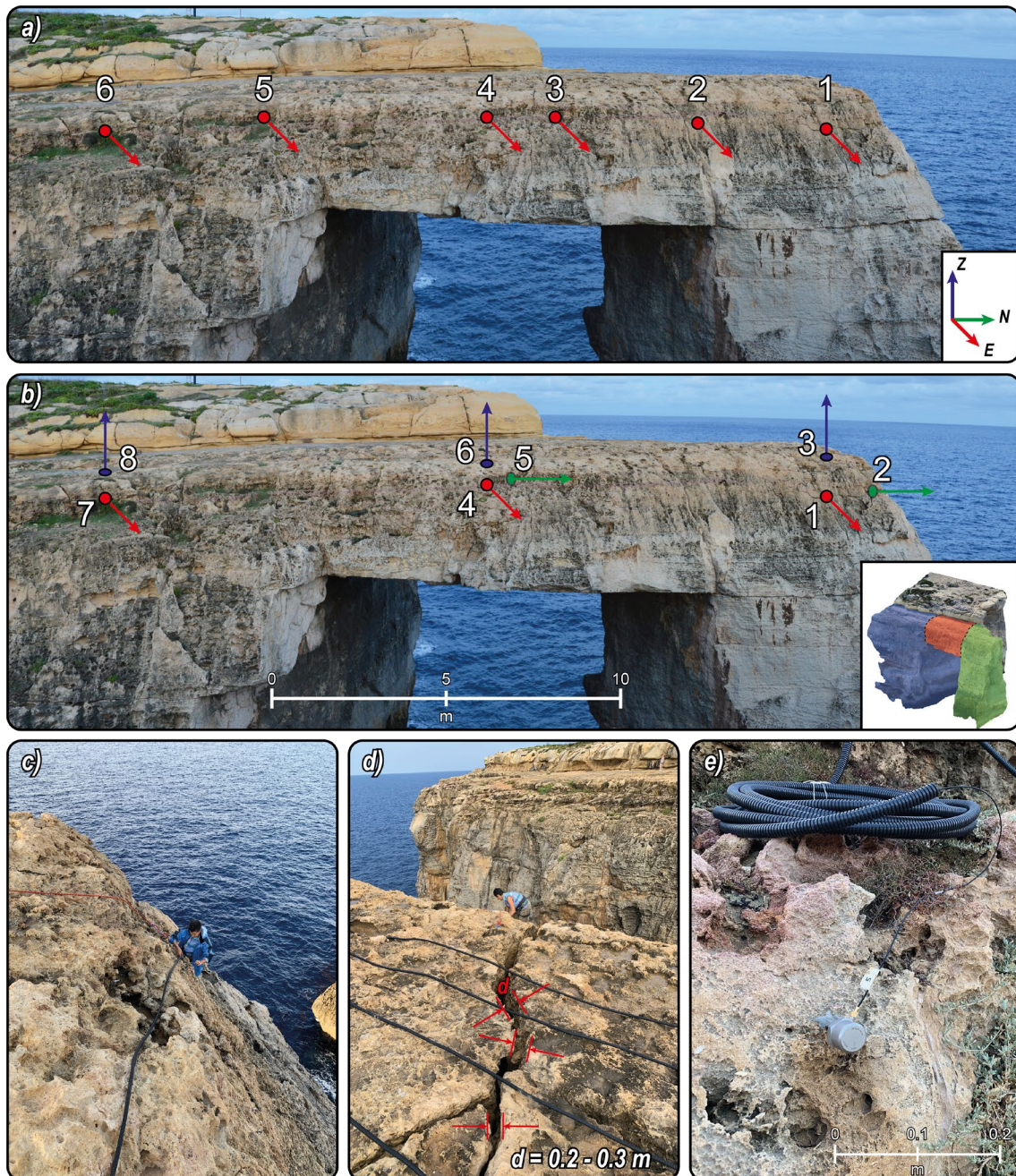


**Figure 3.18.** Schematic view of sensors positioning during ambient vibration monitoring at the Wied II-Mielah sea arch: horizontal alignment along the entire length of the arch (a) and composite triaxial arrays installed on the three compartments of the arch (b). Panels c–e show the different installation stages of the microseismic array.

For what concerns the Wied Il-Mielah sea arch, the monitoring system was installed few hours before the storm event, but it unexpectedly stopped working after only five hours of functioning, probably due to several electrical malfunctions related to water intrusions. Moreover, the system did not work properly after the storm and extraordinary maintenance operations were required to restore the correct functioning of microaccelerometers.

Furthermore, during the monitoring campaign of February 2020 two seismometers were employed to characterize the dynamic behavior of the arch with respect to a reference site. Ambient seismic noise was recorded for three days using two SARA three-component portable seismometers in a site-to-reference configuration and set with 200 Hz sampling frequency: one placed on the outermost sector of the arch (MIE-1), in correspondence of the freestanding pillar, and the other on horizontal bedrock 150 m away as reference (MIE-2) (Figure 3.19).

Monitoring campaign			Array	ID Bedrock	ID Bridge	ID Pillar
N°	Start	End				
<b>I</b>	23/02/2019	25/02/2019	T	7-8	4-5-6	1-2-3
	25/02/2019	27/02/2019	L	5-6	3-4	1-2
<b>II</b>	20/05/2019	22/05/2019	L	5-6	3-4	1-2
	22/05/2019	24/05/2019	T	7-8	4-5-6	1-2-3
<b>III</b>	09/09/2019	11/09/2019	L	5-6	3-4	1-2
	11/09/2019	13/09/2019	T	7-8	4-5-6	1-2-3
<b>IV</b>	21/02/2020	23/02/2020	L	5-6	3-4	1-2
	23/02/2020	25/02/2020	T	7-8	4-5-6	1-2-3

**Table 3.6.** Synthesis of ambient vibration monitoring activities at the Wied Il-Mielah sea arch between 2019 and 2020. T = triaxial array configuration, L = linear array configuration.

The aim of these short-term and seasonal recurrent ambient vibration surveys was to test the potential of ambient seismic noise analyses and microseismic activity monitoring to detect reversible and irreversible modifications of the dynamic behavior of this natural structure in response to continuous and transient environmental stresses without implementing a permanent monitoring network.

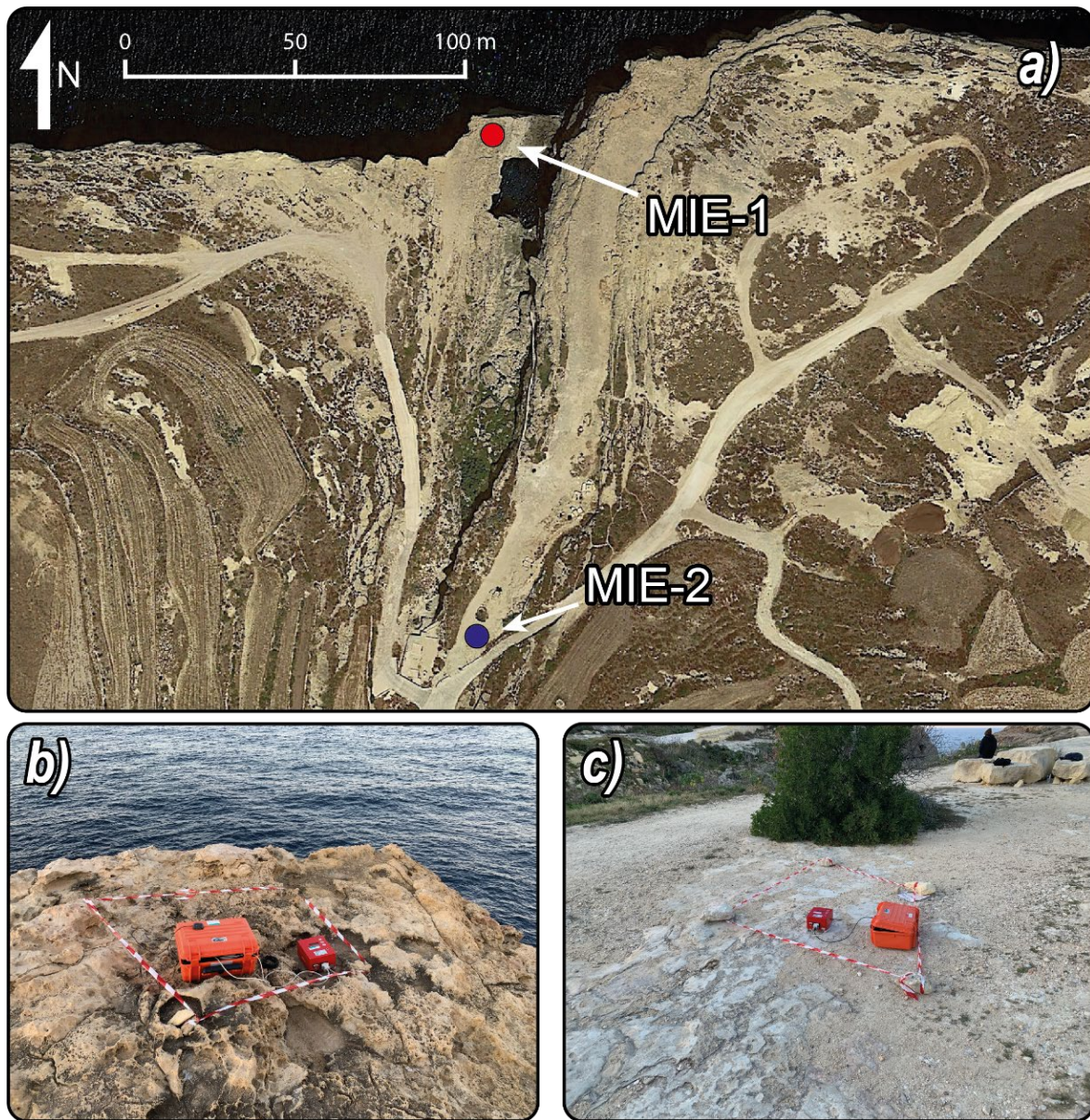


**Figure 3.19.** Aerial view of the Wied II-Mielah sea arch where the location of active and reference seismometers is reported (a). Active seismometer placed on the rock pillar of the arch (b) and reference sensor placed on horizontal bedrock (c).

### 3.2.3 Microseismic event detection and analysis

The ambient seismic noise dataset collected at the two case studies has been thoroughly processed in order to obtain meaningful information from both microseismic events detection and ambient seismic noise analyses. The methodology for ambient seismic noise analysis will be discussed in the next section (Section 3.2.4), while the adopted strategy for the extraction of microseismic events from continuous noise recordings and the preliminary classification of waveforms is described in this section.

The seismic recordings acquired at the Acuto field laboratory and Wied Il-Mielah sea arch were processed following a combined approach encompassing the automatic detection and extraction of energetic events and the preliminary classification of waveforms via manual inspection in order to constitute a dataset of reliable microseismic events, thus avoiding the consideration of false events. The flow chart of Figure 3.20 describes the adopted workflow. The automatic detection of microseismic signals within ambient seismic noise recordings was performed using an STA/LTA triggering algorithm, following the approach proposed by D'Angiò (2019) in his Ph.D. thesis.

Firstly, seismic noise recordings were preprocessed by applying automatic demeaning, detrending, and high-pass filtering above 2 Hz, which in particular allowed to remove any potential disturbances at very low frequencies. After this preprocessing step, an STA/LTA algorithm was launched on every 3-hour file containing acceleration absolute values recorded by each channel of the monitoring array. As previously described, this algorithm is one of the most exploited techniques for detecting seismic transients in various seismological contexts (Li et al., 2016; Withers et al., 1998), allowing for the identification of signals over ambient noise. The functioning principle of STA/LTA trigger algorithms relies on the analysis of the ratio between the average amplitude of signals computed over two different moving time windows. The STA (short-time-average) measures the instant amplitude of the signals, and it is sensitive to transient energetic events, while the LTA (long-time-average) quantifies the average amplitude of the background noise. The ratio between STA/LTA is continuously computed and when it exceeds a user-defined triggering threshold an event is declared, and the related signal is registered until the ratio decreases to a detriggering level. Even though STA/LTA trigger algorithms are among the most widely exploited techniques for the detection of seismic events, the calibration of the length of the

---

two moving windows, as well as the threshold levels, represents a critical task since the incorrect selection of these input parameters may lead to meaningless results. This calibration step should always be performed by considering the characteristics of the events and the background noise at the site under investigation (Trnkoczy, 2012). However, STA windows 2–3 times greater than the dominant period of the microseismic signal and LTA windows 10–100 times greater than the STA window size generally produce good quality results. This calibration step was performed through a preliminary analysis on training datasets aimed at defining the best tuning of STA/LTA input parameters. For the Acuto field laboratory, the size of STA and LTA windows was set to 0.1 s and 10 s, with triggering and detraggering thresholds fixed to 4. For the Wied Il-Mielah sea arch, the duration of STA and LTA windows was set to 0.3 s and 30 s, respectively, with triggering and detraggering levels set to 4. Pre- and post-event time windows were equally set to 5 s to avoid possible losses of information on coda waves or multiple events. Instead of running the event detection algorithm singularly on every channel, the adopted procedure was designed to simultaneously compare seismic traces recorded by all channels of the monitoring array to identify synchronous events. To this aim, and to avoid the collection of false events triggered by electrical and non-natural spurious transients, this procedure embedded two conditions that had to be mandatorily satisfied to declare and extract microseismic events.

The first condition that needs to be met is related to the number of triggered channels by the same microseismic event: when the number of triggered channels ( $N_{Ev}$ ) is equal or greater than a user-defined threshold ( $N_{Th}$ ), the event is extracted. The second condition requires that the time interval between the arrival time on the first and the last triggered channels ( $T_{Ev}$ ) must be shorter than a user-defined duration ( $T_{Th}$ ) that starts in correspondence with the first arrival of the microseismic event. When both these conditions are satisfied, the microseismic event is extracted and further analyzed. In this study, the minimum number of channels that needed to be triggered ( $N_{Th}$ ) to declare an event was set to 4 and 3 for the Acuto and Wied Il-Mielah study sites respectively, while the maximum time interval in which the first arrival on each triggered channel had to be comprised ( $T_{Th}$ ) was equally set to 0.15 s. It is worth specifying that the condition related to minimum number of triggered channels ( $N_{Ev}$ ) was found to be dominant in constraining the number of microseismic events detected by the STA/LTA algorithm.

---

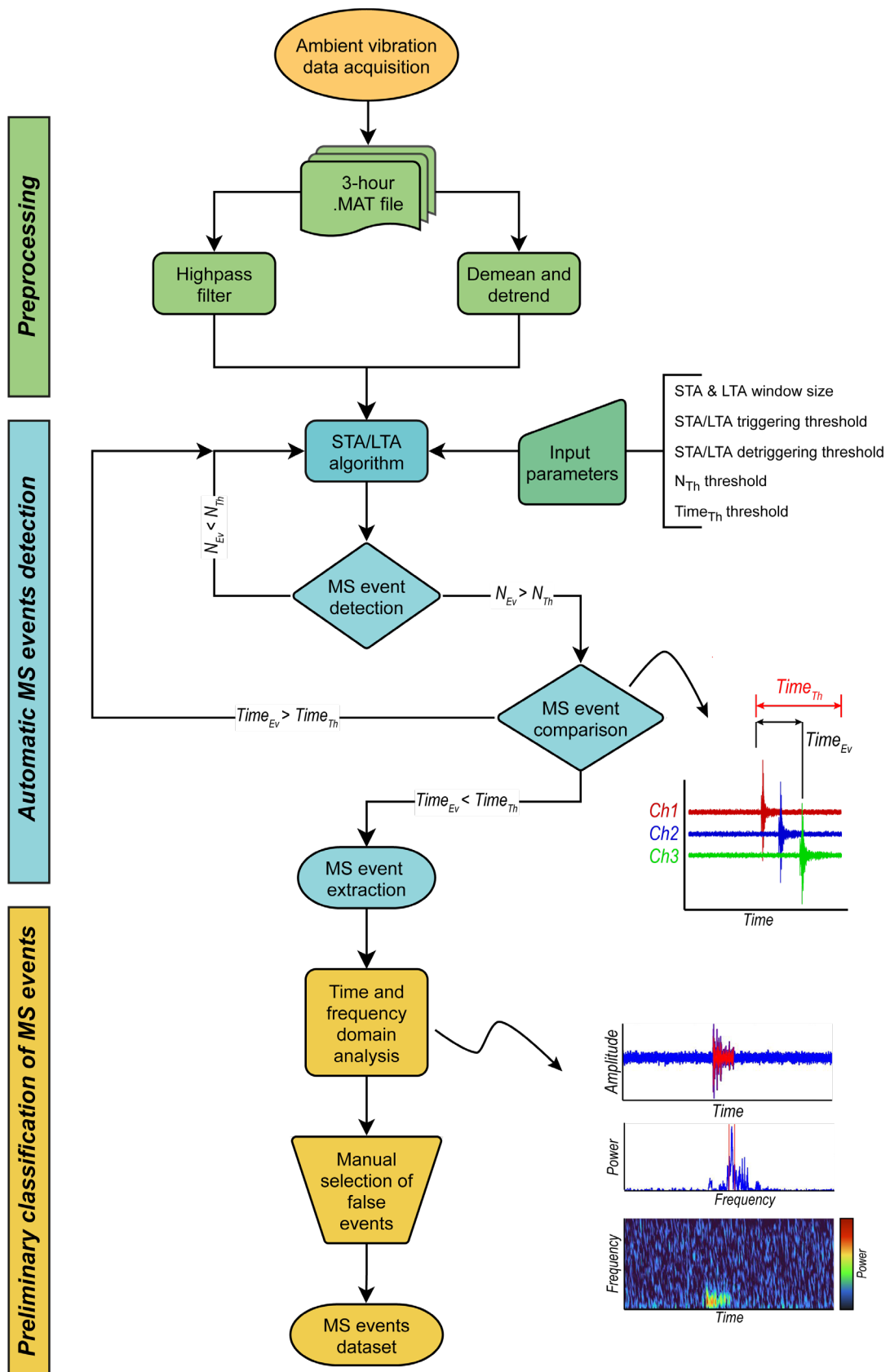


**Figure 3.20.** Flow chart summarizing the adopted workflow for the automatic detection and preliminary classification of microseismic events from ambient seismic noise continuous recordings.

This threshold can vary from one up to the maximum number of recording channels, and the higher its level is selected, the greater the coherence of the signals and the reliability of the resulting microseismic events.

In contrast, when dealing with low signal-to-noise ratio signals it is not rare to miss the detection of events due to different factors that can significantly affect monitoring arrays (e.g., the distance among sensors, the presence of fractures or possible malfunctioning of sensors) and a too conservative triggered channels threshold could lead to a potential loss of information. However, using the abovementioned input parameters of the STA/LTA algorithm, which are summarized for both case studies in [Table 3.7](#), it was possible to constitute a microseismic dataset composed of 864 events.

After the automatic identification and extraction of energetic events from ambient seismic noise recording, a preliminary classification of the collected signals was performed in order to discriminate real microseismic events from false alarms. This stage of the analysis always represents a major task in microseismic monitoring activities and it is of crucial importance when the relationship between environmental factors and microseismicity has to be investigated since, if false events (e.g., related to anthropic or electrical disturbances) are not excluded from the analysis, results might be meaningless. To this aim, a preliminary classification of extracted signals was performed on both the Acuto and Wied Il-Mielah datasets through the manual inspections of waveforms, power spectra and spectrograms of every detected event on each recording channel, which represent one the fastest and most affordable ways to analyze signals characteristics in the time and frequency domain. This analysis allowed to concurrently investigate the coherency of time and frequency domain characteristics of signals over all channels of the recording array, leading to a significant reduction in the number of events within both datasets and the distinction between real microseismic events ([Figure 3.21](#)) and false events ([Figure 3.22](#)). Unfortunately, while the manual classification of events belonging to the dataset of Acuto allowed classifying hundreds of signals as microseismic events, for what concerns the Wied Il-Mielah arch, no reliable microseismic events were identified within the entire collected dataset as potentially related to any natural processes (see [Section 4.1](#) for further details). To corroborate the results of the manual classification of microseismic events and to reduce the influence of subjectivity on this analysis, a statistical comparison between time and frequency domain characteristics of microseismic and false events was performed.

---



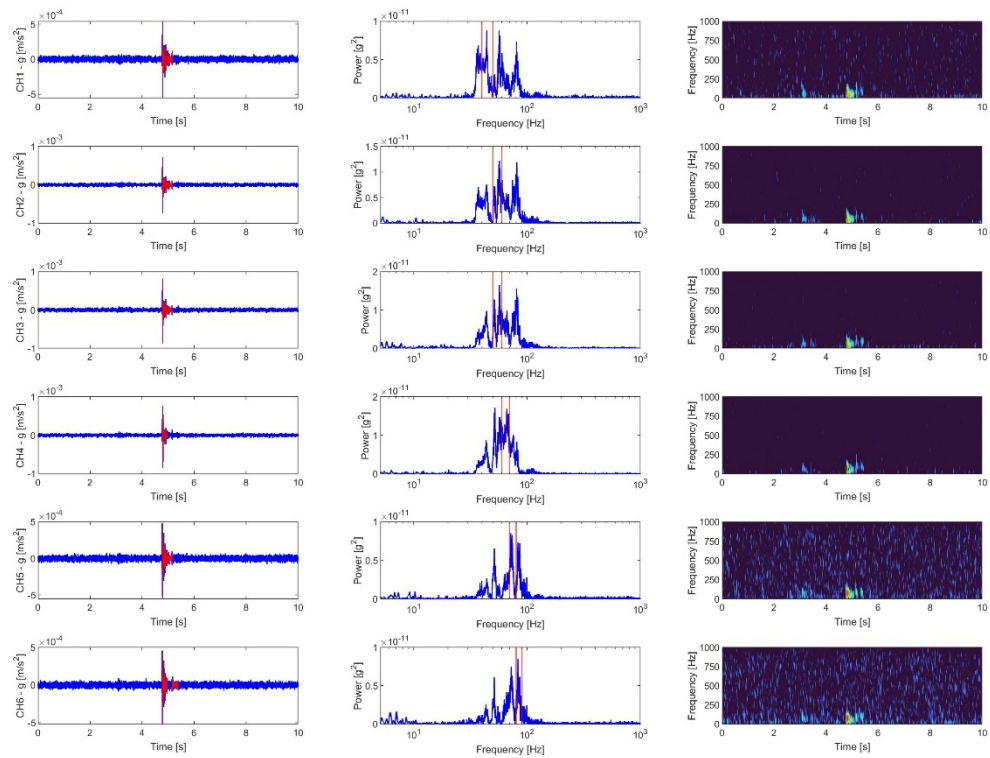


**Figure 3.21.** Example of one event automatically detected and classified as microseismic event through visual screening of its time and frequency domain features (left: signal waveform; center: power spectral density estimate; right: spectrogram).

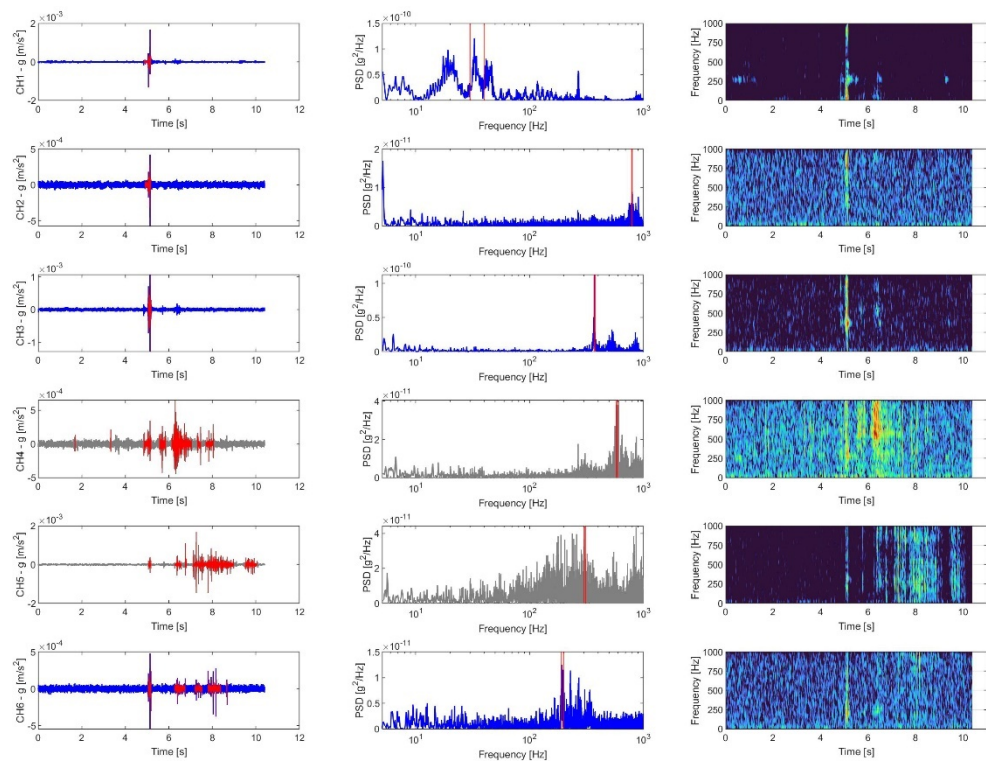


**Figure 3.22.** Example of one event automatically detected and classified as false event through visual screening of its time and frequency domain features (left: signal waveform; center: power spectral density estimate; right: spectrogram).

This task is generally conducted by implementing fully- or semi-automatic procedures that rely on machine learning algorithms—such as Hidden Markov Models (HMMs) (Benitez et al., 2007), Support Vector Machines (SVMs) (Qu et al., 2018), Linear Discriminant Analysis (LDA) (Arosio et al., 2018), Fuzzy Logic (FL) (Hibert et al., 2014), Random Forest (RF) (Hibert et al., 2017; Wenner et al., 2020), Convolutional Neural Networks (CNN) (Meyer et al., 2019), K-Means Clustering (Colombero, 2017)—to identify recurrent classes of events. For this thesis, however, a first attempt was made to give further quantitative insights on the main features of classified events and to strengthen the affordability of the manual inspection procedure.

For this reason, the whole dataset was investigated by analyzing several time- and frequency-domain parameters extracted from every classified event following the workflow proposed by Colombero (2017).

In the time domain, signals were analyzed by extracting information on their duration, shape, and energy content. Concerning their shape, three parameters were considered: the maximum amplitude ( $A_{\max}$  or PGA – peak ground acceleration), the normalized amplitude ( $A_{\max}/A_{\text{mean}}$ ), and the kurtosis of the signal envelope. Concerning their duration, bracketed and uniform duration were computed. The bracketed duration is retrieved as the time interval comprised between the first and the last exceedance of the signal over a fixed threshold. In contrast, the uniform duration is defined as the sum of all time intervals in which the signal exceeds the same threshold (Bommer et al., 2009).

The Arias Intensity ( $I_A$ ) was also calculated to evaluate the energy content associated with every event, given that this parameter is a measure of the cumulative intensity of ground motion obtained as the integral of the squared acceleration of the seismic signal (eq. 3.2):

$$I_A = \frac{\pi}{2g} \int_0^{t_{\max}} a(t)^2 dt \quad (\text{eq. 3.2})$$

where  $a(t)$  is the ground acceleration at time  $t$  and  $t_{\max}$  is the total duration of the seismic signal. In addition, the maximum frequency of Fourier power spectra ( $f_{\max}$ ) and the total amount of spectral energy in 10 Hz frequency bands, spanning from 0 to 1000 Hz, were extracted to characterize spectral features of microseismic and false events were computed. In particular, the spectral energy of each signal in each frequency band was computed as:

---

$$E_{band_{f_0 \rightarrow f_0+10}} = \int_f^{f+10 \text{ Hz}} DFT(f) df \quad (\text{eq. 3.3})$$

where  $DFT(f)$  is the value of the power spectrum at the frequency  $f$ , obtained through the Discrete Fourier Transform of the of the event signal.

<b>Case study</b>	<b>STA</b> (s)	<b>LTA</b> (s)	<b>STA/LTA</b> ratio	<b>Pre-Post event</b> (s)	<b>N<sub>Th</sub></b> (-)	<b>T<sub>Th</sub></b> (s)
<b>WIM</b>	0.3	30	4	5	3	0.15
<b>ACT</b>	0.1	10	4	5	4	0.15

**Table 3.7.** Synthesis of the selected parameters for the analysis of the Acuto (ACT) and Wied Il-Mielah (WIM) datasets through the STA/LTA algorithm.

Another important task that should be performed when dealing with microseismic analysis is related to the location of microseismic sources. For what concerns this work, event location was not performed because it was found to be impossible to pursue at both case studies and for different reasons.

At the Acuto study site, since the two adopted array configurations were organized in a very restricted space, it was not possible to identify any delay in the arrival time of microseismic events on different channels, even considering the high sampling frequency adopted. Concerning the Wied Il-Mielah sea arch, even though the aperture of the arrays was considered to be sufficient for event location purposes, no microseismic events were recognized in the dataset as previously introduced. For these reasons, focusing on the Acuto study site, an attempt was made to retrieve information on the sources of the recorded microseismic events by compiling a modified frequency-magnitude curve according to the Gutenberg-Richter (1954) power law (eq. 3.4):

$$\log_{10} N = a - bM \quad (\text{eq. 3.4})$$

where  $N$  is the cumulative number of events having a magnitude higher than  $M$ , while  $a$  and  $b$  are constants. Given the already discussed impossibility to locate the events and due to the lack of information on the magnitude of the recorded events, the frequency-magnitude

relation was modified considering the Arias Intensity. This parameter is in fact characterized by a log-linear relation to moment magnitude, as empirically verified by Wilson (1993) with strong motion data from several California earthquakes (eq. 3.5):

$$\log_{10}(I_A) = M - 2\log_{10}(R) - 3.99 \quad (\text{eq. 3.5})$$

where  $I_A$  is the Arias Intensity,  $M$  is the moment magnitude and  $R$  is the distance from the seismic source. Then, by considering this linear relation between the logarithm of Arias Intensity and magnitude, and assuming that  $R$  is equal for all recording stations, the adopted relation to analyze frequency-intensity curves was derived as follows:

$$\log_{10}N = a - b \log_{10}(I_A) \quad (\text{eq. 3.6})$$

The most significant parameter in this relation is the b-value, which can vary significantly depending on microseismic activity's predominant source failure mechanism (Hudyma and Potvin, 2010). Even though the approach used for this preliminary characterization is non-canonical, and the parameters obtained through this analysis cannot be interpreted or compared to literature sources, it was regarded as the only possible way to acquire information on potential microseismic sources. Moreover, the same frequency-intensity curve and the related power-law were also computed considering false events, producing a comparison with the one of microseismic events to test if any differences could be noticeable.

### 3.2.4 Ambient seismic noise analysis

Parallel to the analysis of vibration recordings for the detection and extraction of microseismic events, the same dataset collected at the two study sites was processed in order to characterize the dynamic behavior of the investigated rock masses through the spectral analysis of ambient seismic noise.

As previously discussed in [Section 2.2](#) and [3.2](#), the spectral analysis of seismic noise represents a useful tool for the identification of natural resonance frequencies of unstable rock masses since it can highlight the existence of possible amplification or directivity effects that could help assessing the degree of instability of the site under investigation.

In the present study, the ambient seismic noise processing was performed following the methodology proposed by McNamara and Buland (2004).

The standard method for the quantification of ambient seismic background noise relies on the computation of the noise power spectral density (PSD) estimate, that provides information on the distribution of the average power of discrete signals as a function of frequency. The most widely exploited technique for PSD estimation of stationary random seismic signals is using the Fast Fourier Transform (FFT) (Cooley and Tukey, 1965) to compute PSDs on short-length time windows extracted from the original signal, which are then averaged to retrieve the PSD for the entire signal.

The PSD estimate via a finite-range FFT of the original data is particularly advantageous for its computational efficiency. The finite-range Fourier transform  $Y(f)$  of a periodic time series  $y(t)$  is given by:

$$Y(f, T_r) = \int_0^{T_r} y(t) e^{-i2\pi f t} dt \quad (\text{eq. 3.7})$$

where  $T_r$  is the length of time series segment, and  $f$  is the frequency. For discrete frequency values ( $f_k$ ) the Fourier components are defined as:

$$Y_k = \frac{Y(f_k, T_r)}{\Delta t} \quad (\text{eq. 3.8})$$

for  $f_k = k/N\Delta t$ , when  $k = 1, 2, \dots, N - 1$ , where  $\Delta t$  is the sampling interval and  $N$  is the number of samples in each segment,  $N = T_R/\Delta t$ . Then, using the Fourier components as defined, the total PSD estimate is given by:

$$PSD_k = \frac{2\Delta t}{N} |Y_k|^2 \quad (\text{eq. 3.9})$$

As it can be observed from [equation 3.9](#), the total power ( $PSD_k$ ) is the square of the amplitude spectrum normalized by a factor  $2\Delta t/N$ .

Several pre-processing operations were necessary prior to the computation of PSDs for the whole seismic noise dataset collected at both case studies. Firstly, the preliminary spectral analysis of seismic noise acquired through the microseismic monitoring array highlighted the presence of periodically distributed spike-like peaks (i.e., very narrow spectral peaks with an almost constant  $\sim 10$  Hz spacing) within a very broad frequency range ([Figure 3.23a](#)). The origin of such disturbance was not thoroughly understood, but since it was common to all seismic traces recorded at several case studies, it was considered to be related some electrical issues affecting the acquisition chain. This problem was troubleshooted through the design of a specific pre-processing procedure incorporating a Hampel filter, which can detect and remove outliers within an input signal using the Hampel identifier (Liu et al., 2004): the signal is divided into  $N$  segments and, for each of them, the median ( $M$ ) and the median absolute deviation ( $MAD$ ) of the defined samples are computed. If a sample differs from the median by more than three times the median absolute deviation ( $3MAD$ ), the filter automatically replaces that sample with the median value ([Figure 3.23b](#)).

In this framework, for the purpose of removing the abovementioned spectral disturbances from frequency spectra and avoiding any potential modification of the natural spectral content of seismic traces, this filter was applied to Fourier amplitude spectra, computed via FFT, by defining 0.5 Hz frequency bins and achieving good quality results ([Figure 3.23c](#)). Then, the Inverse Fast Fourier Transform (IFFT) was used to obtain filtered and spike-free signals in the time domain ([Figure 3.23d](#)). After this preliminary step, since the acquisition system was set to store data creating 3-hour long files, recordings were firstly divided into 1-hour finite-length time series. No corrections for instrumental response of microaccelerometers was applied during this step because this task is automatically

---

performed by the system datalogger when saving files. Moreover, each 1-h recording was bandpass filtered between 2 and 100 Hz to reduce the size of files, since the monitoring array acquired ambient vibration with a 2400 Hz sampling frequency, and to avoid potential disturbances at very low frequencies related to the limited dynamic range of microaccelerometers.

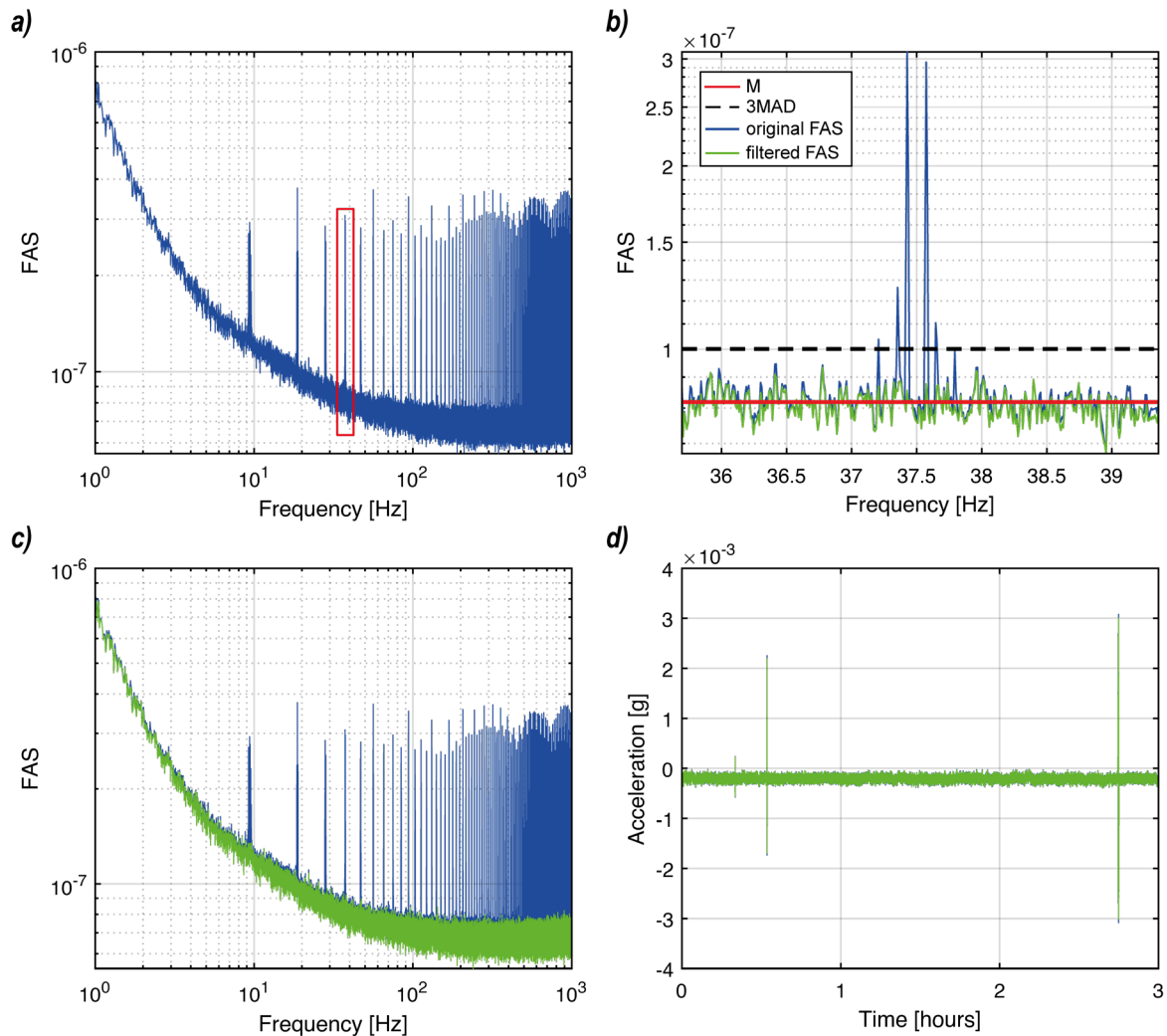


**Figure 3.23.** Fourier amplitude spectrum (FAS) of a 3-hour long recording affected by the presence of periodically recurrent narrow spectral peaks (a). The working principle of the used Hampel filter is described by the plot in panel b: M – median value, 3MAD – threshold value equals to three times the median absolute deviation. Example of FAS before (blue line) and after (green line) the application of the designed filter (c). The efficiency of this approach is witnessed by the perfect similarity between the original and the filtered signal (d).

The recordings were then detrended and transformed to a zero mean in order to avoid possible long-period contaminations (i.e., any frequency component whose period is longer than the record length). If trends are not eliminated in the data, large distortions can occur

in spectral processing, nullifying the estimation of low-frequency spectral contents (McNamara and Buland, 2004). An anti-triggering STA/LTA algorithm was also designed to exclude the influence of energetic transients in ambient vibration measurements, allowing to consider the quasi-stationary seismic noise by rejecting all windows exceeding the defined threshold value. Each 1-hour recording was split into 50% overlapping segments of 409.6 s, in order to reduce the variance of the final PSD estimate and to suppress the effect of spectral leakage. Then, to improve the efficiency and the computation speed of the FFT, the number of samples in each segment was truncated to the next lowest power of 2. A hamming window was also applied to each segment to reduce the effect of spectral leakage. Using these parameters, PSD estimates were computed for each separate overlapping segment and then averaged over the full hour to retrieve the final PSD estimate. Due to segment averaging, the final PSD estimate has a 95% level of confidence that the spectral point lies within -2.14 to +2.87 dB of the estimate (Peterson and Survey, 1993).

Along with the computation of PSDs for the analysis of the spectral content of ambient seismic noise, another adopted method in this work consisted in the computation of site-to-reference spectral ratios (SRSR). This is a very useful tool to analyze local site amplification effects through the direct comparison of ground motion recordings at different sites. The principle of this technique is based on the normalization of the Fourier amplitude spectra calculated at specific sites (e.g., unstable rock mass compartments, pillars or slabs) with respect to the spectra at a reference site characterized by known conditions (e.g., horizontal bedrock or stable rock mass compartments). Through the application of this normalization procedure, the final result is a frequency-dependent relative amplification function of the site with respect to the reference. This technique is in general used on earthquake recordings, where the distance of the source can be constrained and, in case the distance to the source is large enough to consider far-field conditions, it is possible to neglect source directivity and path effects (Andrews, 1986).

When dealing with ambient seismic noise recordings vibration sources are generally unknown, nonetheless SRSR can still be representative in terms of local site effects (Irikura and Kawanaka, 1980; Roten et al., 2006) as also witnessed by several successful applications of this method for the analysis of stability conditions of unstable or prone-to-fall rock masses (Burjánek et al., 2012; Colombero et al., 2018a; Kleinbrod et al., 2017).

---



With the aim of analyzing potential amplification effects at the two sites under investigation, and considering that the microseismic monitoring array employed for seismic noise acquisition is composed of only one-component accelerometers, the spectral ratios were calculated between sensors measuring the same component of ground motion. The procedure for data pre-processing is the same to the one previously described for the computation of PSDs. Spectral ratios were computed by normalizing every 1-h smoothed average spectrum to the corresponding average spectrum of the reference sensor. With regard to the only Wied II-Mielah sea arch study site, two triaxial seismometers were employed in a site-to-reference configuration in addition to the microseismic monitoring array during the last monitoring campaign of February 2020. The acquisition of almost three days of recordings not only allowed to compute spectral ratios between the arch and a reference site identified outside its structure, but it also enabled to study polarization effects of ambient seismic noise at the two stations. This task was accomplished using the WAVEPOL analysis code (Burjánek et al., 2010) that, as previously introduced in [Section 3.2](#), performs the time-frequency dependent polarization analysis from seismic noise measurements by combining the complex polarization analysis from (Vidale, 1986) and the Continuous Wavelet Transform (CWT). This tool then permits to characterize the particle motion of ambient vibrations for each time and frequency through an ellipse oriented in the 3D Euclidean space ([Figure 3.24](#)), defined by three parameters:

- Strike ( $\varphi$ ), that is the azimuth of the major axis measured in degrees from north;
- Dip ( $\delta$ ), that represents the tilt of the major axis measured in degrees downward to the horizontal plane;
- Ellipticity, which is defined as the tangent of the angle ( $\epsilon$ ), which is the ratio between the length of the semi-minor and semi-major axes of the ellipse.

All three parameters can vary in time and frequency, and in order to analyze and retrieve the relative occurrence of polarization parameters, histograms of polarization attributes are constructed over time and for every frequency ([Figure 3.24b](#)). The results of this analysis are then represented in form of polar plots to highlight the combined angular and frequency dependence (Burjánek et al., 2012).

---

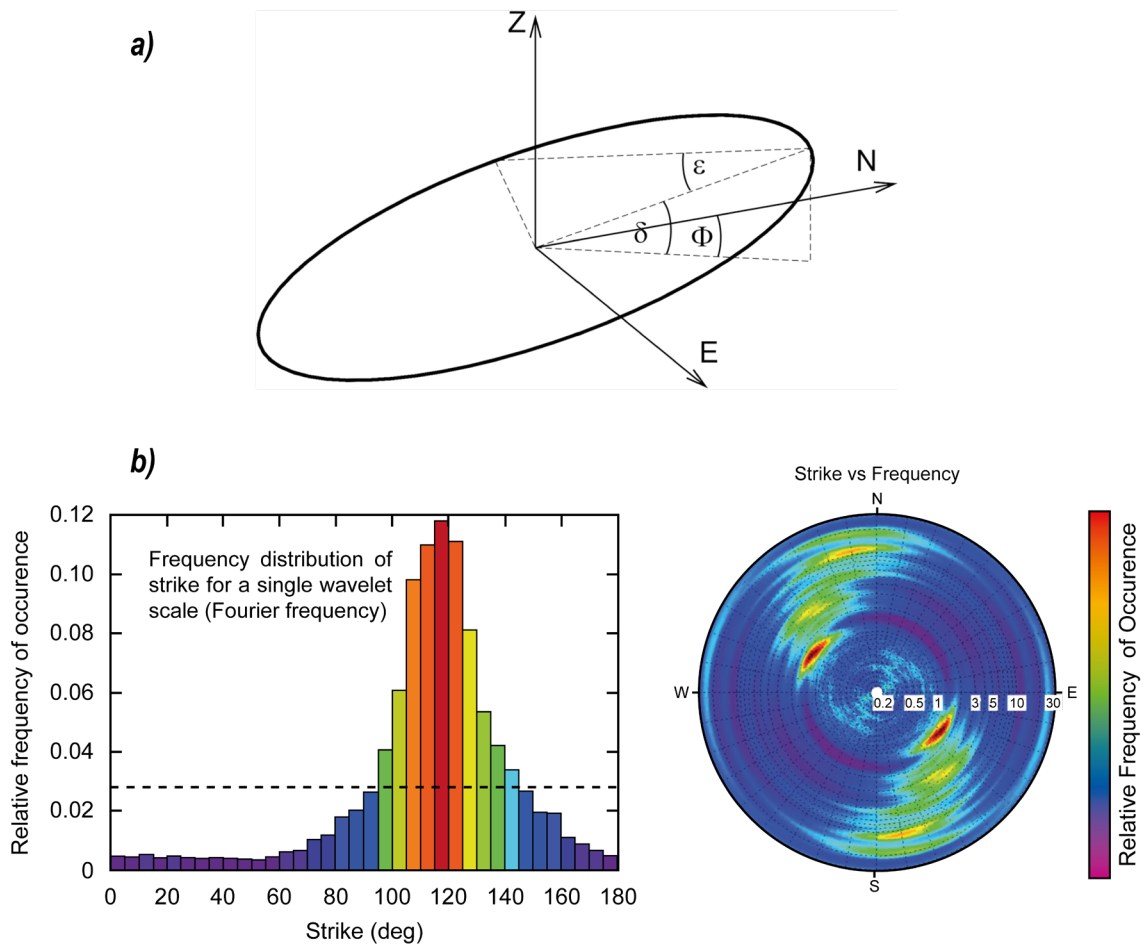


**Figure 3.24.** Polarization ellipse showing the three parameters previously described (strike, dip and ellipticity) **(a)**. Example of the histogram representing the relative occurrence of strike –  $\varphi$  – (azimuth) of ambient vibrations for a single frequency and polar plot representation of histograms for different frequencies, where the color-scale indicated the relative frequency of occurrence **(b)** (modified from Burjánek et al., 2012).

### 3.3 Infrared thermography surveys

#### 3.3.1 The Infrared Thermography technique

The electromagnetic (EM) radiation travels in space in the form of polarized waves which characteristics change over a broad spectrum of frequencies ( $f$ ) and wavelengths ( $\lambda$ ), from very long radio waves ( $\lambda = 10^6\text{--}10^8 \mu\text{m}$ ) to UV-rays ( $\lambda = 10^{-2}\text{--}10^{-1} \mu\text{m}$ ) and  $\gamma$ -rays ( $\lambda = 10^{-6}\text{--}10^{-5} \mu\text{m}$ ) (DeWitt and Nutter, 1991). The EM spectrum is divided into several wavelength bands and, among these, the infrared (IR) band covers the wavelength range 0.78–1000  $\mu\text{m}$ , thus being comprised between visible light and microwaves (Vollmer and Möllmann, 2013). This area of the IR spectrum is defined as the infrared region (Figure 3.25). According to the blackbody theory, all forms of matter with a temperature above absolute zero (i.e.,  $T = -273.15 \text{ }^\circ\text{C}$ ) emit EM radiations due to thermally-excited electron oscillations and transitions within the matter itself (Pappalardo et al., 2016).

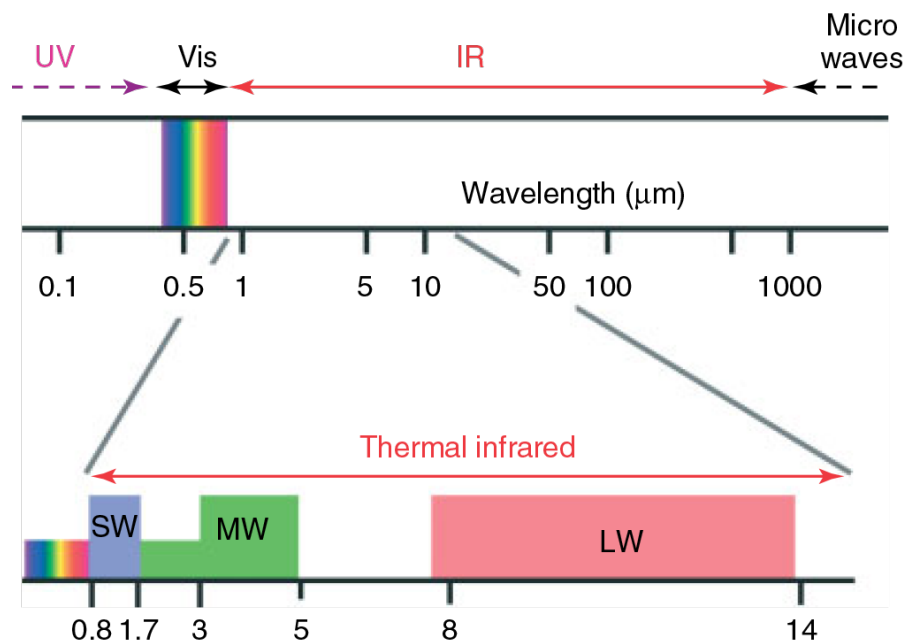


**Figure 3.25.** Partial representation of the EM radiation spectrum. Infrared (IR) and adjacent spectral regions and expanded view of the so-called thermal infrared. This is the region where IR imaging systems for short-wave (SW), mid-wave (MW), or long-wave (LW) cameras exist (from Vollmer and Möllmann, 2013).

Since the maximum radiant power that bodies can emit is a direct function of their temperature, the term thermal radiation was introduced. Thermal radiation occurs in a wide range of the EM spectrum, including part of the UV radiation and the entire IR and visible ranges. Most of the thermal radiation is concentrated in the IR spectral region of and for this

reason, it is not directly detectable by human eyes. For infrared thermography applications, a minimal range of the IR spectrum is considered, and commercial cameras are only available for longwave (LW), mid-wave (MW), and short-wave (SW) regions.

From a physical perspective and according to the Stefan-Boltzmann law, the total amount of energy emitted by a body in the form of thermal radiation ( $J$ ) is proportional to its emissivity ( $\epsilon$ ), to the Stefan-Boltzmann constant ( $\sigma$ ), and to the fourth power of its surface temperature ( $T$ ):

$$J = \epsilon\sigma T^4 \quad (\text{eq. 3.10})$$

In particular, emissivity is a dimensionless parameter mathematically defined as the ratio between the amount of infrared radiation emitted from the surface of an object to that emitted by a blackbody at the same temperature. Emissivity values range from 0, when all the radiation is perfectly reflected, to 1, whereas all the radiation is absorbed. The latter case is related to *black bodies* that can absorb and emit the entire incoming radiation. Since these two extreme conditions are purely theoretical, all bodies in nature are characterized by emissivity values that range within this interval and are commonly known as *gray bodies* (Vollmer and Möllmann, 2013).

Based on the relation of [equation 3.10](#), the infrared thermography (IRT) technique allows determining the temperature of any investigated object from quantifying its emitted thermal radiation. Thermal imaging is a widely used noncontact and nondestructive remote sensing technique with a great variety of applications that can provide the detailed mapping of surface temperature distributions of any object. Infrared (IR) cameras are devices generally operating in the mid-wave infrared band of the EM radiation spectrum (7.5–14  $\mu\text{m}$ ), and their sensors can quantify the received infrared radiation into temperature values through their built-in processors (Frodella et al., 2020). The output of IR cameras is a radiometric image (i.e., thermogram) that consists of a pixel matrix containing the distribution of surface temperatures of the targeted object. Radiometric imagery is commonly visualized through colorimetric scales that enable the visualization of temperature patterns and the consequent recognition of thermal anomalies within or at the surface of the target through color contrasts between adjacent pixels. Because modern IR camera functioning is very similar to digital

---

cameras, thermogram acquisition is accomplished in a fully automatic way. Nevertheless, it is always mandatory to set the sensitivity parameters of the IR sensor which include target emissivity, distance from the target, relative position of camera and target, reflected surface temperature, air temperature and relative humidity, in order to account for a general atmospheric correction. This thermographic calibration protocol is crucial because the incoming thermal radiation (measured by the IR sensor) can be influenced by several factors that are not directly related to the object temperature. In fact, the surrounding environment and the thermal radiation angle of incidence can exert a non-negligible influence on radiometric measurements. This is due to the presence of parasite radiation and the phenomena of atmospheric partial absorption and dispersion of the emitted radiation (Ball and Pinkerton, 2006; Fiorucci et al., 2018; Pappalardo et al., 2016; Prendes-Gero et al., 2013; Vollmer and Möllmann, 2013). However, although IRT surveys may be variably affected by the abovementioned factors, the advantages of this remote sensing technique for studying surface temperatures are consistent and mainly related to its cost-effectiveness and versatility in very different contexts.

### **3.3.2 Infrared thermography applications for jointed rock mass characterization**

The fast technological development and the economic sustainability of high-resolution portable thermal cameras witnessed over the last decade have led to the increasingly widespread application of this remote surveying technique. Due to its great potential, IRT proved to be a useful non-invasive remote sensing technique in various scientific fields, from structural damage detection and energy efficiency analysis in civil engineering (Barreira et al., 2020; Kylili et al., 2014) to cultural heritage management and conservation (Cabrelles et al., 2009; Frodella et al., 2021; Grinzato, 2012). Most IRT applications in earth sciences are related to volcanic systems monitoring, from the study of magma effusion rates (Sansivero and Vilardo, 2019) to the analysis of thermal anomalies related to hydrothermal systems (Della Seta et al. 2021). In the last few years, novel applications of this remote surveying technique were also reported in the field of engineering geology. Innovative monitoring techniques were proposed to investigate temperature-related effects on jointed rock masses. Among all these methods, IRT has undoubtedly demonstrated the greatest potential in studying rock mass characteristics and related hazards, as well as in defining the effect of continuous fluctuations of surface temperatures on jointed rock masses (Fiorucci et al., 2018; Guerin et al., 2021, 2019; Pappalardo et al., 2016; Teza, 2014). For example, Mineo et al. (2015) employed IRT as a complementary technique to geostructural surveys with a view to identifying potential rockfall sources along an unstable rock slope. Several authors employed IRT in multitemporal monitoring surveys, highlighting the crucial role of discontinuity sets in constraining the spatial distribution and evolution of temperatures within rock masses. Guerin et al. (2019) explored the potential of IRT surveys to characterize the stability of two exfoliation sheets at the El Capitan rock cliff and found that not homogeneous temperature patterns (i.e., warm and cold thermal signatures) could be interpreted as the result of both air circulation enveloping detached rock sheets and the presence of rock bridges. Loche et al. (2021) proposed a methodology to evaluate the compressive strength of different rock blocks through integrated IRT surveys and Schimdt hammer tests. Through the comparative analysis of a cooling rate index, computed over the cooling phase of the rock mass, and the obtained rebound values, they observed a strong correlation between these two parameters, proving the potential of IRT for the indirect characterization of not accessible rock mass outcrops.

---

Focusing on the effect of rock mass discontinuity networks, Fiorucci et al. (2018) performed seasonal surveys targeting a prone-to-fall jointed rock block. Their results highlighted that when open joints fall within the thermal active layer of exposed rock masses, air-filled discontinuities can affect the heat propagation leading to the fragmentation of heat fronts and to the related configuration of sharp temperature contrasts across these elements. Such an effect, induced by the contrast of thermophysical parameters between the rock matrix and the air infilling within open joints, was also interpreted as responsible for significant differential heating-cooling cycles of fracture-isolated rock blocks. However, thermal anomalies in jointed rock masses are not only induced by the existence of air-filled discontinuity networks, but are also related to differently oriented surfaces (Guerin et al., 2021, 2019). Highly variable morphological and geostructural conditions of rock masses can determine the presence of exposed surfaces characterized by different orientations (dip angles and directions) that may induce the rise of not homogeneous distributions of surface temperatures. Then, it is evident that to understand better the thermomechanical behavior of jointed rock masses, especially when their attitude in the 3D space cannot be neglected, the characterization of the local geostructural setting (i.e., joint density and attitude) and the definition of both the amplitude and the space-time evolution of near-surface temperatures considering complex 3D geometries is required. In this framework, recent developments in commercial Structure from Motion (SfM) software paved the way for the possibility to create dense point clouds from unordered and uncalibrated thermal infrared (TIR) and RGB optical images (Maset et al., 2017). In particular, SfM is a digital photogrammetry (DP) technique that represents one of the most affordable methods for collecting high-quality 2D and 3D geometric information of investigated areas (e.g., slopes, outcrops, structures) starting from the acquisition of a series of overlapping images (Westoby et al., 2012). While RGB image-based terrestrial and aerial DP represents a well-established methodology for the engineering geological characterization of jointed rock masses (Francioni et al., 2019; Sturzenegger and Stead, 2009; Westoby et al., 2012), only few examples exist in literature dealing with the creation of 3D TIR models through the draping of low-resolution thermal textures on point clouds and 3D meshes (Frodella et al., 2020; Pappalardo et al., 2020). Although 3D TIR applications in engineering fields are continuously increasing, methodological approaches overcoming TIR images draping onto 3D models of complex rock surfaces are still limited for engineering geology purposes.

---

### **3.3.3 Data acquisition and processing**

In the framework of this Ph.D. thesis, two different IRT surveying approaches were employed at the two case studies. At the Wied Il-Mielah, IRT multitemporal surveys were conducted to achieve a preliminary characterization of the thermal attitude of the sea arch under different climatic conditions.

Differently, since the monitored rock block at the Acuto field laboratory was already interested by several IRT monitoring campaigns between 2017 and 2018 to investigate the influence of air-filled discontinuities on the spatial and temporal evolution of near-surface thermal fields, a methodology for the reconstruction of 3D thermal infrared (TIR) point clouds was tested. This method aims at providing a novel and useful tool to describe the evolution and distribution of surface temperature within a geometrically accurate 3D environment through the integration of multitemporal IRT surveys and close-range digital photogrammetry.

The possibility of analyzing the thermal behavior of jointed rock masses through high-quality 3D point clouds directly generated from TIR images may represent a state-of-art pioneering step toward creating new methodological approaches to analyze the thermomechanical behavior of jointed rock masses. Moreover, while thermogram analysis can be very complicated because it is usually performed manually by the operator and without having an overall and comprehensive view of the investigated target, 3D thermal models might solve potential ambiguity issues by merging surveyed thermal and geostructural features of complex rock masses.

The reconstruction of 3D models could significantly enhance the spectrum of analyses and interpretations concerning the relationship between the main features of jointed rock masses and their surface thermal fields.

The acquisition and processing strategies adopted in this work for the two case studies are described in the next sections.



### 3.3.3.1 Multitemporal IRT surveys at the Wied II-Mielah sea arch

The multitemporal thermal mapping of the Wied II-Mielah sea arch was performed during eight daily monitoring campaigns with seasonal recurrence (from September 2018 to February 2020) to characterize the thermal behavior of this natural structure under different climatic conditions. A summary of all performed surveys is presented in [Table 3.8](#).

Survey	Season	Start	End	Weather
Sep-2018	Summer	06:00	21:00	Sun
Oct-2018	Autumn	06:00	19:00	Sun
Dec-2018	Autumn	07:00	19:00	Cloud/Rain
Jan-2019	Winter	07:00	18:00	Sun
Apr-2019	Spring	06:00	19:00	Sun
May-2019	Spring	06:00	19:00	Sun/Cloud
Sep-2019	Summer	07:00	19:00	Sun
Feb-2020	Winter	07:00	17:00	Cloud/Rain

**Table 3.8.** Synthesis of IRT surveys at the Wied II-Mielah sea arch.

As far as it was possible, every monitoring survey was scheduled during periods with similar weather conditions, choosing days characterized by the absence of rain or cloud coverage in order to account for the contribution of solar radiation to the heat balance of the rock mass (Fiorucci et al., 2018) Although only five seasonal surveys were characterized by constant and unperturbed sunny conditions, they can be still considered representative of different climatic conditions. Image collection was carried out by employing a high-sensitivity IR camera, whose technical specification are reported in [Table 3.9](#). To ensure the camera stability a tripod was employed and placed on the right flank of the gorge at a distance of ~20 m from the arch, then allowing to achieve a maximum geometric resolution in the range 3–3.5 cm ([Figure 3.26a, b](#)). In order to guarantee the replicability of image acquisition and to maintain the same acquisition spot, multiple markers were placed both on the framed surface of the sea arch and on the ground where the tripod was located. Additionally, a portable weather station and several thermocouples cable-connected to a datalogger were

also employed to monitor environmental parameters (i.e., air temperature, relative humidity and wind speed-direction) and the surface temperature of the rock arch.

<b>Model</b>	TESTO 885-1
<b>FPA</b>	Uncooled microbolometer
<b>Spectral range</b>	7–14 $\mu\text{m}$
<b>IR resolution</b>	320 x 240 pixels
<b>Focal length</b>	15 mm
<b>Measuring range</b>	-30–100 $^{\circ}\text{C}$
<b>Accuracy</b>	$\pm 2\%$ of measured values
<b>NETD</b>	30 mK at 30 $^{\circ}\text{C}$
<b>FOV</b>	30 $^{\circ}$ x 24 $^{\circ}$

**Table 3.9.** Main technical specification of the employed IR camera; FPA – Focal Plane Array, NETD – Noise Equivalent Temperature Difference, FOV – Field of View.

Since the sea arch has a 0–10  $^{\circ}\text{N}$  orientation of its major axis, the monitored vertical cliff is characterized by an almost perfect eastward exposure: this surface is then normally exposed to the incident solar radiation of the first hours of the day over the whole climatic year even if considering the seasonal variability of solar paths.

Monitoring activities were performed by designing a standard acquisition protocol consisting in the collection of multiple, partially-overlapped thermograms with 1-hour sampling interval and within a time window spanning from sunrise to sunset in order to completely frame the sea arch during its heating and cooling stages. Start and end times of all the IRT surveys are reported in [Table 3.8](#).

Due to the camera horizontal FOV ( $\sim 30^{\circ}$ ) and the relatively close distance from the target ( $\sim 20$  m), six different thermograms were acquired by turning the camera on the tripod axis of a  $20^{\circ}$  angle, and thus covering a total angle of view ( $\theta$ ) of  $105^{\circ}$  ([Figure 3.26c](#)). The emissivity of the rock mass was estimated in the range 0.93–0.95, average value 0.94, following the standard method ISO-18434-1 and by employing a reference material with known emissivity (i.e., aluminum foil).

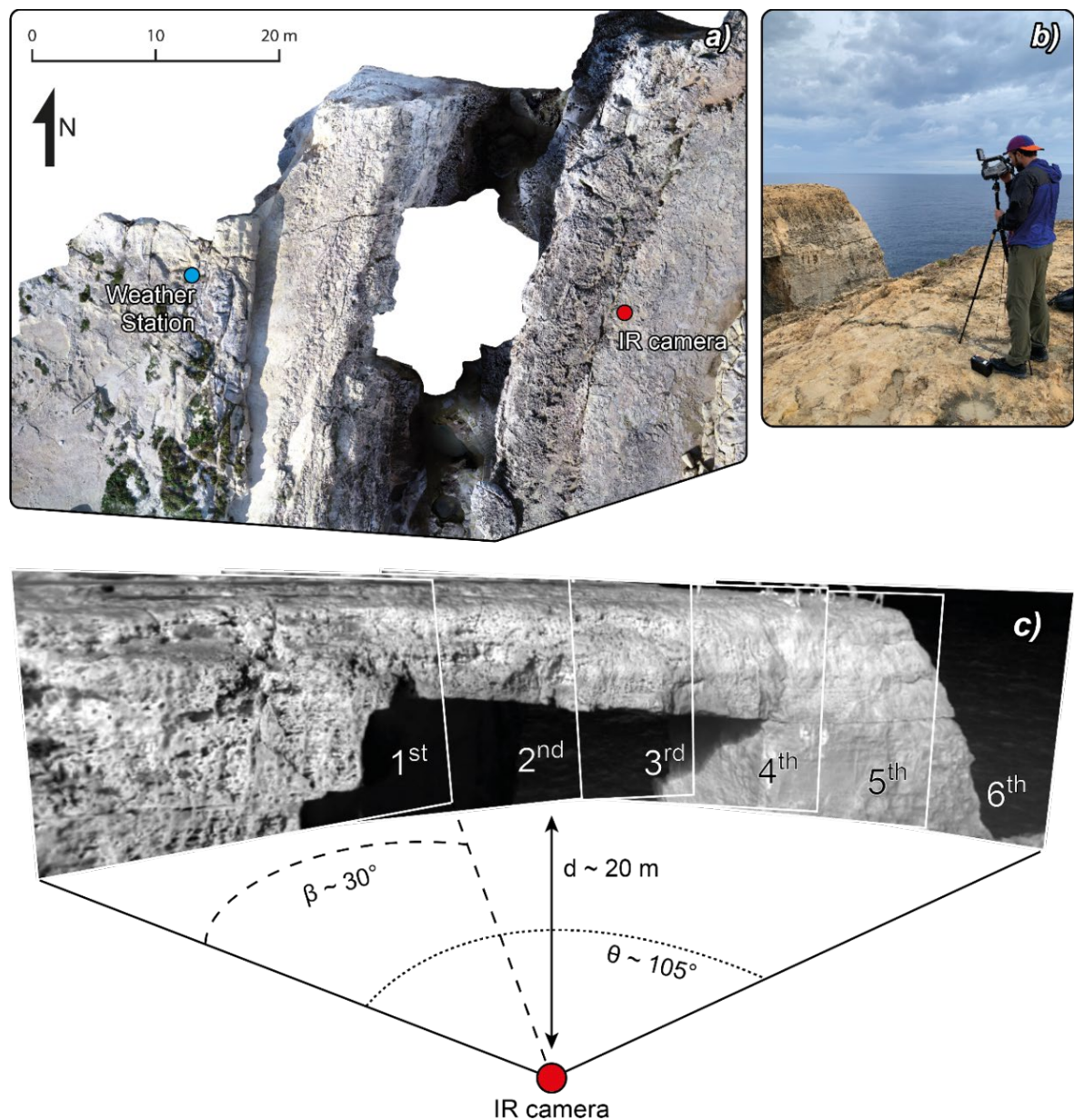


**Figure 3.26.** Aerial view of the Wied II-Mielah sea arch in which the location of the weather station and the acquisition point of IR images (i.e., where the tripod was located) are shown (a, b). Simplified sketch of the georeferencing process of IR images for reconstructing a panoramic view of surface temperature of the arch (c):  $d$  – acquisition distance,  $\beta$  – horizontal angle of view of the IR camera,  $\theta$  – total angle of view of the panoramic image obtained by mosaicking overlapped thermograms.

This value is in accordance with the results obtained by Fiorucci et al. (2018) and Mineo et al. (2015) for limestone samples. Furthermore, apparent reflected temperature, as well as air temperature, relative humidity and the acquisition distance were inputted in the built-in software of the IR camera during each acquisition to apply standard corrections of measured temperature values. The collected imagery was processed in order to obtain perfectly-overlapped panoramic TIR images of the arch for each acquisition of every monitoring

survey. To this aim, thermal images were firstly converted from a radiometric file format to floating 32bit Tiff matrixes through a MATLAB compiled script (The MathWorks Inc., 2021). Temperature matrixes were then imported within a GIS environment to perform a manual georeferencing of the whole dataset in a relative coordinate system. In particular, this task was crucial for quantitatively analyze the distribution and evolution of surface temperatures, and consisted of two main steps. At first, all images belonging to the same 1-hour acquisition were manually georeferenced and overlapped by finding common features and thermal signatures within adjacent thermograms. An affine transformation was applied to avoid, or at least reduce, significant distortions during this rearrangement process. The so defined dataset was then mosaicked together for reconstructing single raster files containing temperature information of the six stacked thermograms (Figure 3.26c). Once TIR mosaicking was achieved for every acquisition of each survey, an overlap optimization was further performed through a second manual georeferencing. The adopted approach allowed reconstructing surface temperature distributions of the framed area of the sea arch over all hours and seasons of remote surveying (Figure 3.27b).

The quantitative analysis of the TIR dataset was carried out following the methodological approach proposed by Fiorucci et al. (2018). A 1D analysis was performed through the extraction of temperature time series from multiple control points located in distinct areas of the sea arch (Figure 3.27c). In particular, three conditions were considered of particular interest for this analysis: (i) the rock mass surface, (ii) a fracture zone and (iii) a hollow area genetically related to a rockfall (Figure 3.27a). Surface temperatures of the identified areas were extracted by rosettes of points and averaged over nine neighbors in order to ensure statistical significance of measured values and to guarantee the filtering of local temperature heterogeneities due to due minor surface asperities (Figure 3.27b).

A 2D analysis, devoted to the comprehension of spatial and temporal patterns of near-surface temperature, was conducted by computing distributed daily mean temperatures and thermal ranges for every seasonal survey. This task was performed exploiting specific GIS-based functions which allowed calculating the minimum, maximum and mean values for every cell of TIR raster mosaics.

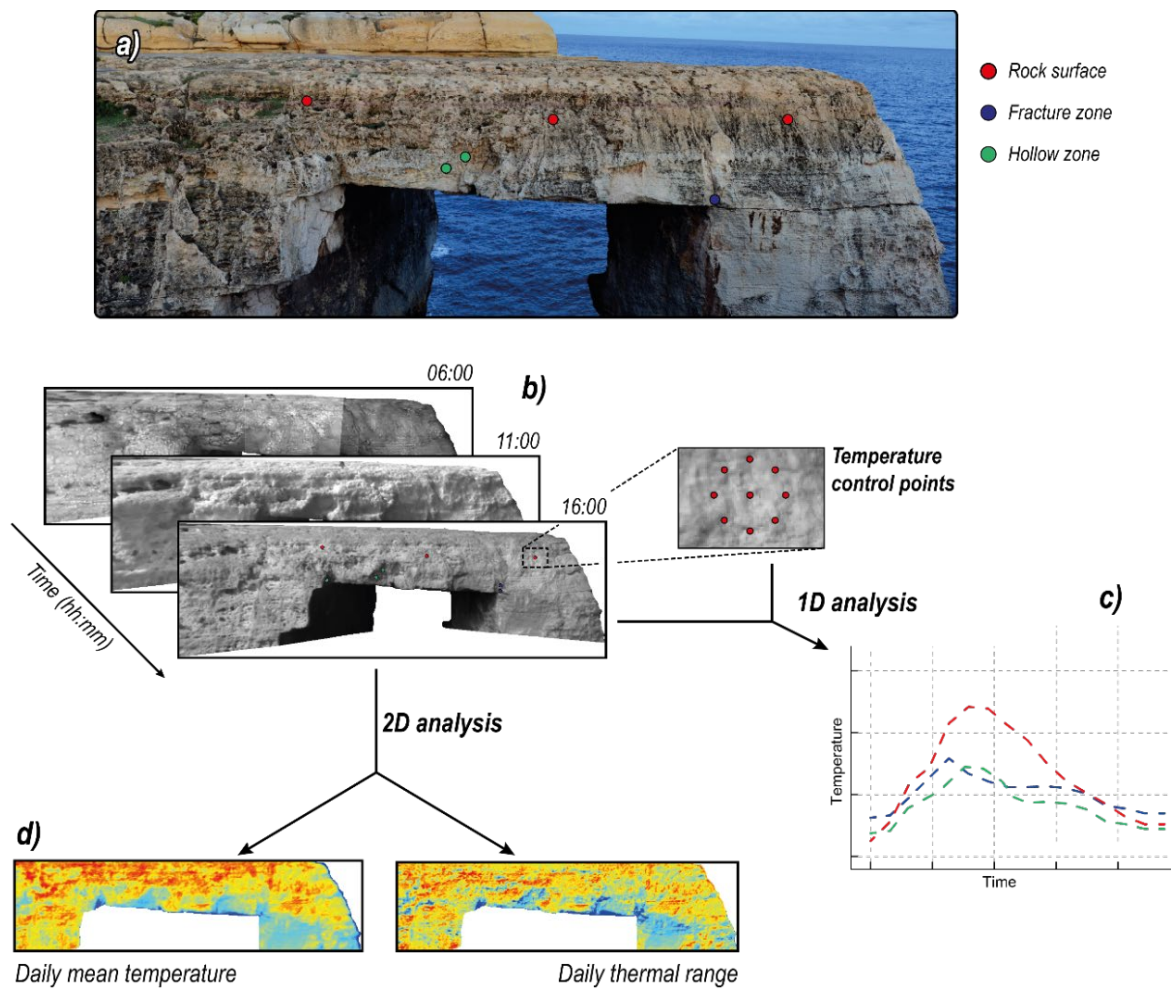


**Figure 3.27.** Front view of the arch where the location of control points for the extraction of temperatures is indicated by colored circles (a). Example of TIR imagery processing and analysis (b): 1D and 2D analyses were performed by extracting temperature time series from the abovementioned control points (c) and through the computation of distributed daily mean temperatures and thermal ranges (d).

### 3.3.3.2 Reconstruction of thermal point clouds at the Acuto field laboratory

IRT surveys were performed in autumn, winter, spring and summer, acquiring thermal images at four different hours of the day (11:30, 13:00, 16:00 and 17:00) to monitor the heating and cooling stages of the jointed rock block. Thermal mapping activities were carried out during days characterized by comparable insolation and cloud coverage to reduce variability in thermal boundary conditions. This approach aimed at highlighting the thermal behavior of the rock block in different climatic conditions at the daily and seasonal time scale. The TIR image acquisition was performed using the same IR camera described in [Table 3.9](#). A DSLR digital camera (Canon PowerShot SX730 HS) was used during every survey to acquire optical imagery to reconstruct one high-resolution 3D point cloud representing the reference base for TIR point clouds. A monopod was employed to ensure the stability of cameras and resolve common issues in image acquisition, such as frame blurriness due to inevitable tremors of the operator.

The DSLR camera calibration was achieved using the lens calibration tool of Agisoft Metashape Pro (Agisoft LLC, 2020). This tool allows calibrating internal camera parameters (i.e., focal length, principal point coordinates, radial and tangential distortion coefficients) for the correct reconstruction of 3D point clouds by acquiring several images of an on-screen visualized chessboard from different observation angles. Thermal mapping of the rock block was performed following a standardized acquisition. Several control points were permanently marked on the ground before the first monitoring campaign to address the need for a complete 3D reconstruction of the rock block and to guarantee the replicability of surveys. After a preliminary calibration step of their positions, these control points were organized into a specific pattern of rays coming from the rock block ([Figure 3.28a, b](#)) in order to frame the target from different observation angles and distances (always within 2 and 15 m), securing a good image overlap. The adopted acquisition distances allowed the obtainment of a maximum geometric resolution of IR images in the range 3.4–25.5 mm for the closest and furthest acquisition spots, respectively. Optical and IR images were collected through close-range terrestrial acquisitions. Due to the unavailability of neither georeferenced data nor external calibration parameters, numerous Ground Control Points (GCPs) were placed on the targeted sector of the quarry rock wall. Model georeferencing from a relative to an absolute geographic coordinate system is deemed to be mandatory to remove scale and orientation ambiguities between point clouds that were separately reconstructed.

---

In most applications, natural or artificial GCPs are employed for optical image georeferencing (e.g., geometrical markers with known dimension and position). Differently, for IRT applications it is not always possible to find sharp and stable GCPs based only on their shape or color contrasts with environment.

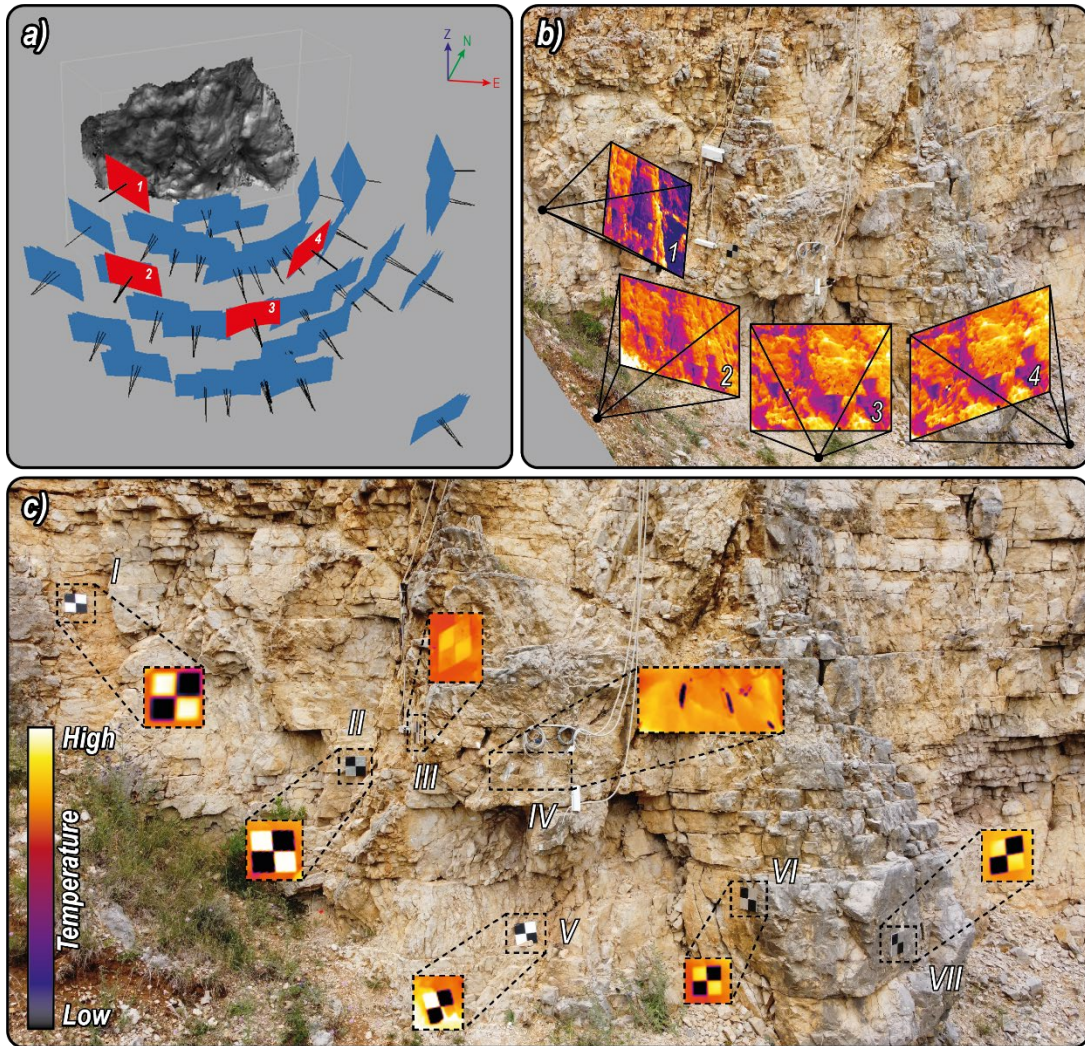


**Figure 3.28.** Acquisition method used for the reconstruction of 3D point clouds of the rock block from IRT surveys (a, b). Front view of the rock block from which the cold signatures of the employed highly reflective aluminum GCPs are evident (c) (modified from Grechi et al., 2021).

To solve this potential issue, seven low-emissivity aluminum squared reflectors (20x20 cm) were employed. Aluminum foil is characterized by mean emissivity values between 0.03–0.06 (i.e., it reflects 94–97% of the incoming thermal radiation) and thus determines high-visibility cold thermal signatures on thermograms (Figure 3.28c). The coordinates of all GCPs were extracted from a georeferenced point cloud that was acquired through a total station survey performed using a Leica MS60 MultiStation. The IR camera calibration was

performed before every survey and during the post-processing steps through the collection of air temperature and relative humidity data, the reflected temperature from the rock surface (ISO 18434-1) and the distance and relative position of every acquisition spot from the target rock block.

The adopted workflow for the reconstruction of merged TIR and optical point clouds is summarized in [Figure 3.29](#). The first step consisted in reconstructing the high-resolution optical point cloud from the RGB optical imagery acquired with the DSLR camera. All images were processed using Agisoft Metashape Pro, and the resulting point cloud was georeferenced using 9 GCPs placed on the rock wall. After the optical dense point cloud was generated (9 million points dense point cloud), it was imported in CloudCompare (Girardeau-Montaut, 2021) to optimize the alignment with the reference derived by the laser scanner and from which GCPs coordinates were extracted. The alignment optimization was achieved using the Iterative Closest Point (ICP) method (Rusinkiewicz and Levoy, 2001). The ICP algorithm computes the correspondences between point clouds starting from an initial estimate for the relative rigid-body transform and iteratively refines it until the convergence is reached (Maset et al., 2017). The ICP algorithm returned RMSE registration values in the range 0.005–0.01 m.

To process the TIR imagery, thermograms were exported as temperature matrixes through the proprietary software of the IR camera (TESTO-IRsoft). These matrixes were converted into a floating 32bit Tiff file format through a MATLAB compiled script in order to import them into the Agisoft Metashape working environment. Because the employed IR camera does not provide EXIF data of collected thermograms, the image processing was performed relying on the automatic calibration of initial camera parameters. The first step of the SfM processing consisted of the Block Bundle Adjustment: the TIR dataset was processed by the SfM software to estimate image key-points, camera locations, orientations, and internal calibration parameters to build sparse point clouds (Westoby et al., 2012). Sparse point clouds were then manually georeferenced by identifying the low-emissivity GCPs placed on both the rock block and the adjacent quarry wall within the dataset ([Figure 3.28c](#)). The last step consisted of the detailed reconstruction of the investigated area by generating the dense point cloud for each IRT acquisition. The main result of this processing step is a considerable increase in point density, as described in [Table 3.10](#) for one of the performed surveys.

---



Acquisition Time	No. of photos	Sparse points	Dense points
11:30	142	1.47E+4	2.87E+5
13:00	145	1.51E+4	3.17E+5
16:00	173	1.85E+4	3.83E+5
17:00	181	2.33E+4	3.89E+5

**Table 3.10.** Example of the relation between the number of acquired photos during one seasonal survey and number of points characterizing TIR sparse and dense point clouds (modified from Grechi et al., 2021).

To solve possible errors of nonperfect alignment between TIR point clouds and the high-resolution optical one, considering that because of the high density of GPCs employed for the target-based co-registration they are very close to each other in space, the alignment of TIR point clouds to the reference RGB point cloud was optimized using the ICP algorithm. Moreover, to evaluate if TIR dense point clouds were correctly generated and co-registered to the reference one and to estimate their spatial and geometric accuracy, the analysis of residual distances was performed using the Multiscale Model to Model Cloud Comparison (M3C2) algorithm implemented in CloudCompare (Lague et al., 2013). In particular, this tool was selected over the common Cloud-to-Cloud (C2C) distance method because of its robustness in computing local residual distances and considering changes in point density and noise. Statistical parameters of residual distances between TIR and optical point clouds were computed for every survey and acquisition. After the alignment optimization and subsequent verification steps, TIR point clouds were further processed to convert thermal attributes stored by every point from relative RGB intensity to real temperature values. In fact, even though Agisoft Metashape does not directly deal with most TIR imagery file formats, it is possible to visualize thermograms (imported as one-band floating 32bit Tiff files) by setting a color-scale according to the range of temperature values stored in the pixel matrix and applying a raster transformation to every image.

Using this approach, the generated point cloud is characterized by a color-coded scalar field, and its intensity (expressed in RGB values) is directly proportional to absolute temperature values. A MATLAB script was designed to retrieve real temperature values from RGB intensities following [equation 3.11](#):

$$T_i = \frac{(i - i_{min})(T_{max} - T_{min})}{(i_{max} - i_{min})} + t_{min} \quad (\text{eq. 3.11})$$

where for the  $i$ -th point,  $T_i$  is the real temperature value,  $i_{min}$  and  $i_{max}$  are the minimum and maximum RGB intensity values,  $T_{min}$  and  $T_{max}$  are the minimum and maximum temperature values that were equally set for the whole TIR dataset before the SfM processing. The last step of this workflow consisted of transferring the real temperature information of TIR point clouds to the reference high-resolution RGB optical point cloud. This task was accomplished using a CloudCompare built-in algorithm to perform a euclidean distance-based Nearest Neighbor Search (NNS) within TIR point clouds for every point of the reference point cloud (Guilbert et al., 2020). This operation allowed the merging of temperature scalar fields of TIR point clouds to the high-density optical point cloud. To quantify the accuracy of the final output in the description of surface temperatures, a comparison between temperature distributions of original and interpolated point clouds was performed, aiming at estimating their grade of correspondence. Following this workflow, which is summarized in [Figure 3.29](#), it was possible to obtain a high-resolution dense point cloud that stores temperature attributes for every seasonal survey acquisition. A comparison between 2D thermograms and 3D point clouds was performed to analyze the representativeness and reliability of TIR point clouds for the characterization of surface temperatures of the investigated rock block. In particular, two sections of interest were selected on the rock block for the extraction of temperature distribution and evolution. By availing of multitemporal (infraseasonal and infradaily) TIR point clouds, it was then possible to compute differential surface temperatures and temperature ranges at different time scales and analyze their spatial distribution with respect to the differently exposed surfaces of the rock block.

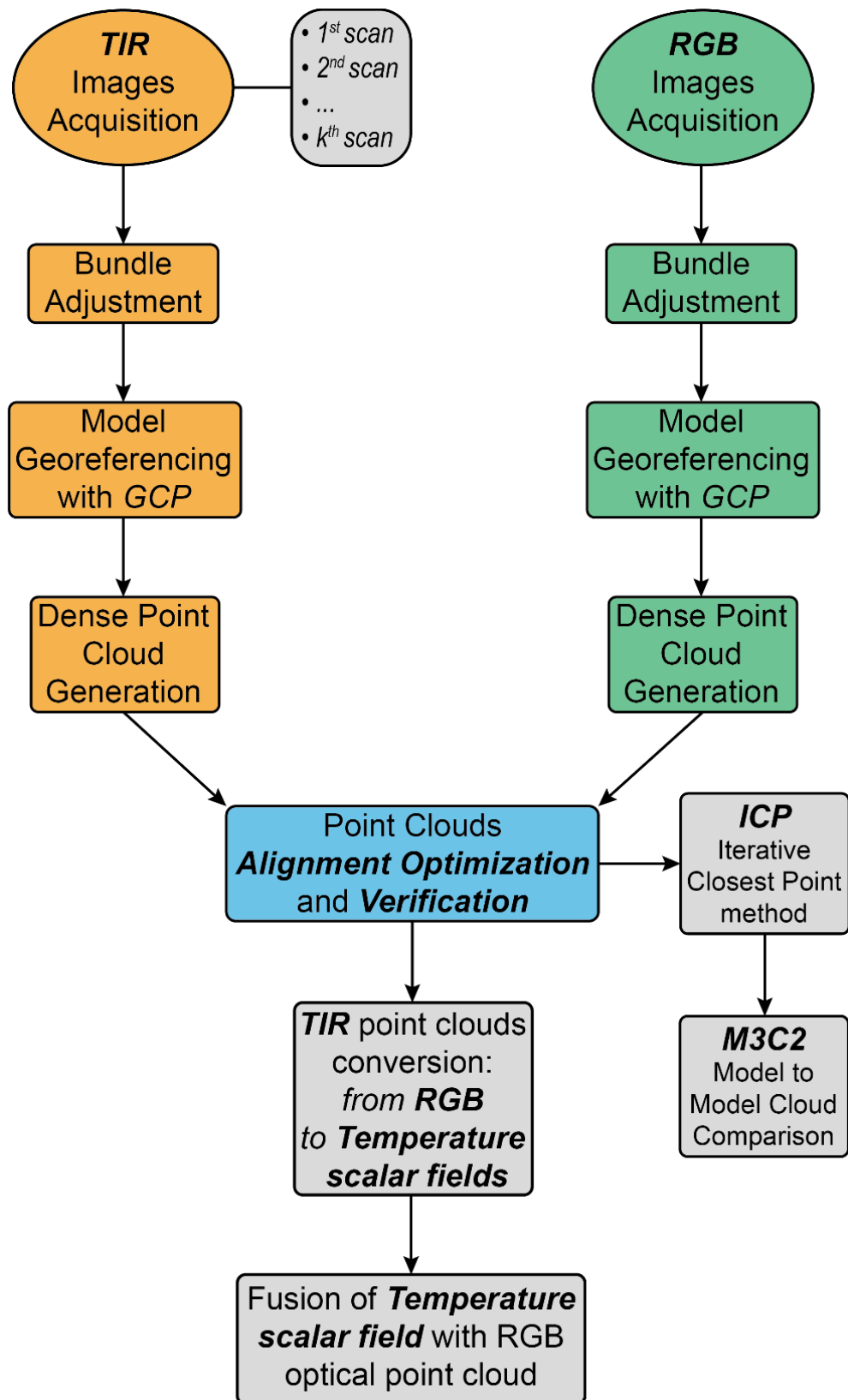


Figure 3.29. Adopted workflow for the generation of TIR point clouds (from Grechi et al., 2021).

# Chapter 4

## Results

### 4.1 Results of microseismic monitoring

The entire dataset of ambient seismic noise recordings acquired at both case studies was processed according to the adopted workflow for microseismic event detection and analysis described in [Section 3.2.3](#). This analysis was performed to retrieve information on the local microseismic activity at the two selected jointed rock masses and to search for correlations with environmental factors (i.e., temperature fluctuations, rainfall intensity).

As previously introduced, the analysis of microseismic events from ambient noise recordings was unsuccessful on the dataset collected at the Wied Il-Mielah case study for different reasons. At first, the calibration of input parameters for the STA/LTA triggering algorithm represented a challenging task for the whole process. In fact, in virtue of the short duration of monitoring campaigns, it was not possible to predispose a training dataset representative of the background noise conditions of the site for the calibration of the STA/LTA parameters. Since the successful capturing of microseismic events depends on proper trigger parameters settings, a sensitivity analysis aimed at finding the best compromise between the number of events and their reliability was performed on every single campaign dataset.

The input parameter that was found to be the most significant in constraining the number of detections was the  $N_{Th}$  (i.e., number of channels simultaneously triggered by the same event). Therefore, after selecting the length of moving windows (i.e.,  $STA = 0.3$  s and  $LTA = 20$  s) and the triggering threshold ( $STA/LTA = 5$ ), that parameter was varied from 1 to 4 in order to observe to which extent it could have influenced the detection of potential microseismic events. An example of the results obtained following these steps is presented in [Figure 4.1](#) for the last monitoring campaign of February 2020, where the number of event detections is plotted for different values of  $N_{Th}$ . It is clear that how values of  $N_{Th}$  (i.e.,  $N_{Th} = 1-2$ ) lead to an unreliable number of events during the four-day monitoring period with up to thousands of detections ([Figure 4.1b](#)) and occurrence rates ranging from 30 to 160 events per hour ([Figure 4.1a](#)).

---

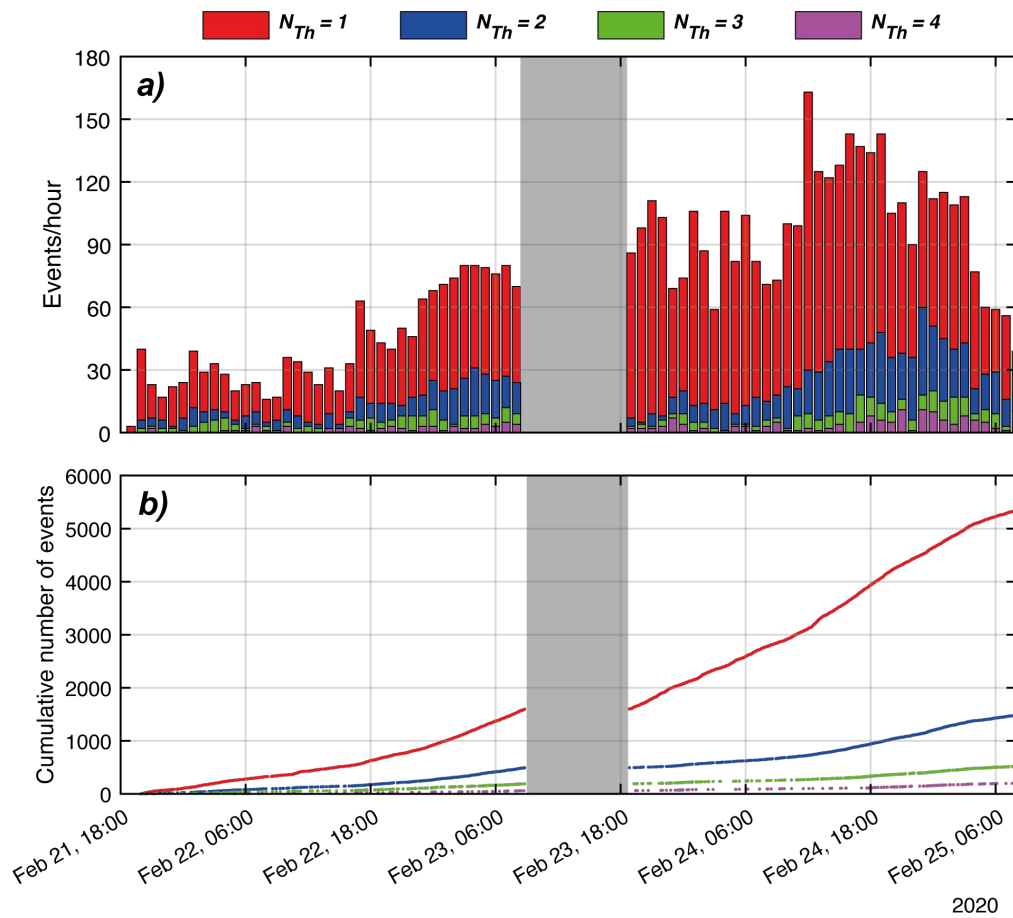


**Figure 4.1.** Results of the sensitivity analysis performed on the  $N_{Th}$  (i.e., number of channels simultaneously triggered by the same event) considering the microseismic dataset collected during the monitoring campaign of February 2020: number of detected events per hour (a) and cumulative number of events (b).

On the contrary, higher threshold values (i.e.,  $N_{Th} = 3-4$ ) resulted in more conservative results, with lower detections and occurrence rates. For this reason and to obtain sufficient data, the entire microseismic dataset collected during the four monitoring campaigns was analyzed by setting the threshold value to 3.

The so derived events were then processed and manually classified through the visual screening of waveforms, power spectra, and spectrograms to discriminate microseismic events from false detections. The manual classification enabled the recognition of recurrent spike-like signals within seismic traces that were interpreted as electrical transients randomly affecting all channels of the monitoring system.

However, even though the most evident false detections were recognized and excluded from the dataset, the remaining events were still characterized by ambiguous features both in the

time and frequency domain since they appeared as short duration, low amplitude, and monofrequential signals embedded in noise recordings (Figure 4.2). In particular, their peak frequency (i.e., the highest peak in the power spectrum) was constantly centered around 10 Hz, which, as will be discussed in Section 4.2, was recognized as the frequency of a resonance mode of the arch.

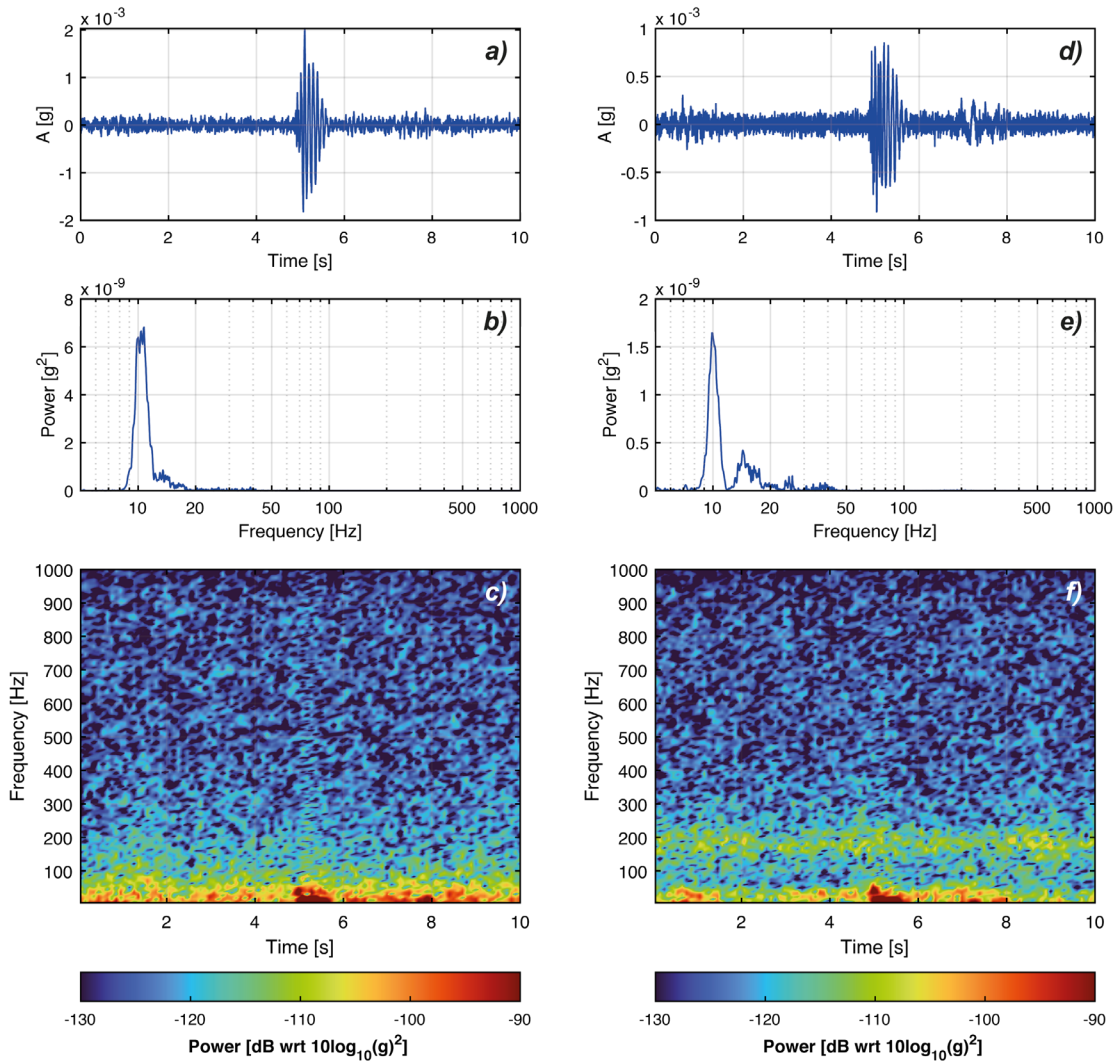


**Figure 4.2.** Example of two unclassified events recorded by the microseismic monitoring system at the Wied Il-Mielah sea arch during the campaign of February 2020: waveforms (a, d), power spectra (b, e) and spectrograms (c, f).

In order to evaluate whether these features showed possible variations during the whole monitoring period, the maximum frequency ( $f_{\max}$ ), normalized amplitude ( $A_{\max}/A_{\text{mean}}$ ), and uniform duration of all events preliminarily classified as non-false detections were extracted and analyzed.

The results of this analysis are presented in [Figure 4.3](#). All three plots show a significant time-invariance of event characteristics with no variations in the frequency domain ([Figure 4.3a](#)) nor in the time domain ([Figure 4.3b, c](#)). These results evidenced not negligible uncertainties in the reliability of classified signals as microseismic events potentially deriving from fracturing processes.

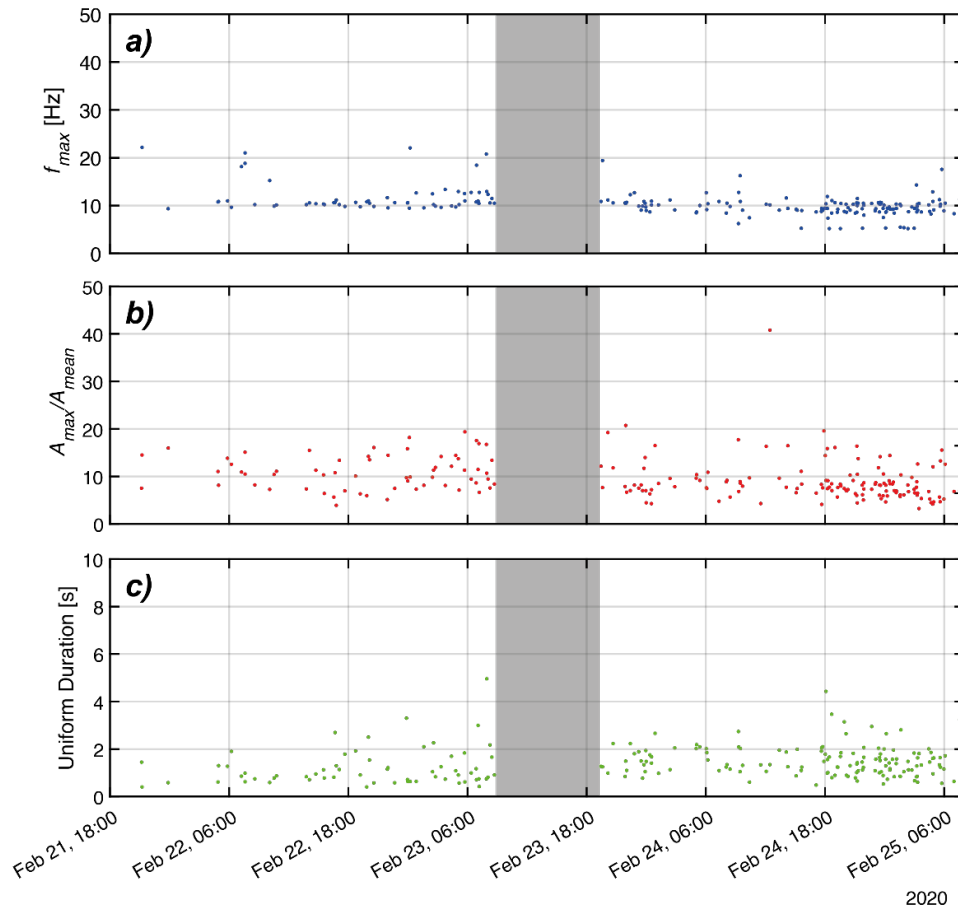


**Figure 4.3.** Temporal evolution of maximum frequency –  $f_{\max}$  – (a), normalized amplitude –  $A_{\max}/A_{\text{mean}}$  – (b), and uniform duration (c) of the events composing the manually classified dataset for the monitoring campaign of February 2020.

For this reason, and considering that their origin was not completely understood, they were all rejected and not considered to investigate potential correlations with environmental factors. The absence of microseismic events in the ambient seismic noise recordings may derive from different causes. In particular, the short duration of monitoring activities could have played a significant role since it did not permit the definition of a long-term training dataset for the extraction of characteristic microseismic signals, which is a mandatory step for the calibration of input parameters of STA/LTA triggering algorithm.

Regarding the microseismic monitoring campaigns at the Acuto case study, the availability of a vast dataset consisting of almost 5000 hours of continuous ambient noise recordings allowed to calibrate STA/LTA triggering algorithm parameters more efficiently. Moreover, since several analyses had already been conducted on part of the here discussed monitoring data (D'Angiò, 2019; D'Angiò et al., 2021b, 2021a), it was possible to optimize the event detection algorithm from the results obtained by D'Angiò (2019) during his Ph.D. thesis. In that framework, a total amount of 115.000 events were detected over a period spanning from February 2018 to April 2019, then only considering half of the second monitoring campaign, employing the same STA/LTA algorithm but with different settings (STA = 0.01 s, LTA = 30 s, STA/LTA = 4 and  $N_{Th} = 2$ ). The obtained results by D'Angiò (2019) were considered valid in terms of number of detections, but no manual or automatic event classification was performed on the extracted signals because it was considered not relevant for the final objective of that Ph.D. thesis.

However, when dealing with the analysis of potential correlations between microseismic activity and external conditioning factors (i.e., rainfalls and temperature variations), the consideration of false events could vitiate the outcomes, especially when they may represent the great majority of the investigated dataset. For this reason, in order to reduce the number of detections within the considered monitoring periods and at the same time avoiding significant losses of information, the STA/LTA algorithm settings were calibrated on a training dataset of several months, and the best compromise between the number of events and the coherence of collected signals was achieved for the parameters previously presented in [Table 3.7](#) ([Section 3.2.2.1](#)). The most significant difference between the here proposed parameters and those adopted in previous studies is represented by the size of the STA window and the selected value of  $N_{Th}$ . In this study, they were increased to reduce the algorithm's sensitivity to very short and low-coherency signals.

The results obtained using the abovementioned STA/LTA algorithm are presented in [Figure 4.4](#), where the raw number of triggered events is plotted. During the first monitoring campaign (February 2018 - May 2018) a total amount of 507 events were detected, while only 357 were extracted from the second campaign (November 2018 - October 2019). Moreover, from the mere observation of the detected events during the considered monitoring period, it is possible to discern different rates and trends ([Figure 4.4a, b](#)) in the occurrence of events between the two campaigns conducted.

---



This evidence may be a consequence of the different array configurations employed during the two monitoring windows. If considering the different spacings between the deployed accelerometers in the two adopted configurations and the potential attenuation of seismic waves due to the presence of discontinuities, a dense array such as the one arranged from February 2018 to May 2018 may have the ability to detect a higher number of events common to different channels (Figure 4.4c, d).

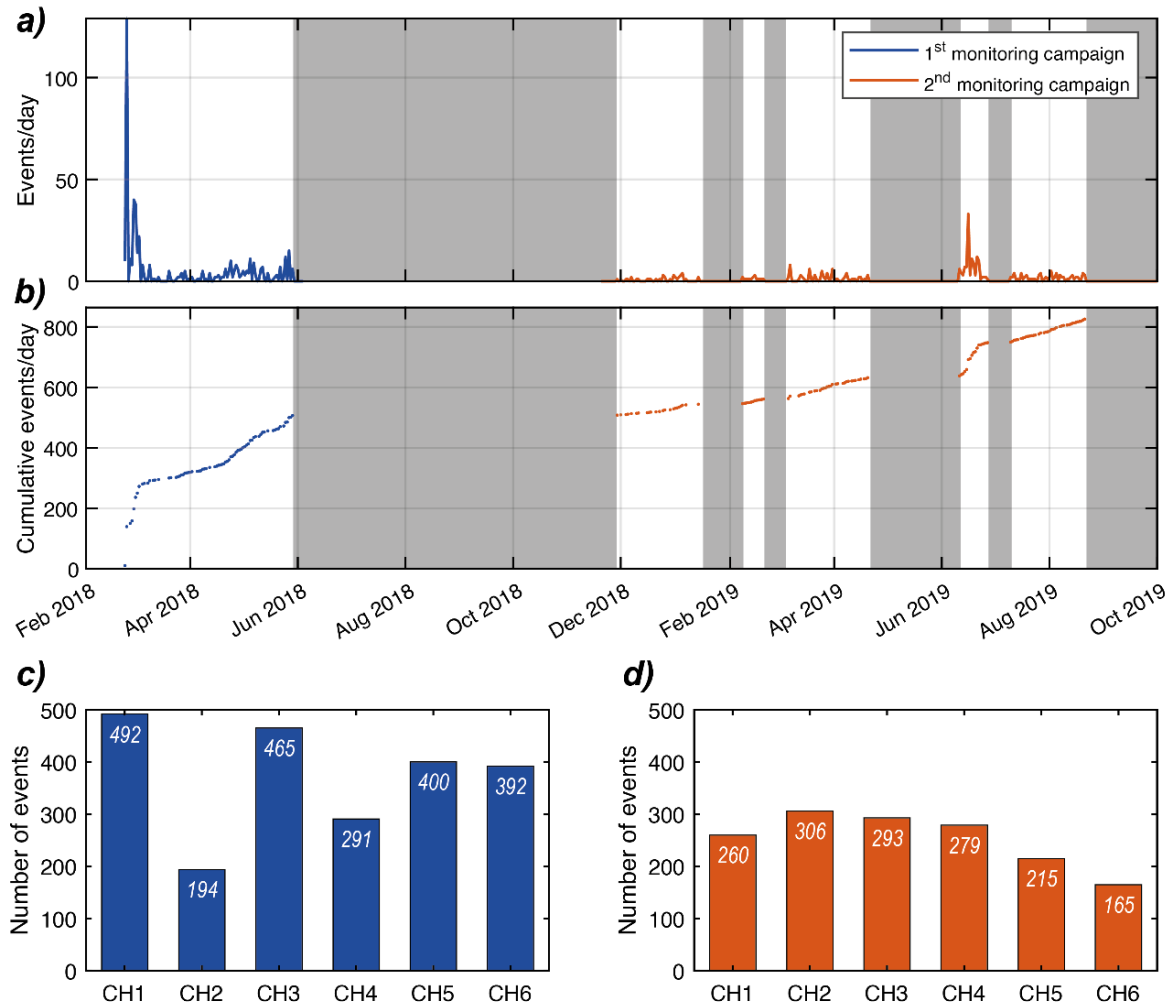


**Figure 4.4.** Microseismic dataset collected at the Acuto field laboratory during the two monitoring campaigns conducted between February 2018 and October 2019. Number of events per day (a), cumulative number of events (b), number of events detected per accelerometers during the first (c) and second monitoring campaign (d).

In Figure 4.5a the distributions of the 864 triggered events are described in terms of the hour of the day in which they occurred. Interestingly, while the events belonging to the first monitoring campaign tend to distribute almost homogeneously during the day, with no evident or isolated peaks, the second monitoring campaign is characterized by a suspicious

maximum between 11:00 and 12:00. However, this outcome may be in part biased by the almost complete absence of events during night hours for the second monitoring period. In fact, as previously introduced, the monitoring system suffered from recurrent interruptions of power supply from after sunset to some hours after sunrise (Figure 4.5b).

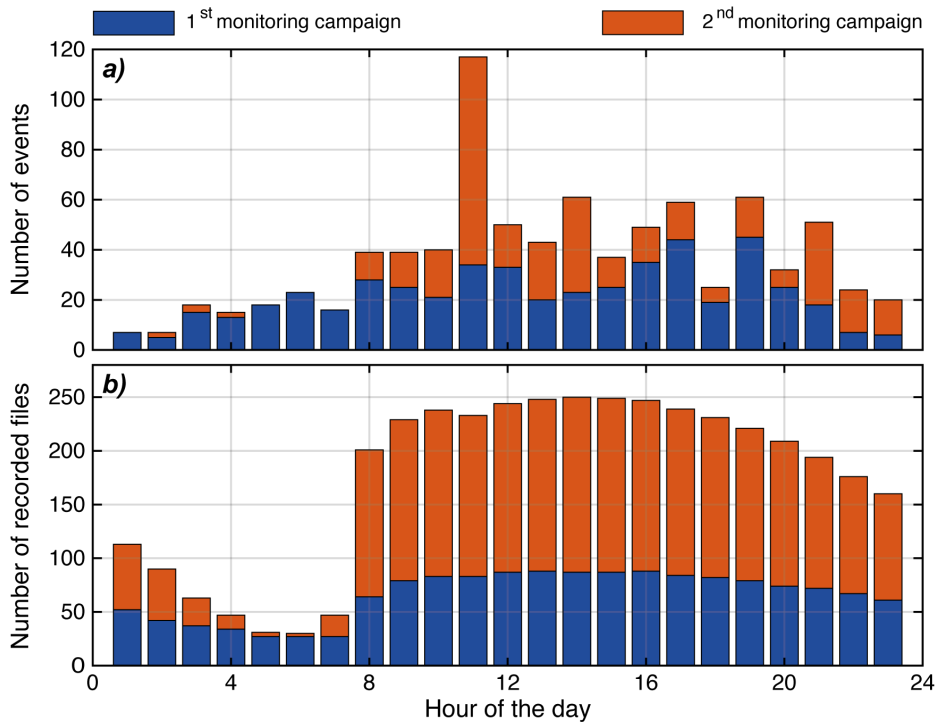


**Figure 4.5.** Distributions of the detected events (a) and of the 1-hour recorded files (b) during both monitoring campaigns as a function of the hour of the day.

After the automatic extraction of signals from the continuous noise recordings, the derived dataset was classified by visual screening to exclude false detections from the analysis of the local microseismic activity. The manual classification was performed by jointly observing waveforms, power spectra, and spectrograms of every array channel (Figure 3.21, Figure 3.22). This technique is considered one of the fastest and most accurate methods to concurrently analyze the time and frequency characteristics of signals (Colombero, 2017). This analysis led to the identification of multiple recurrent types of events. However, for the aim of this work, the event classification was performed between only two classes: the first one clustering all evident disturbances that could not be considered as natural events, and a second one comprising all signals potentially related to the stability conditions of the monitored rock mass and rock block. Differently from several authors (Arosio et al., 2018; Colombero, 2017; Provost et al., 2018), within the latter class no further classification was made because it was considered not essential for the objective of this analysis.

The results of manual classification highlighted that the microseismic monitoring network was affected by frequent electrical disturbances. These electrical transients simultaneously appear on all channels as single or multiple impulsive spike-like signals (Figure 4.6a, d) and are either characterized by a very broadband frequency content (Figure 4.6b, e) or by narrow frequency peaks systematically located above 200 Hz (Figure 4.6c, f).

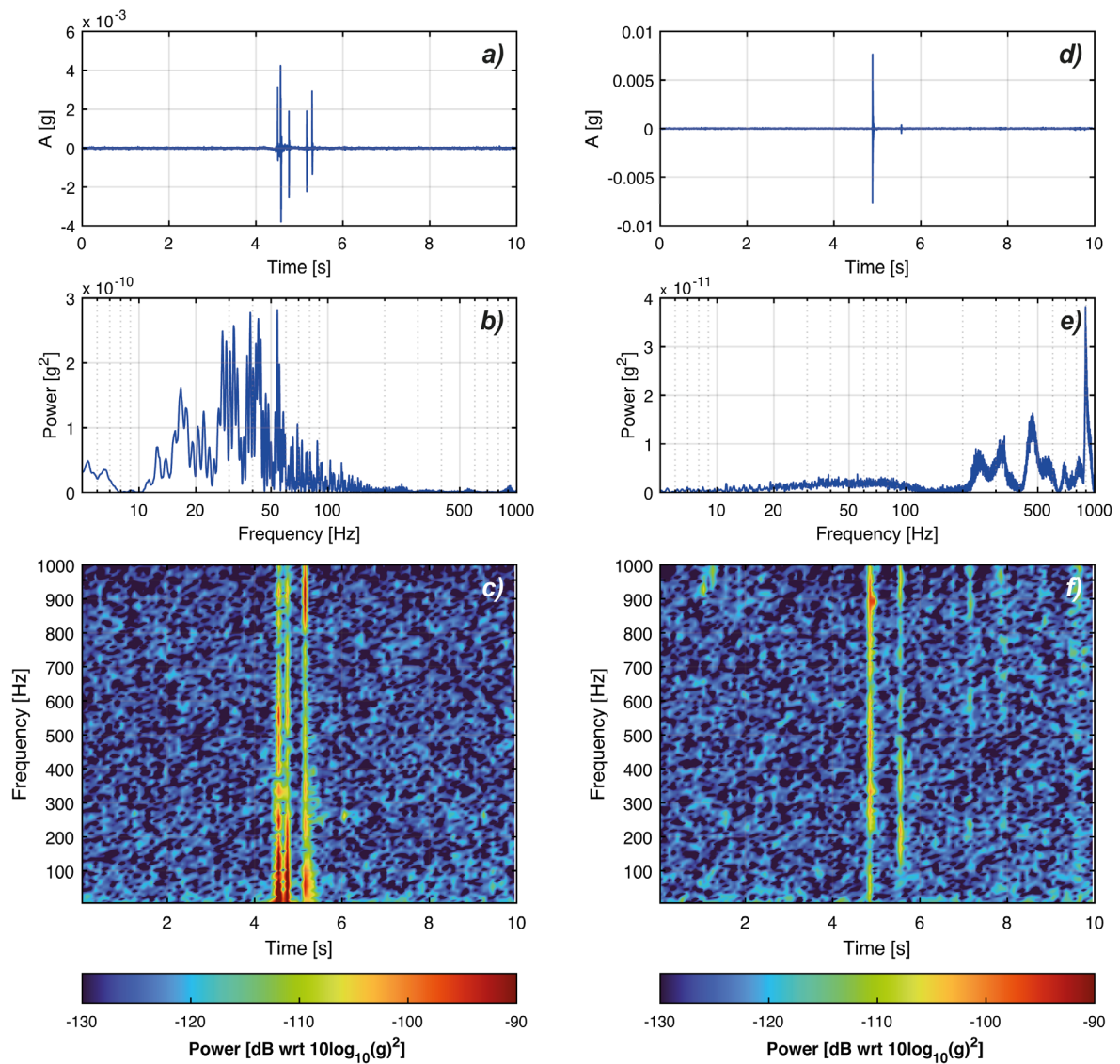


**Figure 4.6.** Examples of electrical disturbances recorded at the Acuto field laboratory and manually classified as false events: waveforms (a, d), power spectra (b, e) and spectrograms (c, f).

The origin of these events is controversial, but they are widely considered to be caused by atmospheric electromagnetic transients or other electrical disturbances affecting the entire acquisition system (Arosio et al., 2018; Colombero, 2017; Spillmann et al., 2007). Within the analyzed dataset a total amount of 591 electrical transients were identified (68% of the

dataset) and classified as false events. The remaining 273 events, manually classified as possible microseismic events, show common recurrent frequency and time domain characteristics. Generally, these signals are characterized by short durations (from less than a second up to a few seconds), impulsive onsets, and a well-defined triangular shape of their envelope (Figure 4.7). Their spectral range is mostly concentrated between 30 and 150 Hz, and they were found to occur singularly and in short duration sequences (Figure 4.8).

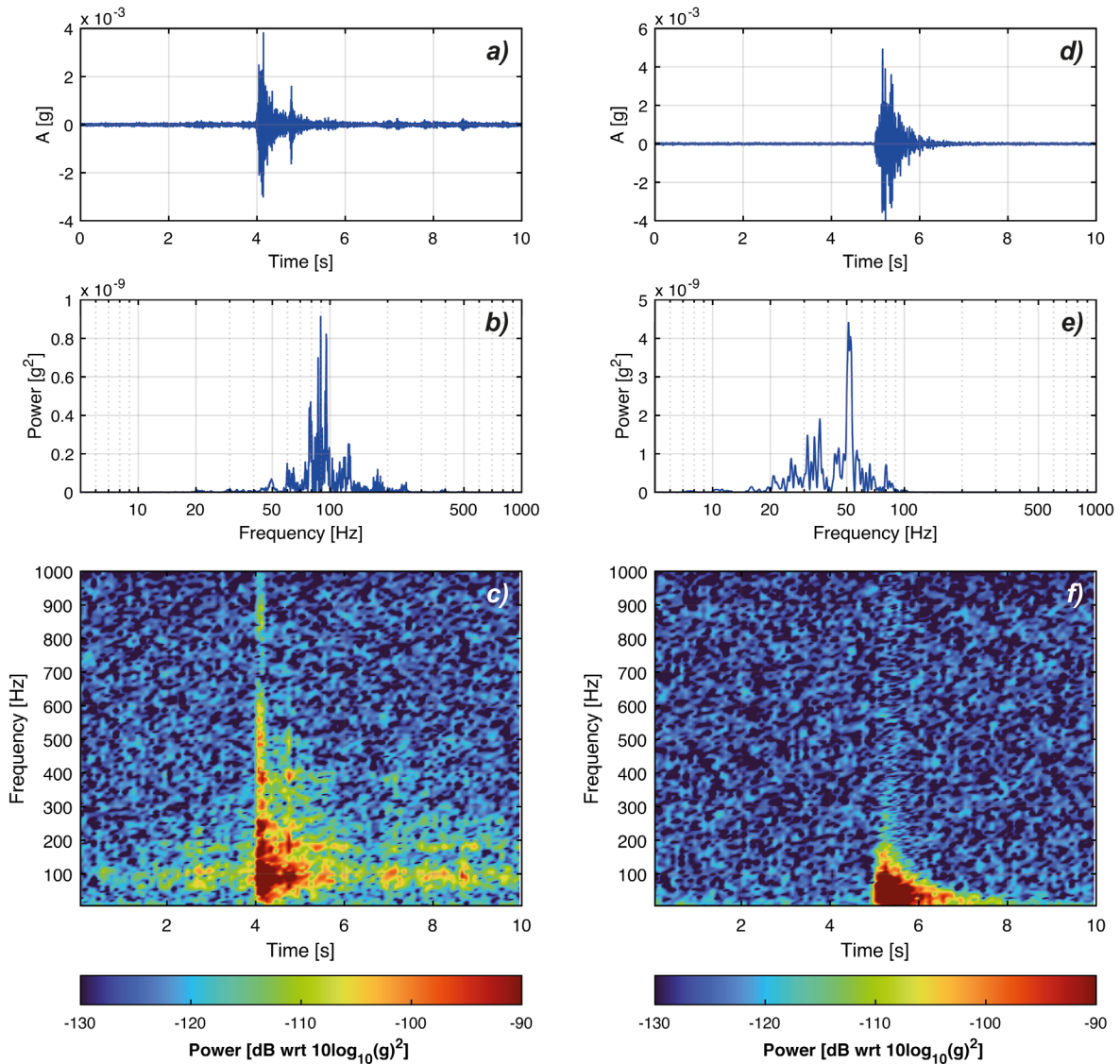


**Figure 4.7.** Examples of two typical events recorded at the Acuto field laboratory and manually classified as microseismic events: waveforms (a, d), power spectra (b, e) and spectrograms (c, f).

Several authors have already recognized these features as typical of microseismic events (Arosio et al., 2018; Colombero, 2017; Colombero et al., 2018b; Lévy et al., 2011). In particular, the triangular shape of spectrograms is interpreted as caused by the attenuation

of higher frequencies due to the presence of dense discontinuity networks (Arosio et al., 2018; Spillmann et al., 2007). During the entire monitoring period only one small-size rockfall (1 m<sup>3</sup> ca.) occurred in the area close to the monitored rock block (between March 9th–11th), but no signals were recorded because the microseismic monitoring array was not functioning due to an interruption of power supply. Similarly, no evidence of local earthquakes occurred within a radius of 50 km were found in ambient noise recordings over the whole monitoring period (D’Angiò, 2019)

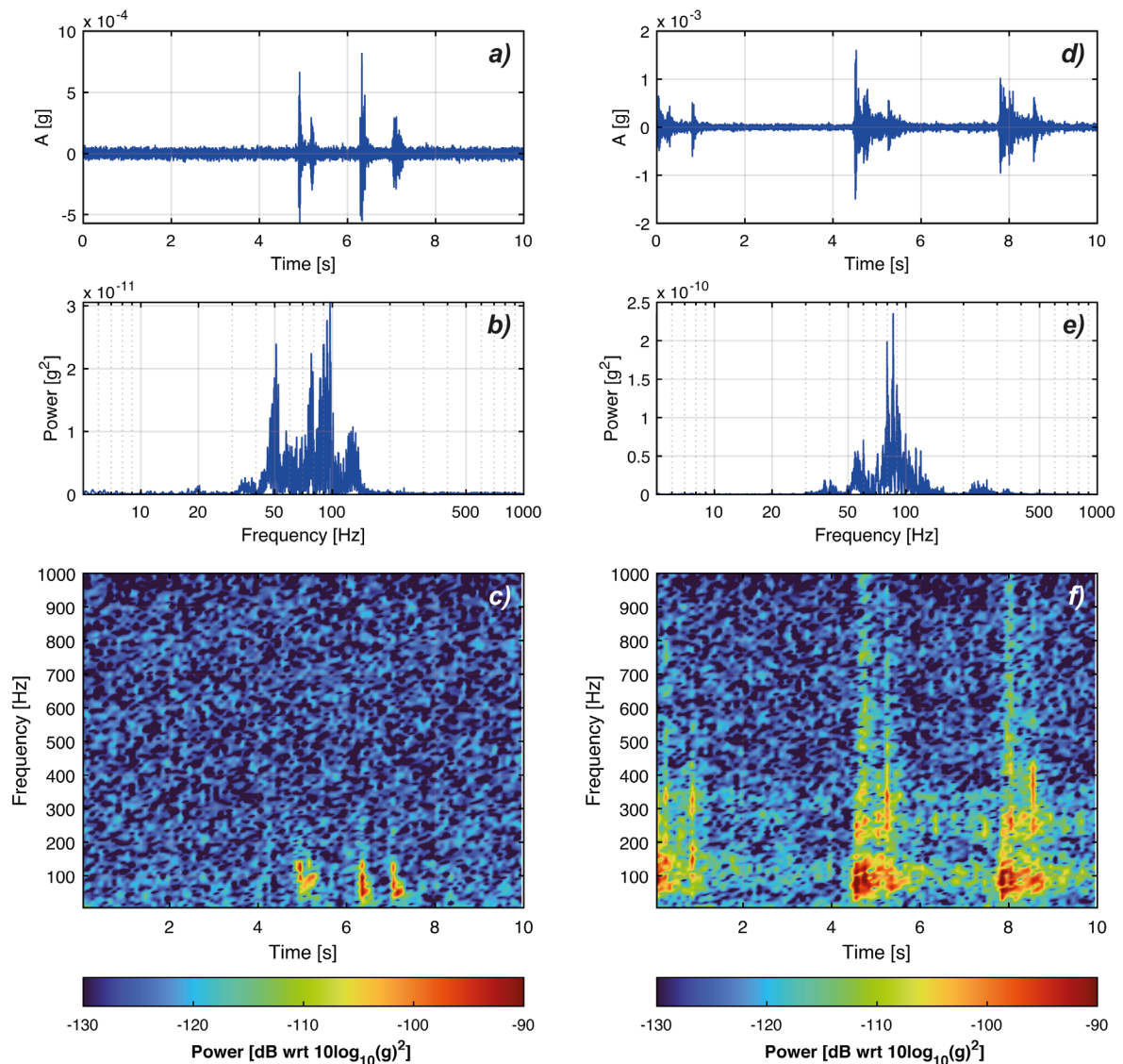


**Figure 4.8.** Examples of two event sequences recorded at the Acuto field laboratory and manually classified as microseismic events: waveforms (a, d), power spectra (b, e) and spectrograms (c, f).

Nevertheless, even though the analyzed dataset was composed of less than one thousand events, the manual classification of signals may be still affected by variable degrees of

uncertainty as it is highly dependent on a subjective criterion of selection. To evaluate the goodness of the manual classification, a quantitative comparison between the two identified classes was performed by analyzing several characteristic time and frequency domain parameters of the extracted signals, as described in [Section 3.2.3](#). In [Figure 4.9](#), each panel compares couples of parameters that were considered for the investigation of the two clusters.

The analysis of the relationship between kurtosis and event durations (bracketed and uniform) highlights how false events concentrate in the left region of both plots ([Figure 4.9a, b](#)), thus confirming their very short and impulsive onset. In contrast, microseismic events show distributions characterized by variable durations. This evidence could derive from the fact that both single events (uniform duration > 1–2 s) and sequences of multiple events (bracketed duration > 3–4 s) are present within this class. The most evident difference between kurtosis values of these clusters is the broader variability that characterizes the class of false events, with values ranging from  $10^1$  up to more than  $10^3$  ([Figure 4.9a, b](#)). In particular, since the kurtosis of the envelope describes the flatness or peakedness of a random variable distribution compared to a normal distribution, high values of this parameter are expected for impulsive transients, while low values are in general typical of noise (Colombero, 2017; Hibert et al., 2014).

By observing the almost linear relationship between the normalized maximum amplitude ( $A_{\max}/A_{\text{mean}}$ ) and the Arias Intensity ( $I_A$ ) two distinct alignments of microseismic and false events are evident ([Figure 4.9c](#)), with the latter class which is characterized by higher  $A_{\max}/A_{\text{mean}}$  values than the former within the same interval of  $I_A$ . Besides, a clear cluster of false events is concentrated at very low  $A_{\max}/A_{\text{mean}}$  and  $I_A$  values, probably describing noise transients rather than energetic electrical disturbances.

Along with these results, the most significant differences observed between the two manually identified classes is shown by panels d and e of [Figure 4.9](#), where the spectral content of all events, in terms of peak frequency ( $f_{\max}$ ) and 10-Hz frequency bands ( $f_{\text{band}}$ ), was compared to their  $A_{\max}/A_{\text{mean}}$  values. The cluster of microseismic events is particularly apparent as it is characterized by a frequency range concentrated between 40 and 110 Hz. On the contrary, false events exhibit an evident bimodal distribution with two isolated local maxima located at very low (< 10 Hz) and very high frequency ranges (> 300 Hz).

---

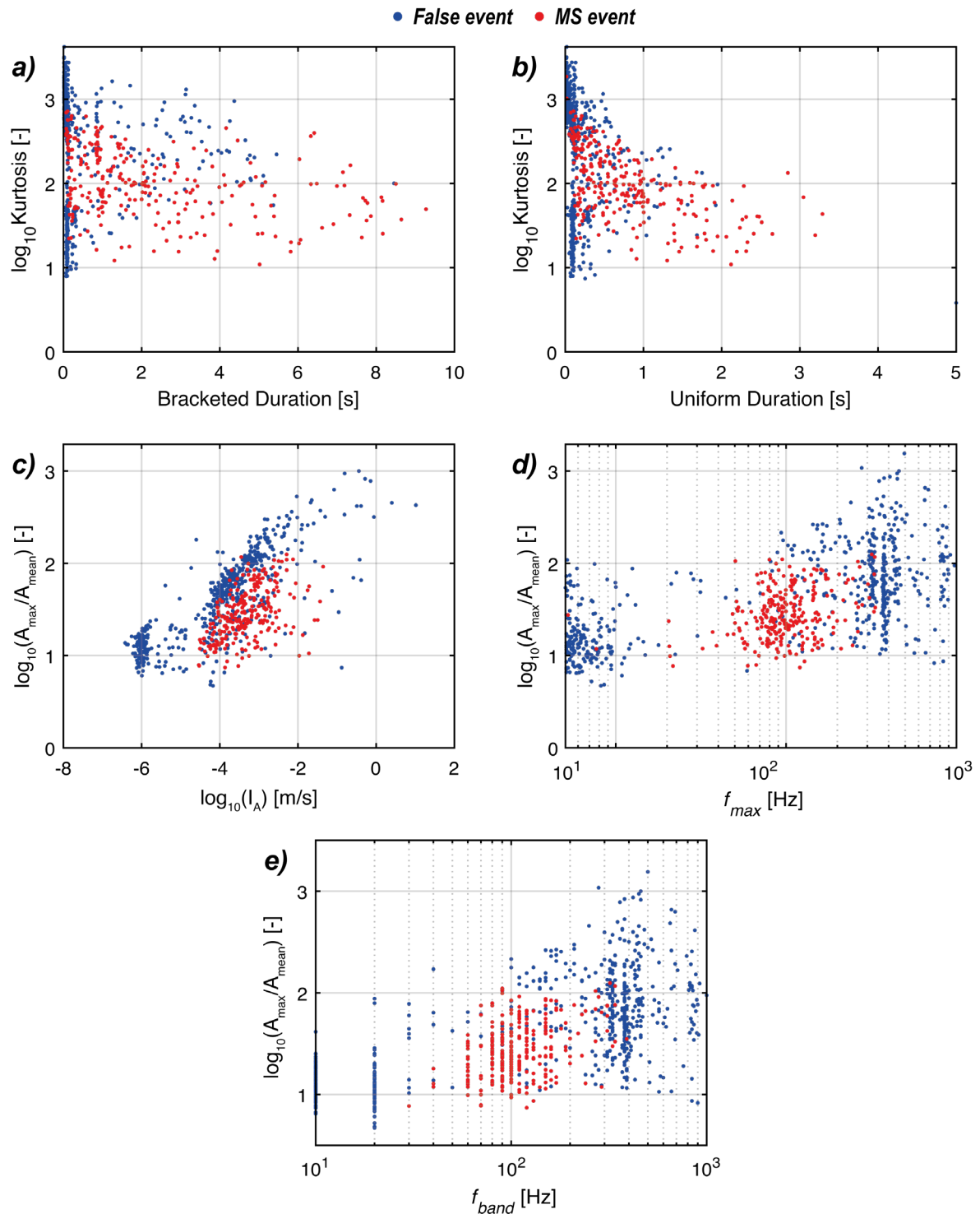


**Figure 4.9.** Results of the comparison between manually classified false and microseismic events based on time and frequency domain features. The following plots are presented: kurtosis vs bracketed duration (a), kurtosis vs uniform duration (b), maximum amplitude normalized to the mean of the envelope of the signal ( $A_{\max}/A_{\text{mean}}$ ) vs Arias Intensity ( $I_A$ ) (c),  $A_{\max}/A_{\text{mean}}$  vs the frequency peak of power spectra ( $f_{\max}$ ) (d) and the 10-Hz frequency band with the maximum spectral content ( $f_{\text{band}}$ ) (e).

A synthesis of the eight parameters considered to compare the identified classes of events is presented in [Figure 4.10](#). As previously stated, the objective of this analysis was to produce a comparison between microseismic and false events that could strengthen the outcomes of manual classification through a quantitative control on time and frequency domain parameters.

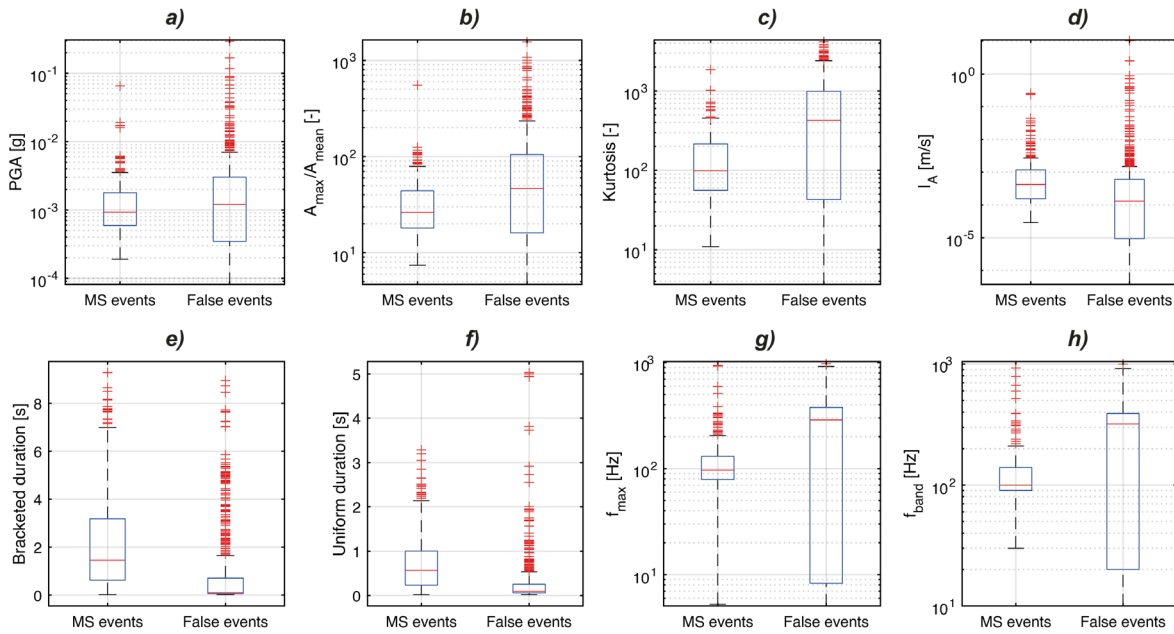


**Figure 4.10.** Synthesis of results obtained from the statistical comparison the two manually identified classes of detected events at the Acuto field laboratory for the period February 2018 – October 2019. For each class, the extension of the blue boxes represents the interquartile range (IQR, defined as the difference between the upper (Q3) and lower (Q1) quartiles), red lines are median values, black whiskers extend to extreme values and red crosses are the not considered outliers. The parameters considered for this analysis are: PGA (a), normalized amplitude (b), kurtosis (c), Arias Intensity (d), bracketed (e) and uniform duration (f), peak frequency (g) and most energized frequency band (h).

Based on the obtained results, which confirmed the validity of events manual classification, and considering microseismic and false events as two separate clusters characterized by distinct features and possible difference sources, the relationships between event frequency and intensity were analyzed for both clusters according to the modified Gutenberg & Richter (1954) power-law already described in [Section 3.2.3](#). Due to the impossibility of locating event sources and estimating their magnitudes, these frequency-intensity curves were built considering the cumulative number of events having  $I_A$  values greater than a certain  $I_A$ . Their b-values were computed through linear regression ([Figure 4.11](#)). From the obtained results, which can be considered statistically significant in virtue of the high values of R-square ( $\sim 0.98$ ), it is evident that these two clusters are characterized by different frequency-intensity



distributions, with microseismic and false event clusters having b-values of 0.69 (Figure 4.11a) and 0.46 (Figure 4.11b), respectively.

No inferences can be proposed in terms of failure mechanism assessment, which are in general among the main purposes of the analysis of frequency-magnitude distributions of events since different b-values of frequency-magnitude distributions are generally interpreted as signatures of different seismic sources and mechanisms (Hudyma and Potvin, 2010; Zhan, 2017). However, the observed differentiation between frequency-intensity distributions of microseismic and false events may be interpreted as an element that further corroborates the goodness of the manual classification process. Even though these results are insufficient to constrain and characterize the source of microseismic events, this analysis can be regarded as a preliminary attempt to obtain valuable insights to distinguish possible source mechanisms responsible for the local microseismic activity.

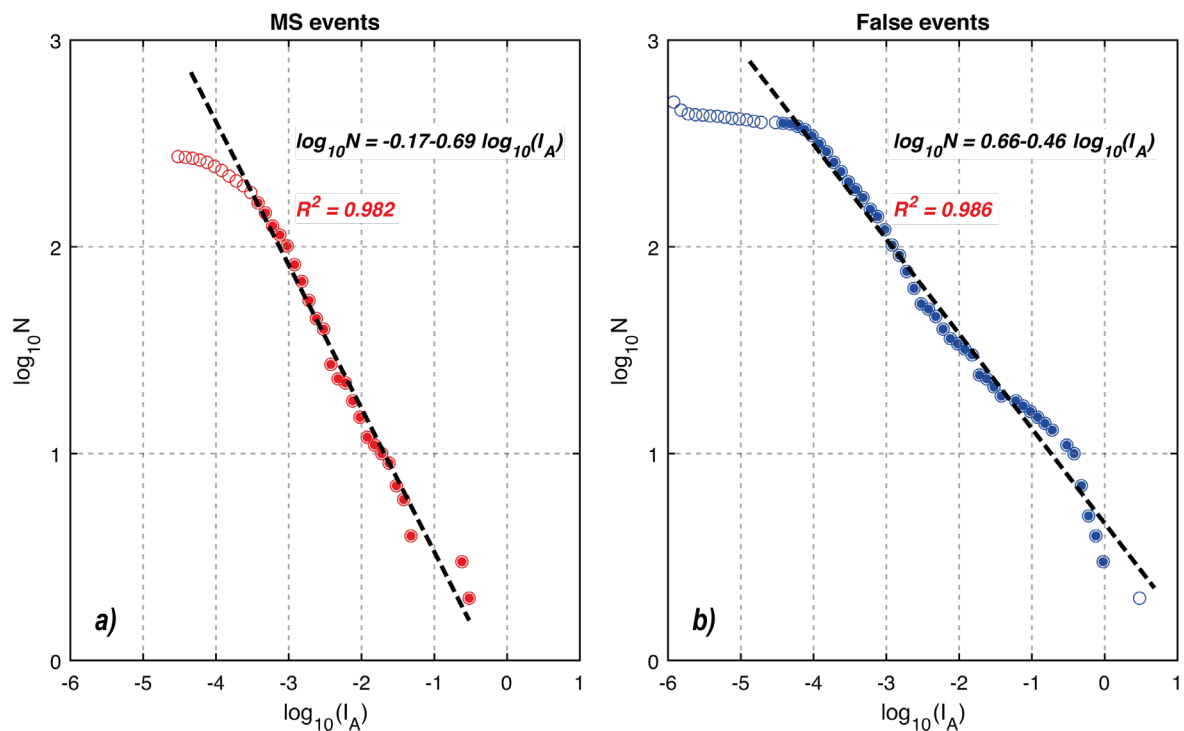


**Figure 4.11.** Comparison between the logarithm of Arias Intensity ( $I_A$ ) and the logarithm of the cumulative number of occurrences ( $N$ ) for microseismic events (a) and false events (b), following the modified Gutenberg & Richter (1954) power-law relation.

On the basis of the obtained results from the classification of the microseismic dataset collected at the Acuto field laboratory, the potential correlation between microseismic activity and meteo-climatic factors (i.e., temperature fluctuations and rainfalls) was

investigated. At first, by observing the cumulative curves of both microseismic and false events for the entire monitoring period, different trends in the occurrence of these two event classes are particularly apparent (Figure 4.12). Although both curves are characterized by increasing rates during periods with similar climatic and meteorological conditions ( $P_1$ ,  $P_2$ ,  $P_3$ ), characterized by concomitant marked temperature drops and consistent rainfalls, the rate of false event occurrence is significantly higher than the one of microseismic events. By contrast, another peak in the event occurrence is found in the absence of rainfall and significant temperature fluctuations ( $P_4$ ) (Figure 4.12). As already discussed, this effect can be interpreted as the result of the influence of meteorological factors on the onset of frequent electrical disturbances. However, it must be noted that even microseismic events show not negligible increasing rates during the same time intervals except than for  $P_3$ .

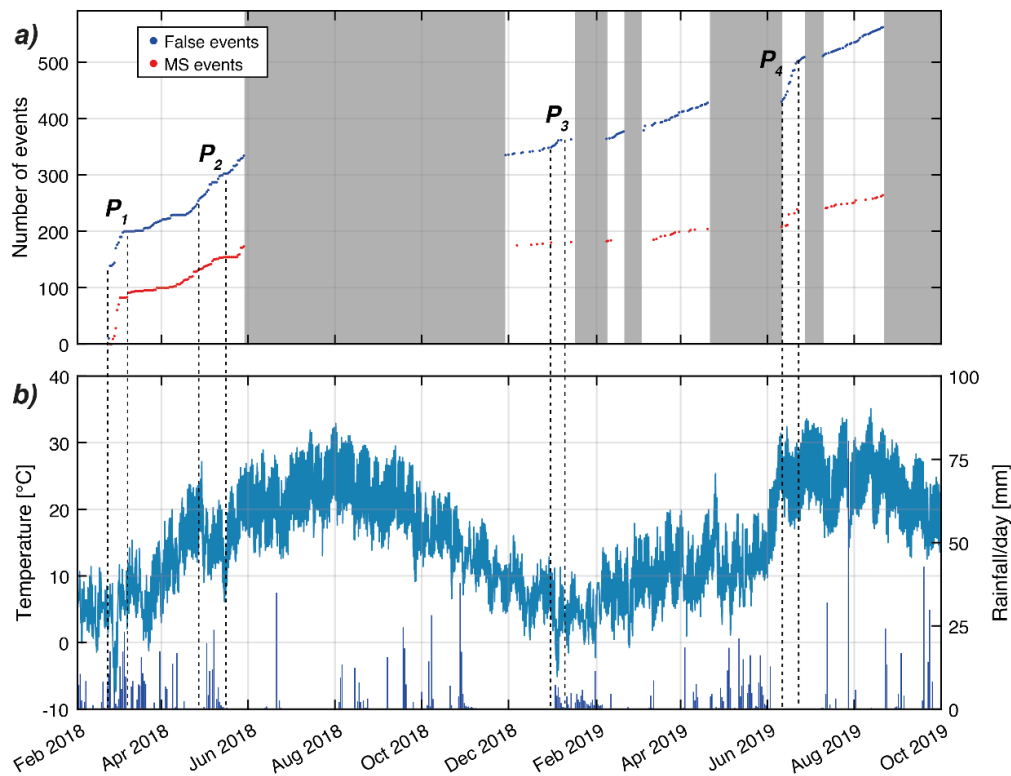


**Figure 4.12.** Cumulative number of microseismic and false events computed over the entire monitoring period (a). 1-hour air temperatures and daily rainfall recorded by the weather station installed inside the quarry area (b). Four time intervals ( $P_1$ – $P_2$ – $P_3$ – $P_4$ ) are highlighted in both plots representing the periods in which the highest increments in the event occurrence were observed. Gray areas in panel a represent periods in which the microseismic monitoring network was not working due to power supply interruptions.

The analysis of the temporal evolution of the microseismic events highlighted the existence of several days in which more than five events occurred (Figure 4.13a). These peaks mostly

concentrate during the period between February and April 2018, during the first monitoring campaign, when 63% of all events were detected. In particular, the highest peak in the daily distribution of microseismic events (32), which is also preceded and followed by days of intense microseismic activity, is located within a time interval characterized by a marked decrease in rock mass temperatures (Figure 4.13b) and persistent rainfalls/snowfalls (Figure 4.13c).

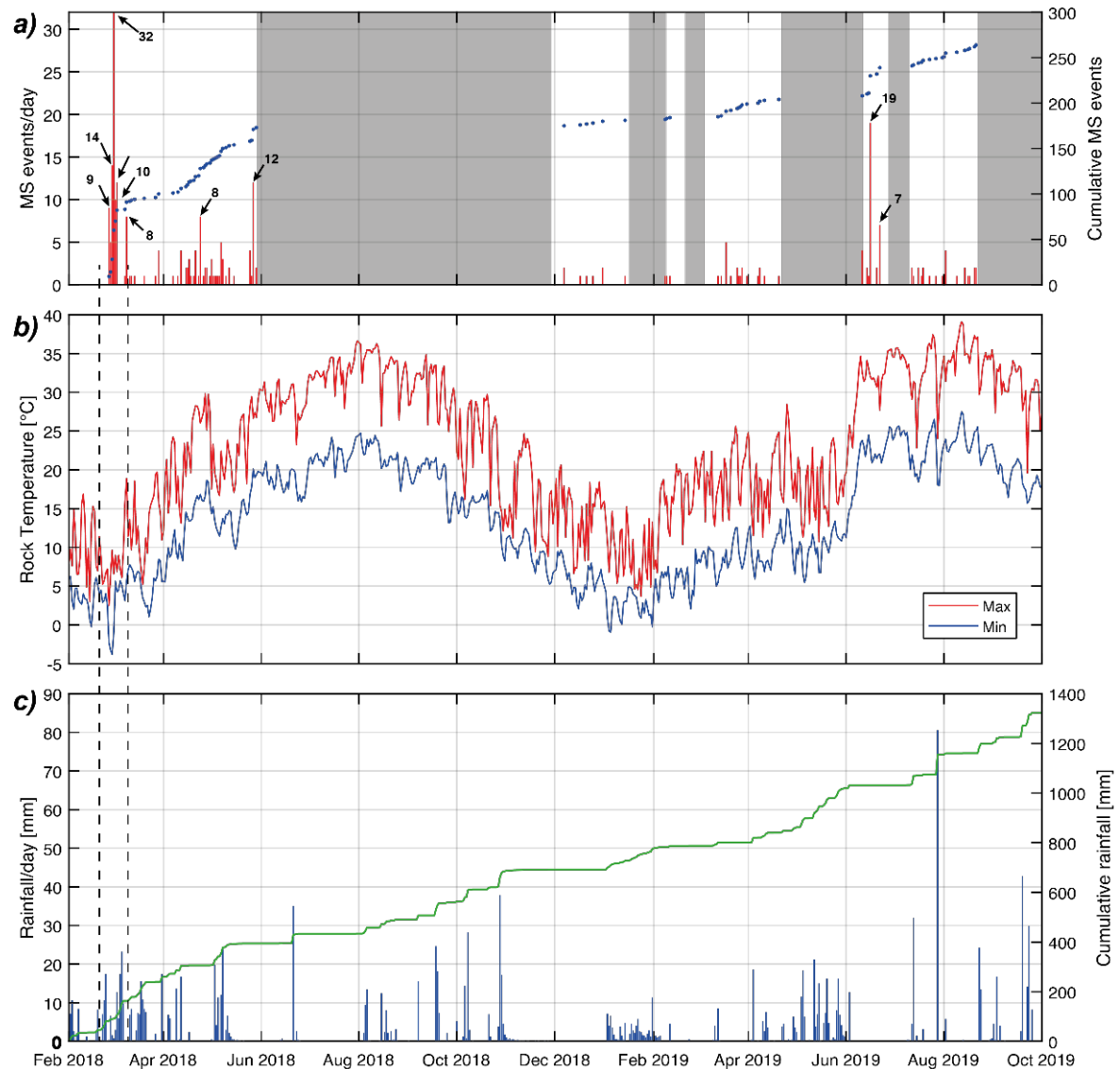


**Figure 4.13.** Comparison between the temporal evolution of MS events and environmental factors at the Acuto field laboratory: daily and cumulative number of events (a), daily maximum and minimum rock temperatures (b), daily and cumulative rainfall (c). Dashed lines highlight a 10-day period in which rock mass temperatures experienced a sharp decrease due to an extreme meteorological event. Gray areas in panel a represent periods in which the microseismic monitoring network was not working due to power supply interruptions.

Between the end of February and March 2018, the entire region of central Italy experienced an extreme meteorological event due to an incoming perturbation associated with the *Buran*, a cold north-easterly wind that is typical of the steppes of the Siberian region (D'Angiò et al., 2021a). At the Acuto field laboratory, air and rock mass temperatures reached their minimum values of  $-7.7$  °C and  $-3.8$  °C, respectively, and almost 106 mm of rainfalls occurred within a 7-day time interval. The sharp temperature decrease caused freezing conditions that remained stable for four days (from 25/02/2018 to 01/03/2018). This winter storm was responsible for a short and intense thermal transient in the seasonal temperature trend, representing an unprecedented event in the five-year meteo-climatic monitoring dataset collected at the Acuto field laboratory (2016-2021).

Apart from this short-term, dramatic variation of environmental boundary conditions that caused a significant acceleration in the occurrence of MS events, with 83 MS events concentrated in 12 days, other isolated MS peaks can be observed in [Figure 4.13](#), especially during April 2018 (8 MS events on 24/04/2018), May 2018 (12 MS events on 27/05/2018), and June 2019 (16 MS events on 19/06/2019, and 7 MS events on 22/06/2019). However, their correlation with external continuous (i.e., thermal variations) and transient (i.e., rainfalls) stresses are not as evident as for the period in which the rock mass experienced freezing conditions.

Unfortunately, it must be stated that due to the limited number of MS events collected during the discontinuous 20-month microseismic monitoring, a statistical analysis aimed at deepening the correlations between rainfall, temperature fluctuations, and the occurrence of MS events based on cross-correlations, as suggested by Helmstetter and Garambois (2010) and Arosio et al. (2018) was not performed. However, to achieve preliminary insights on potential cause-to-effect relationships between the abovementioned factors, the analysis of the temporal evolution and distribution of MS events was approached employing an observational-based approach.

An attempt to investigate the influence of temperature fluctuations on the local microseismic activity was made by analyzing the distribution of MS events during heating and cooling phases of the rock mass ([Figure 4.14](#)). To this aim, heating and cooling ramps of rock temperature timeseries were analyzed, and the minimum and maximum recorded values were extracted along with their timing and duration for each day of the monitoring period.

---

Based on this approach, MS events were classified according to the ramp in which they occurred to highlight any recurrent pattern in their distribution at the daily timescale (Figure 4.14a). The amplitude of temperature ranges was then computed for each cooling ramp as the difference between the maximum daily temperature and the subsequent minimum, while for heating ramps they were computed oppositely (Figure 4.14b).

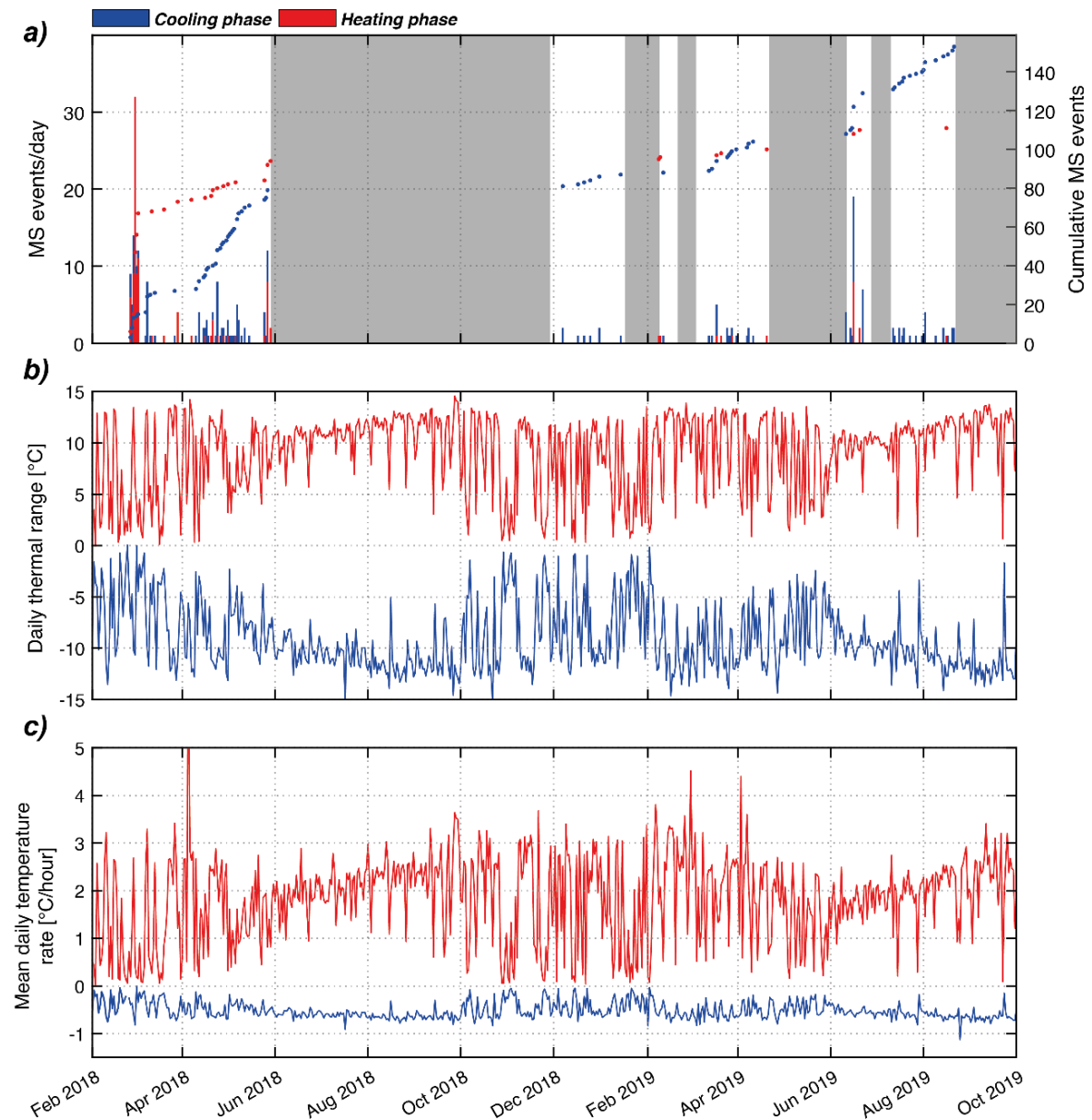


**Figure 4.14.** Comparison between the distribution of MS events (a), daily thermal ranges (b) and mean daily temperature rates (c). In each plot, the distinction between heating (in red) and cooling (blue) phases of the rock mass is proposed with a view to investigating the response of the jointed rock block to different thermal regimes of increasing (heating) or decreasing (cooling) temperatures. Gray areas in panel a represent periods in which the microseismic monitoring network was not working due to power supply interruptions.

Furthermore, the mean rate of rock mass heating and cooling ramps was computed dividing their amplitude by their time duration (Figure 4.14c). It is interesting noting that MS events show an evident differentiation in their distribution between heating and cooling phases, with 111 and 153 MS events respectively. More in detail, during the 4-day freezing period of February 2018, 69 MS events occurred in correspondence of an increasing temperature regime (i.e., heating phase), while only 14 of them were recorded during a regime of decreasing temperatures, meaning that the 63% of all MS events that occurred during cooling phases are clustered during this very extreme meteorological transient. The magnitude of temperature ranges of both heating and cooling ramps is comparable, also showing a significant variability throughout the entire period, but the mean rates of heating ramps are consistently higher than the ones characterizing cooling ramps. On the contrary, if excluding this period characterized by not common meteorological conditions, it can be noted that MS events tend to concentrate during the cooling phases of the rock mass, as also highlighted by the different trends of their cumulative curves of Figure 4.14a.

However, since the microseismic monitoring is affected the presence of several month-long gaps, the comprehension of the relationship between thermal boundary conditions and the local microseismicity is difficult to discern. For this reason, and since MS events show a very discontinuous distribution during the whole monitoring period with a limited number of short time windows in which a significant concentration of MS events is recorded, the investigation of three distinct periods characterized by the highest MS event peaks was performed. Furthermore, these periods were selected as they are also representative of different climatic and meteorological conditions. For each time interval, the comparison between rainfall intensity, temperature fluctuations and MS event distribution was performed, with a view of highlighting the influence of highly variable environmental conditions on the potential acceleration of fracturing processes (Figure 4.15, Figure 4.16, Figure 4.17).

The first period comprises a time window spanning from 23/02/2018 to 14/03/2018 when, as previously introduced, the quarry area experienced an unprecedented weather event, and a synoptic chart describing the evolution of near-surface temperatures, rainfalls and MS events is presented in Figure 4.15. In this period the highest peaks of events are concentrated in correspondence of few days characterized by a marked drop of temperatures that caused freezing conditions and by a small amount of cumulated rainfalls (Figure 4.15a, c).

---

---

In such circumstances, MS events seem to be better correlated to temperature variations rather than to the occurrence of rainfalls. This evidence is also strengthened by the almost perfect correlation between the 1-h rate of event occurrence and the evolution of daily temperature ranges and 1-hour temperature rates, with the absolute highest MS peak (32 events) that occurred immediately a day characterized by a 14.5 °C daily thermal excursion and a maximum temperature rate of 4 °C/hour (Figure 4.15b). The occurrence of MS events during the winter storm appears to be mostly clustered during heating phases of the rock mass, also showing a greater variability in Arias Intensity values ( $I_A$ ) with respect to post storm stages, (Figure 4.15d, e).

However, it must be considered that the scarce correlation between MS events and rainfalls during this time interval may be in part biased by the fact that the rain gauge mostly measured snow melt. In fact, the weather station was not equipped with a nivometer and, since the quarry was completely covered by snow during those days, the analysis of the correlation between MS events and rainfalls cannot be investigated. Nevertheless, after the end of the Buran storm, a significant increase in rainfalls was observed between 05/03 and 08/03, but no MS events were recorded, except for an isolated peak triggered with a delay of two days. This evidence could highlight the fact the microseismicity observed during the freezing period is more likely related to the rapid decrease and increase of near-surface temperatures. Thermally-induced stresses are in fact able to drive differential strain variations especially in the outermost layers of rock masses, where their amplitude is highest, resulting in the superposition of contraction and expansion stages of fractures and microfractures that can eventually lead to the genesis or propagation of cracks (Amitrano et al., 2010; Occhiena et al., 2012; Occhiena and Pirulli, 2012). In addition, if considering the not negligible amount of rainfalls occurred before the winter storm, a freezing and thawing mechanism may be also invoked to justify the numerous MS events detected during this short time interval. In fact, the persistent freezing conditions might have favored the formation of ice inside fractures and microcracks during cooling phases of the rock mass, leading to the accumulation of inelastic strain at the tip of discontinuities (Frayssines and Hantz, 2006). Then, the rise of temperatures during the first stages of heating phases driven by high positive thermal gradients may have caused rapid ice melting, and the consequent stress release could be regarded as responsible for the intense microseismic activity. These evidences are however limited to this time window which, as previously stated, is

---

characterized by extreme and non-representative conditions of the normal climatic setting of the Acuto quarry area.

The other two investigated periods of the microseismic monitoring are instead more representative of the environmental boundary conditions of the area. For example, during the second period that spans from 08/04/2018 to 25/04/2018, a total amount of 29 MS events was detected, but this value is certainly underestimated due to the periodic interruption of the microseismic monitoring system during nighttime (Figure 4.16). Near-surface temperatures show a decreasing trend during the first days (from 08/04 to 13/04) that is related to a minor meteorological perturbation which, along with rainfalls, caused temperature rates and gradients to significantly vary (Figure 4.16b). One of the most distinct features of this monitoring interval with respect to the winter storm is represented by the higher correlation that can be found between MS events and rainfalls rather than temperature fluctuations. Two rainfall events characterized by different intensities ( $E_1$  and  $E_2$ , Figure 4.16c) may be regarded as the primary cause of the MS events that occurred during and immediately after these rainfalls (Figure 4.16d), while daily temperature ranges and rates do not exhibit significant variations. The last days of this period are instead characterized by the absence of rainfalls and by a steady increase in MS events, with a maximum peak of 8 events on April 24<sup>th</sup> that is associated with an overall increasing trend of temperatures which in turn determined the stabilization of high temperature ranges and rates.

Similar conditions are found in the period presented in Figure 4.17 (10/06/2019 – 24/06/2019) which is representative of typical warmer climatic conditions characterized by the complete absence of rainfalls. Here, MS events cannot be correlated with rainfalls and their occurrence is more likely caused by the continuous effect of daily thermal cycles. From the observation of the 1-hour cumulative occurrence of MS events, three peaks are particularly apparent and mostly clustered during the cooling stages of the rock block (Figure 4.17d).

The higher concentration of MS events during periods characterized by rapid temperature variations (i.e., high temperature rates), and especially during cooling phases, is in agreement with what was already observed by several authors at different case studies (Amitrano et al., 2010; Occhiena et al., 2012).

---



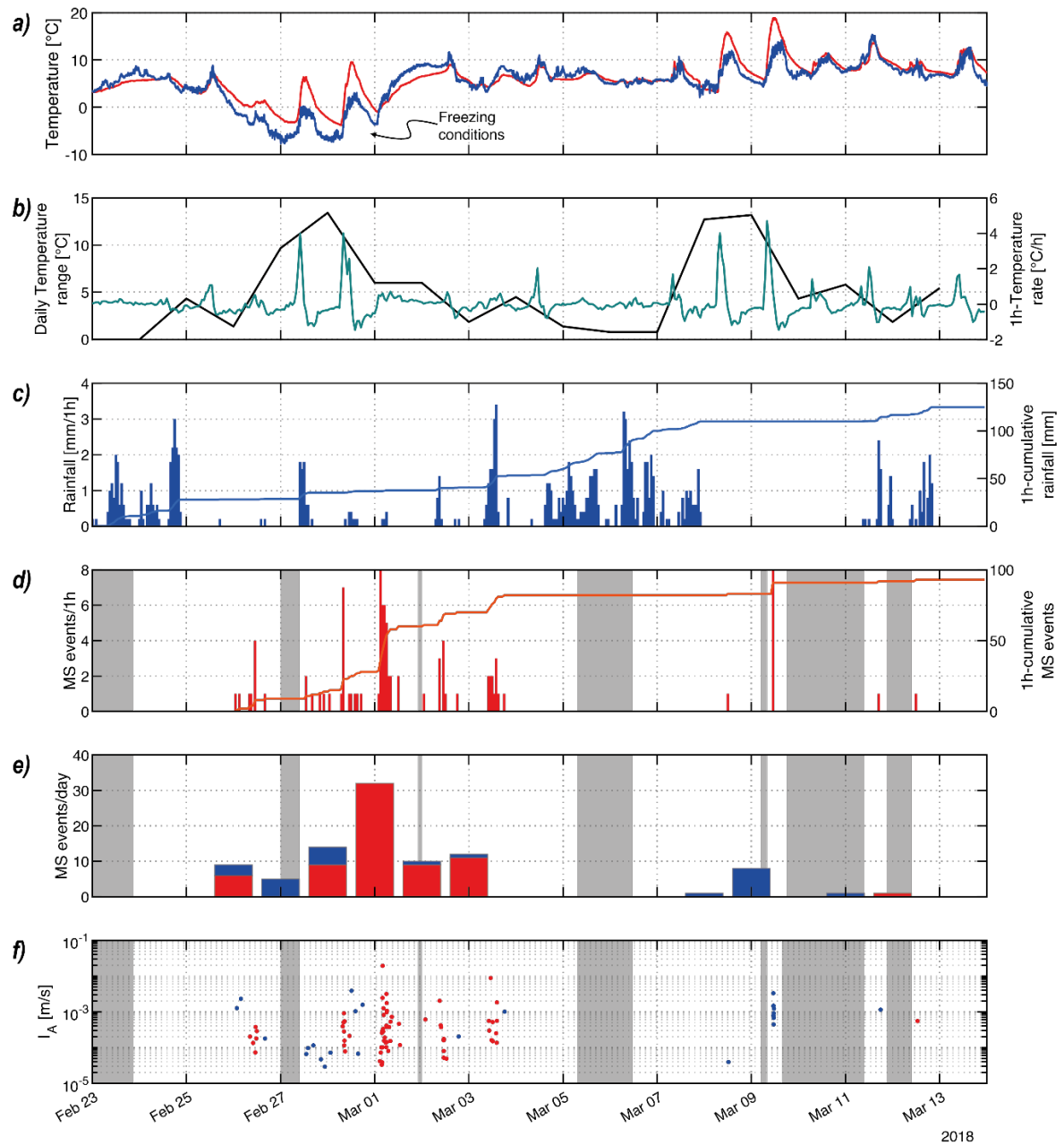


**Figure 4.15.** Comparison between environmental factors and the occurrence of MS events for the period comprised between 23/02/2018 and 13/03/2018, when the quarry area was interested by an intense winter storm: 10-minute air (blue line) and rock mass temperature (red line) (a), daily temperature range (i.e., thermal excursion) (black line) and 1-hour rock temperature rate (blue line) (b), 1-hour cumulated rainfalls (blue bars) and relative 1-hour cumulative curve (blue line) (c), 1-hour cumulated MS events (red bars) and relative 1-hour cumulative curve (red line) (d), daily distribution of MS events occurred during the heating phase (red bars) and cooling phase (blue bars) of the rock mass (e), temporal evolution of Arias Intensity ( $I_A$ ) of the MS events occurred during the heating phase (in red) and cooling phase (in blue) of the rock mass (f). Gray areas in panel d-f represent periods in which the microseismic monitoring network was not working due to power supply interruptions.

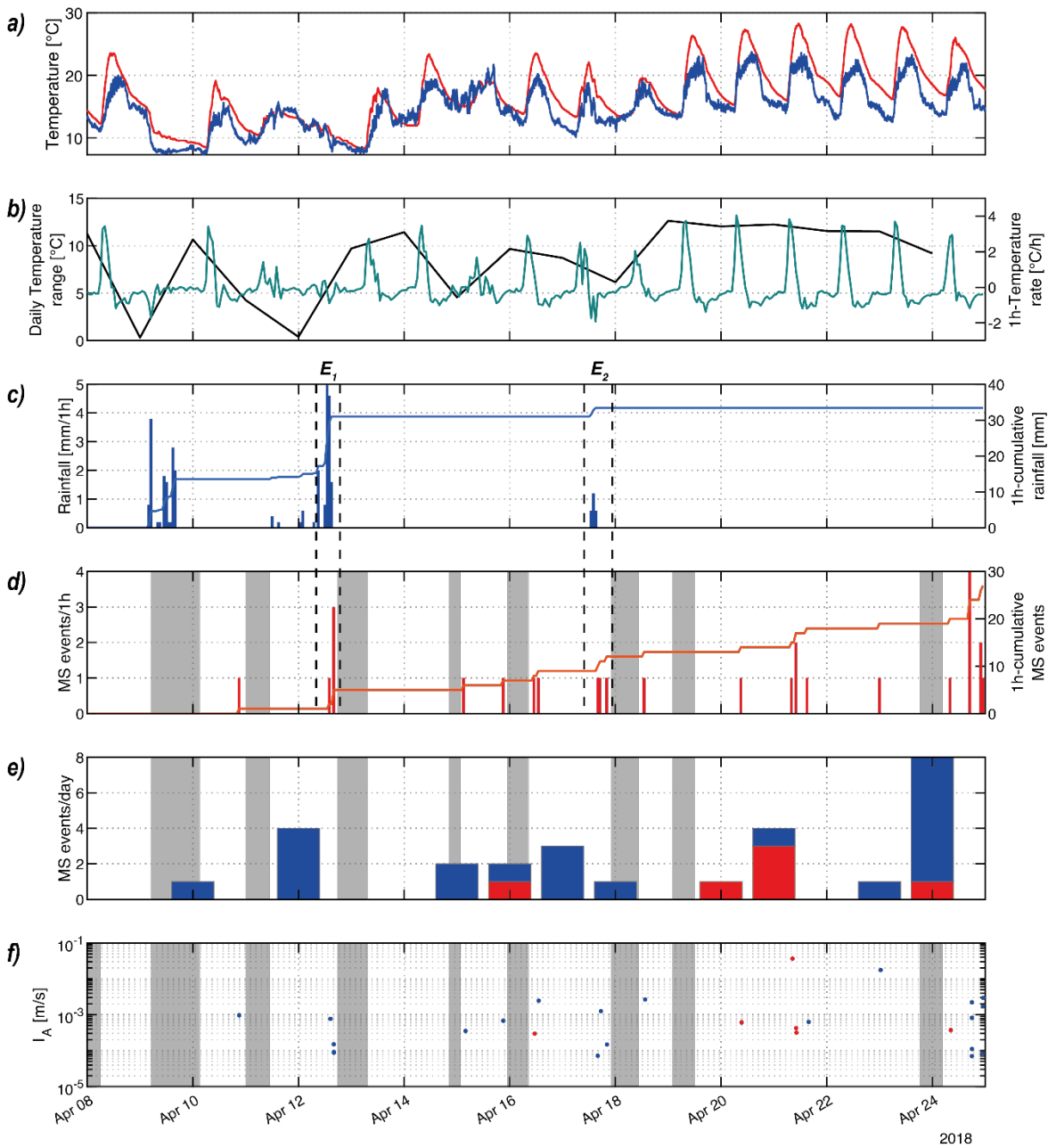


**Figure 4.16.** Comparison between environmental factors and the occurrence of MS events for the period comprised between 08/04/2018 and 25/04/2018: 10-minute air (blue line) and rock mass temperature (red line) (a), daily temperature range (i.e., thermal excursion) (black line) and 1-hour rock temperature rate (blue line) (b), 1-hour cumulated rainfalls (blue bars) and relative 1-hour cumulative curve (blue line) (c), 1-hour cumulated MS events (red bars) and relative 1-hour cumulative curve (red line) (d), daily distribution of MS events occurred during the heating phase (red bars) and cooling phase (blue bars) of the rock mass (e), temporal evolution of Arias Intensity ( $I_A$ ) of the MS events occurred during the heating phase (in red) and cooling phase (in blue) of the rock mass (f). Gray areas in panel d–f represent periods in which the microseismic monitoring network was not working due to power supply interruptions.

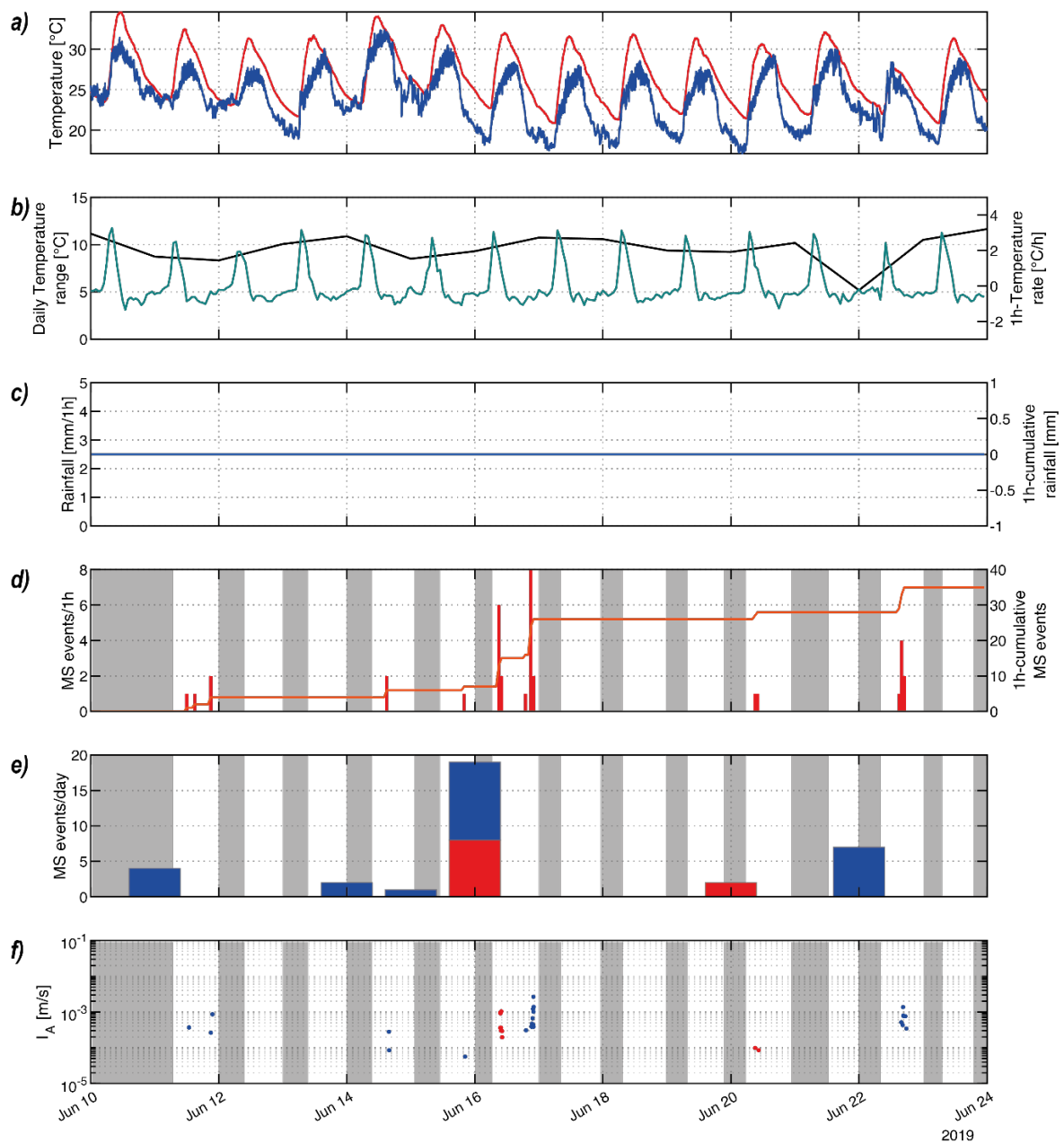


**Figure 4.17.** Comparison between environmental factors and the occurrence of MS events for the period comprised between 10/06/2019 and 24/06/2019: 10-minute air (blue line) and rock mass temperature (red line) (a), daily temperature range (i.e., thermal excursion) (black line) and 1-hour rock temperature rate (blue line) (b), 1-hour cumulated rainfalls (blue bars) and relative 1-hour cumulative curve (blue line) (c), 1-hour cumulated MS events (red bars) and relative 1-hour cumulative curve (red line) (d), daily distribution of MS events occurred during the heating phase (red bars) and cooling phase (blue bars) of the rock mass (e), temporal evolution of Arias Intensity ( $I_A$ ) of the MS events occurred during the heating phase (in red) and cooling phase (in blue) of the rock mass (f). Gray areas in panel d–f represent periods in which the microseismic monitoring network was not working due to power supply interruptions.

The most interesting preliminary outcome that emerges from the comparison between the above-presented monitoring periods is probably the different distribution of MS events during heating and cooling phases of the investigated rock mass. Although the analyzed dataset is also affected by numerous time gaps and by a limited number of MS events, the temporal distribution of microseismic activity registered in average climatic conditions (second and third periods – [Figure 4.16](#), [Figure 4.17](#)) mostly concentrates within cooling phases of the rock mass, contrarily to what is observed during the winter storm of February 2018. The plots of [Figure 4.18](#) clearly summarize this differentiation of MS event distributions, showing that if excluding the winter storm of February 2018 from the analysis, more than 70% of all detected events occur during cooling phases of the rock mass ([Figure 4.18c](#)).

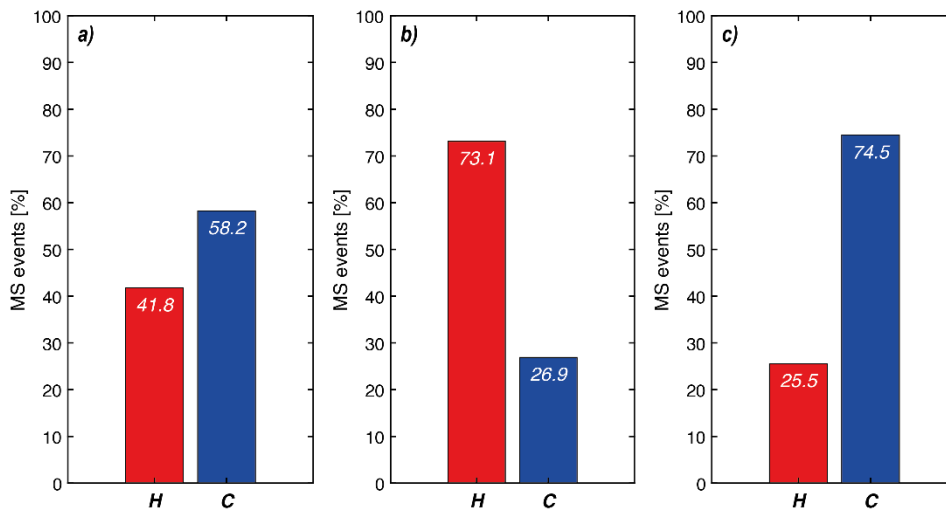


**Figure 4.18.** Percentage distribution of MS events during heating (in red) and cooling phases (in blue) for the whole monitoring period (a), the only winter storm of February 2018 (b), and for the entire monitoring period excluding the winter storm (c).

## 4.2 Results of ambient seismic noise analysis

The ambient seismic noise recordings collected at both study sites were analyzed following the workflow described in [Section 3.2.4](#), with the aim of characterizing the dynamic behavior of the two investigated natural structures.

The analysis of ambient seismic noise at the Acuto field laboratory led to ambiguous results since it highlighted the complete absence of spectral peaks compatible with the vibrational dynamics of the rock block during the two long-term monitoring campaigns. The computation of background noise levels in the time domain (i.e., mean and standard deviation) for each deployed sensor and over almost 5000 hours of recordings evidenced no differences between the reference rock wall and the target rock block considering all measuring components of ground motion ([Figure 4.19b](#)).

The spectral analysis pointed out not only the absence of predominant spectral peaks potentially related to resonance frequencies of the rock block in the frequency band of interest (i.e., 2–30 Hz), but it also allowed to observe a significant drift of power spectral densities (PSD) in the low-frequency range ([Figure 4.19c](#)). In particular, this low-frequency drift in PSD is known as *flicker noise* or *1/f noise* (i.e., the noise power is inversely proportional to the frequency), and even if its origin is still unclear, it is considered to be generally related to the acquisition chain and the transducer element's electrical and mechanical properties. Moreover, these spectral features were found to be constant during the entire monitoring period, as can be observed from [Figure 4.20d](#), where the temporal evolution of hourly PSDs over 12 days is presented. These outcomes are in contrast with the results obtained by Fiorucci (2017) and D'Angiò (2019) who identified the natural resonance frequency of the rock block around 20 Hz through different induced vibrations experiments. Therefore, it is unlikely that the results obtained from the analyzed recordings represent the actual dynamic behavior of the investigated rock block.

The physical and mechanical characteristics of the employed microaccelerometers could be responsible for the inability to characterize the dynamic behavior of the rock block from ambient seismic noise recordings. In particular, the level of residual noise of microaccelerometers (i.e., instrumental noise) may have affected the recording of ambient vibrations, thus completely covering the contribution of low amplitude and low frequency vibrations. The comparison between the PSD values and the residual spectral noise of the

---

employed microaccelerometers (Figure 4.19c), which highlights a very low signal-to-noise ratio (SNR), shows significant evidence that the low-frequency interval of ambient noise is mainly dominated by instrumental noise. The instrumental noise can derive from various factors, among which ground loops (i.e., electrical currents flowing in the shield of accelerometer cables) and triboelectric noise (i.e., disturbance induced by the mechanical motion of cables) affecting long cables might be not negligible. Moreover, their contributions to the overall residual noise of the acquisition chain can completely mask natural low amplitude vibrations (Serridge and Licht, 1987). Based on these considerations, the spectral analysis of ambient seismic noise recordings at the Acuto field laboratory highlighted the limitations of the adopted vibration monitoring system in investigating the dynamic behavior of the rock block due to the impossibility of measuring natural vibrations at the site.

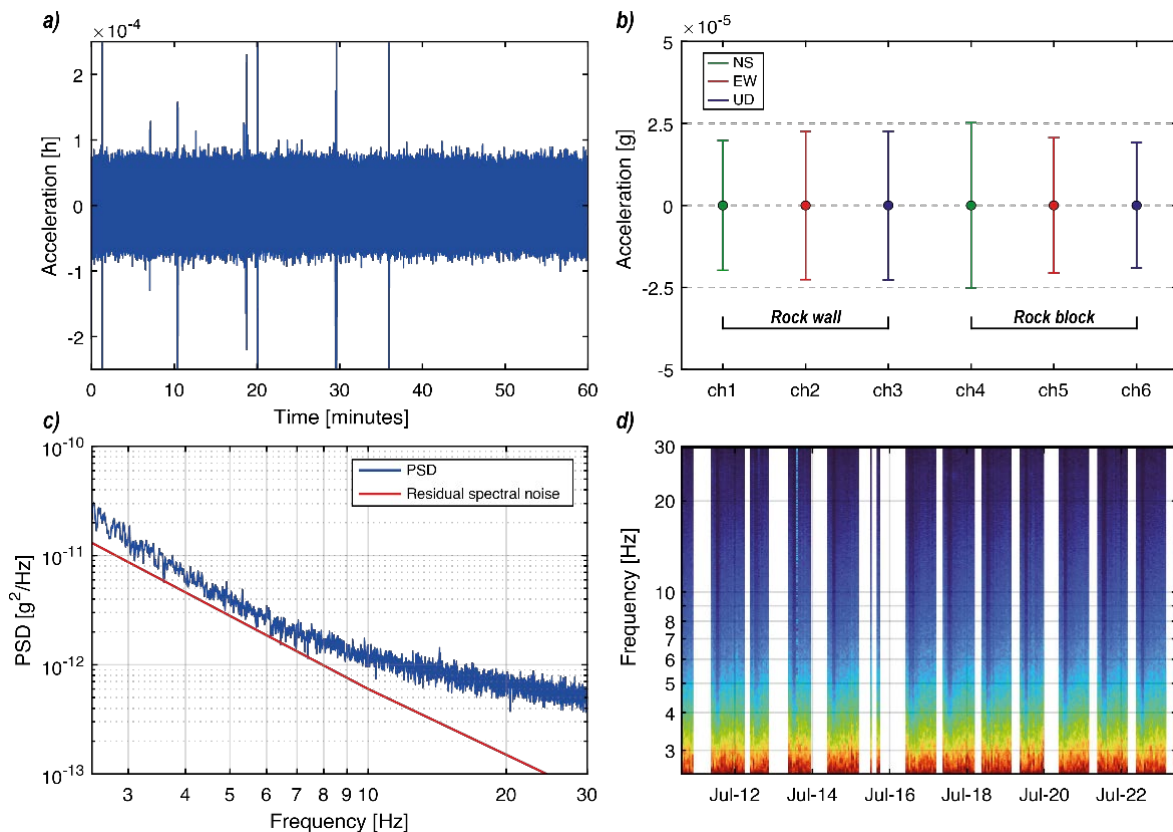


**Figure 4.19.** Synthesis of the results obtained from the analysis of ambient seismic noise at the Acuto field laboratory: example of 1-hour time history (a); mean and standard deviation of background noise levels recorded during the second monitoring campaign (November 2018 – October 2019) by each microaccelerometer (b); power spectral density (PSD) and residual spectral noise of the employed Bruel & Kjaer Type 8344 microaccelerometers (c); evolutionary power spectral density (EPSD) for a 12-day period (d).

On the contrary, the preliminary analysis of ambient seismic noise measurements at the Wied Il-Mielah study site allowed observing a general higher background noise level, which results in a significantly higher SNR and the consequent absence of the issues encountered at the Acuto field laboratory (Figure 4.20). Although the employed monitoring network was used adopting the same configuration of the Acuto case study (e.g., microaccelerometers, cables, signal amplifier and acquisition modules), the higher amplitude of ambient vibrations recorded on the arch (Figure 4.20a, b) enable neglecting the effect of instrumental noise. This evidence fosters the hypothesis that the inability of the monitoring system to investigate the dynamic behavior of the rock block at the Acuto study site might depend on the limited sensitivity of microaccelerometers with respect to the very low amplitude of local natural vibrations.

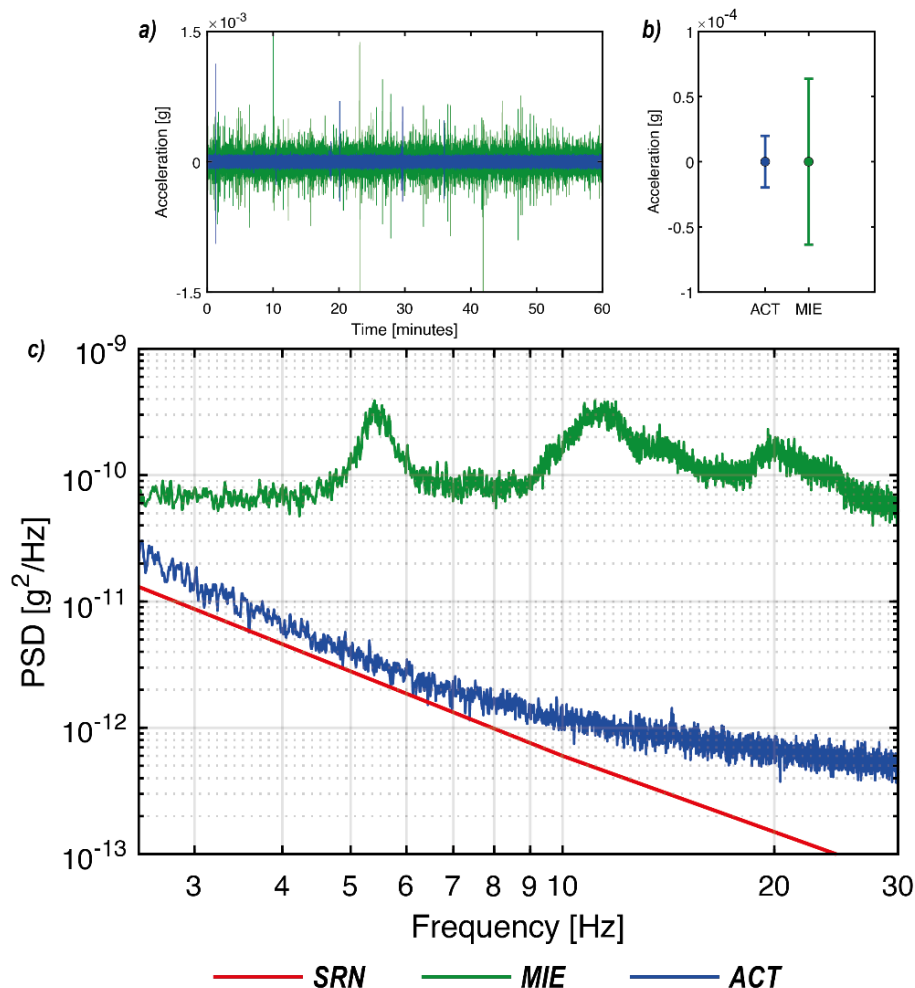


**Figure 4.20.** Comparison between ambient seismic noise recordings at the two case studies (MIE – Wied Il-Mielah; ACT – Acuto): 1-hour acceleration time histories (a); mean and standard deviation of background noise levels (b); power spectral densities (PSD) and the level of spectral residual noise of microaccelerometers derived from calibration charts (SRN) (c).

The ambient seismic noise measurements carried out at the Wied Il-Mielah sea arch during the monitoring campaign of February 2020 employing two seismometers in a site-to-reference configuration (Figure 3.19) allowed isolating signals of interest related to resonances of the arch with respect to a reference spot. The results of the spectral analysis performed on these recordings are shown in Figure 4.21 (a–c).

The primary evidence obtained from the computation of PSDs is represented by the presence of three prominent spectral peaks on station MIE-1 (i.e., the one located on the arch) that are almost absent on the reference station MIE-2. The first peak is centered around 4 Hz ( $f_1$ ), and although it is present in all spectra, it exhibits the highest spectral amplitude on the NS component of ground motion (Figure 4.21b). By contrast, the other two spectral peaks, centered around 5 Hz ( $f_2$ ) and 11 Hz ( $f_3$ ), are visible only on the EW and UD components (Figure 4.21a, c). The amplitude of all spectral peaks is almost comparable on all components, even though the UD component shows the absolute lowest values (Figure 4.21c).

Furthermore, the site-to-reference spectral ratios between homologous components of MIE-1 and MIE-2 were computed, and the results of this analysis are shown in Figure 4.21 (d–e). The so derived relative amplification functions show clearly visible peaks in correspondence of the already mentioned frequencies of interest ( $f_1$ ,  $f_2$  and  $f_3$ ). The amplification factors of these frequencies reach considerable values:  $f_1$  reaches a factor around 200 on the NS component (Figure 4.21e), and the same value is found for  $f_2$  on the EW component (Figure 4.21d), while  $f_3$  reaches its maximum amplification factor around 40 on the same component (Figure 4.21d). In agreement with what was already observed from the plot of PSD, the relative amplification function of ground motion on the UD component shows the lowest values (Figure 4.21f).

The observed correspondence between spectral peaks derived from PSDs and SRSRs, along with the high amplification factors, strengthens the evidence that  $f_1$ ,  $f_2$  and  $f_3$  can be interpreted as resonance frequencies of the arch. In particular, for what concerns the obtained amplification factors, they can be considered typical of freestanding structures, both natural and anthropic (e.g., rock towers, arches, tall buildings and bridges), that in virtue of their geometry are less constrained by physical boundaries, then characterized by greater kinematic freedom, and are more prone to vibrate freely (Kleinbrod et al., 2017).

---



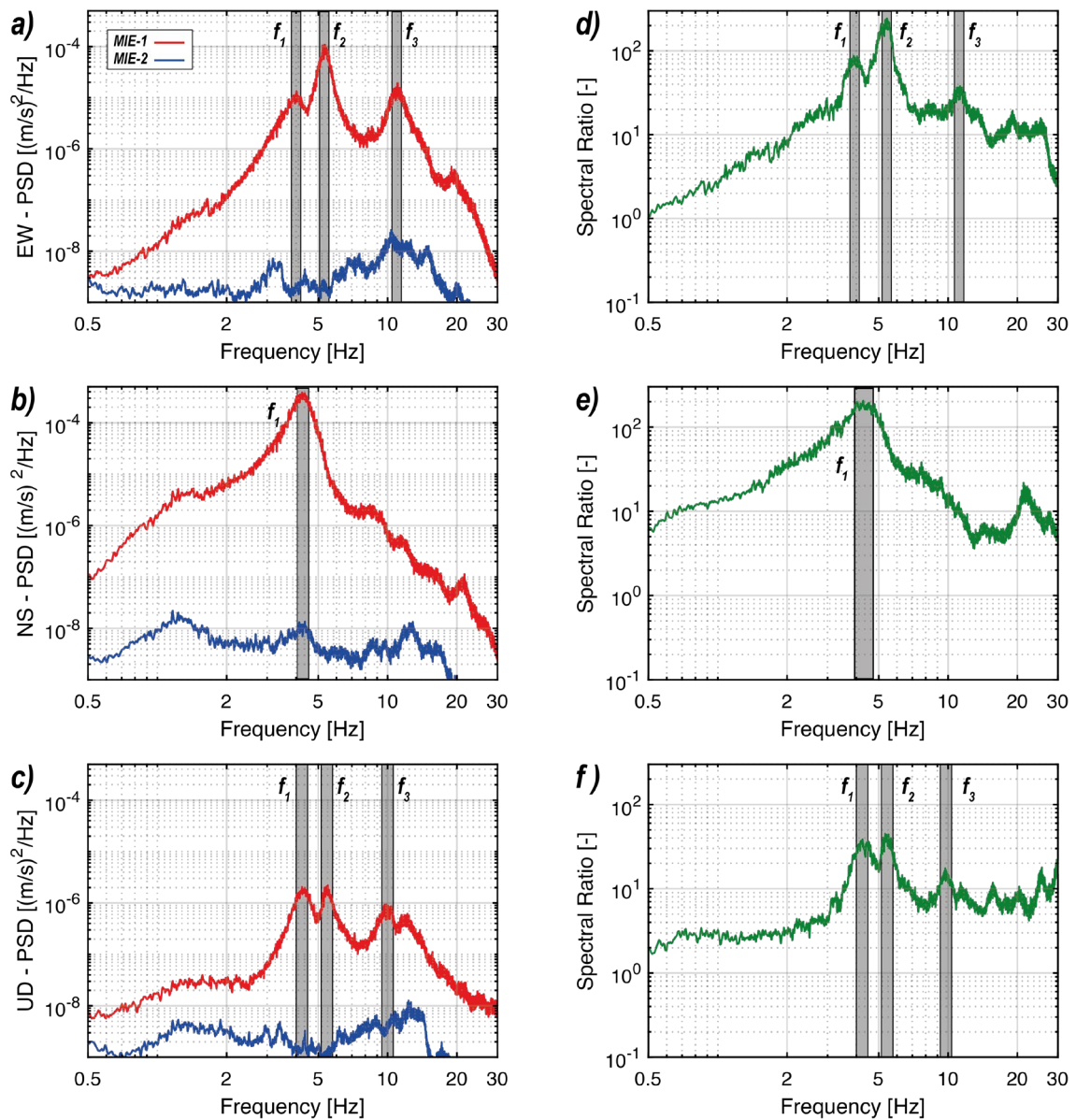


**Figure 4.21.** Results of spectral analysis for the reference station (MIE-2, in blue) and the active station (MIE-1, in red) located on the arch (a, c, e) and SRSR (site-to-reference spectral ratio, in green) computed for each component of ground motion (b, d, f): EW component (a, b), NS component (c, d), UD component (e, f). Gray bands highlight the three spectral peaks ( $f_1$ ,  $f_2$ ,  $f_3$ ) interpreted as resonance frequencies of the Wied II-Mielań arch.

The analysis of polarization attributes of ambient seismic noise carried out through the WAVEPOL code (Burjáněk et al., 2012, 2010) confirms the characteristic features observed from PSDs and SRSRs. The clear distinction between the polarization attributes of ambient noise at the two stations is well represented by the polar plots of Figure 4.22. The reference station (MIE-2) shows no significant polarization of particle motion within the entire analyzed frequency range (2–20 Hz), with constant values of ellipticity in the range 0.4–0.5 (Figure 4.22a) and only a slight azimuthal directionality N-S oriented around 2–4 Hz, and

NE-SW oriented at 6 Hz and 12Hz (Figure 4.22c) and mostly concentrated in the horizontal plane (Figure 4.22e). These results, together with the outcomes of spectral analysis, which showed the absence of spectral peaks relating to the dynamic behavior of the arch, corroborate the hypothesis that MIE-2 can be considered an affordable reference site.

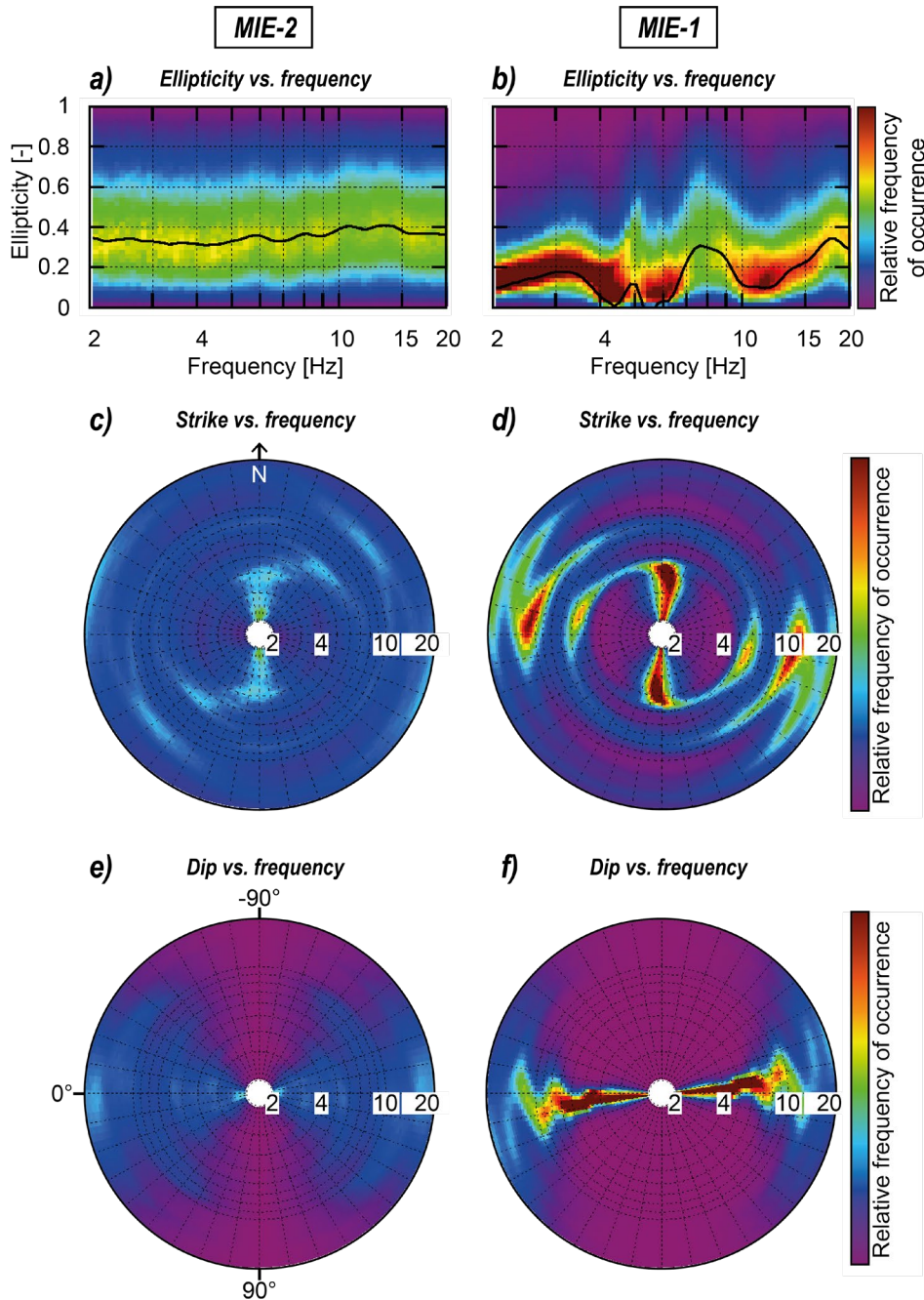


**Figure 4.22.** Results of polarization analysis for the reference station (MIE-2) and the active station (MIE-1) located on the arch; colormaps are indicative of the relative frequency of occurrence of a specific frequency in the noise recording; plot of ellipticity vs. frequency (a, b); plot of strike vs. frequency – frequencies are represented along the log-scaled radius – (c, d); plot of dip vs. frequency – frequencies are represented along the log-scaled radius (e, f).

On the contrary, MIE-1 highlights a strong polarization of ground motion at specific frequencies and orientations. The particle motion is characterized by marked linearity in the investigated frequency range, with minimum peak values (ellipticity  $\sim 0-0.1$ ) found in correspondence of the three resonance frequencies of the arch ( $f_1$ ,  $f_2$  and  $f_3$ ) (Figure 4.22b). Observing the polar strike plot of Figure 4.22d, the first resonance frequency ( $f_1$ ) is roughly NS-oriented ( $5-10^\circ\text{N}$ ), whereas the second ( $f_2$ ) and third ( $f_3$ ) share an almost identical EW direction of maximum polarization ( $95-105^\circ\text{N}$ ). The clear distinction in the direction of maximum polarization of resonance frequencies agrees with what was already inferred from the computation of PSDs and spectral ratios. Moreover, the polar dip plot (Figure 4.22f) shows an almost constant incidence angle value centered around  $0-5^\circ$ , witnessing the concentration of ground motion in the horizontal plane. With respect to the local setting of the arch, these results indicate that  $f_1$  is oriented parallelly to its major axis, while  $f_2$  and  $f_3$  are perpendicular. This differentiation in the polarization direction of resonance frequencies has already been observed at different sites for 2D rock columns, and rock arches (Bottelin et al., 2013a; Geimer et al., 2020; Lévy et al., 2010; Moore et al., 2016) and may reflect the geometric and geological complexity of this structure. If considering the orientation of the main discontinuities affecting the integrity of the arch,  $f_1$  is perpendicular to J1 and parallel to J2. The opposite attitude is observed for  $f_2$  and  $f_3$  (Figure 4.23).

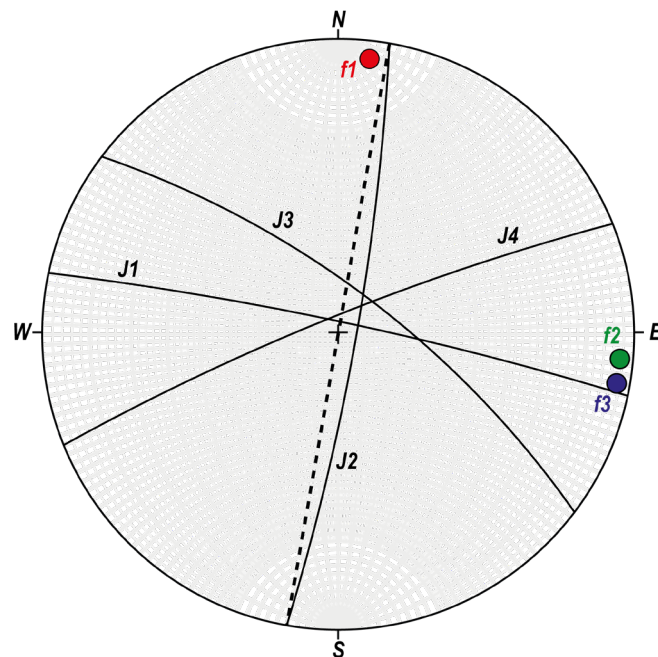


**Figure 4.23.** Stereographic projection (equal-angle, lower hemisphere) representing the comparison between the orientations of the three resonance frequencies ( $f_1$ ,  $f_2$ ,  $f_3$ ) and the main discontinuity sets (J1, J2, J3, J4). The black dashed line indicates the orientation of the major axis of the arch.

Such complex conditions, where the geometry of the rock mass and the discontinuity network may constrain the relative amplification and polarization of vibrations, are not easily interpretable through the analysis of single station measurements, and a higher density array of sensors would be required to understand if the relative amplification and different polarization of resonance frequencies can be related to the influence of main rear discontinuities, as already observed by several authors (Burjánek et al., 2018, 2012; Iannucci et al., 2020b; Kleinbrod et al., 2017). Nevertheless, the results obtained from the comparison between ambient seismic noise recorded at MIE-1 and MIE-2 provided valuable information concerning the dynamic behavior of the arch with respect to a reference site, allowing the clear identification of three resonance frequencies along with their polarization attributes.

The ambient vibration monitoring campaigns carried out by employing the already described microseismic monitoring system were instead focused on studying the relationships and the vibrational behavior of the arch's compartments through the installation of dense arrays composed of one-component microaccelerometers (Figure 4.24). Furthermore, these surveys were scheduled with seasonal recurrence in order to investigate potential changes in the dynamic behavior of the structure in response to different climatic conditions.

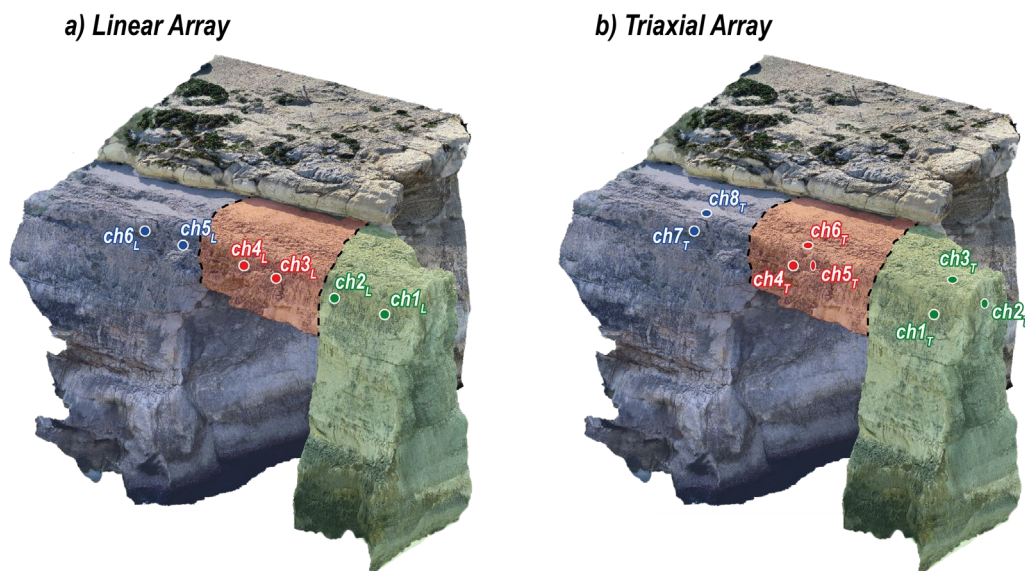


**Figure 4.24.** Summary of the two array configurations employed for ambient seismic noise recordings at the study site. The linear array is composed of six microaccelerometers recording only the EW component of ground motion (a); the triaxial array is composed of 8 microaccelerometers deployed to record all components of ground motion on the pillar (EW – ch1<sub>T</sub>, NS – ch2<sub>T</sub>, UD – ch3<sub>T</sub>) and bridge compartments (EW – ch4<sub>T</sub>, NS – ch5<sub>T</sub>, UD – ch6<sub>T</sub>). Differently, the bedrock sector was instrumented with only two microaccelerometers (EW – ch7<sub>T</sub>, UD – ch8<sub>T</sub>).

---

The results obtained from the spectral analysis of seismic noise recordings acquired using the linear array configuration, recording the EW direction of ground motion, during one of the performed multitemporal surveys are shown in [Figure 4.25](#). The second and third resonance frequencies ( $f_2 \approx 5.4$  Hz and  $f_3 \approx 10.8$  Hz) of the arch clearly emerge on sensors installed in correspondence of the pillar ([Figure 4.25a, b](#)) and bridge compartments ([Figure 4.25c, d](#)). The first resonance frequency ( $f_1 \approx 4.3$  Hz) is only visible in the PSD of  $ch_{2L}$  ([Figure 4.25b](#)), and its presence is interpreted as the consequence of a non-perfect alignment of the microaccelerometer toward E. In contrast, no evidence of spectral peaks potentially related to resonances of the arch are found in the anchored bedrock sector. This outcome is absolutely non-trivial if considering the relatively small aperture of the array ( $\sim 40$  m), and might be indicative of a strong attenuation effect along the direction of the arch.

It is interesting noting that the spectral amplitude of  $f_2$  and  $f_3$ , which are not casually the most evident frequencies in PSDs since all sensors measured the EW component of ground motion, shows marked and opposite variations from the pillar to the bridge sectors.

The spectral amplitudes of  $f_2$  are found to be the highest at  $ch_{1L}$  and  $ch_{2L}$ , while they strongly decrease moving toward  $ch_{4L}$ , located in the central part of the bridge compartment. In contrast,  $f_3$  is characterized by an opposite behavior, with maximum spectral amplitudes that are concentrated in correspondence of  $ch_{3L}$  and  $ch_{4L}$  and that progressively decrease toward the outermost part of the arch.

Similar results were obtained analyzing the ambient noise recordings collected employing the triaxial array configuration, which also allowed considering the NS and UD components of ground motion. Unfortunately, due to the unavailability of nine microaccelerometers, the stable sector of the arch (i.e., the anchored bedrock) was instrumented with only a couple of sensors measuring the EW and UD components. The results of spectral analysis are presented in [Figure 4.26](#).

The same marked spatial differentiation of the spectral amplitudes of  $f_2$  and  $f_3$  is particularly visible from the observation of PSDs computed for channels measuring the EW component and located on the three sectors of the arch ([Figure 4.26a, d, g](#)). On the contrary,  $f_1$  does not show the same attitude.

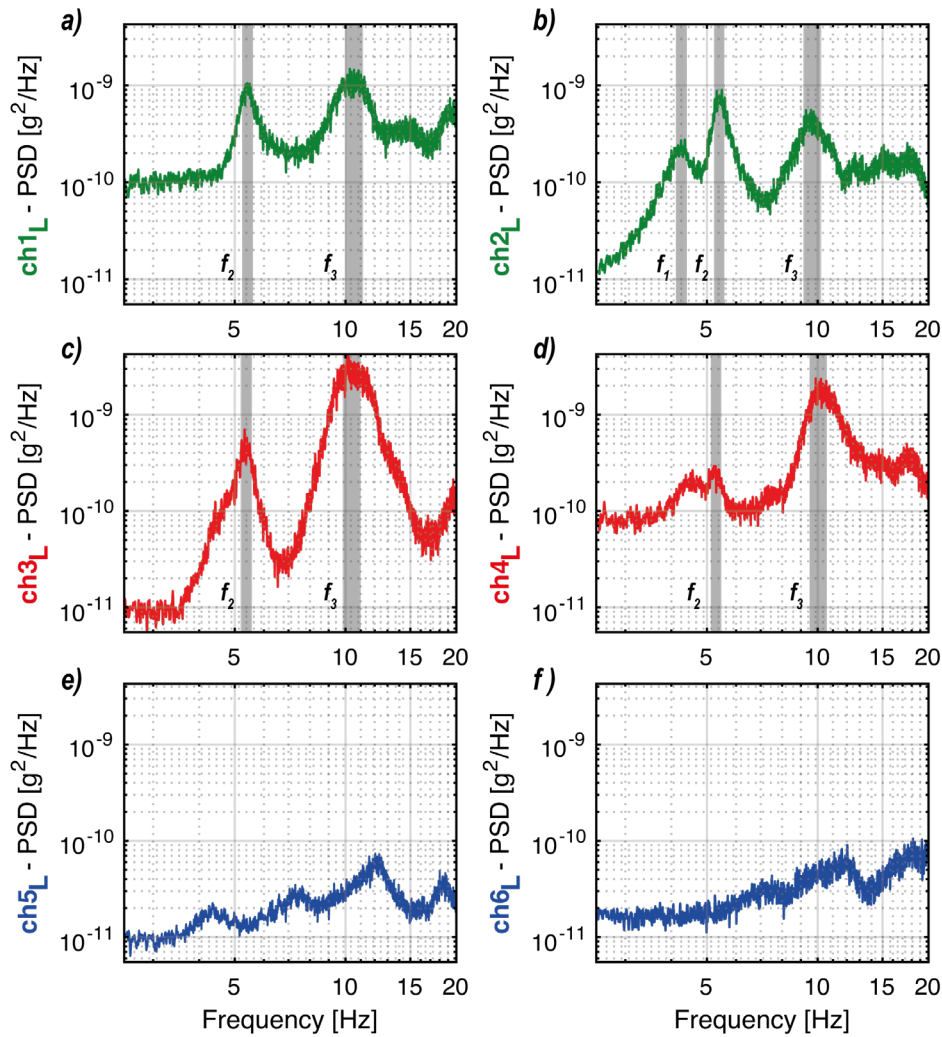


**Figure 4.25.** Results of spectral analysis for each channel of the linear array: hourly power spectral densities (PSDs) for channels located in correspondence of the pillar (**a**, **b** – in green), of the bridge (**c**, **d** – in red) and of the bedrock (**e**, **f** – in blue) compartments. Gray bands highlight the three spectral peaks ( $f_1$ ,  $f_2$ ,  $f_3$ ) interpreted as resonance frequencies of the arch.

Although the NS component of ambient vibrations was not recorded on the stable sector of the arch, if considering only the PSDs of channels located on the pillar (**Figure 4.26b**) and bridge (**Figure 4.26e**) compartments, the spectral peak related to  $f_1$  does not highlight any remarkable variation, as it is instead found for both  $f_2$  and  $f_3$ .

The PSDs of vertical components of ground motion are also presented for completeness (**Figure 4.26c**, **f**, **i**), and even though they allow observing all three resonance frequencies of the arch, they were not further considered because showed the greatest disturbances during all monitoring campaigns. The poor quality of the recordings acquired by these channels probably derives from a not perfect coupling of microaccelerometers to the surface of the arch.

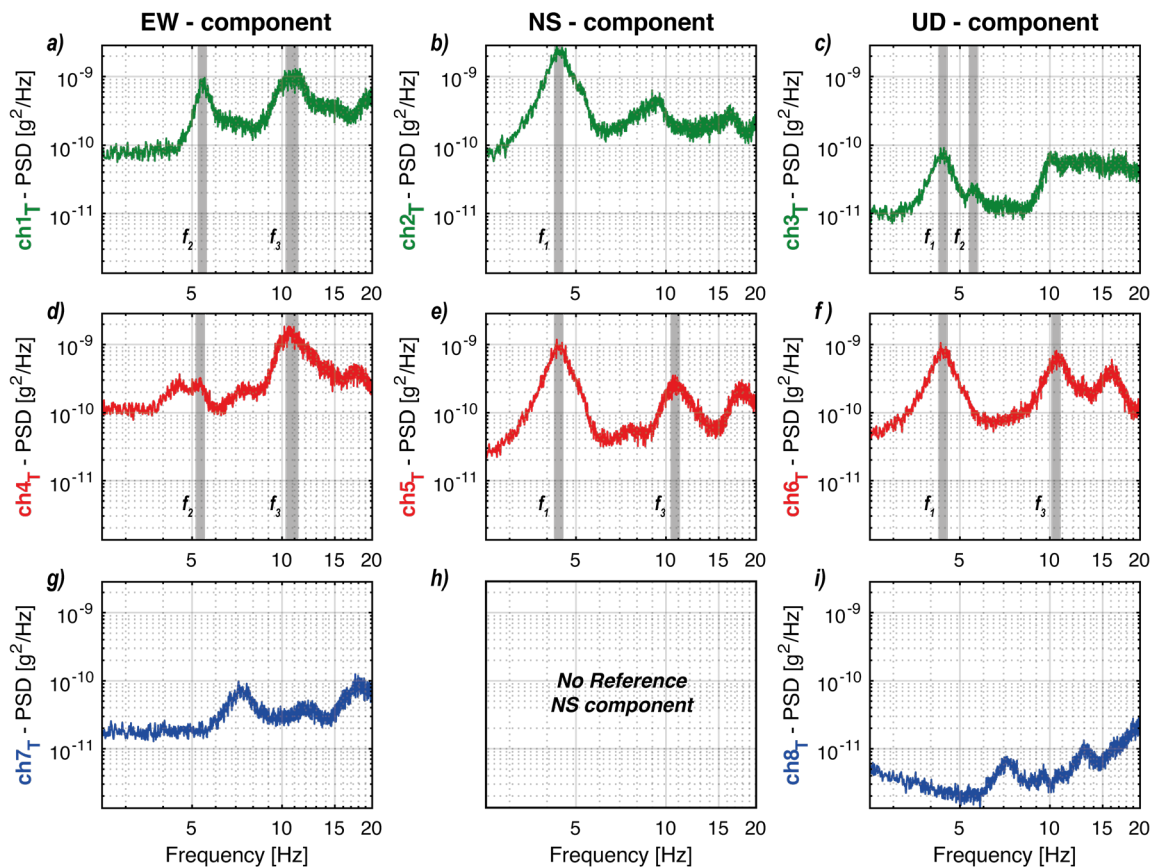


**Figure 4.26.** Results of spectral analysis for each channel of the triaxial array: hourly power spectral densities (PSD) for channels located in correspondence of the pillar (**a**, **b**, **c** – in green), of the bridge (**d**, **e**, **f** – in red) and of the bedrock (**g**, **i** – in blue) compartments. The NS component of ground motion was not recorded in correspondence of the bedrock sector. Gray bands highlight the three spectral peaks ( $f_1$ ,  $f_2$ ,  $f_3$ ) interpreted as resonance frequencies of the arch.

The results of the spectral analysis performed on ambient vibration data collected by the microseismic monitoring network well reproduce the same spectral features observed from MIE-1. Moreover, since multiple sensors were deployed in a dense array configuration spanning from the stable rock cliff to the freestanding rock pillar, they provide a more detailed characterization of the dynamic behavior of different partially detached compartments of the arch.

The observed spatial variation of resonance frequencies spectral amplitudes (i.e., from the pillar to the anchored bedrock) might be indicative of a complex dynamic behavior that could be resulting from the interaction between the extreme geometry of the arch and the major discontinuities dissecting its structure.

In particular, the absence of spectral peaks related to resonance frequencies on PSDs of sensors installed in proximity of the arch represents an unexpected result.

It is well known that in particular geological contexts the discontinuity-driven attenuation of surface waves can arise even in very short distances, especially when intensely fractured and dislodged rock slopes close to collapse are concerned and where site effects can be regarded as primary indicators of the instability conditions (Burjánek et al., 2012; Iannucci et al., 2020b; Moore et al., 2011a), but still some evidence of resonance frequencies of the arch was expected.

To better comprehend the local response and the relative amplification of ground motion within the structure of the arch, SRSRs were computed considering the linear array of microaccelerometers. The same analysis was not performed for the other adopted configuration (i.e., triaxial) because it does not guarantee a dense distribution of measuring station along the arch. Since no evidence of resonance frequencies were found at ch6<sub>L</sub>, this sensor was deemed to be a good reference station even if it is located in proximity of the arch. Therefore, all power spectral densities computed at the five “active” stations were normalized to this reference station.

The results of SRSR analysis for the monitoring campaign of February 2020 are presented in [Figure 4.27](#). From the observation of normalized amplitude spectra ([Figure 4.27a](#)) and relative amplification functions ([Figure 4.27b](#)), it is apparent the already discussed variation of f2 and f3 spectral intensities with respect to the different sectors of the arch.

Concerning f1, the highest peak of amplification functions reaches a factor of 7.1–7.2 in correspondence of the outermost sector of the arch pillar (ch1<sub>L</sub>, ch2<sub>L</sub>), while moving inland the amplification of ground motion tends to decrease almost linearly, ranging from 4.7–5.7, in the central sector of the arch, to none amplification effects at ch5<sub>L</sub>. Differently, f3 reaches an amplification factor of 9.6 and 7.6 at station ch3<sub>L</sub> and ch4<sub>L</sub> respectively, thus in correspondence of the central compartment or the rock bridge. The distribution of relative amplification of f3 on the arch seems to produce a complex spatial pattern. However, it is worth considering that this overall complexity is probably vitiated by an installation issue concerning station ch2<sub>L</sub>. In fact, as previously introduced, this sensor suffers from a non-perfect alignment toward E and for this reason the relatively low amplification factor observed (3.2) might be not reliable. SRSRs further confirm the results of spectral analysis, highlighting the marked spatial differentiation of amplification factors at f2 and f3 throughout the whole length of the arch.

---



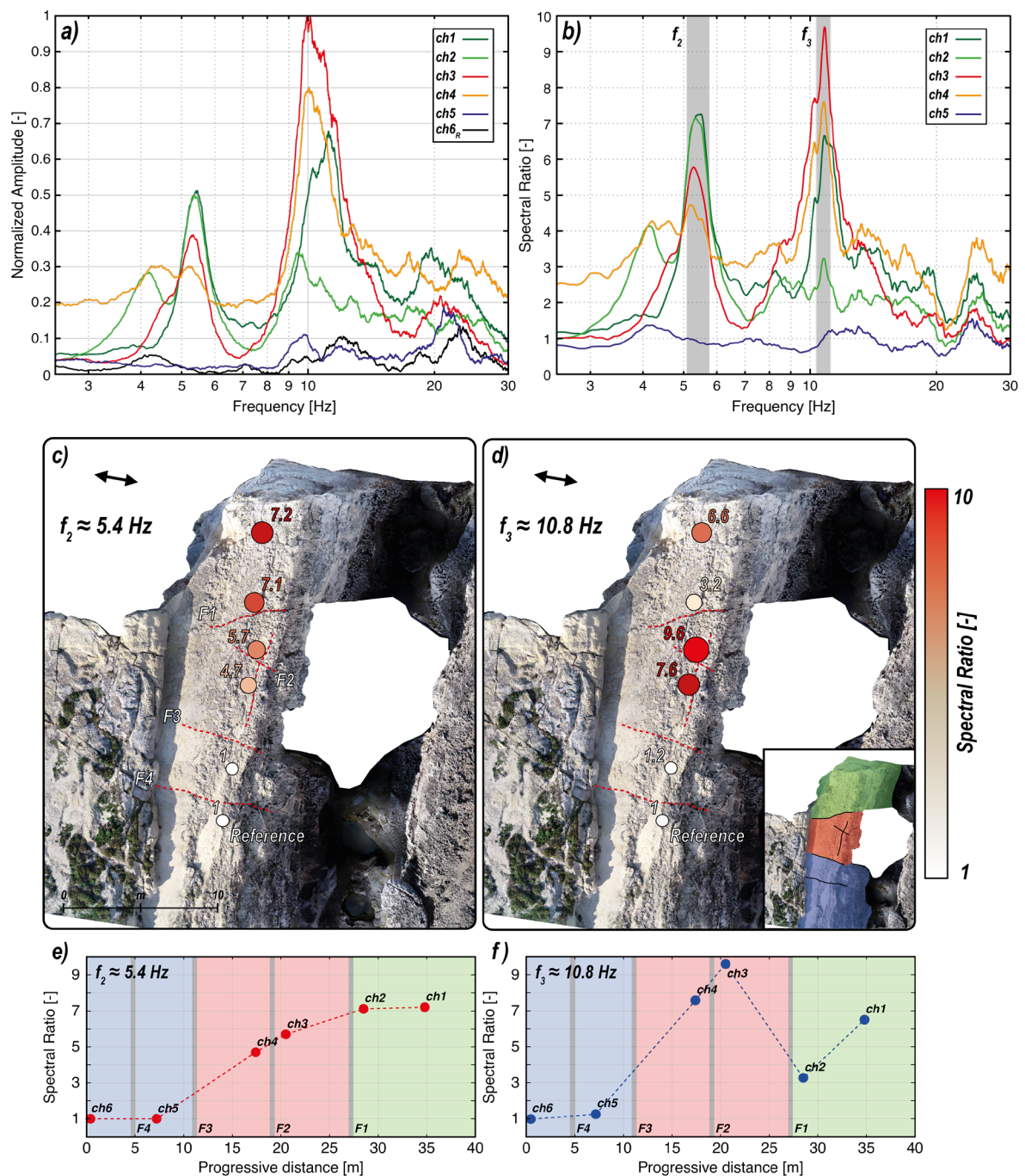


**Figure 4.27.** Results of SRSR (site-to-reference spectral ratio) analysis considering the linear array of one-component microaccelerometers deployed on the Wied Il-Mielah arch (see **Figure 4.24**). Normalized amplitude spectra (**a**), and spectral ratios computed between ch1–ch5 and the reference sensor ch6 (**b**). Gray bands highlight two of the three resonance frequencies of the arch ( $f_2$  and  $f_3$ ). Spatial distribution of spectral ratios at  $f_2 = 5.4$  Hz (**c**, **e**) and  $f_3 = 10.8$  Hz (**d**, **f**) (black arrows describe the direction of maximum polarization for  $f_2$  and  $f_3$ ). The size and color of each point varies according to the relative amplification factor. In panel **e** and **f**, the amplification factor at each measuring channel is plotted against the progressive distance between ch6 ( $x = 0$  m) and the external boundary of the arch ( $x = 40$  m), where the relative position of main discontinuities (F1–F4) is also reported. The distinction between the three sectors of the arch is defined by the three colored areas: anchored bedrock – blue, rock bridge – red, rock pillar – green.

The relative amplification factors provide an estimate of how much a structure is free to vibrate, and the values obtained for  $f_2$  and  $f_3$  on the two protruded sectors of the arch with respect to the stable cliff might be regarded as strictly dependent on the geological setting and morphological features of the arch itself.

When dealing with fractured rock slopes, amplification factors around 4 are in general considered typical indicators of general weakened conditions, mostly deriving from major discontinuities separating different compartments, whereas higher values can be associated to prone-to-fall conditions (Kleinbrod et al., 2017).

In the specific context of the investigated arch, the same observations cannot be immediately transposed. In fact, different from natural rock slopes, which are mostly characterized by 1D or 2D laterally bounded geometries, the extreme 3D geometry of the arch is certainly responsible for a higher degree of mobility that could be invoked to explain the observed amplifications with respect the stable cliff.

However, the role played by discontinuities cannot be completely neglected since, how can be observed from [Figure 4.27](#) (panels c–f), the distribution of amplification factors follows a spatial pattern that seems to find correspondence with the location of major discontinuities (F1–F4) dissecting the arch ([Figure 4.27e, f](#)). Such a complex pattern of amplification factors might reflect the internal subdivision of the arch in partially dislodged compartments, or even smaller rock volumes, that could be capable of inducing marked amplifications of ground motion in virtue of their higher mobility.

However, the comprehension of the contribution of discontinuities on the observed distribution of amplification factors is not easy to discern, and further analysis are required in order to strengthen this hypothesis. In particular, the detailed characterization of subsurface conditions of the arch may provide valuable information on the persistence of fracture in depth, allowing for a better evaluation of its structural integrity.

The temporal evolution of power spectral densities was analyzed for all performed monitoring surveys in order to further improve the investigation of resonance frequencies of the Wied II-Mielah sea arch. Several authors have already observed that environmental factors, especially temperature fluctuations, can exert a strong control on the dynamic behavior of rock masses mainly determining cyclic variations of fundamental frequency

---

values both at daily and seasonal scales (Bottelin et al., 2013a; Colombero et al., 2018a; Starr et al., 2015). Therefore, ambient seismic noise data collected by the microseismic monitoring network and the MIE-1 station were further processed with the objective of understanding if the same dynamic response to environmental factors could be observed at the site.

The results obtained from the computation of the 54 hourly power spectral densities at MIE-1 during the three-day survey of February 2020 are presented in [Figure 4.28](#) for all components of ground motion. These plots, representing the time-frequency evolution of ambient seismic noise intensity, were constructed by stacking each hourly computed PSD in the frequency range from 2 to 20 Hz. They were also normalized to their maximum value to enhance the identification of temporal trends of resonance frequencies. By observing the temporal evolution of PSDs, the three resonance frequencies of the arch markedly emerge during the entire monitoring period.

As expected, the arch's fundamental frequency ( $f_1$ ) is dominant on the NS component and centered around 4.5 Hz ([Figure 4.28a](#)), whereas no evidence of  $f_2$  or  $f_3$  is found. These two higher resonance frequencies ( $f_2 = 5.5$  Hz and  $f_3 = 10.5$  Hz) are instead found on the EW and UD components ([Figure 4.28b, c](#)). Differently from horizontal components, the vertical component is able to jointly show the evolution in time of all the three resonance frequencies, even if their normalized spectral amplitude tends to vary between different days. No sharp spectral peaks concentrated in very narrow frequency bands are observed, witnessing the absence of disturbances deriving from anthropic sources in proximity of the study area.

Although recordings are affected by two 12-hour long gaps, it is possible noting that all three resonance frequencies show not negligible fluctuations at the daily scale. This phenomenon can be better framed through the observation of [Figure 4.29](#), where the same plots are presented with the only difference that frequency axes are centered around the average value of each resonance frequency to enhance frequency shifts.

Moreover, the evolution of rock surface temperatures ([Figure 4.29d](#)), relative humidity, and wind speed ([Figure 4.29e](#)) is also reported to provide a comparison between environmental factors and frequency fluctuations. Within this two-day monitoring window, all three resonance frequencies exhibit significant cyclic variations.

---

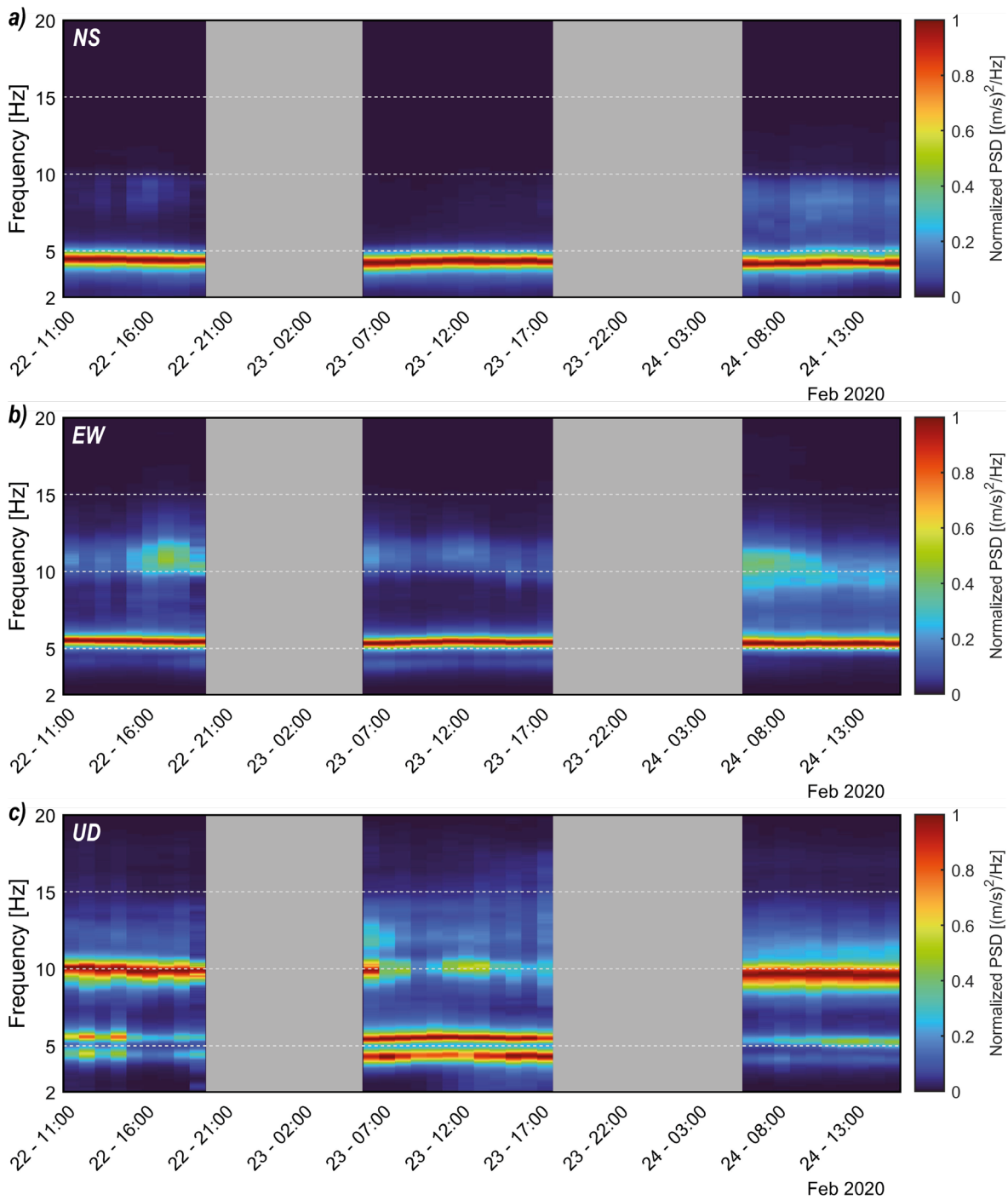


**Figure 4.28.** Temporal evolution of the 54 hourly normalized power spectral densities (PSDs) recorded at the MIE-1 station during the monitoring campaign of February 2020 for the NS (a), EW (b) and UD (c) components. PSDs were hourly normalized to their maximum value to better follow their temporal evolution. Two 12-hour gaps are present in the recording and are highlighted by gray bands.

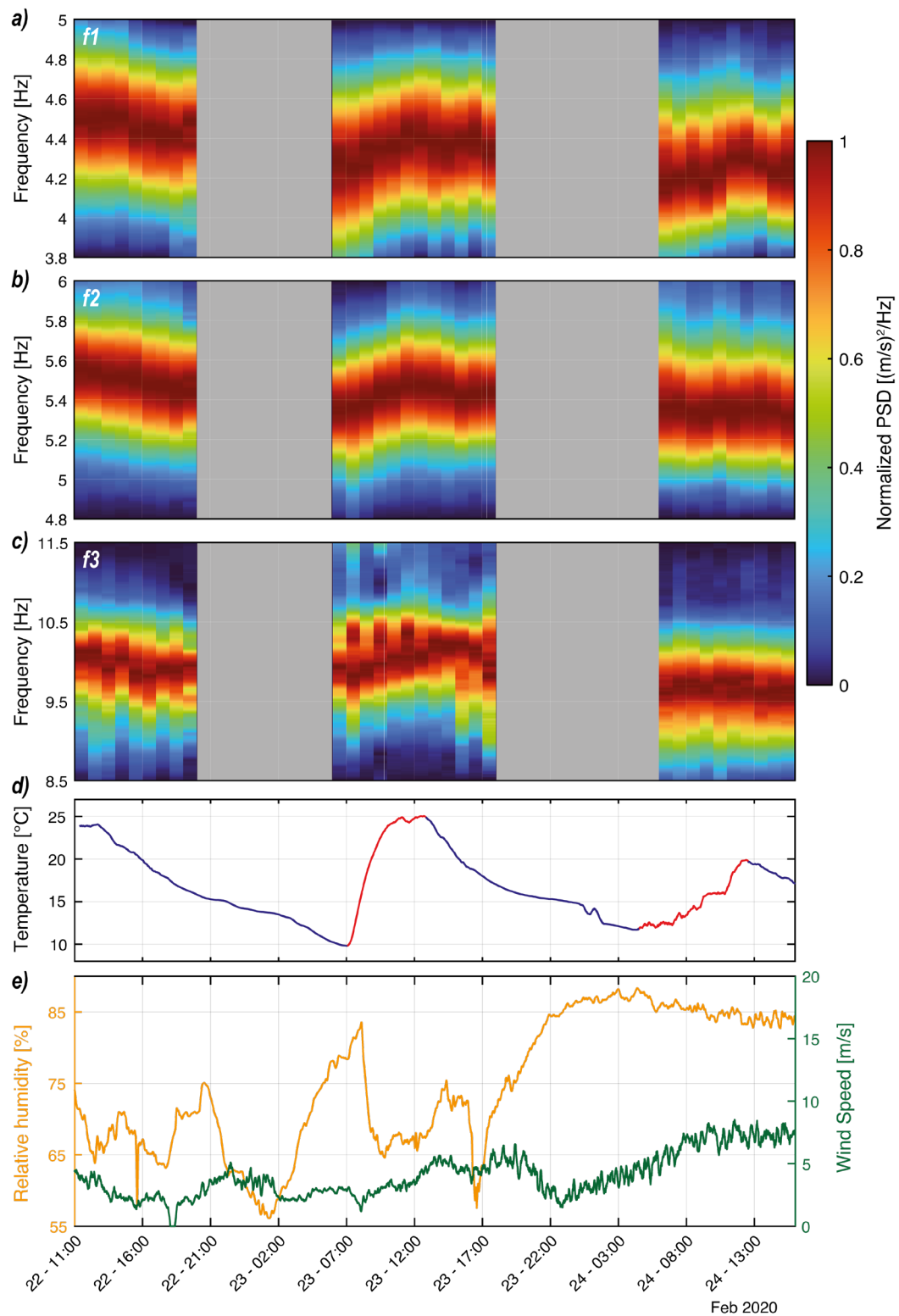


**Figure 4.29.** Temporal evolution of hourly normalized power spectral densities (PSDs) centered on the three identified resonance frequencies of the arch –  $f_1$  (a),  $f_2$  (b) and  $f_3$  (c). 10-minute averaged rock temperatures recorded at the surface of the arch (d). 10-minute average relative humidity (yellow line) and wind speed (green line) recorded by the weather station located in proximity of the arch. PSDs were normalized to their maximum value in each frequency band to better follow their temporal evolution. Two 12-hour gaps are present in the recording and are highlighted by gray bands.

The presence of long gaps in recordings does not allow quantifying the peak-to-peak amplitude of such oscillations, but still an estimate of this amplitudes can be retrieved by considering the evident increasing trend between 07:00 and 12:00 of February 23th (central section of [Figure 4.29](#)). The first two resonance frequencies show a similar behavior in terms of trend and amplitude:  $f_1$  linearly varies from 4.25 to 4.42 Hz ( $\Delta f = 0.17$  Hz), and  $f_2$  replicates the same trend varying from 5.33 to 5.46 Hz ( $\Delta f = 0.13$  Hz). In contrast,  $f_3$  is characterized by the greatest shift, with a net increase of almost 0.5 Hz from 9.8 to 10.3 Hz.

An evident in-phase correlation of resonance frequencies daily changes can be observed with rock temperatures, while no direct relationships are apparent if considering other environmental parameters. This correspondence between temperature highlights the strong control exerted by temperature fluctuations on the dynamic behavior of the arch. This mechanism can be interpreted as deriving from the cyclic contraction and expansion of the rock mass driven by the superposition of heating and cooling phases. As it can be observed by [Figure 4.29](#), the increase of temperatures causes resonance frequencies to increase as well, probably due to a closing of the fractures that isolate the different compartments of the arch. Then, the increase in fracture closing during heating phases of the arch might be responsible for the stiffening of the entire structure that causes resonance frequencies to increase. On the contrary, the decrease of temperatures causes the opposite effect: the thermal contraction of the rock mass determines the opening of fractures and the consequent loss in contact stiffness between the sectors of the arch, which eventually results in a decrease of resonance frequencies values.

Based on the available data, a cross-correlation analysis was conducted to provide a quantitative connotation to the observed in-phase relationship between temperature and resonance frequencies fluctuations. Cross-correlation is a statistical operator that allows assessing the degree of similarity between time series and estimates their offset in terms of temporal lags. The daily variations of resonance frequencies and surface temperatures were analyzed following the approach proposed by (Colombero et al., 2021b). At first, both data sets were demeaned, detrended, and normalized to their average value to filter daily effects. Then, they were interpolated with sine curves to eliminate scattered trends and enhance the overall periodicity of frequencies and temperatures. The result of this preprocessing step is shown in [Figure 4.30](#) (panels d–f), along with the relative R-square values to provide the estimate of the fitting goodness. The best fittings were obtained for  $f_1$ ,  $f_2$ , and temperature

---

data (R-square > 0.9), while the interpolation of f3 gave poor quality results (R-square = 0.71).

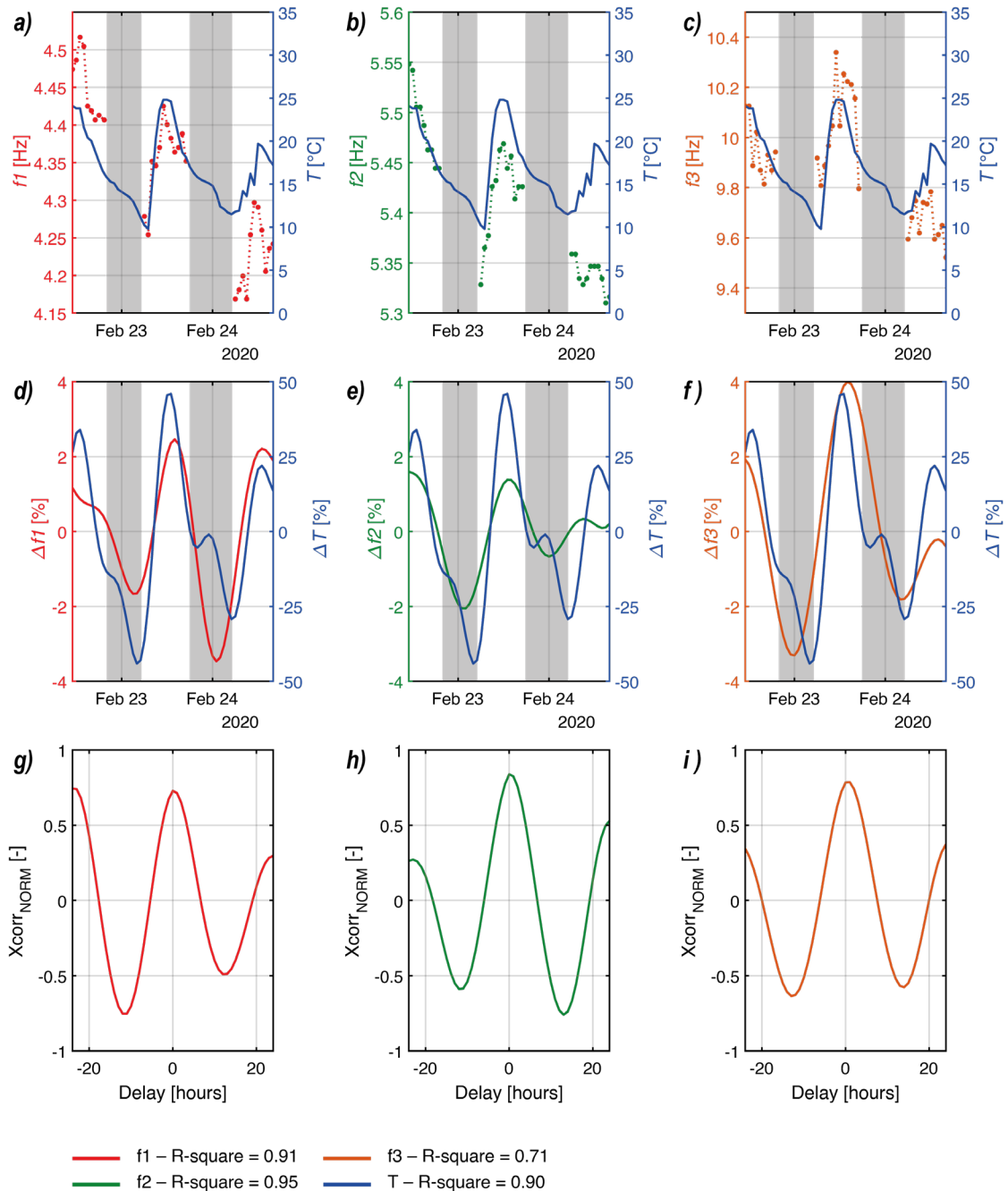


**Figure 4.30.** Results of cross-correlation between the three resonance frequencies of the arch and rock surface temperatures at the daily scale. Comparison between the temporal evolution of f1, f2 and f3 and rock surface temperatures (a–c). Results of the sine curves fitting on raw data (e–f). Normalized cross-correlograms for each resonance frequency (g–i).

It must be noted that sine interpolants cannot be considered reliable in reproducing the timing of negative peaks for f1, f2, and f3 since they anticipate the corresponding negative

temperature peak. This issue is strictly related to the discontinuity of recordings, since nighttime gaps do not allow following the evolution of resonance frequencies in response to decreasing temperatures.

The normalized cross-correlograms of each resonance frequency show maximum positive peaks in correspondence of 0-hours delays (Figure 4.30g–h). Despite the discontinuity of data and the related issues, the obtained results well reproduce what was qualitatively observed from Figure 4.29. However, continuous recordings over longer monitoring time windows can provide more complete datasets for a more robust estimate of delays between the considered parameters.

The same analysis concerning the temporal evolution of PSDs was performed on data collected by the microseismic network during the four seasonal monitoring campaigns. Although multiple sensors were deployed on the arch during all surveys, most of them suffered recurrent disturbances and malfunctioning, probably deriving from the adverse environmental conditions to which they were exposed. The only sensors that recorded almost undisturbed traces are  $ch1_L$  and  $ch6_L$  of the linear array, and  $ch2_T$  of the triaxial array (Figure 4.24). Fortunately, these sensors allowed to analyze the temporal evolution of both  $f1$  and  $f2$  since they measured the EW and NS components of ground motion.

The results obtained by the computation of PSDs for the abovementioned sensors over all monitoring surveys are presented in Figure 4.31 for  $f2$ , and in Figure 4.32 for  $f1$ . The same in-phase correlation between resonance frequencies and temperature changes can be inferred at the seasonal scale. The value of first resonance frequency ( $f1$ ) shows a cyclic behavior characterized by a progressive increase from 4.1 Hz (in winter) to 5.7 Hz (in summer) and a subsequent decrease to 4.4 Hz after exactly one annual thermal cycle (Figure 4.32a). This trend perfectly matches the seasonal variation of recorded temperatures, thus evidencing a perfect in-phase correlation with the thermal conditions at the site, which are as well characterized by mean temperature values following the same annual cyclicity (Figure 4.32b).

The same observations can be transposed to  $f2$ , which shows an identical evolutionary pattern with average frequency values ranging from 5.4 Hz (in winter) to 6.3 Hz (summer) (Figure 4.31).

---



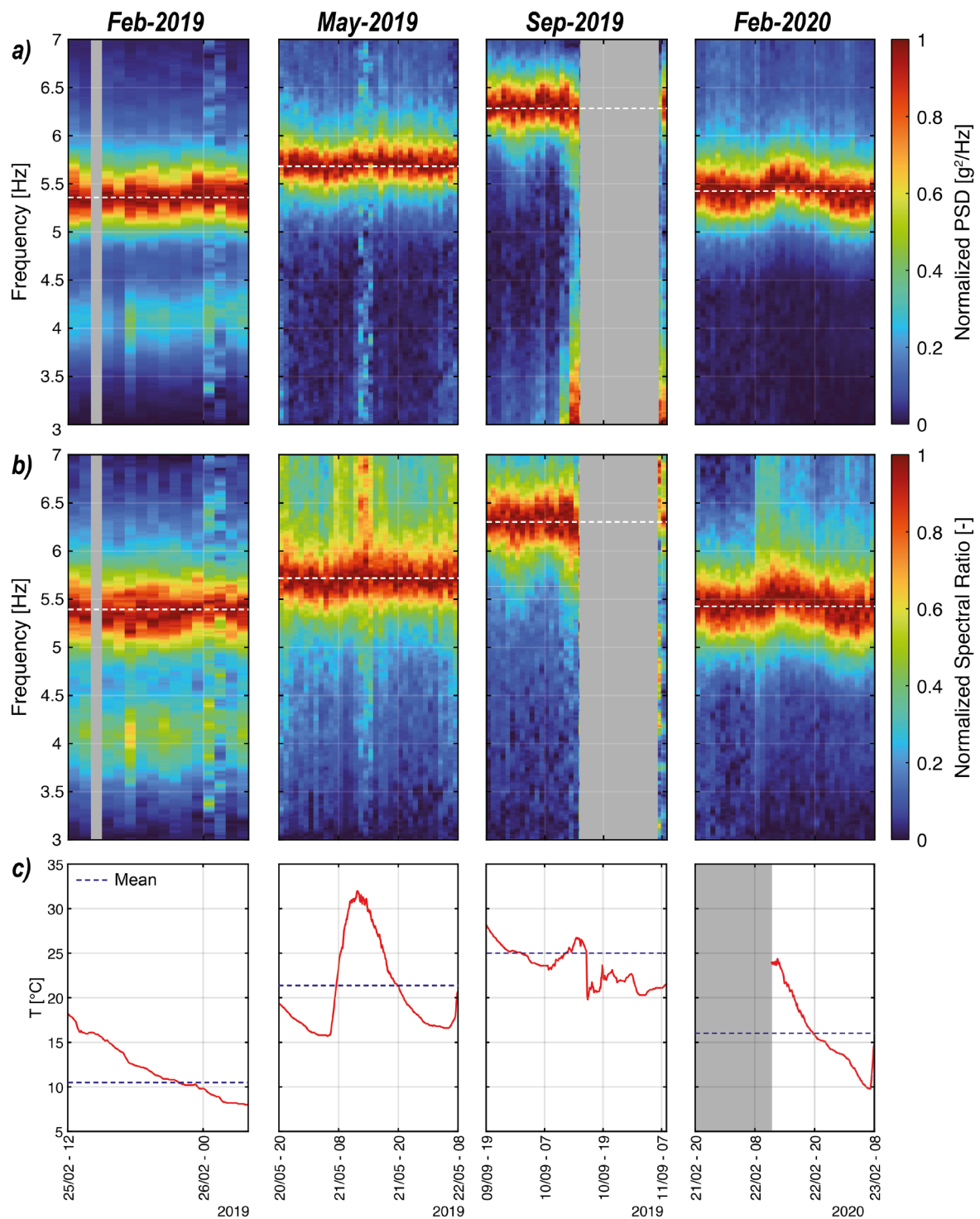


**Figure 4.31.** Temporal evolution of hourly normalized power spectral densities (PSDs) (a) and site-to-reference spectral ratios (SRSRs) (b), centered around  $f_2$ , during the four monitoring campaigns conducted from February 2019 and February 2020. Evolution of rock surface temperatures recorded at the site, where blue dashed lines indicate the mean value computed over the considered monitoring period (c). PSDs in panel a were computed for ch1 of the linear array, located on the pillar sector of the arch, and SRSRs in panel b were compiled considering ch6 of the same array as the reference station. Gray bands highlight time gaps in the recordings due to instrumental malfunctioning.

Besides, the SRSRs computed between the rock pillar (i.e., ch1L) and the reference bedrock (i.e., ch6L) highlight the same seasonal increasing and decreasing trend of  $f_2$  in response to different thermal boundary conditions (Figure 4.31b, c). Cross-correlation analyses were performed by considering seasonal fluctuations of resonance frequencies and temperatures following the already described approach used for analysis at the daily scale. Since the amount of data collected in the framework of this work was not sufficient to characterize the annual cycle, two 1-hour single station measurements performed at the Wied Il-Mielaħ site in June and October 2018 were analyzed.

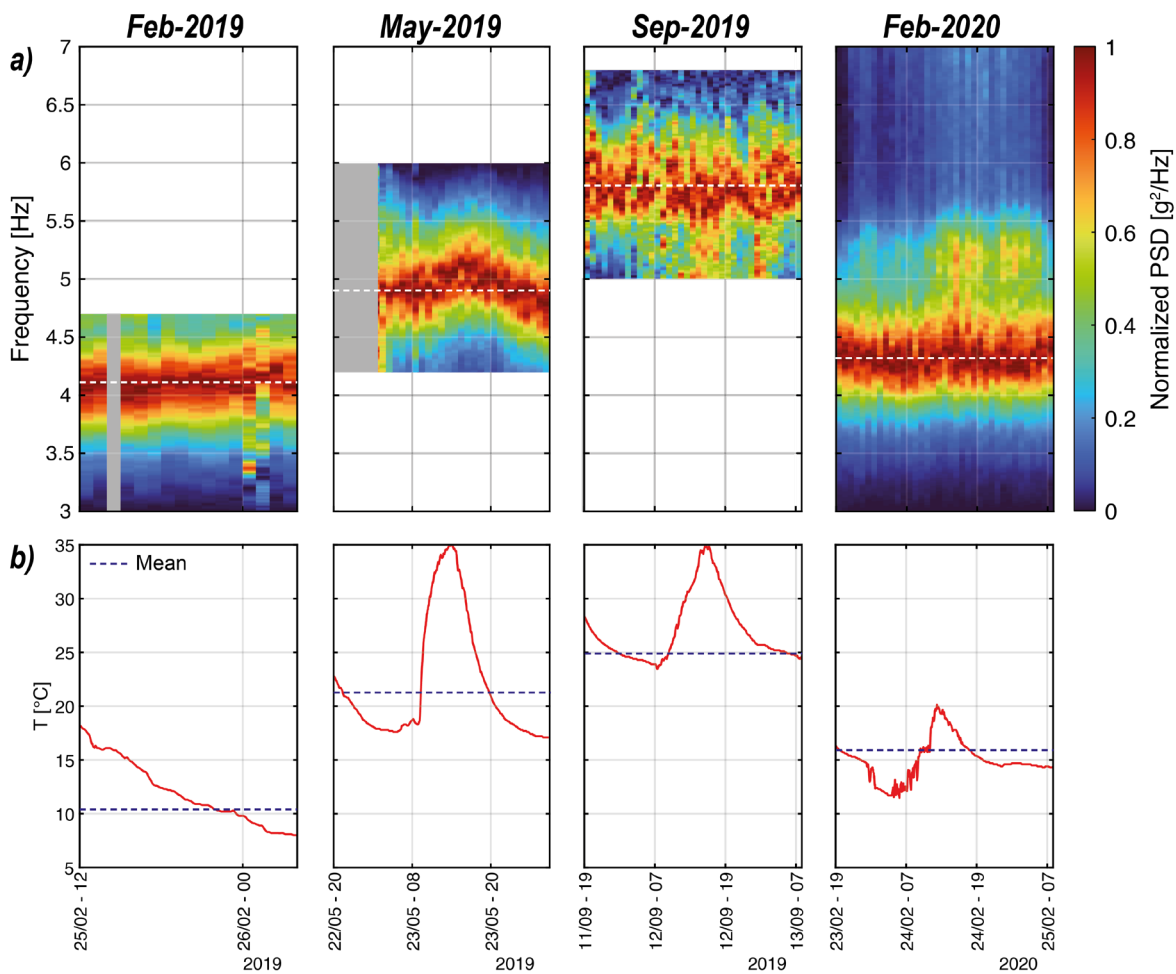


**Figure 4.32.** Temporal evolution of hourly normalized power spectral densities (PSDs) (a) centered around  $f_1$ , during the four monitoring campaigns conducted from February 2019 and February 2020. Evolution of rock surface temperatures recorded at the site, where blue dashed lines indicate the mean value computed over the considered monitoring period (b). PSDs were computed for ch2 (NS component) of the triaxial array installed on the pillar sector of the arch. The PSDs of all monitoring campaigns are bandpass filtered around  $f_1$  to enhance the recognition of its temporal evolution, with the exception of February 2020, because several spectral disturbances influenced lower and higher frequencies. Gray bands highlight time gaps in the recordings due to malfunctioning of the monitoring systems.

By proceeding this way, it was possible to reconstruct a discontinuous, yet reliable, temporal evolution of  $f_1$  and  $f_2$  in different seasons spanning from summer 2018 to winter 2020. At the same time, the lack of continuous temperature time series at the site forced us to consider mean monthly air temperatures for characterizing the seasonal variability of climatic conditions. The results of cross-correlation confirm the perfect in-phase relationship between resonance frequencies and temperature fluctuations, highlighting delays comprised between 0 and 1 month for both  $f_1$  and  $f_2$  (Figure 4.33).

It is worth noting that such values must be carefully interpreted and treated as a pure estimates, since they are certainly vitiated by the limited number of samples considered. Even though no irreversible modifications of  $f_1$  and  $f_2$  can be detected from the analyzed dataset, the observed peak-to-peak amplitude of the resonance frequencies seasonal change is considerable, with  $f_1$  and  $f_2$  that varied by almost  $\sim 30\%$  and  $\sim 16\%$ , respectively.

However, these results suggest that the investigated arch is highly responsive to the periodical variation of temperatures at both the daily and seasonal scale. This immediate response might highlight the role played by fractures in controlling its thermomechanical and dynamic behavior. In fact, if comparing the obtained results with other case studies in literature, the in-phase correlation characterized by none or very short delays between fundamental frequencies and temperature changes is commonly considered to be driven by a major contribution of fractures (Colombero et al., 2018a, 2021b, 2021a).

If considering the classification of the thermally-induced mechanisms at the base of the wandering of fundamental frequencies proposed by (Colombero et al., 2021b), the here observed behavior of the arch may be explained as the combination of a surface-effect (SE) and a fracture-effect (FE) acting on different temporal scales.

The Surface-effect, also defined as stress-stiffening by Starr et al. (2015), might be dominant at the daily scale. In fact, the daily fluctuation of temperatures is able to cause modifications in the stress conditions of the shallowest layers of rock masses (i.e., thermal active layer), which eventually determines increased grain contact stresses, closure of microcracks and differential expansions and contractions between the rock surface and bulk. The result is a zero-lag, in-phase variation of resonance frequencies with temperatures. Such effect is particularly evident at the daily scale since the short period of thermal fluctuations does not allow near-surface heat fronts to penetrate in depth.

---

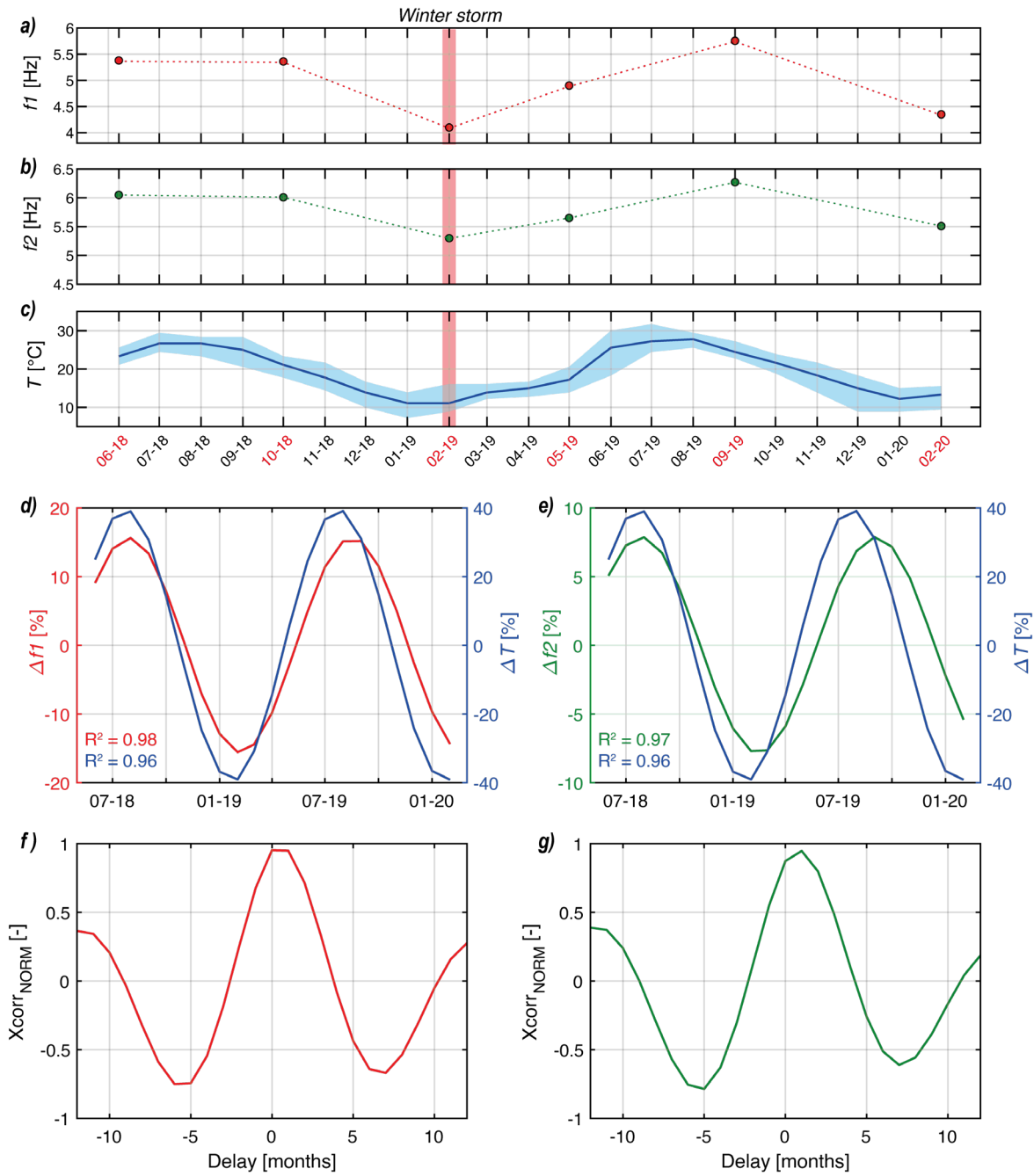


**Figure 4.33.** Results of cross-correlation of  $f_1$  and  $f_2$  with air temperature at the seasonal scale. The temporal evolution of  $f_1$  (a) and  $f_2$  (b) from June 2018 to February 2020 was compared to mean monthly air temperature time series (c) extracted from the database of the permanent weather station of the International Luqa Airport (Malta). Results of the sine curves fitting on raw data (e–f). Normalized cross-correlograms for each resonance frequency (g–i). The red bands in panels a–c highlight the monitoring campaign during which during which a violent storm invested the entire Maltese Archipelago.

However, open rear fractures may host air circulations allowing temperatures to vary at greater depths than the thermal active layer, causing rock thermal expansion and contractions that may drive as well the increase and decrease in resonance frequencies

values. Based on the available data, which are discontinuous and lack direct measurements of deformations and temperatures inside open joints, the contribution operated by fractures to the observed variation of resonance frequencies cannot be easily discerned at the daily scale. In contrast, if considering the seasonal fluctuations of near-surface temperatures, which cause the deepening of the thermal active layer in virtue of their longer period, the role of discontinuities in constraining the dynamic behavior of the arch becomes more evident. In the ideal case of a continuous rock medium and according to [equation 1.4](#) (see [Section 2.2](#)), a decrease in its Young's Modulus ( $E$ ) and resonance frequency would be expected with an increase in temperature. This thermally-driven change in bulk stiffness is known as Bulk-effect, and should produce negative correlations characterized by significant delays between temperature and resonance frequencies. This is not the case of the Wied Il-Mielah study site, where the opposite behavior is observed, probably because of major discontinuities dissecting its structure. In this context, the decrease in temperatures during the transition from warm to cold months ([Figure 4.33](#)) can be regarded as responsible for the opening of fractures, and the consequent decrease in contact stiffness between dislodged compartments of the arch determines the decrease in resonance frequencies values. Conversely, the opposite effect occurs when temperatures increase, with the closure of discontinuities and the increase in contact stiffness due to thermal expansion of the rock matrix that determines the general contraction of the arch. In order to better understand the role of major discontinuities on the observed frequency wandering, further analysis should be conducted and aimed at better assessing the entity of the delays between temperature and resonance frequencies fluctuations.

However, it is interesting noting that the peak-to-peak amplitude of the observed seasonal fluctuations of the first two resonance frequencies might be hiding the superimposed contribution of different thermomechanical effects. In particular, the comparison between the reversible seasonal shift of the first resonance frequency of the arch ( $\Delta f_1 \sim 30\%$ ) and other literature results for similar case studies (Colombero et al., 2021b) highlights the considerable magnitude of the observed frequency wandering. It could be hypothesized that if considering the high porosity characterizing the lithologies constituting the arch's structure—mostly related to their bioclastic composition and grain supported texture—thermal cycling might operate a reversible modification of the size of pores and texture voids. In fact, if neglecting the potential irreversible increase in the effective porosity due to thermal

---

degradation processes (Franzoni et al., 2013; Siegesmund et al., 2000; Villarraga et al., 2018; Villarraga Diaz, 2018; Yavuz et al., 2010), the high porous rock matrix might absorb the expansion and contraction of minerals at the microscale driven by the progressive seasonal thermalization (i.e., heating and cooling), in turn determining an in-phase stiffening or relaxation effect which could overlap to the more evident role played by major discontinuities. This consideration must be intended as a preliminary hypothesis, and laboratory analyses are needed and will be conducted to test whether high porous rock matrixes subjected to low-amplitude thermal cycles might experience such an inverse dilation-contraction effect in response to their temperature variations.

---

### 4.3 Results of infrared thermography surveys at the Wied Il-Mielah sea arch

Multitemporal IRT surveys enabled the reconstruction of the evolution in time and space of near-surface temperatures (i.e., at the air-rock interface) during each seasonal survey at the Wied Il-Mielah sea arch. In particular, since the acquisition of thermograms was only performed from sunrise to sunset, monitoring activities allowed deriving temperature distributions during heating and cooling phases of the rock mass within the diurnal part of thermal cycles. The evolution of temperatures during nighttime was not analyzed in the framework of this study. The analysis of diurnal heating and cooling ramps was considered of greater interest since they represent time intervals in which the thermal response of the rock mass subjected to direct solar radiation is more evident.

In [Figure 4.34](#), hourly surface temperature distributions of the Wied Il-Mielah arch are presented for the monitoring survey of April 2019. All the presented thermal maps show temperature distributions of the monitored rock vertical surface in a false color-scale rendering, covering an area of the rock mass of almost 120 m<sup>2</sup>. Moreover, the color scales are normalized to the daily maximum and minimum recorded values to highlight the spatial and temporal evolution patterns of temperature fields throughout the daily thermal cycle.

From a preliminary observational analysis, multiple isothermal bands clearly highlight the differentiation between heating and cooling phases of the monitored rock mass. During the first hours of the day, then immediately after sunrise, surface temperatures are characterized by a remarkable spatial homogeneity ([Figure 4.34a–c](#)).

This initial condition derives from the thermal equilibrium between air and rock temperatures that is reached during nighttime due to the absence of thermal gradients between the rock mass and the outer environment. However, slight differences in temperature distributions can be observed. Higher temperature values tend to cluster in correspondence of areas representing either morphological irregularities, main open fractures or differently oriented sectors with respect to the monitored surface. During the heating phase of the rock mass, thus in correspondence of daily maximum temperature peaks ([Figure 4.34d–g](#)), the inversion of temperature distributions with respect to early morning stages occurs: isothermal bands describe heterogeneous thermal fields characterized by considerable spatial gradients.

---

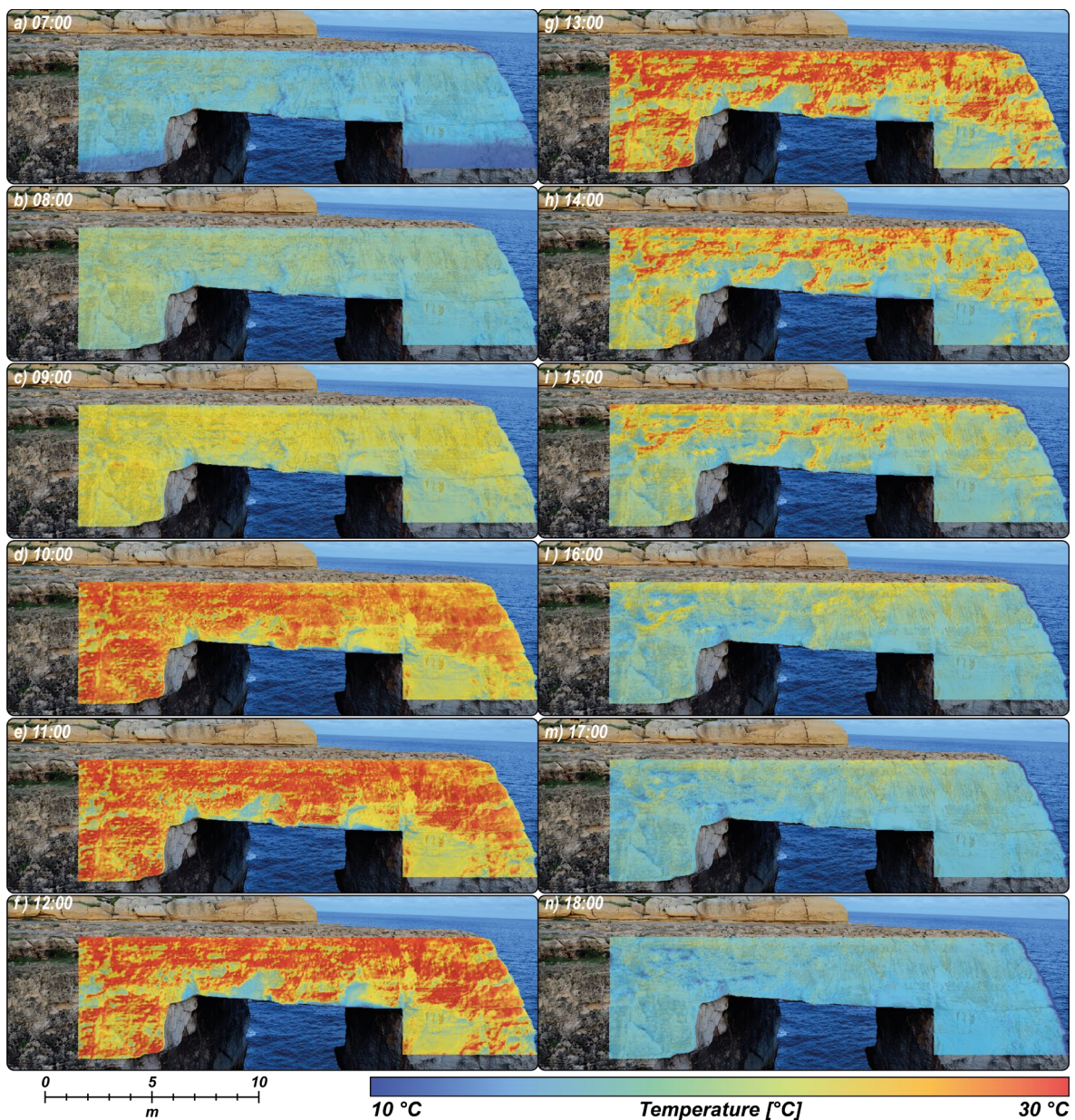


**Figure 4.34.** Results of the IRT monitoring performed in April 2019 showing the 2D evolution of surface temperature distributions from 07:00 (at sunrise – a) to 18:00 (after sunset – n). Thermograms are overlapped to visible images of the arch to enhance the comparison between near-surface temperatures and morphological features of the monitored cliff. Color scales are normalized to daily maximum and minimum values to highlight the temporal evolution of distributed thermal fields throughout the analyzed daily thermal cycle.

In these stages, corresponding to the hours in which the intensity of solar radiation is highest and its contribution to the heat transfer is dominant, the lowest temperatures tend to be spatially limited to those sectors characterized by cold thermal anomalies. These areas mostly correspond to morphological irregularities, such as scar areas, hollows and variously oriented surfaces which are not directly exposed to solar radiation because of local



shadowing effects. In addition, even if the geometrical resolution of thermograms is not high enough to guarantee the detailed reconstruction discontinuities, few wide-open joints can be recognized as their traces show not negligible temperature contrasts with the surrounding rock mass. The presence of fractures and oriented surfaces and their effect in modifying the distribution of surface temperatures can be better observed from [Figure 4.35](#), where the comparison between the visible image and the thermal map of the arch is provided.

Conversely, rock mass areas directly exposed to the incident solar radiation show a net and more homogeneous increase in their temperature values. Then, when temperatures start decreasing and the rock mass enters its cooling phase, since its surface is no more directly exposed to solar radiation, isothermal bands describe relatively homogeneous temperature distributions similar to those of early day hours ([Figure 4.34h–n](#)).

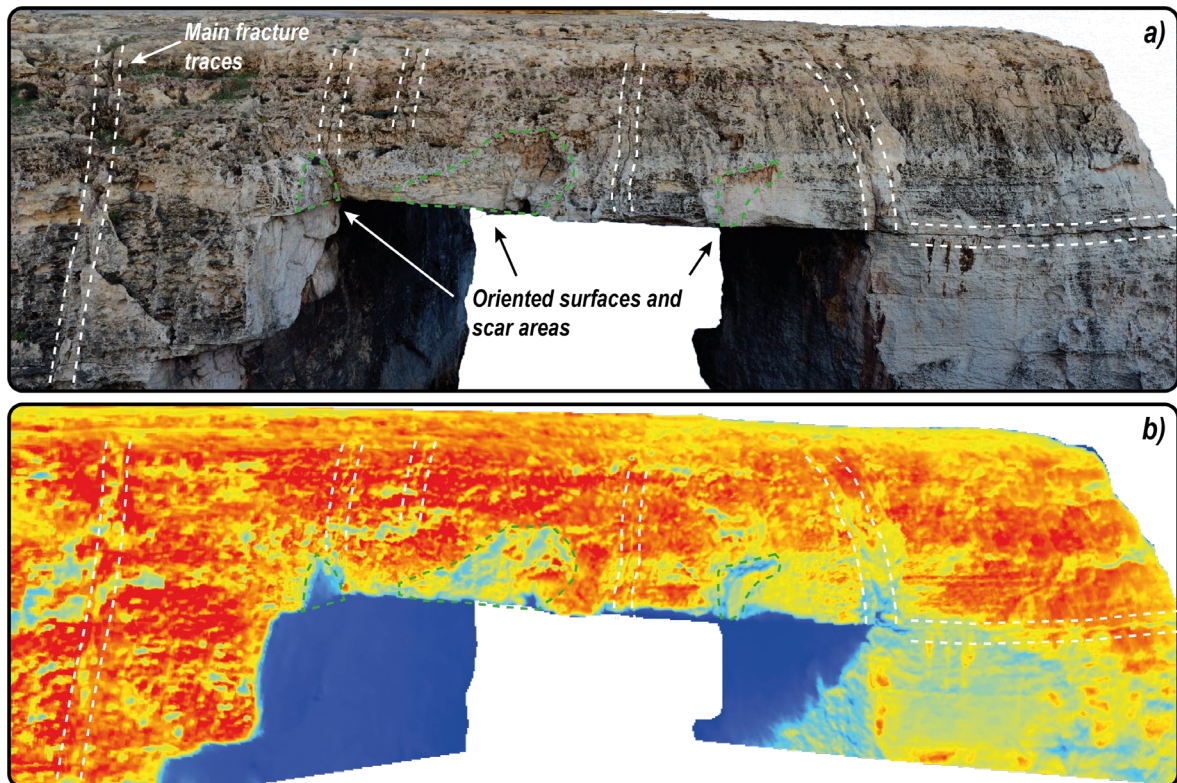


**Figure 4.35.** Visible (a) and thermal (b) images of the monitored surface where the traces of main fractures (i.e., white dashed lines), as well as oriented surfaces and scar areas (i.e., green dashed areas) are reported. It is evident that such elements, along with minor morphological irregularities, are responsible for the heterogeneity of surface temperature distributions since they cause marked thermal contrasts to rise.

For each thermogram, the relative frequency distribution of surface temperatures was computed in order to quantitatively investigate how near-surface thermal fields evolve during the daily thermal cycle. The results of this analysis are presented in [Figure 4.36](#), where

hourly temperature distributions are plotted along with their statistical descriptors. In particular, the median (M) and interquartile range (IQR) values were preferred over mean and standard deviations because considered more representative for non-normal frequency distributions (Figure 4.36a).

The shift of median values toward higher temperatures due to the slow heating of the rock mass during early morning hours (07:00–10:00) is evident, as it is equally evident the increase in IQR values. Temperature distributions tend to flatten and widen as the contribution of direct insolation to the overall heat transfer process becomes progressively dominant. Then, the highest temperatures and the greatest spatial thermal excursions are reached in correspondence of the daily positive peak (12:00–13:00). When the monitored surface of the arch is completely shadowed because the sun reaches its zenith position, and thus the influence of insolation becomes negligible, near-surface thermal fields invert their evolutionary trend in virtue of the convective-driven heat exchange with colder air masses.

The progressive cooling of the rock mass causes temperature distributions to slide toward lower median values and the concurrent decrease in surface temperature variability is also recorded. This characteristic thermal behavior of the rock mass during its heating ramps is mainly caused by the presence of marked morphological irregularities on the monitored surface of the arch. In fact, the effectiveness of solar radiation in determining sharp temperature increases during heating phases strictly depends on the geometric and morphological features of the exposed surfaces (Fiorucci *et al.*, 2018, Guerin *et al.*, 2019). Therefore, when scattered and irregular surfaces are exposed to the same thermal input, they configure near-surface temperature fields that are highly heterogeneous. Such effect is particularly evident when the magnitude of the thermal forcing is the highest, while it progressively ceases during those periods characterized by the absence of solar radiation (e.g., early morning hours and cooling phases) (Figure 4.36b).

Based on these preliminary considerations, the analysis of daily temperature evolutions over four seasonal monitoring campaigns was performed to investigate the effect of different climatic conditions influencing the rock arch. Following the previously described approach for the 1D analysis of thermograms (Section 3.3.3.1), temperature timeseries were extracted from each thermogram by selecting three areas of interest and compared to air temperatures for each seasonal survey (Figure 4.37).

---

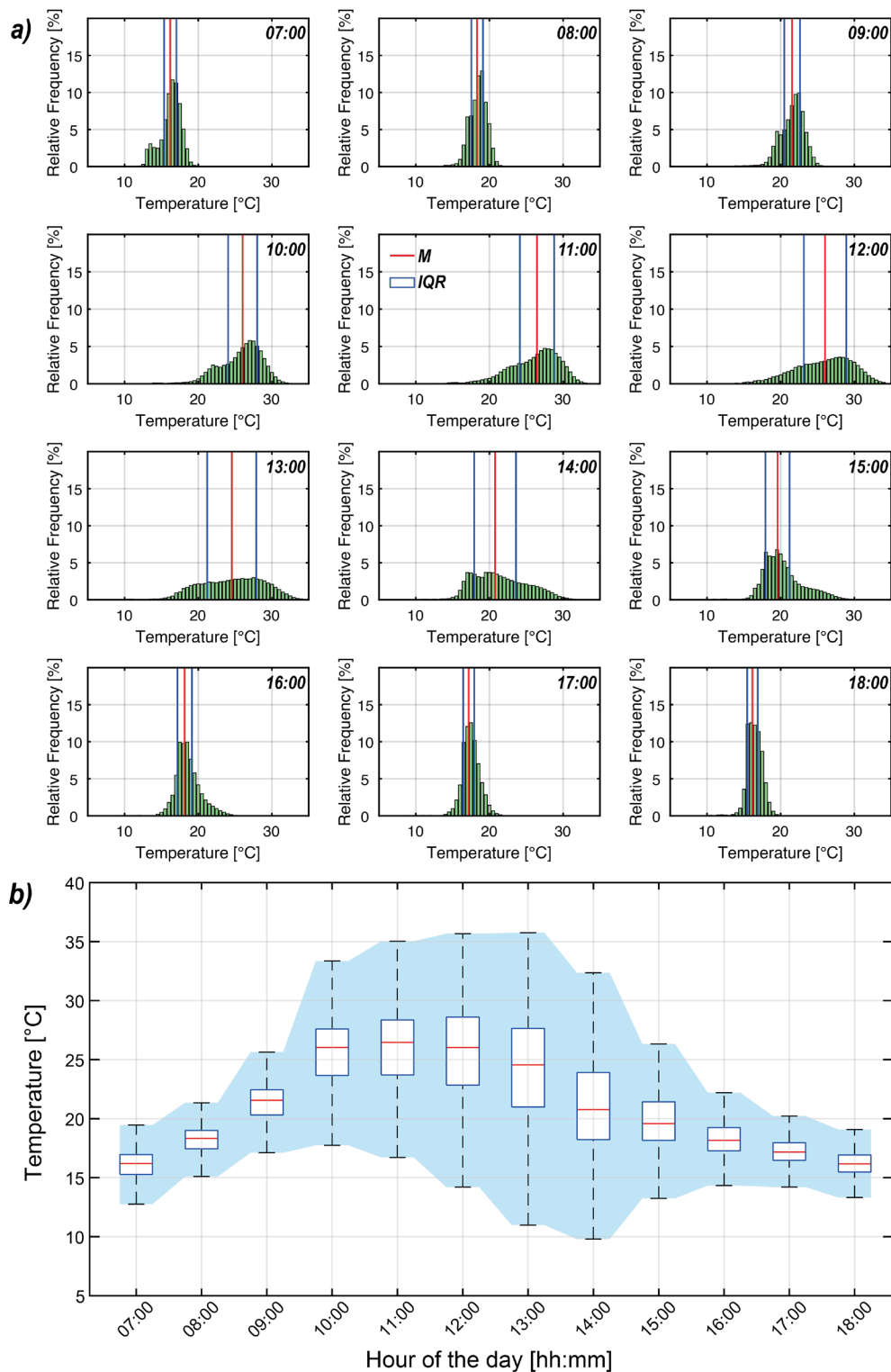


**Figure 4.36.** Surface temperature distributions computed for the IRT survey of April 2019 (a). In each chart, the median (M, red line) and interquartile range (IQR, blue box) values are plotted to enhance the great variability affecting surface temperature distributions during different hours of the day. Synthesis of the results obtained for every hour of IRT monitoring (b). For each hour, the extension of the blue boxes represents the interquartile range (IQR, defined as the difference between the upper (Q3) and lower (Q1) quartiles), red lines are median values, and black whiskers extend to extreme values. The light blue area in panel b highlights the amplitude of the observed thermal excursion.

These areas were considered of particular interest because considered representative of different morphological features of the monitored surface: the exposed surface of the arch ( $T_R$ ), a constantly shadowed hollow corresponding to a rockfall scar area ( $T_H$ ), and a major open fracture that can potentially host air circulations ( $T_F$ ).

By observing the four charts of [Figure 4.37](#), it is possible noting that the daily evolution of surface temperatures is considerably dissimilar between the monitored seasons. During autumn and winter IRT surveys ([Figure 4.37a, b](#)) the absolute lowest thermal ranges are recorded ( $< 10^\circ\text{C}$ ), with air temperatures that showed variations in the range  $1\text{--}2^\circ\text{C}$ , thus remaining constant for the entire daily intervals. In contrast, spring and summer surveys are characterized by significant thermal excursions ( $> 15^\circ\text{C}$ ) that are also accompanied by the highest temperature values recorded at the site ( $\sim 40^\circ\text{C}$ ). These results can be easily explained as deriving from the different boundary climatic conditions and lengths of heating phases that are typical of cold and warm periods.

The comparison between temperature evolutions of the considered sectors allows the detection of not negligible differences in their thermal behavior. Although the amplitude of the experienced thermal ranges is not comparable between different seasons, it is evident how the rock surface always experiences higher thermal excursions than the hollow and fracture areas. This is particularly apparent from the results obtained for the spring and summer surveys ([Figure 4.37c, d](#)). Furthermore, the time of the day in which their maximum temperatures are reached is delayed, with peaks of  $T_H$  that anticipate those related to  $T_F$  and  $T_R$ . Consequently, heating ramps of  $T_H$  are characterized by a shorter duration than  $T_F$  and  $T_R$ .

The observed differences in the amplitude and timing of heating ramps between the three analyzed sectors of the arch can be interpreted as the result of a different contribution of solar radiation to their heat balance. The effectiveness of solar radiation in causing high and rapid heating of the exposed rock mass is well represented by  $T_R$ , while shadowed areas ( $T_H$ ) and fracture zones ( $T_F$ ) are less influenced. Different from heating ramps, cooling ramps of the investigated sectors show similar features at the daily and seasonal scale. In particular, immediately after those periods characterized by the highest insolation levels (i.e., 10:00–12:00), all temperature curves show a progressive decrease toward isothermal conditions with the outer atmosphere.

---

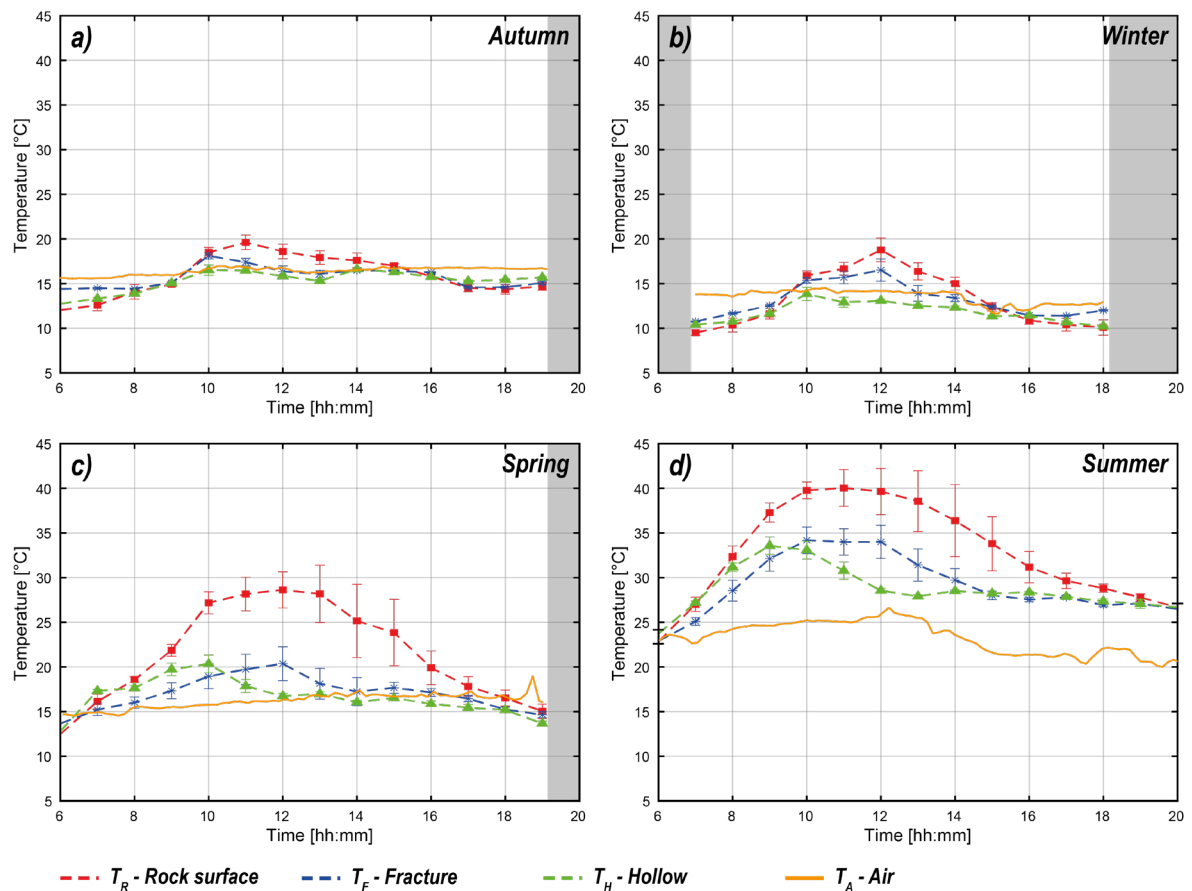


**Figure 4.37.** Daily and seasonal variability of temperatures derived from the 1D analysis of thermograms performed on Autumn (a), Winter (b), Spring (c) and Summer (d) surveys. In each plot, the evolution of temperatures extracted from clusters of points in correspondence of the rock surface ( $T_R$ ), a fracture zone ( $T_F$ ) and a hollow area ( $T_H$ ) is compared to the evolution of air temperature ( $T_A$ ). Gray bands highlight time gaps in IRT acquisitions.

To indicate better the relationships between the evolution of rock mass and air temperatures, the hourly difference between IRT-extracted time series and air temperatures was computed over all seasons (Figure 4.38). The same behavior is observed for winter and autumn surveys, with rock mass temperatures that experience three different phases during the diurnal thermal cycle (Figure 4.38a, b). In correspondence of early morning hours, thus when the contribution of solar radiation is limited, rock mass temperatures are lower than air temperatures ( $\Delta T < 0$ ).

This trend is then inverted by the superposition of marked heating ramps that cause rock mass temperature to rapidly increase, resulting in the consequent rise of positive thermal contrasts ( $\Delta T > 0$ ). Successively, after maximum thermal contrasts between rock and air temperatures are reached, rock temperatures decrease until a second thermal inversion occurs (Figure 4.38a, b). It is interesting noting how the duration and amplitude of positive

thermal contrast conditions tends to markedly vary not only as a function of the investigated sector of the rock mass, as it could already be expected, but also depending on different seasonal climatic conditions. In fact, if considering both summer and spring surveys (Figure 4.38c, d), the warmer boundary conditions, as well as the longer duration and higher amplitude of heating ramps, cause the rock mass to undergo long-lasting positive thermal excursions that are not completely recovered during the monitored cooling phases. This effect is particularly evident for the summer survey, when no thermal inversion between rock mass and air temperatures is observed during the entire monitoring interval.

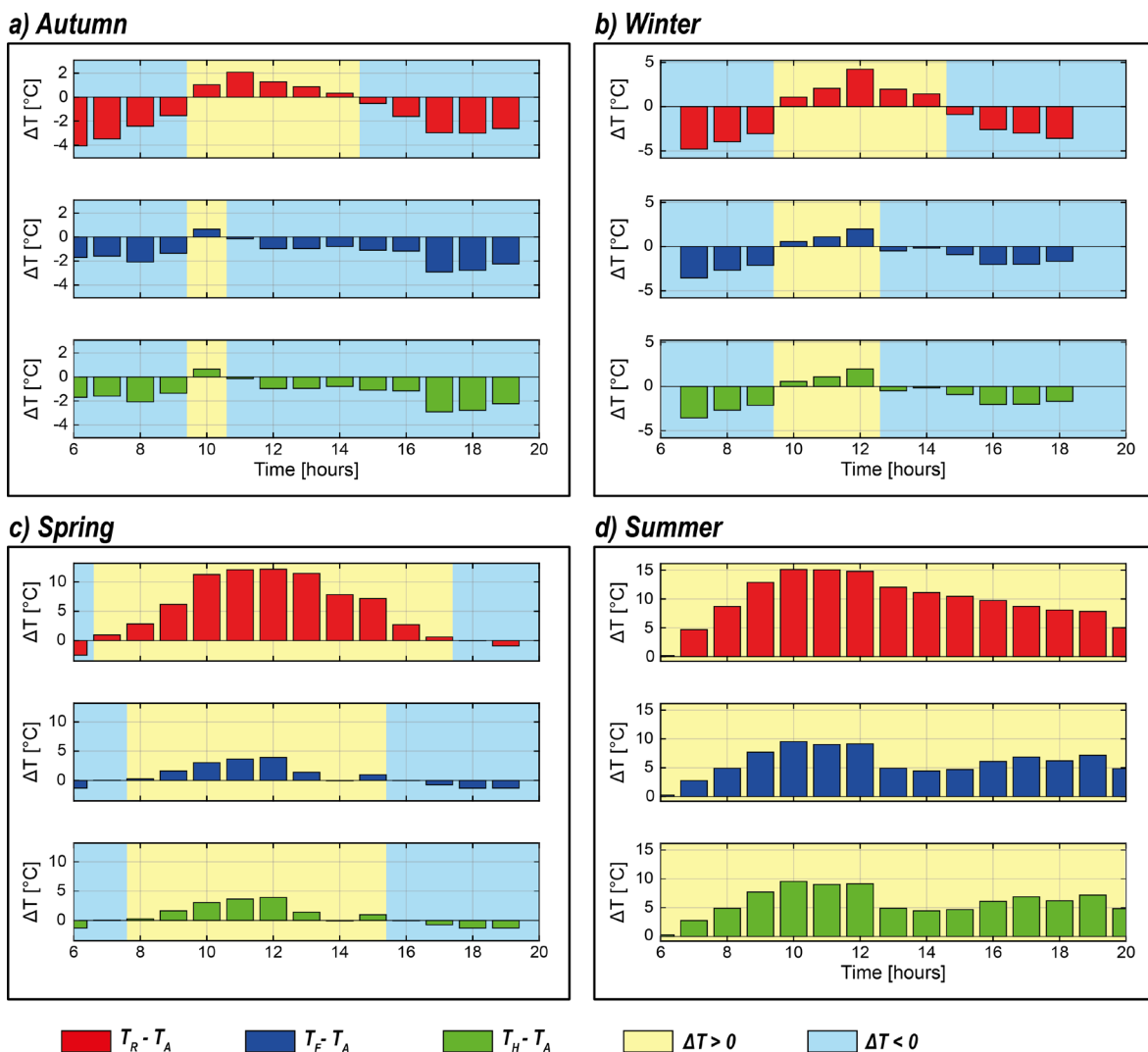


**Figure 4.38.** Comparison of hourly computed differences between temperature timeseries derived from IRT and air temperatures recorded by the weather station during the Autumn (a), Winter (b), Spring (c) and Summer (d) IRT surveys. In these bar charts, yellow boxes highlight time intervals in which IRT-derived temperatures were higher than air temperature ( $\Delta T > 0$ ), while blue boxes indicate the opposite condition ( $\Delta T < 0$ ).

Based on the results of IRT monitoring surveys, heating and cooling thermal ranges and hourly rates were computed for the investigated sectors of the arch to further analyze the combined effect of different surface conditions and seasonal climatic variability in determining the configuration of significant spatial and temporal gradients. In particular, thermal rates were computed following the approach proposed by (Fiorucci et al., 2018) (eq. 4.1):

$$TR = \frac{\Delta T}{\Delta t} \quad (\text{eq. 4.1})$$

where  $\Delta T$  is the thermal excursion between 07:00 and 11:00 for heating ramps (HTR) and between 14:00 and 18:00 for cooling ramps (CTR), while  $\Delta t$  is the considered time interval. This analysis allows observing peculiar features of the rock mass thermal behavior. At the seasonal scale, a net increasing trend in thermal rates is observed from colder to warmer months for both heating (HTR) and cooling (CTR) ramps (Figure 4.39). The slowest variation in surface temperatures is observed in autumn and winter, when all three considered sectors show comparable and very low thermal excursion and rate values during heating and cooling phases. Conversely, spring and summer are the seasons where a remarkable differential behavior is found between the investigated sectors. In particular, the highest residuals between heating and cooling rates of the exposed rock surface with respect to the hollow area and fracture zone is observed in the spring survey. Considering the heating phase of the rock mass,  $T_R$  experienced a thermal excursion of 11.2 °C, resulting in 2.7 °C/hour thermal gradient, while  $T_H$  and  $T_F$  were subjected to a considerably lower temperature range (3.1–3.7 °C) that resulted in very low thermal rates (0.9–1.15 °C/hour) (Figure 4.39a, c). In the cooling phase an identical trend is observed (Figure 4.39b, d). This result suggests that when the influence of solar radiation is high due to the longer duration heating ramps during spring and summer months, the existence of sectors on the rock mass surface characterized by different exposures can determine the configuration of temperature fields that tend to heterogeneously evolve in time and space, as witnessed by the rise in significant contrasts between the considered sectors of the arch. On the contrary, such effect is less apparent when the contribution of solar radiation to heating phases is limited in time. These considerations based on the punctual 1D analysis of IRT-extracted temperature evolutions can be equally extended to the results obtained from the 2D analysis of collected thermograms, which are presented in Figure 4.40 and Figure 4.41.

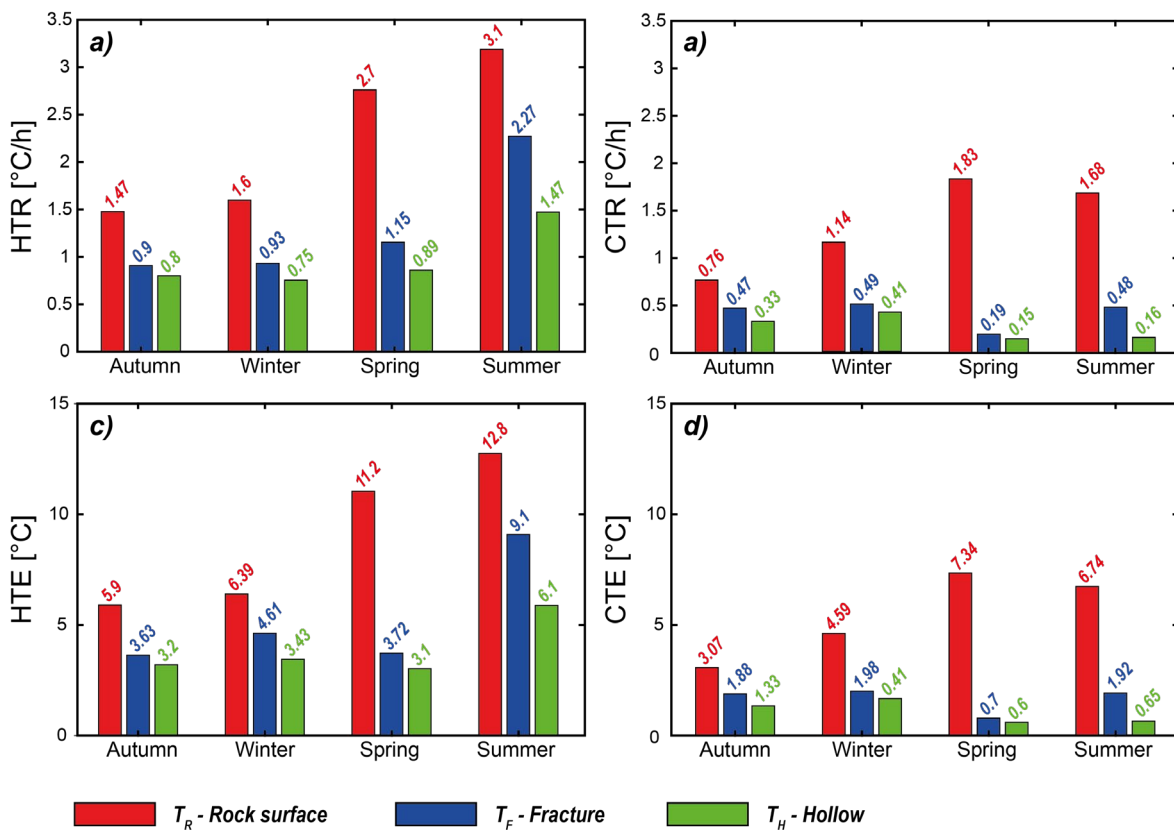


**Figure 4.39.** Results of the comparison between quantitative descriptors of heating and cooling ramps of the monitored arch during different seasons: Heating Thermal Rate (HTR) (a), Cooling Thermal Rate (CTR) (b), Heating Thermal Excursion (HTE) (c), Cooling Thermal Excursion (CTE) (d). The amplitude and time duration of heating ramps were calculated considering the first measurement and the positive temperature peak (generally found around 10:00–12:00), while cooling ramps characteristics were derived after the stages of maximum insolation, thus when the effect of the incident solar radiation can be neglected (14:00–18:00).

The 2D multitemporal analysis performed on the TIR imagery acquired in four different seasons enable the reconstruction of the pixel-to-pixel spatial distribution of daily mean temperatures (Figure 4.40) and daily temperature ranges (Figure 4.41) experienced by the monitored surface of the rock arch. Focusing on daily mean temperature distributions, an overall spatial homogeneity can be observed over all seasons. The absolute lowest values are recorded in autumn and winter (Figure 4.40a, b), while the higher values observed in spring and summer witness the general increasing trend of surface temperature due to the progressive shift toward warmer climatic conditions (Figure 4.40c, d). The spatial variability of daily mean temperatures during colder months is characterized by a limited dispersion, with IQR values typically in the range 0.7–1.1  $^{\circ}\text{C}$ , that results in homogeneous surface mean temperature fields. A different behavior can be discerned in spring, when the highest variability of average temperature values is observed (IQR = 3 $^{\circ}\text{C}$ ). In this case, isothermal



---

bands are able to highlight surface thermal contrasts mostly clustered in correspondence of the already analyzed sectors of the arch, which can be identified by cold thermal anomalies (Fig. 4.40c). The same evidence is valid for the summer survey, even though the spatial mean temperature variability is reduced (Figure 4.40d).

The analysis of the spatial distribution of daily mean temperature allows inferring how the seasonality of near-surface temperatures can determine different levels of thermalizations at the rock mass external interface. In fact, despite the spatial distribution of average surface temperatures is markedly homogeneous, the absolute difference between winter and summer values is remarkable ( $> 15\text{ }^{\circ}\text{C}$ ).

For what concerns daily temperature ranges, a significant heterogeneity in spatial distributions can be observed during all monitoring surveys (Figure 4.41). Similar to mean temperatures, the lowest thermal excursions suffered by the rock mass are observed in winter and autumn, with median values of 6 and 8  $^{\circ}\text{C}$  respectively. Thermal excursions are instead significantly higher in spring (13  $^{\circ}\text{C}$ ) and summer (17  $^{\circ}\text{C}$ ) seasons. This marked difference in the amplitude of the observed thermal excursions can be interpreted as resulting from the higher efficiency of solar radiation in causing the rock mass to experience longer heating ramps during the daily thermal cycle. In fact, and as previously observed from the 1D analysis of temperature time series, the duration of heating phases of the rock mass directly depends on the climatic season, and the longer their duration, the higher is the amplitude of temperature ranges. Furthermore, another interesting outcome that emerges from the observation of 2D daily temperature ranges is the higher heterogeneity described from thermal maps during all seasons, then independently from the intensity of thermal inputs.

The overall homogeneity of the presented daily thermal excursion maps is fragmented by several colder thermal anomalies, which locations are the same in each seasonal survey (Figure 4.41). These anomalies, representing sectors of the rock mass that experienced low amplitude temperature variations, find perfect correspondence with the morphological irregularities of the monitored surface of the arch. Then, if neglecting the seasonal variability in the magnitude of daily thermal cycles, the role played by a scattered and irregular morphology in constraining the thermal behavior of a rock mass is not trivial and must be considered of primary importance since it can actively contribute to the configuration of high temperature spatial and temporal temperature gradients.

---

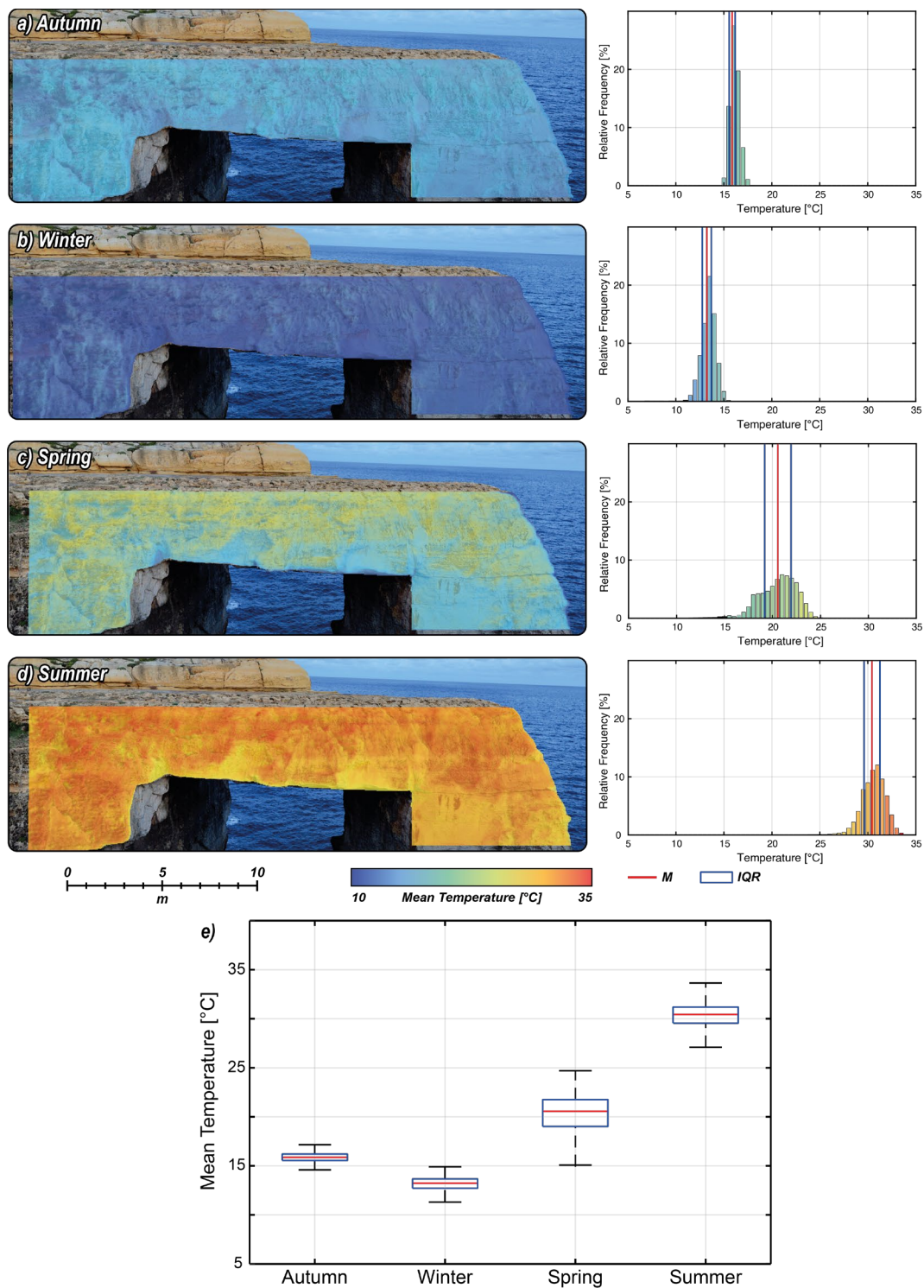


**Figure 4.40.** 2D color-scaled visualization of daily mean temperature distributions computed for the Autumn (a), Winter (b), Spring (c) and Summer (d) surveys. The respective histograms, where bars are colored according to the same color-scale of thermograms, show how the amplitude and distribution of mean temperatures strongly vary under different climatic conditions. In each chart, the median (M, red line) and interquartile range (IQR, blue box) values are also plotted. Synthesis of the results obtained for every seasonal survey (e). For each season, the extension of the blue boxes represents the interquartile range (IQR, defined as the difference between the upper (Q3) and lower (Q1) quartiles), red lines are median values, and black whiskers extend to extreme values.

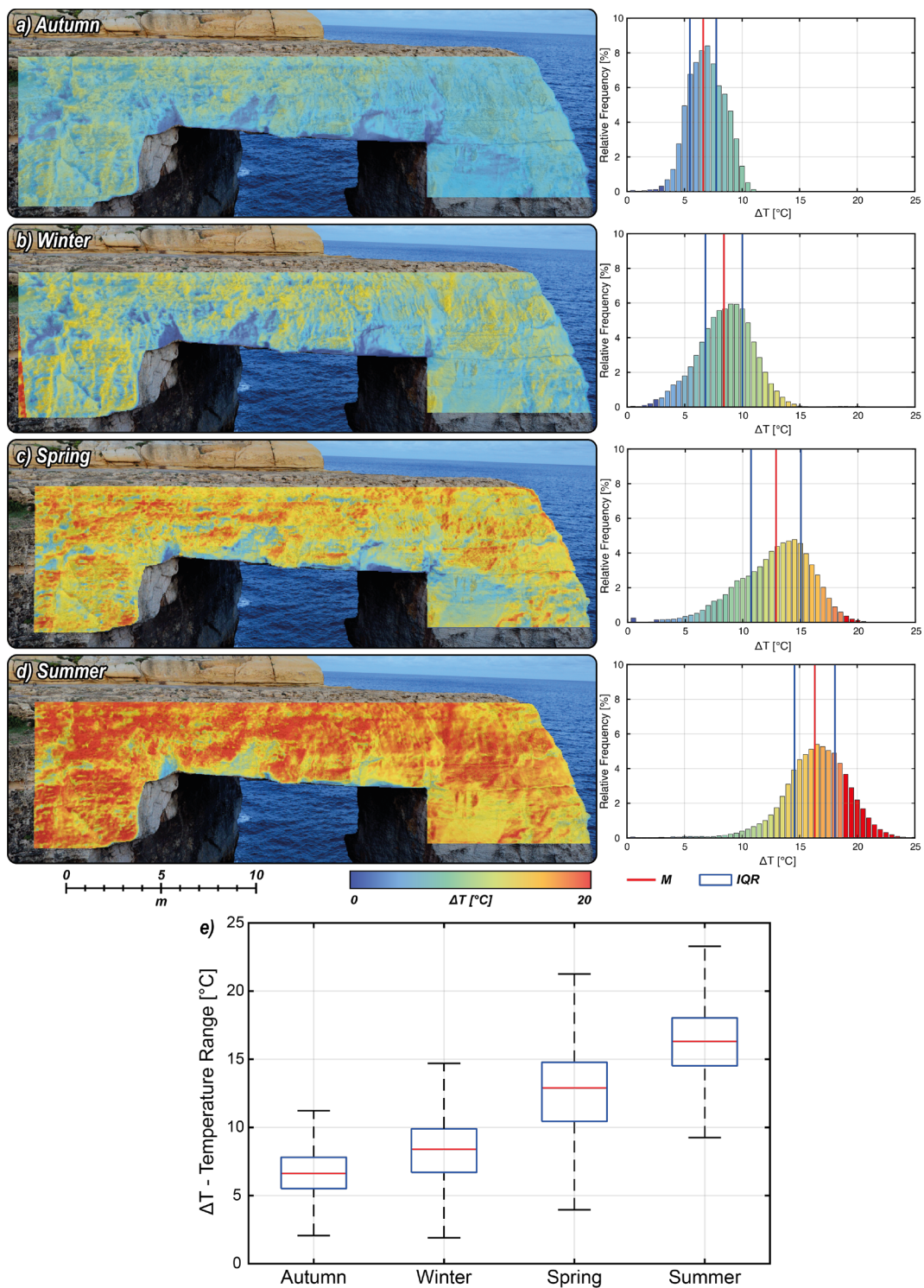


**Figure 4.41.** 2D color-scaled visualization of daily temperature range distributions computed for the Autumn (a), Winter (b), Spring (c) and Summer (d) surveys. The respective histograms, where bars are colored according to the same color-scale of thermograms, show how the amplitude and distribution of temperature ranges strongly vary under different climatic conditions. In each chart, the median (M, red line) and interquartile range (IQR, blue box) values are also plotted. Synthesis of the results obtained for every seasonal survey (e). For each season, the extension of the blue boxes represents the interquartile range (IQR, defined as the difference between the upper (Q3) and lower (Q1) quartiles), red lines are median values, and black whiskers extend to extreme values.

## 4.4 Results of 3D thermal point cloud reconstruction

The acquisition of more than 2400 thermograms during four intraday seasonal surveys allowed the reconstruction of 16 TIR point clouds to describe the distribution and evolution of surface temperatures of the rock block due to daily and seasonal temperature fluctuations. An example of the outcomes obtained following the proposed approach is shown in [Figure 4.42](#). The visualization of 3D TIR models enhances the recognition of perceptible differences in temperature distribution patterns at different times of the day. Through the observation of the rock block from different angles, it is possible to monitor the evolution of temperatures for the whole monitoring period, evidencing how the presence of differently oriented surfaces leads to a marked heterogeneity of the surface thermal fields ([Figure 4.42](#)), especially during the maximum insolation stages (i.e., 11:30). This effect attenuates toward the cooling stage of the rock mass because the influence of the direct solar radiation is diminished on the irregular surface of the rock mass, and the convective heat exchange with the atmospheric air dominates thermal balance with the outer environment. From a qualitative perspective, the 3D representation of surface temperatures allows the achievement a more comprehensive visualization of the target characteristics and enables the investigation of geospatial relationships between temperature distributions and morphological features of the rock block (i.e., differently oriented surfaces and surficial irregularities), which would be either too difficult or impossible through the observation of 2D thermograms. After the co-registration optimization of TIR point clouds to the reference, TIR point clouds were analyzed in terms of geometric and spatial accuracy through the computation of residual distance distributions for each acquisition. This analysis was crucial because a high level of correspondence between all generated point clouds is needed to proceed with the quantitative analysis of temperature distribution and evolution. As shown in [Figure 4.43](#), the results of this analysis show a high level of confidence for the co-registration optimization outcomes. Residual distances are plotted for every point cloud in a color-scaled view, enhancing the high grade of correspondence between TIR point clouds and the reference point cloud.

It is worth noting that the statistical descriptors of residual distance distributions tend to vary from the first to the last acquisition performed during the survey, with median values and interdecile ranges (IDR) drifting from 0.00–0.002 m and 0.032–0.069 m, respectively.

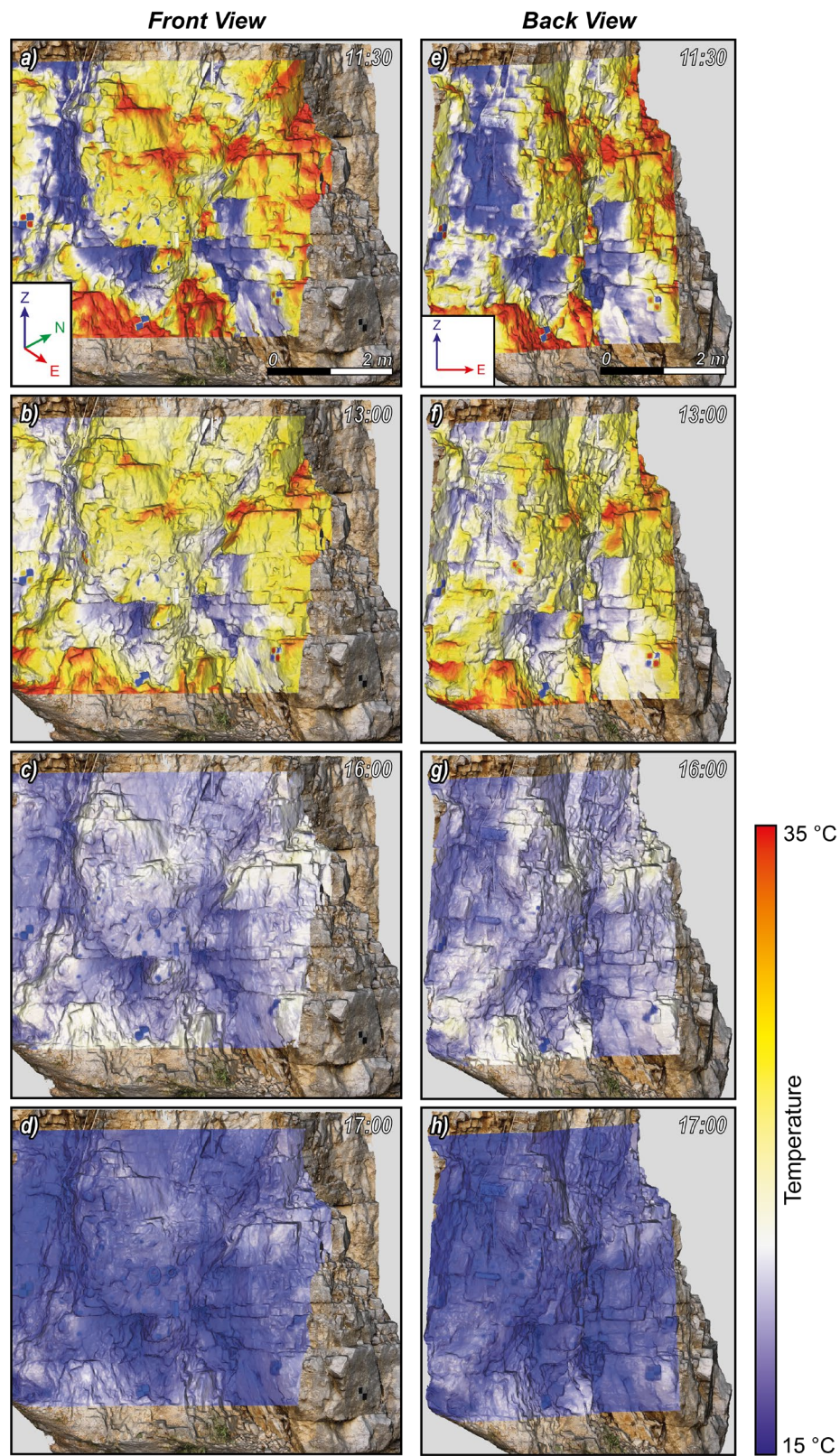


**Figure 4.42.** 3D TIR merged point clouds of the Spring survey at four different acquisition times; (a-d) The front view (i.e., eastward) and (e-h) back view (i.e., southward) of the rock block are shown for each point cloud in order to demonstrate the great enhancement in the visualization of surface temperature distributions and evolution in time (modified from Grechi et al., 2021).

This effect was interpreted as the consequence of the net decrease in temperature contrasts within thermograms of the 16:00 and 17:00 acquisitions (Figure 4.43c, d) due to the progressive homogenization of surface temperatures during the cooling stage of the rock mass, which eventually affected the number of geometric details. Moreover, the homogeneity of surface temperatures during late afternoon acquisitions is considered responsible for generating non-correspondence areas between TIR and reference point clouds. It is possible to note that in the upper-right corner of 16:00 and 17:00 point clouds, a small red area describes residual distances from the reference point cloud in the range 0.05–0.1 m. Nevertheless, considering that the uncertainties related to a nonperfect reconstruction of the rock block geometry from TIR images are clustered in small areas of the point clouds and taking into account the impossibility of acquiring more detailed thermograms during the cooling stage of the rock mass, the results of the co-registration optimization guarantee a high level of geometric detail and geospatial confidence.

After having verified the geometric accuracy of TIR point clouds and converted the thermal attributes from RGB intensity values to real temperature values, the last step of processing consisted of merging temperature scalar fields of TIR point clouds with the optical reference one.

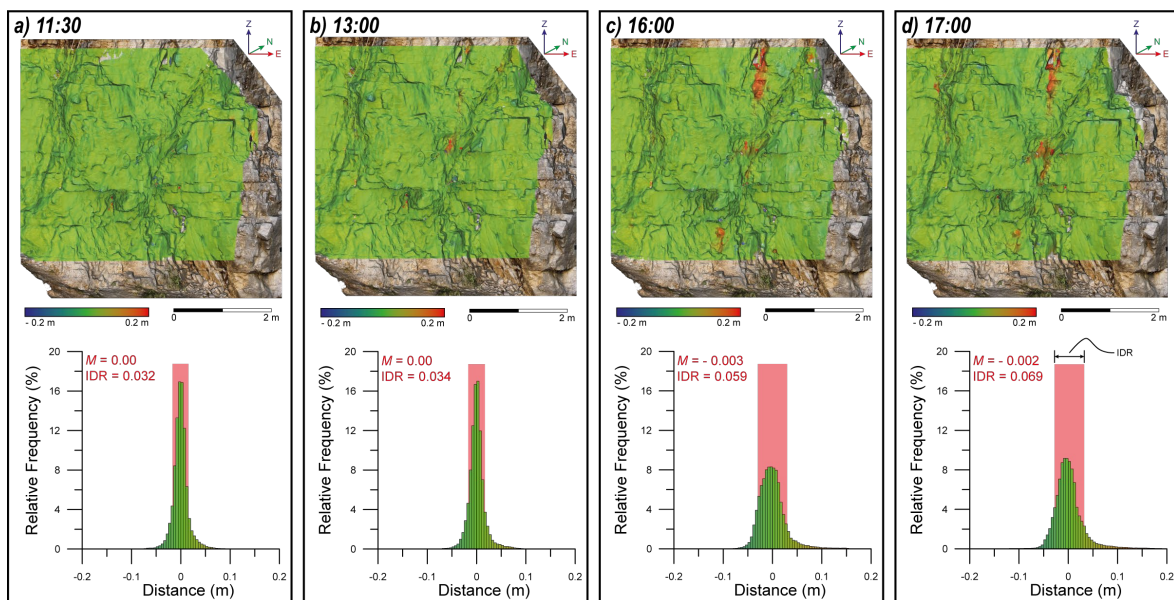


**Figure 4.43.** Color-scale maps of residual distances between TIR point clouds, acquired at 11:30 (a), 13:00 (b), 16:00 (c) and 17:00 (d) during the spring survey, and the reference high-resolution RGB optical point cloud. For each map, the distribution of residual distances is plotted along with their statistical descriptors: M – median value, IDR – interdecile range (from Grechi et al., 2021).

This operation aimed at creating a 3D model able to merge the high-resolution reconstruction of the rock block morphological features with surface temperature distributions recorded in different seasons and at different hours of the day. A comparison between temperature distributions of original and merged point clouds was performed to evaluate possible errors related to the merging operation (Figure 4.44).

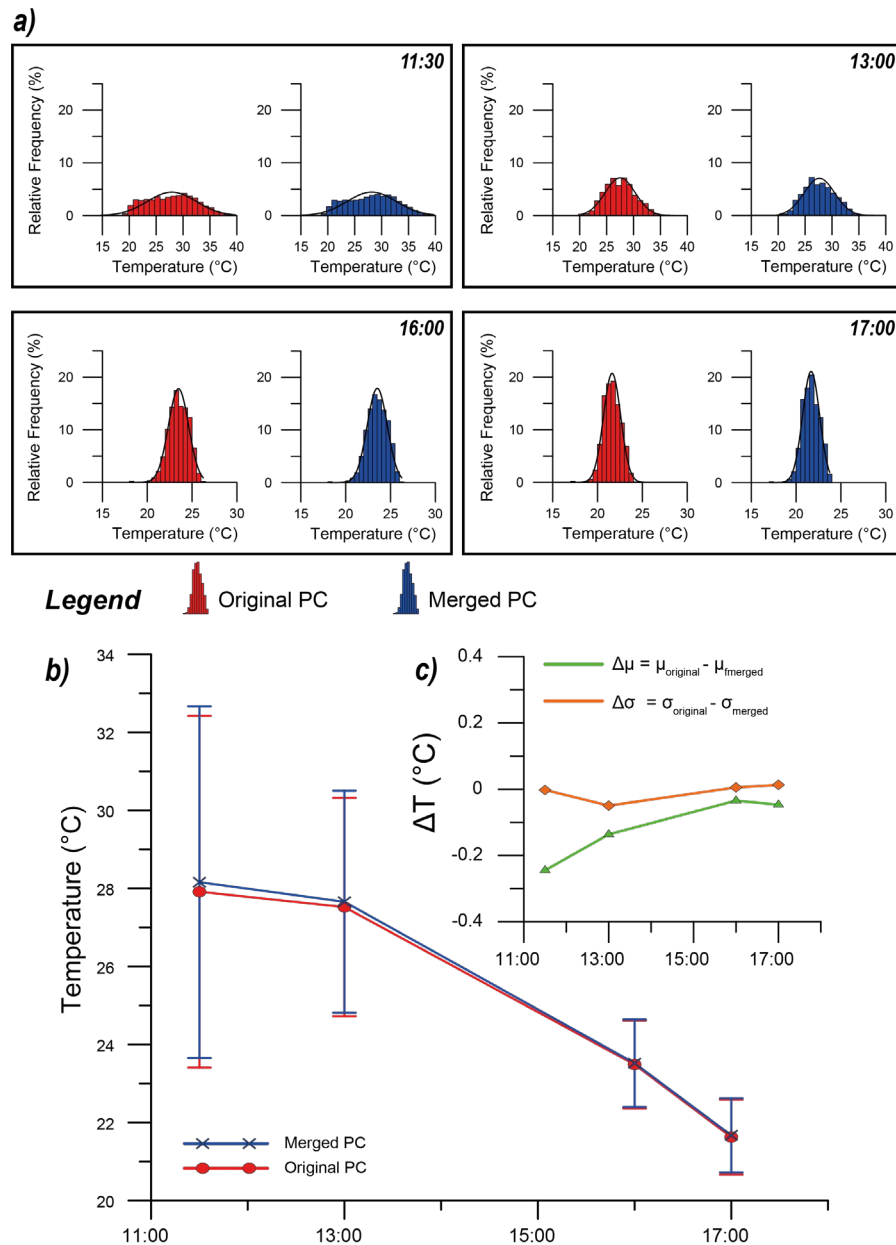


**Figure 4.44.** Temperature distributions derived from original (red bars) and merged point clouds (blue bars) (a). Comparison between mean temperature values and standard deviations of original and merged point clouds (b). The high grade of correspondence between derived values is also highlighted, both in terms of central tendency and dispersion values, by the computation of the absolute difference in mean ( $\Delta\mu$ ) and standard deviation ( $\Delta\sigma$ ) values for each original and merged point cloud (c) (modified from Grechi et al., 2021).

From the observation of the distribution of point cloud temperature classes, it is possible to discern a high level of similarity between relative frequency distributions of different acquisitions (Figure 4.44a). Statistical parameters such as the mean and standard deviation of every distribution were computed to obtain a more accurate estimate of the grade of correspondence between original and merged point clouds. From the plot of Figure 4.44b, where the mean and standard deviation values of original and merged point clouds are shown for different acquisition times, it can be observed that only negligible shifts between these values exist. However, these temperature differences can be considered negligible since, as better highlighted in Figure 4.44c, mean and standard deviation values range from  $-0.05\text{ }^{\circ}\text{C}$  to  $-0.2\text{ }^{\circ}\text{C}$  and from  $0\text{ }^{\circ}\text{C}$  to  $-0.05\text{ }^{\circ}\text{C}$ , respectively.

The obtained results demonstrate that the proposed approach produces high-confidence and geometrically accurate 3D TIR point clouds that provide information concerning both morphological features and surface temperatures of the investigated rock block. A quantitative comparison between temperatures extracted from TIR images and 3D merged point clouds was performed to evaluate the affordability of surface thermal fields described by TIR point clouds. This analysis aimed at highlighting any significant difference in the representation of 3D surface temperatures that could be potentially related to errors inherited from the processing workflow by comparing TIR point clouds with the well-established technique of temperature extraction from 2D thermograms.

Two cross-sections (AB and CD) which belong to different rock block sectors and are characterized by different exposures and degree of surficial roughness were selected for the extraction of temperature distributions relative to one of the performed seasonal surveys (Figure 4.45a–d). Section AB is located on the Southeastward surface of the rock block and is characterized by a smooth and regular surface. On this section, temperature distributions tend to show spatial homogeneity, which highlighted no significant thermal contrasts for the entire profile length (Figure 4.45f). The homogeneity of temperature distributions is evident for values extracted from both thermograms and TIR point clouds. Only slight differences arise between 2D and 3D temperature distributions (Figure 4.45h), but since they are within the confidence interval of the IR camera measurement sensitivity ( $\pm 2\text{ }^{\circ}\text{C}$  buffer zone), they can be considered negligible. Section CD is located on the Southward surface of the rock block and is characterized by a scattered and irregular profile.

---



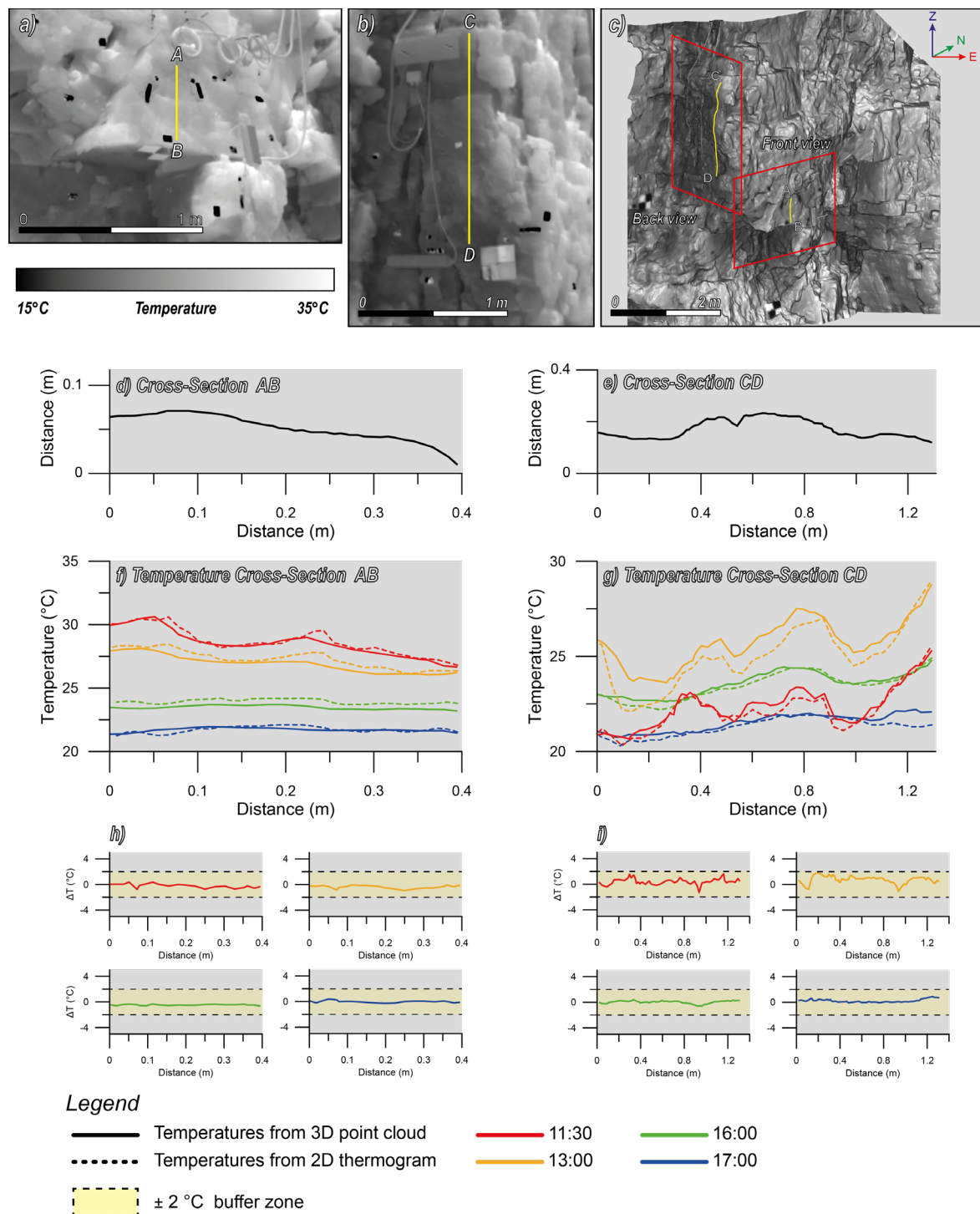


**Figure 4.45.** Results of the comparative analysis between temperatures extracted from 2D thermograms (a-b) and 3D TIR point clouds (c) for the Spring survey. Surface profiles from which temperatures were extracted (AB and CD) are marked both in 2D thermograms and for an example of a 3D point cloud visualization (d-e). None of the two profiles intercept any instrumental device of the monitoring system. Absolute temperature values are plotted against the length of the respective section for 3D and 2D data (f-g). For each analyzed section and for every acquisition, the difference between absolute temperature values ( $\Delta T$ ) was computed (h - section AB, i - section CD). A  $\pm 2$  °C buffer zone, representing the calibrated temperature accuracy of the IR camera, is also highlighted (yellow box) (from Grechi et al., 2021).

This section exhibits a more complex and heterogeneous spatial distribution of temperatures (Figure 4.45g). In particular, temperature heterogeneities are evident during the heating phase of the rock mass (between 11:30 and 13:00 - red and yellow lines respectively), when spatial thermal contrasts exceed 5 °C. Moreover, sharp thermal contrasts emerge for the entire length of the analyzed section, highlighting the existence of high spatial gradients of temperature. This effect attenuates at the end of the heating phase when the rock mass enters its cooling phase (16:00–17:00, green and blue lines, respectively). Similarly, differences in temperature distributions recorded by 2D thermograms and 3D point clouds are always within the  $\pm 2$  °C confidence interval and have their maximum values at the 13:00 acquisition (Figure 4.45i) and progressively decrease toward homogeneity between 2D and 3D extracted values during the cooling phase.

The heterogeneity of temperature distributions analyzed along section CD can be interpreted as a consequence of the irregularities and asperities characterizing the rock mass surface. Even the limited protruded elements are capable of shadowing adjacent areas, which is not only responsible for generating areas that are not directly exposed to the incident solar radiation but also for originating non-negligible spatial temperature gradients. It is also worth noting that the relative position of camera and target could play a role in the generation of heterogeneous temperature distributions, especially if a significant roughness and irregularity characterize exposed surfaces. Furthermore, when the solar radiation is diminished and the thermal convection dominates the heat balance (during cooling stages of the rock mass) (Fiorucci et al., 2018) the attenuation of spatial temperature gradients strengthens the hypothesis of a significant interaction between differently exposed surfaces and the incident solar radiation (Chicco et al., 2019).

As a result of the geometric and thermal validation of merged TIR point clouds, as well as due to the high grade of correspondence between temperature values extracted from 3D models and 2D thermograms, each point of the point clouds ( $P_i$ ) affordably stores 3D coordinates and multitemporal temperatures,  $P_i (X_i, Y_i, Z_i, T_i, \dots, T_n)$ .

Starting from the high-resolution TIR point cloud storing multiple thermal parameters, it was possible to compute the distribution of daily surface temperature ranges for the investigated rock block. Following the above-described method, a point cloud containing temperature information collected during every acquisition of each seasonal survey was

---

created. This step allowed the creation of three merged TIR point clouds characterized by four different thermal attributes (e.g., 11:30, 13:00, 16:00 and 17:00) and the maximum and minimum temperature values recorded during all acquisitions were retrieved for every point of TIR point clouds by implementing a MATLAB routine. The computation of the difference between these values enabled the reconstruction of the distribution of temperature ranges for the rock block (Figure 4.46).

As shown in Figure 4.46, where the outcomes of this analysis are presented in the form of point clouds and frequency distribution histograms, daily temperature ranges appear to significantly vary in terms of absolute amplitude and spatial distribution during the four seasonal surveys, even though cloud coverage and insolation conditions were considered comparable. This color-scale visualization allows appreciating the distribution of temperature ranges on the rock block surface, highlighting areas that were subjected to different thermal stress amplitudes. The greatest temperature ranges were recorded during the Winter and Spring monitoring surveys when the median value (P50) reached respectively 7.1 °C and 6.9 °C, whereas in Summer and Autumn it reached 3.3 °C and 4.1 °C. Moreover, temperature values associated with the 25th and 75th percentiles (P25 and P75) are highlighted in all histograms to mark significant deviations in temperature range distributions.

To further analyze the variability of the rock block thermal behavior in response to different meteo-climatic conditions, the percentile corresponding to a temperature range greater than 8 °C was computed. This statistical descriptor helps to quantify the point cloud percentage that showed considerable thermal stress in the four seasonal campaigns. It can be observed from the histograms of Figure 4.46 that in Autumn and Summer surveys only 11–12% of the point cloud exhibited temperature ranges greater than 8 °C.

Differently, in the Spring and Winter surveys 38% and 42% of the point cloud underwent significant temperature fluctuations. Such a result enables the observation of the amplitude and spatial distribution of surface temperature ranges as well as the quantification of non-trivial information concerning the thermal behavior of the rock block under variable climatic conditions within a 3D geometrically accurate environment. This approach can be devoted to the reconstruction of 3D models that can concurrently store multitemporal temperature values and 3D coordinates (X, Y, Z).

---

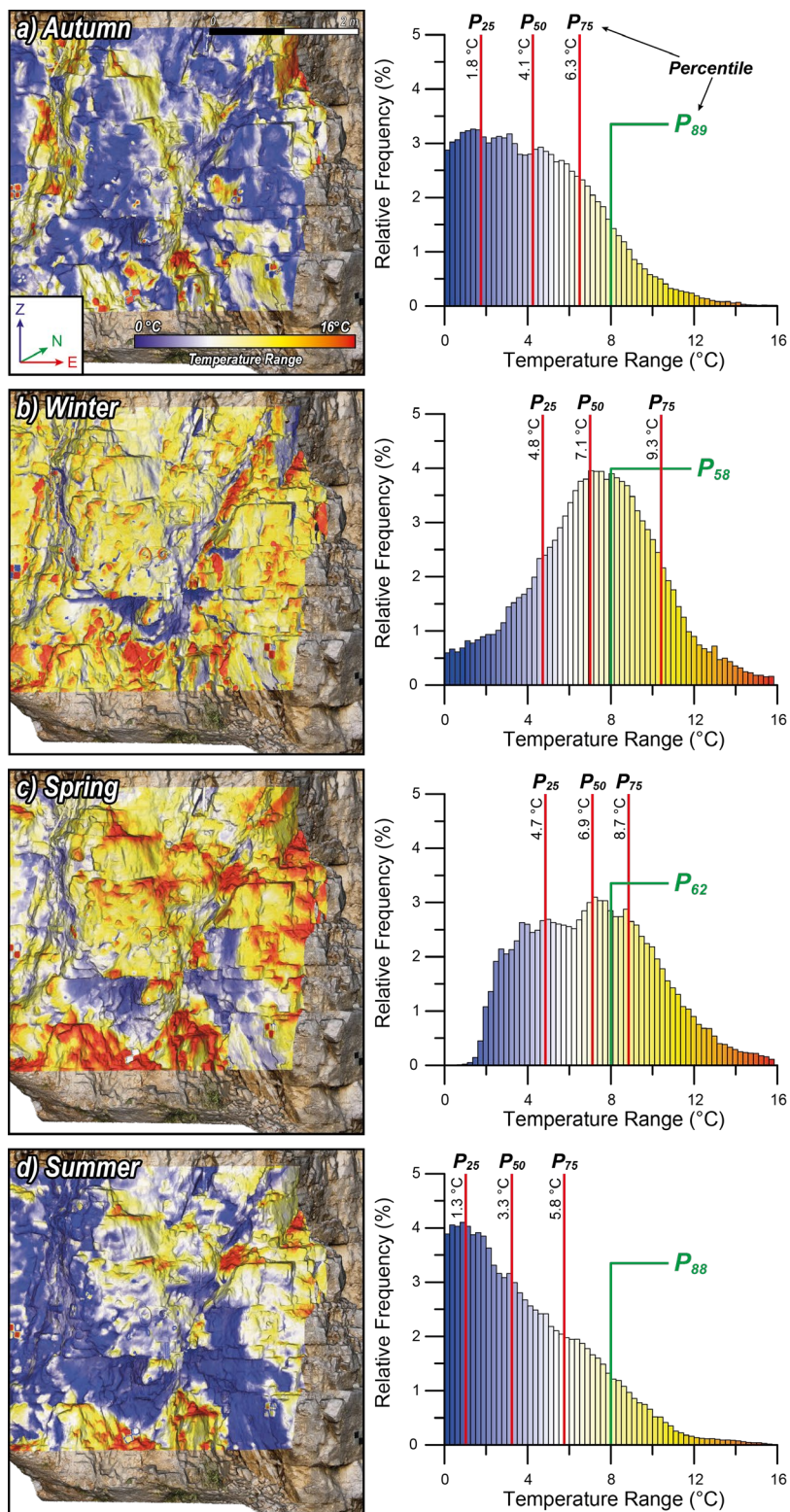


**Figure 4.46.** 3D color-scale visualization of daily temperature ranges of the investigated rock block computed for the Autumn (a), Winter (b), Spring (c) and Summer (d) survey. The respective histograms show how the amplitude and distribution of temperature ranges strongly vary under different climatic conditions. Three percentiles (P25, P50 and P75), along with the *i*-th percentile corresponding to a temperature range equal or greater than 8 °C, are also presented to highlight the main differences between the four distributions of temperature range (modified from Grechi et al., 2021).

The obtained model provides a tool to deepen the relationship between 3D features and thermal processes by evaluating the effect of shadowing and geometric irregularities on the resulting temperature distribution. In this framework, a preliminary attempt was made to analyze the correlation between differently exposed surfaces of the rock block and recorded temperature ranges, relying on the consideration of point cloud dip and dip direction values. These two parameters were selected to describe the spatial orientation variability of the rock block surfaces and were derived from the computation of point cloud normal vectors in Cloud Compare via estimation of local surface models interpolating point neighbors. Since the distribution of point cloud dip angles showed a significant tendency toward very high values (Figure 4.47a), highlighting how 73% (P27) and 50% (P50) of the point cloud are characterized by dip angles higher than 60° and 75° (Figure 4.47b), this parameter was neglected during the analysis by assuming a constant subvertical inclination.

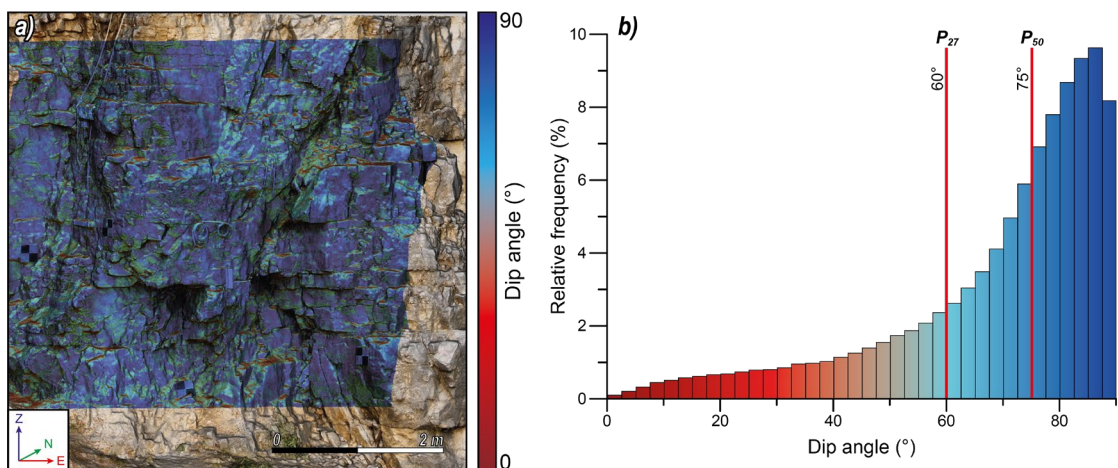


**Figure 4.47.** Color-scale representation of the 3D point cloud dip angle values (a) along with the relative frequency distribution of dip angle classes (b). Dip angle values corresponding to the 27th and 50th percentiles are marked in the histogram (from Grechi et al., 2021).

This approximation is admissible because of the overall subvertical configuration of the rock block that is derived from both the steepness of the rock wall and the existence of high-angle joint sets affecting its integrity. In light of these considerations, all point clouds were classified only by taking into account the dip direction parameter. Eight classes were defined to represent the main differences in the orientation of the rock block surfaces considering dip direction values variability. Points belonging to surfaces with equal orientation were clustered. The color-coded 3D representation of eight dip direction classes, shown in panels a and b of Figure 4.48, highlights a considerable differentiation of exposure classes of the rock block surfaces. Even though all classes were singularly treated and analyzed, it was

decided that opposite classes should be represented by assigning congruent colors. Due to the direction of the rock wall and the overall sub-verticality of the rock block surfaces, opposite dip direction classes are characterized by the same exposure. The only non-negligible differences that may arise between high-angle surfaces characterized by opposite dip directions could be related to local morphological conditions, such as overhanging rock volumes or large-scale surficial irregularities. However, a preliminary manual identification should be performed in order to take into account local surficial features. All points belonging to each directional class were extracted, and the distribution of temperature ranges was computed for every cluster. A normal distribution was then applied to retrieve the mean and standard deviation values of every distribution. This step quantitatively merges thermal and geospatial information of 3D point clouds by relating specific temperature attributes to each dip direction class. The results of this analysis are presented as polar plots (Figure 4.48c) and describe the relationship between the seasonal thermal forcing and the rock block surfaces characterized by different orientations. These polar plots enable to infer how the amplitude of temperature ranges varies depending on the orientation of surfaces exposed to the incident solar radiation. Even though significant differences in absolute temperature ranges arise between different seasonal records, the enhanced visualization of directional classes (i.e., E, SE and S) that experienced the relative greatest temperature ranges is provided. Despite the need for new IRT acquisitions to achieve good data redundancy, it should be noted that the independence from different seasonal thermal boundary conditions of the greatest temperature range distributions on the same directional classes represents a significant and non-random result, as highlighted by Figure 4.48. The pattern of temperature range distributions clustered on surfaces characterized by Eastward to Southward dip directions can be interpreted as the consequence of an almost perfect alignment to the solar path trajectories during the heating phase of the rock mass. The probability of experiencing greater daily thermal stress on surfaces therefore strongly depends on the local surface shapes, exposures, and geological conditions. Local morphological features of rock slopes can strongly constrain the insolation homogeneity (e.g., in terms of magnitude and distribution). Surface shapes and geological elements such as the N20°E direction of the rock wall and the high-angle joint sets could be considered as primary causes of the observed directional differentiation of temperature range distributions since they contribute to the generation of a complex geometry characterized by surfaces with heterogeneous exposures.

---

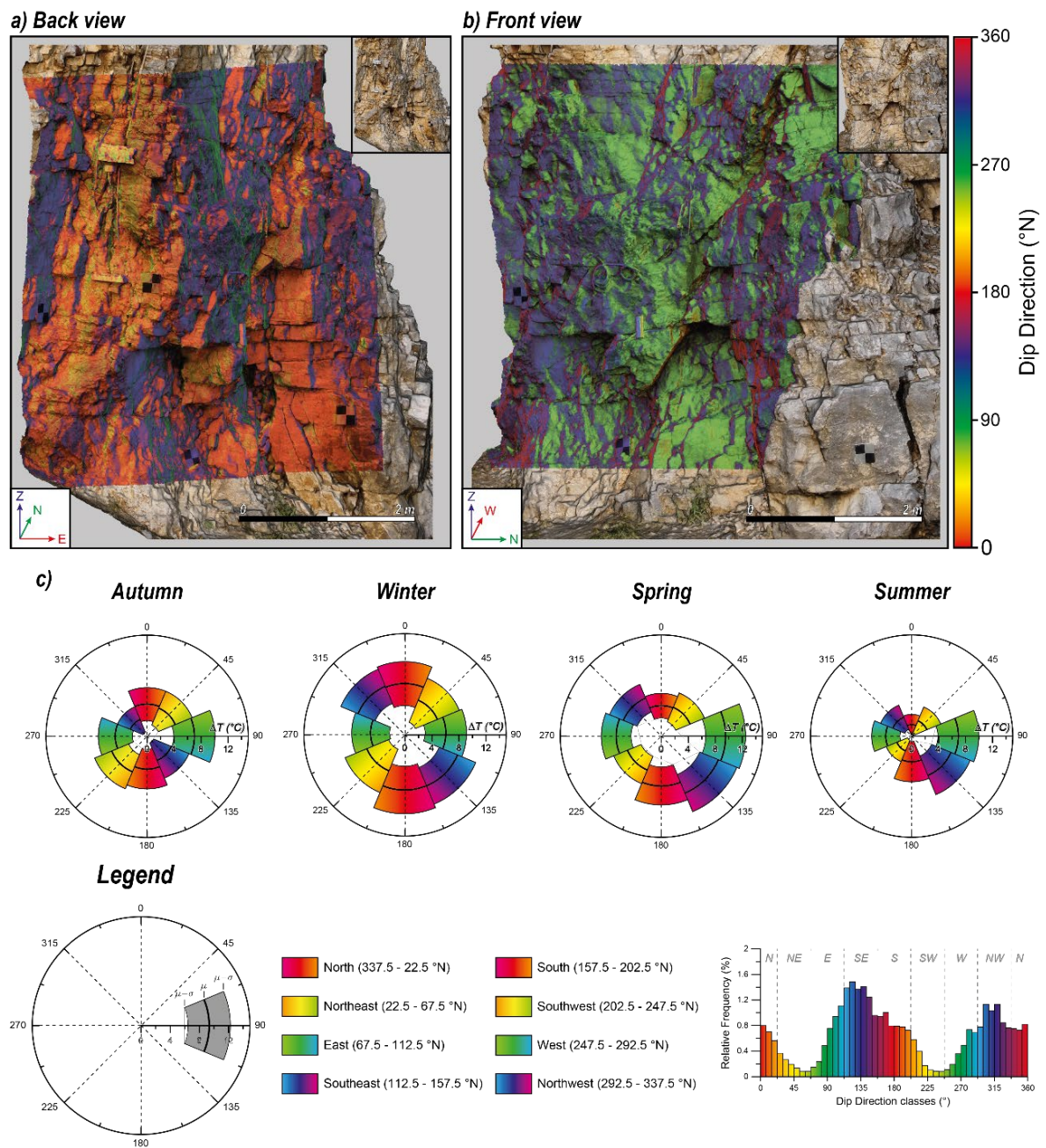


**Figure 4.48.** 3D plot showing the eight dip direction classes from two different perspectives, clearly enhancing the existence of differently oriented surfaces of the rock block (**a-b**). Polar plots of the eight dip direction classes representing temperature ranges as derived for the four performed surveys (**c**). Every colored area describes, according to its color band and radial extension, the mean ( $\mu$  - thick black line) and standard deviation values ( $\mu \pm \sigma$ ) of the temperature range recorded during each seasonal survey for every class of dip direction (from Grechi et al., 2021).

## Chapter 5

### Discussion

The here presented multimethodological approach, integrating IRT remote surveying and passive seismic monitoring techniques, was designed and tested with a view to retrieving novel insights concerning cause-to-effect relationships between the continuous action of surface thermal stresses and the response of jointed rock masses, where their geometric complexity and the presence of discontinuities can be considered of primary importance in influencing the intensity of thermally-driven damaging processes. The study of thermomechanical processes mandatorily requires the combined analysis of thermal stresses and resultant deformative effects. To this aim, the employed monitoring strategies were considered to be valuable in providing different levels of information:

- Ambient seismic noise measurements were acquired to observe potential changes in the dynamic properties of the investigated structures;
- Microseismic monitoring was aimed at assessing irreversible deformations related to progressive rock mass damaging processes involving the considered jointed rock masses;
- IRT multitemporal surveys were aimed at characterizing the intensity, spatial distribution and temporal evolution of near-surface temperature fluctuations.

Moreover, and concerning passive seismic monitoring techniques, different strategies were pursued at the two case studies. The acquisition of continuous ambient seismic noise recordings at the Wied Il-Mielah sea arch was performed through the execution of short-term monitoring campaigns scheduled with seasonal recurrence. The reason behind the implementation of such monitoring strategy is mainly ascribable to impossibility of predisposing a permanent monitoring system for the long-term acquisition of noise recordings.

However, this operative limitation gave the possibility to test the feasibility of discontinuous ambient vibration monitoring campaigns for the analysis of thermomechanical processes.

---



Conversely, a 20-month long continuous monitoring of ambient vibrations was conducted at the Acuto field laboratory. The analysis of seismic noise datasets collected at the two case studies pointed out the impossibility to produce the direct comparison between them. Nevertheless, not trivial insights were obtained with regard to the influence of temperature fluctuations on the investigated natural systems.

At the Wied Il-Mielah sea arch, the analysis of ambient vibration recordings highlighted how short-term and discontinuous monitoring activities are not applicable for investigating of the microseismic activity at the site. Too short monitoring surveys might be not suitable for investigating the microseismic activity at sites not actively involved in gravitational instabilities, since they could not be able to deal with the temporal scale of low-evolving fracturing processes. Such hypothesis is corroborated by the results obtained at the Acuto field laboratory, where several week-long time intervals are present in which no MS events were recorded (Figure 5.1).

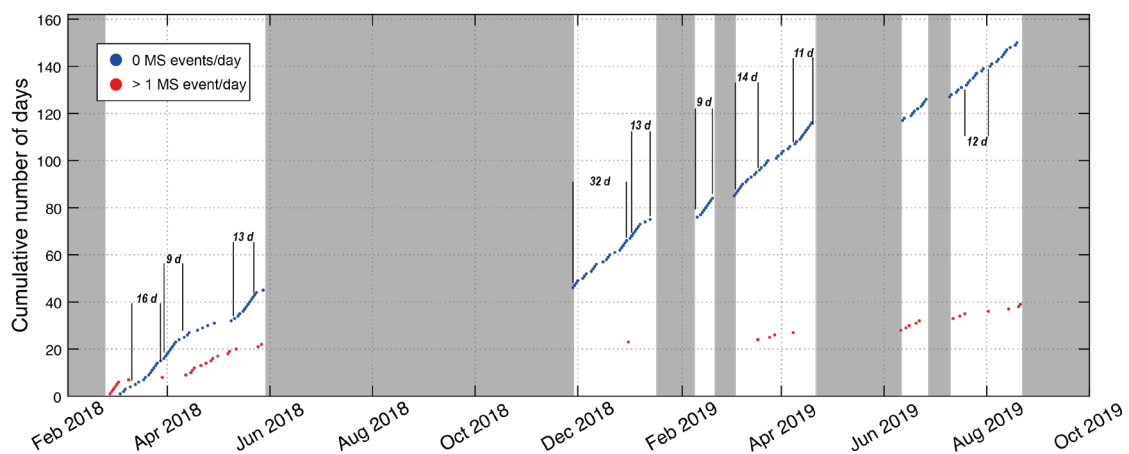


**Figure 5.1.** Comparison between the cumulative number of days in which more than 1 MS event was recorded (in red) and the number of days characterized by no MS events (in blue) at the Acuto field laboratory. The longest time intervals in which microseismic activity was absent are highlighted within the entire monitoring period (February 2018–October 2019). Gray areas represent periods in which the microseismic monitoring network was not working due to power supply interruptions.

On the contrary, interesting results were obtained from spectral and polarization analyses of ambient seismic noise traces. The here obtained results represent a preliminary step toward the comprehension of the vibrational behavior of this natural rock arch under the continuous action of near-surface thermal stresses. Experimental analyses allowed the recognition of three spectral peaks, located around 4.5 Hz (f1), 5.4 (f2) and 10.8 (f3) that were interpreted as resonance frequencies of the arch. The SRSRs computed between MIE-1 and MIE-2

evidenced the greater mobility of the arch respect to the surrounding area, with amplification factors of those resonance frequencies that reach extreme values up to 200.

However, this is not an unexpected outcome since its marked 3D geometry and the absence of lateral boundaries confer a significant degree of kinematic freedom to this structure. In contrast, if focusing on the behavior of the different compartments of the arch (i.e., anchored bedrock, bridge and rock pillar), which was investigated through a microseismic monitoring network composed of several one-component microaccelerometers, a peculiar distribution of amplification factors of two resonance frequencies (i.e.,  $f_2$  and  $f_3$ ) was observed. This spatial pattern seems to be correlated to the characteristic setting of the arch and to the location of major discontinuities, with amplification factors that significantly drop from the protruding sectors of the arch toward the stable rock cliff.

However, further analyses are required to better understand the contribution of discontinuities in controlling the detected differential dynamic behavior of the partially detached compartments of the arch.

The temporal evolution of the three resonance frequencies highlighted the existence of daily and seasonal variations, but no irreversible modifications in their values potentially related to a progressive damaging process and acceleration toward failure of the structure were observed. At both these temporal scales, the cross-correlation analysis performed between temperature fluctuations and resonance frequencies allowed observing in-phase correlations characterized by negligible delays. This evidence suggests that the detected cyclic changes in resonance frequency values are strongly controlled by the fluctuation of near-surface temperature fields at the daily and seasonal scale. The decrease in temperatures during cooling stages of the rock mass causes a general thermal contraction of the rock mass and the opening of fractures. The progressive but not irreversible decoupling of the arch's compartments is witnessed by the almost immediate and in-phase decrease in the three resonance frequency values. In contrast, the increase in temperatures determines the opposite effect, with the thermal expansion of the rock mass that causes main discontinuities to progressively close. This phenomenon leads to the gradual increase in contact stiffness between partially detached sectors of the arch and the concurrent increase in the resonance frequency values. The amplitude of thermally-induced frequency shifts at the site is in agreement with the results obtained by several authors for nearly 2D rock columns (Bottelin

---

et al., 2013a; Colombero et al., 2021a), natural freestanding rock arches (Starr et al., 2015), and fractured rock slopes (Colombero, 2017; Colombero et al., 2018a).

The role played by main discontinuities in influencing the evolutionary trend of such changes can be indirectly derived from resonance frequencies monitoring surveys characterized by seasonal recurrence, as derived from the comparison of the obtained results with the classification of thermally-driven mechanisms proposed by (Colombero et al., 2021b). This means that when permanent monitoring systems cannot be implemented due to logistic or site-specific issues, such as in the case of the Wied Il-Mielah sea arch, the discontinuous acquisition of seismic noise recordings may still represent a feasible monitoring strategy for the assessment of structural health conditions.

It is worth underlying that the stability of the Wied Il-Mielah sea arch is not only threatened by the continuous effect of temperature fluctuations, since coastal areas are fast-evolving environments under the pressure of intense weathering processes related to the mechanical action of sea waves and the physical-chemical degradation operated by marine aerosols. In such circumstances, transient and violent phenomena can considerably increase the intensity of external stresses on this structure, as observed during the sea storm of February 2019. Hence, the thermally-induced modifications of the dynamic behavior of the arch might represent a preparatory factor of instability, leading the structure toward conditions of higher susceptibility to extreme external stresses.

At the Acuto field laboratory, the spectral analysis of ambient seismic noise recordings highlighted the limitations of the adopted vibration monitoring system in investigating the dynamic behavior of the rock block due to the impossibility of measuring natural vibrations at the site. Conversely, availing of long-term monitoring timeseries, the study of potential correlations between continuously varying environmental boundary conditions and the evolution of microseismic activity at the site was conducted.

The adopted semi-automatic approach for the detection and classification of energetic signals led to the construction of a microseismic dataset comprising 273 MS events over the 20-month monitoring period. As previously described, the monitoring dataset is affected by several issues, among which the most impacting are surely the presence of periodic time gaps in recordings, the limited number of detected microseismic events, and the impossibility to locate those events within the monitored rock mass. In particular, the lack of information

---

concerning the genesis of MS events derives from the poor geometry and spatial distribution of the monitoring array that did not permit the location of their sources. As a consequence, some uncertainties related to their origin still remain and cannot be completely neglected. Nevertheless, the statistical analysis performed on the manually identified classes of events allowed to reliably consider the identified MS events as indicators of irreversible deformations deriving from fracturing processes of the rock mass. Based on the available data, the here conducted analyses allowed to discern not trivial insights concerning the role played by continuous near-surface temperature fluctuations and extreme thermal transients in influencing the stability of the intensely fractured rock block. Although the limited number of event detections did not enable to perform a robust statistical analysis between environmental stressors (e.g., rainfalls and temperature fluctuations) and the occurrence of MS events, some interesting inferences could be still derived from the obtained results.

In particular, the comparison of three monitoring windows characterized by the highest concentrations of MS events highlighted a peculiar distribution during heating and cooling phases of the rock mass in relation to different environmental conditions. These behaviors can be interpreted as the consequence of different driving mechanisms at the base of local failures.

For what concerns the transient and extreme meteorological perturbation (i.e., the *Buran* storm) that caused the rock mass to experience freezing conditions, the combined effect exerted by ice formation inside fractures, freezing-thawing cycles and high positive thermal gradients may have significantly contributed to the rapid acceleration of incipient fracturing processes, as witnessed by the evident increase in the MS activity observed during the heating phases of a four-day time window. On the contrary, in the absence of brief and violent meteorological events, the occurrence of MS events could be interpreted as the response of a complex interaction between the intensely jointed rock block and the continuous fluctuations of near-surface thermal fields which may eventually cause cyclic expansion and contraction of fractures and microcracks. This mechanism could act as a thermal fatigue process able to drive a slow, yet continuous accumulation of unrecovered deformations that, if exceed yielding thresholds of plastic deformations, can cause localized failures accompanied by the release of energy in the form of MS signals. Though, a clear cause-to-effect relationship between MS events and near-surface temperature fluctuations is not easy to discern, since several environmental factors actively exert their influence on the

---

monitored rock block. For this reason, longer monitoring intervals comprehensive of a higher number of MS detections are required to better isolate the contribution of continuous and transient factors to the destabilization of the investigated rock block. Nevertheless, the limited number of MS events recognized during the entire monitoring period might be related to the general stable conditions of the monitored rock block, as also witnessed by the absence of irreversible deformation trends of major fractures and microcracks (Figure 5.2).

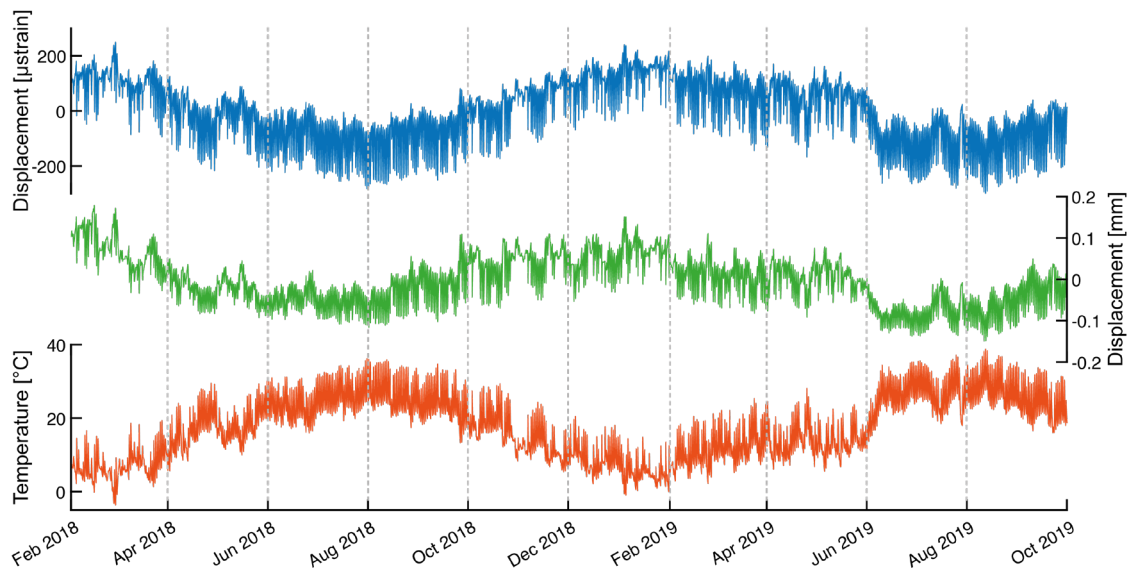


**Figure 5.2.** Temporal evolution of displacement and rock temperature monitoring timeseries recorded by the permanent multiparametric monitoring system at the Acuto field laboratory.

This evidence might also be extended to the Wied Il-Mielaħ sea arch. Here, even though direct measurements of deformation are missing, the stable condition of this structure can be derived from the absence of irreversible shifts of resonance frequency values.

Parallel to the investigation of deformative effects induced by the continuous fluctuations of temperatures, IRT monitoring surveys were performed at both case studies focusing on the analysis of their thermal behavior. At the Wied Il-Mielaħ sea arch, thermal mapping of the rock mass was conducted through day-long, seasonal monitoring campaigns which allowed to observe how the role of solar radiation and varying thermal boundary conditions can constrain the temporal evolution and spatial distribution of near-surface temperature fields.

Two different approaches encompassing 1D and 2D data analysis were tested. The extraction of temperature timeseries from selected point cluster, as well as the computation of 2D daily mean temperatures and thermal excursions, allowed to quantify the influence of

morphological irregularities and open joints in modifying the magnitude of the thermal input on the exposed rock mass surface.

The performed analyses and relative results foster the hypothesis that multiple factors can actively contribute to the development of heterogeneously evolving surface temperature distributions. The seasonal variability in climatic conditions directly controls the magnitude of solar radiation contribution to the rock mass heat balance, since warmer periods are characterized by longer durations of insolation stages. Under such circumstances, the existence of major morphological irregularities capable of inducing localized shadowing effects, as well as open fractures hosting air circulations, can play a primary role in the generation of spatial and temporal thermal gradients which entity, especially within the thermal active layer of rock masses, is remarkable.

However, the limited area framed by thermograms and the impossibility to quantitatively compare geospatial and temperature attributes of the monitored surface represent the greatest limitations of the adopted monitoring approach.

With a view of overcoming such limitations, a novel methodology based on the generation and co-registration of 3D TIR and RGB optical point clouds through SfM techniques was tested at the Acuto field laboratory. The obtained results shed light on the applicability of SfM techniques to reconstruct 3D fused thermal and optical models. In fact, despite the low resolution of the IR sensor, the geometric accuracy and the correspondence between 2D and 3D temperature measurements are high enough to consider 3D thermal point clouds suitable to describe surface temperature distributions and adequate for monitoring purposes of jointed rock mass. The potential of this approach lies in the possibility of obtaining queryable models that can describe surface temperature fluctuations of target elements as well as deepen the existing relationships between morphological features of rock masses and their continuously varying thermal boundary conditions. In this framework, while the quantification of temperature-related indexes (e.g., temperature rates and thermal excursions) can be achieved by acquiring 2D thermograms, as tested at the Wied Il-Mielah case study, the analysis of the relationships between such indexes and the geospatial and geological characteristics of exposed surfaces (e.g., dip directions, dip angles, morphological irregularities and jointing conditions) can only be approached through correctly scaled and oriented 3D models concurrently storing accurate geometric and thermal information. The

---

greatest limitations of this novel approach are mostly related to the fact that when investigating more extended areas, or when greater distances of acquisition are required (e.g., as for the Wied II-Mielah sea arch), the consequent loss in thermograms resolution could directly impact the quality of 3D models. Moreover, the need for a sufficient amount of artificial and highly reflective GCPs detectable from thermograms might limit the applicability of this method to not accessible areas, where target positioning is not possible.

As a principal application, the acquisition of multitemporal daily and seasonal fused thermal and optical models will support the quantification of thermal conditions acting at the boundary of potentially unstable rock volumes. For example, on selected potentially unstable volumes or exposed surfaces, daily and seasonal amplitudes of thermal stress can be quantitatively assessed, evaluating the effects of variable rates in heating and cooling cycles.

The accurate 3D geometric reconstruction of surface temperature fields can then provide further insights for the assessment of the role played by preparatory thermal stresses in the distribution of elastic and plastic deformation in jointed rock masses, weighting the contribution of lighting and shadowing effects on slopes or block volumes characterized by variable exposures and hence differentially heated by the solar radiation (Figure 5.3). Besides, with the upcoming rise in IR sensors resolution, the role played by open joints in constraining the behavior of isolated rock blocks could be better understood by evaluating the conditions in which joint sets can thermally influence their stability. In this sense, multitemporal 3D models (both optical and thermal) can support and enhance the spectrum of analysis focused on the comprehension of cause-to-effect relationships between thermal forcings and induced deformation, especially in geological contexts where significant geometric complexities and variable jointing conditions can constrain the spatial and temporal evolution of slow-evolving gravitational instabilities.

In light of the presented results and considering the highlighted methodological limitations encountered concerning the adopted monitoring strategies, the weight of different dimensional scales of thermally stressed natural rock structures could not be thoroughly evaluated.

The obtained outcomes at the two case studies shed light on how major discontinuities and dense fracture networks, acting as controlling factors of the dynamic and mechanical

---

behavior of potentially unstable rock structures, represent critical elements to be further investigated and comprehended since they can be regarded as primary causes of the susceptibility to thermomechanical effects on these natural systems.

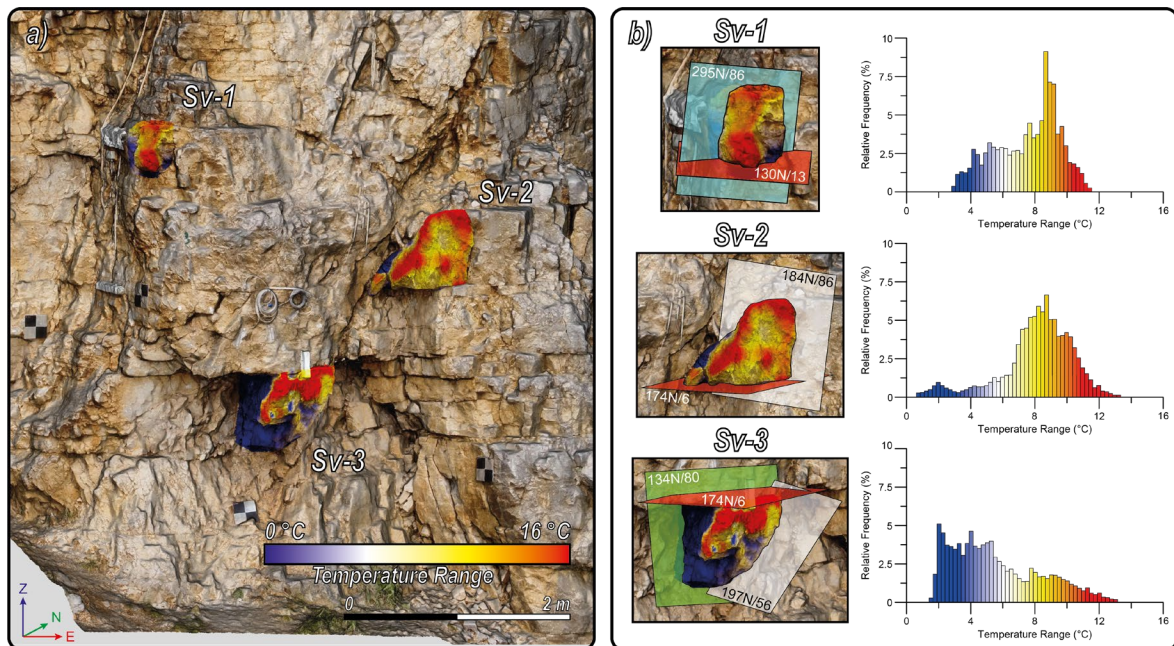


**Figure 5.3.** From the preliminary identification of potentially unstable subvolumes (Sv) the reconstruction of merged thermal and optical point clouds could allow to assess their thermal behavior. On such elements, the analysis of temperature distributions and evolution in time, as well as their geomechanical conditions, can provide useful information to constrain the role near-surface temperature fluctuations in controlling their stability (from Grechi *et al.*, 2021, modified).

Although the adopted monitoring approaches were unsuccessful in providing comparable datasets at the two case studies, thus precluding the opportunity to get new insights on the interaction between different structural settings and near-surface temperature fluctuations, some interesting results were still obtained paving the way to novel scenarios of analysis. The most significant element of distinction and novelty of this research with respect to the existing literature is probably represented by the results obtained from detailed 2D and 3D remote thermal monitoring. Based on the proposed methodologies, it is evident how the characterization of thermal stresses acting on markedly 3D rock structures cannot be oversimplified through the consideration of localized measurements. Such an approach might still be valid when the dimensional scale of targets under investigation is high enough to consider minor the role of geometric features and morphological irregularities, but when



smaller volumes are subjected to strongly different spatial and temporal thermal stresses, a detailed study of thermal forcings is mandatory.

Further improvements are expected to result in an improved understanding of the role played by variable fracturing degrees and major discontinuities at different dimensional scales of potential gravitational instabilities, then where daily and seasonal temperature fluctuations might induce different degrees of thermalization.

In this context, the analysis and the comparison between integrated monitoring datasets collected on natural rock structures characterized by different conditions (e.g., different geometries, volume sizes, jointing conditions, proneness to instability, and susceptibility to near-surface thermal stresses) could allow to better comprehend the constraining role of such conditions at the base of thermomechanical processes on jointed rock masses. As an example, the possibility to effectively couple all the proposed monitoring techniques on the rock block at the Acuto field laboratory might enable the quantification of the contribution operated by all the abovementioned factors since the dynamic and mechanical behavior of this unstable rock volume is strongly controlled by (i) its marked 3D geometry, (ii) the presence of a wide-open and bearing fracture, and (iii) the interconnection of a dense fracturing degree.

It would follow that the comprehension of the role played by the here discussed factors at different dimensional scales could also enable the investigation of the intra-structure dynamic behavior of even more geometrically complex and voluminous structures (e.g., such as the Wied Il-Mielah sea arch), where near-surface temperature fluctuations could differently interact with single elements, such as partially isolated rock compartments, representative of smaller dimensional scales (i.e., single fractures, rock blocks or rock columns) (Figure 5.4).

The original experimental plan scheduled in the framework of this Ph.D. thesis has been limited by the outbreak of the Covid-19 pandemic. Starting from February 2020, most field activities had to be interrupted entirely at both case studies, and the possibility of troubleshooting all encountered issues was precluded. With the objective of giving continuity to the here discussed results and homogeneity to the adopted multimethodological approach to comprehend thermomechanical effects on jointed rock masses at different dimensional scales, several experimental activities have already been

---

planned. For what concerns the Wied Il-Mielah sea arch, fields activities will be focused on widening the ambient vibration monitoring dataset and characterizing the 3D thermal behavior of the structure.

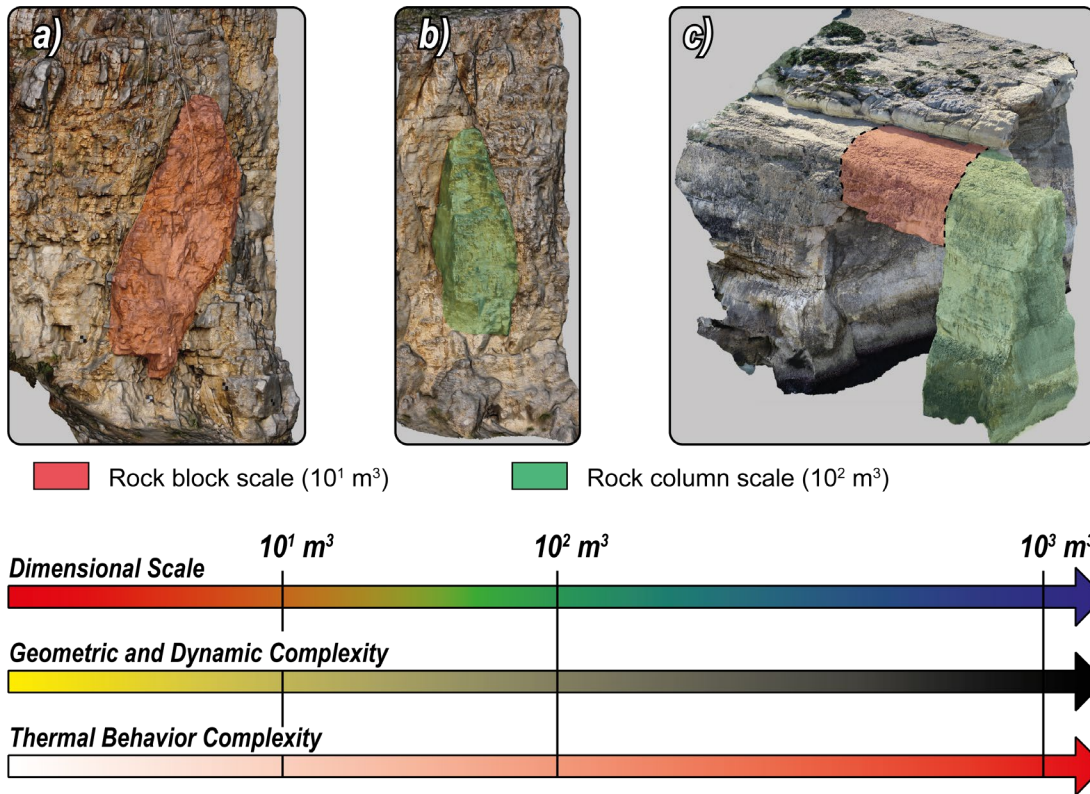


**Figure 5.4.** Exemplary sketch that summarizes the logic behind the need for investigating thermomechanical effects on jointed rock structures at different dimensional scales: **a)** rock block ( $10^1 \text{ m}^3$ ), **b)** rock column ( $10^2 \text{ m}^3$ ), **c)** rock arch ( $10^3 \text{ m}^3$ ). From a theoretical perspective, the comprehension of the interaction mechanisms between near-surface daily and seasonal temperature fluctuations and rock masses at progressively increasing dimensional scales might lead to the identification of the contribution of single elements in the dynamics of thermomechanical effect on jointed rock masses.

To this aim, the acquisition of long-term ambient seismic noise measurements will help pointing out the role of major discontinuities in controlling the complex dynamic behavior of the arch and their interaction with continuously varying thermal boundary conditions at the daily and seasonal scale. Remote thermal monitoring activities will be aimed at reconstructing 3D thermal models of the arch. In this case, since the reconstruction of 3D temperature distributions cannot be achieved via close-range terrestrial acquisition cannot be conducted due to topographical constraints of the area, unmanned aerial vehicles (UAVs) will be employed. From a methodological perspective, the use of UAV platforms with built-in or mounted IR cameras will allow assessing the potential of such an approach in pushing the boundary of IRT performances for 3D thermal monitoring purposes. In this sense, the

possibility to successfully employ UAVs will also support the investigation of wider sectors of rock slopes and cliffs involved in instability processes, where extensive coverages and great acquisition distances are required.

At the Acuto field laboratory, field activities will be instead devoted to the investigation of the thermomechanical behavior of potentially unstable rock blocks and columns at different dimensional scales through the combined analysis of multiparametric data collected by a novel integrated geophysical and geotechnical monitoring system. In fact, starting from 2018, experimental activities at the Acuto field laboratory are supported by the Department of Excellence project of the Italian Ministry of Education Universities and Research funding attributed to the Department of Earth Sciences of Sapienza University of Rome.

In this framework, the field laboratory is undergoing a structural upgrade aimed at the investigation of new sectors of the abandoned quarry wall. In particular, one of these new sectors is a 16 m high potentially unstable rock column ( $\sim 200 \text{ m}^3$ ) delineated by a vertical and open rear fracture that separates this volume from the rock wall behind. Such conditions can be considered representative of the same geostructural setting of the already monitored jointed rock block at a greater dimensional scale of potential gravitational instability (Figure 5.5). The new monitoring targets will be instrumented with innovative thermal profile probes, fiber Bragg grating technologies, joint meters, and strain gauges for coupled thermal and stress-strain monitoring purposes. Besides, high- and low-frequency geophones have already been installed on the monitored rock block, and will be placed on other monitoring targets, for ambient seismic noise and microseismic activity monitoring at the site. This novel geophysical integration has to be strictly considered as a direct result of the analysis performed in the framework of this Ph.D. thesis. In fact, the comprehension of the limitations related to the already employed microseismic array led to the design and implementation of a new monitoring system that will allow to efficiently and jointly characterize the dynamic response of the rock block and rock column to daily and seasonal fluctuations of their near-surface temperatures both in terms of resonance frequencies shifts and microseismic activity. The main goal of such improvement will be both technical and methodological and will shed light on the application of integrated geophysical and geotechnical monitoring approaches in investigating thermally-induced multiscale rock mass damaging processes using non-conventional combinations of geotechnical and broadband geophysical devices.

---

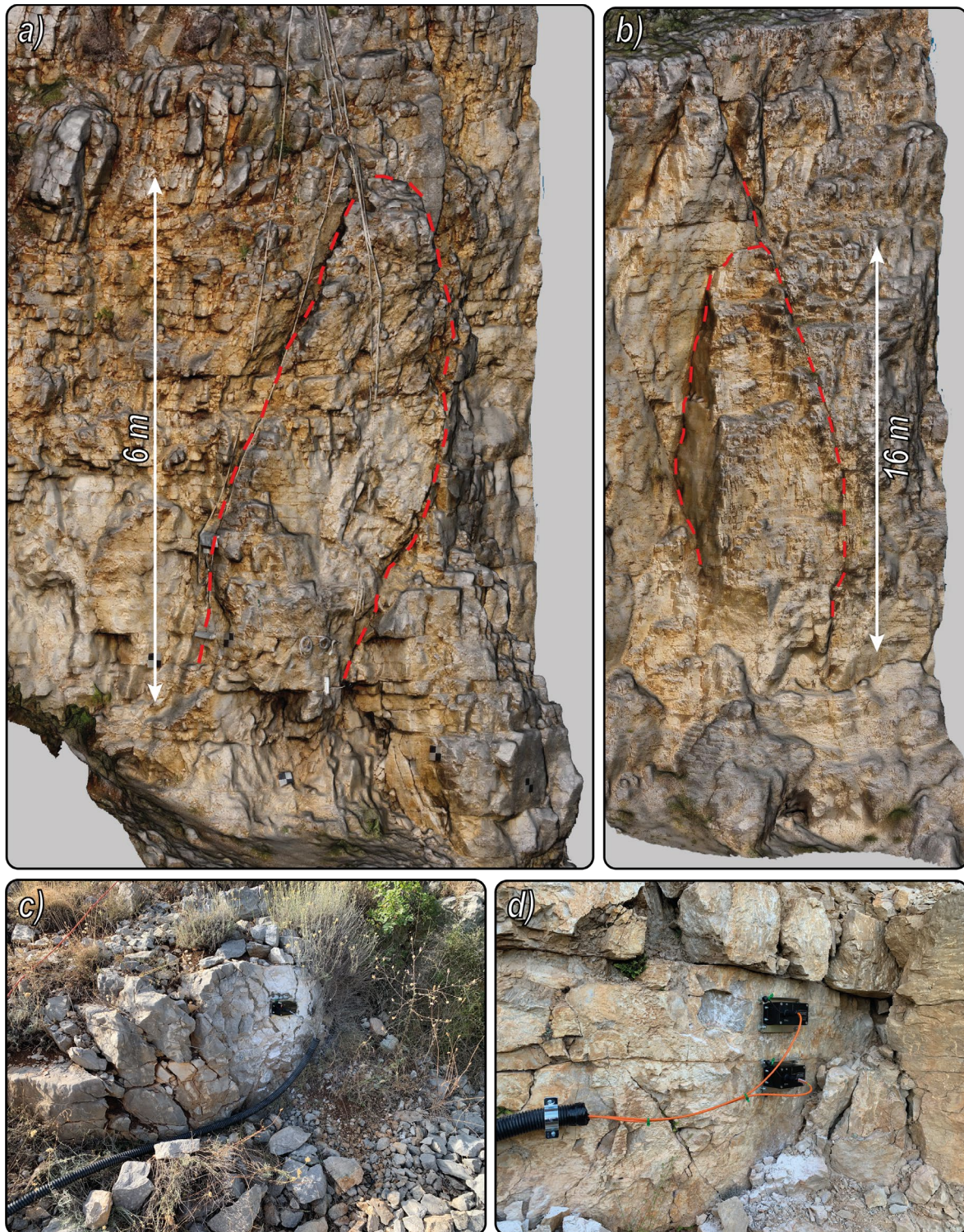


**Figure 5.5.** 3D models of the jointed rock block (a), main target of multiparametric monitoring activities at the Acuto field laboratory since 2016, and the jointed rock column (b) that will be instrumented with multiple geotechnical and geophysical devices. Low- and high-frequency geophones already installed inside the Acuto field laboratory (c, d).

The structural upgrade of the Acuto field laboratory along with the already scheduled plan of experimental activities at the Wied II-Mielah sea arch will enrich the spectrum of information concerning the influence of shallow and continuous thermal stresses on jointed rock masses. In particular, the possibility to better analyze the thermomechanical behavior of complex jointed rock structures at different dimensional scales (from the rock block- to the rock arch-scale) could allow to evaluate the weight of multiple factors in controlling the thermomechanical behavior of such natural rock systems.

Such future perspectives will not only better reveal the preparatory role of temperature fluctuations to the progressive damaging of outcropping rock masses, but through the comprehension of the temporal and spatial scale of interaction between thermal fields and multiscale gravitational instabilities, it could be possible to define effective defensive strategies aimed at attenuating and delaying the effect of progressive thermomechanical damaging processes.

## Chapter 6

### Conclusion

Thermally-induced deformations are among the less intuitive and less studied effects that can directly control rock mass stability. The assessment of the role played by near-surface temperature fluctuations in preparing jointed rock masses toward prone-to-fall conditions represents a research topic that is acquiring a growing interest from engineering geology researches. In fact, the interest in thermomechanical rock mass damaging is considerably increased over recent years, especially in relation to the analysis of thermally-induced strain effects and progressive mechanical weathering processes caused by daily and seasonal temperature fluctuations affecting rock slopes, for the purpose of understanding how preparatory factors can control their mechanical and dynamic behavior.

The experimental activities carried out in the framework of this Ph.D. thesis were specifically designed with the objective of understanding the role of near-surface temperature fluctuations in inducing irreversible deformations on jointed rock masses. Two case studies were investigated aiming at highlighting potential differences in the interaction of daily and seasonal temperature fluctuations on natural rock structures characterized by complex 3D geometries, different dimensional scale of potential instabilities and fracturing degrees.

The two case studies were investigated through a multimethodological approach encompassing passive seismic and thermal remote monitoring techniques with the objective of deciphering the ability of near-surface temperature fluctuations to cause irreversible deformations on jointed rock systems.

Passive seismic monitoring techniques allowed to retrieve interesting insights on the interaction between the discontinuity networks of rock masses and the continuous daily and seasonal fluctuations of near-surface temperature fields. Although the comparison between potential differences in the thermomechanical behavior of the two monitored rock masses cannot be performed, which might have enabled to ponder the influence of thermally-induced strain effects at different dimensional scales, the following conclusions can be drawn:

- The analysis of microseismic datasets over long-term monitoring time windows is able to give evidence of irreversible deformations even in the absence of brief and violent phenomena, such as earthquakes or extreme meteorological perturbations. On the contrary, short-term monitoring campaigns are not feasible for the purpose of characterizing the local microseismic activity.
- The analysis of ambient seismic noise aimed at investigating possible fluctuations of resonance frequency values is effective even within short duration monitoring surveys. This means that, even if long-term multiparametric monitoring activities certainly provide more robust and consistent datasets, when permanent installations cannot be implemented, the execution of recurrent day-long surveys might still represent a valuable monitoring tool for the structural health assessment of monitored rock masses.

The possibility to couple ambient seismic noise and microseismic monitoring techniques could significantly enhance the spectrum of analysis aimed at evaluating the preparatory role of near-surface temperatures in causing the progressive damaging of jointed rock masses. However, the possibility to jointly analyze the temporal evolution of resonance frequencies and MS events is strongly constrained by the need for long-term monitoring campaigns.

Along with the study of the seismic response of these jointed rock systems, Infrared thermography surveys were carried out at both sites for the characterization of their thermal behavior through different methodological approaches. At the Wied II-Mielah sea arch, the multitemporal acquisition of thermograms allowed to achieve a preliminary characterization of the thermal behavior of the rock arch in response to the continuous fluctuation of near-surface temperatures at the daily and seasonal scale, highlighting the importance of considering the effect solar radiation and its interaction with complex morphological settings.

At the Acuto field laboratory, the adopted simplified method integrating SfM and IRT revealed that through the generation and co-registration of thermal and optical point clouds, the transfer of temperature attributes from low- to high-density point clouds results in a composite output that provides a detailed and accurate 3D representation of geometric features and surface temperature distributions. Such a novel approach can pave the way to

---

further advances in the analysis of thermally-induced effects on jointed rock masses. In particular, Multitemporal 3D thermal models will also support numerical modeling analyses devoted to the reconstruction of heat transfer processes in 3D that can condition the mechanical and dynamic response of jointed rock masses over different dimensional and temporal scales.

Although the experimental activity plan originally designed in the framework of this Ph.D. thesis was not completely accomplished due to major limitations imposed by the Covid-19 pandemic, the here presented results might still represent a valuable contribution to the state-of-art knowledge on thermomechanical effects in jointed rock masses.



---

## References

- Accordi, G., Carbone, F., Civitelli, G., Corda, L., de Rita, D., Esu, D., Funicello, R., Kotsakis, T., Mariotti, G., Sposato, A., **1986**. Lithofacies map of Latium-Abruzzi and neighbouring areas. *Quaderno C.N.R. "La Ricerca Scientifica"* 114, 223.
- Agisoft LLC, 2020. Agisoft Metashape Professional. <https://www.agisoft.com>.
- Alcaino-olivares, R., Perras, M.A., **2019**. Cliff stability at tomb KV42 in the Valley of the Kings , Egypt : A first approach to numerical modelling and site investigation. *53rd US Rock Mechanics/Geomechanics Symposium* 1–10.
- Aldred, J., Eppes, M.C., Aquino, K., Deal, R., Garbini, J., Swami, S., Tuttle, A., Xanthos, G., **2016**. The influence of solar-induced thermal stresses on the mechanical weathering of rocks in humid mid-latitudes. *Earth Surface Processes and Landforms* 41, 603–614. <https://doi.org/10.1002/esp.3849>.
- Alexander, D., **1988**. A review of the physical geography of Malta and its significance for tectonic geomorphology. *Quaternary Science Reviews* 7, 41–53.
- Amitrano, D., Arattano, M., Chiarle, M., Mortara, G., Occhiena, C., Pirulli, M., Scavia, C., **2010**. Microseismic activity analysis for the study of the rupture mechanisms in unstable rock masses. *Natural Hazards and Earth System Science* 10, 831–841. <https://doi.org/10.5194/nhess-10-831-2010>.
- Amitrano, D., Gaffet, S., Malet, J.-P., Maquaire, O., **2007**. Understanding mudslides through micro-seismic monitoring: the Super-Sauze (South-East French Alps) case study. *Bulletin de la Société Géologique de France* 178, 149–157. <https://doi.org/10.2113/gssgfbull.178.2.149>.
- Amitrano, D., Grasso, J.R., Senfaute, G., **2005**. Seismic precursory patterns before a cliff collapse and critical point phenomena. *Geophysical Research Letters* 32, 1–5. <https://doi.org/10.1029/2004GL022270>.

- Andrews, D.J., **1986**. Objective determination of source parameters and similarity of earthquakes of different size. *Earthquake source mechanics* 37, 259–267.
- Arosio, D., Longoni, L., Mazza, F., Papini, M., Zanzi, L., **2013**. Freeze-Thaw Cycle and Rockfall Monitoring, in: Margottini, C., Canuti, P., Sassa, K. (Eds.), *Landslide Science and Practice: Volume 2: Early Warning, Instrumentation and Monitoring*. Springer Berlin Heidelberg, Berlin, Heidelberg, pp. 385–390. [https://doi.org/10.1007/978-3-642-31445-2\\_50](https://doi.org/10.1007/978-3-642-31445-2_50).
- Arosio, D., Longoni, L., Papini, M., Boccolari, M., Zanzi, L., **2018**. Analysis of microseismic signals collected on an unstable rock face in the Italian Prealps. *Geophysical Journal International* 213, 475–488. <https://doi.org/10.1093/gji/ggy010>.
- Arosio, D., Longoni, L., Papini, M., Scaioni, M., Zanzi, L., Alba, M., **2009**. Towards rockfall forecasting through observing deformations and listening to microseismic emissions. *Natural Hazards and Earth System Sciences* 9, 1119–1131. <https://doi.org/10.5194/nhess-9-1119-2009>.
- Arosio, D., Longoni, L., Papini, M., Zanzi, L., **2015**. Analysis of Microseismic Activity Within Unstable Rock Slopes, in: Scaioni, M. (Ed.), *Modern Technologies for Landslide Monitoring and Prediction*. Springer Berlin Heidelberg, Berlin, Heidelberg, pp. 141–154. [https://doi.org/10.1007/978-3-662-45931-7\\_7](https://doi.org/10.1007/978-3-662-45931-7_7).
- Bakun-Mazor, D., Hatzor, Y.H., Glaser, S.D., Carlos Santamarina, J., **2013**. Thermally vs. seismically induced block displacements in Masada rock slopes. *International Journal of Rock Mechanics and Mining Sciences* 61, 196–211. <https://doi.org/10.1016/j.ijrmms.2013.03.005>.
- Bakun-Mazor, D., Keissar, Y., Feldheim, A., Detournay, C., Hatzor, Y.H., **2020**. Thermally-Induced Wedging–Ratcheting Failure Mechanism in Rock Slopes. *Rock Mechanics and Rock Engineering* 53, 2521–2538. <https://doi.org/10.1007/s00603-020-02075-6>.

- 
- Baldassini, N., di Stefano, A., **2017**. Stratigraphic features of the Maltese Archipelago: a synthesis. *Natural Hazards* 86, 203–231. <https://doi.org/10.1007/s11069-016-2334-9>.
- Ball, M., Pinkerton, H., **2006**. Factors affecting the accuracy of thermal imaging cameras in volcanology. *Journal of Geophysical Research: Solid Earth* 111, 1–14. <https://doi.org/10.1029/2005JB003829>.
- Barreira, E., Almeida, R.M.S.F., Simões, M.L., Rebelo, D., **2020**. Quantitative infrared thermography to evaluate the humidification of lightweight concrete. *Sensors (Switzerland)* 20, 1–14. <https://doi.org/10.3390/s20061664>.
- Barton, N., Choubey, V., **1977**. The shear strength of rock joints in theory and practice. *Rock mechanics* 10, 1–54.
- Benitez, M.C., Ramirez, J., Segura, J.C., Ibanez, J.M., Almendros, J., Garcia-Yeguas, A., Cortes, G., **2007**. Continuous HMM-Based Seismic-Event Classification at Deception Island, Antarctica. *IEEE Transactions on Geoscience and Remote Sensing* 45, 138–146. <https://doi.org/10.1109/TGRS.2006.882264>.
- Bialik, O.M., Zammit, R., Micallef, A., **2021**. Architecture and sequence stratigraphy of the Upper Coralline Limestone formation, Malta: Implications for Eastern Mediterranean restriction prior to the Messinian Salinity Crisis. *The depositional record: a journal of biological, physical and geochemical sedimentary processes* 7, 256–270. <https://doi.org/10.1002/dep2.138>.
- Billi, A., Tiberti, M.M., **2009**. Possible causes of arc development in the Apennines, central Italy. *Bulletin of the Geological Society of America* 121, 1409–1420. <https://doi.org/10.1130/B26335.1>.
- Biolchi, S., Furlani, S., Antonioli, F., Baldassini, N., Causon Deguara, J., Devoto, S., di Stefano, A., Evans, J., Gambin, T., Gauci, R., Mastronuzzi, G., Monaco, C., Scicchitano, G., **2016**. Boulder accumulations related to extreme wave events on the eastern coast of Malta. *Natural Hazards and Earth System Sciences* 16, 737–756. <https://doi.org/10.5194/nhess-16-737-2016>.
-

- Blasi, C., **1994**. Fitoclimatologia del Lazio, in: Fitosociologia.
- Bommer, J.J., Stafford, P.J., Alarcón, J.E., **2009**. Empirical Equations for the Prediction of the Significant, Bracketed, and Uniform Duration of Earthquake Ground Motion. *Bulletin of the Seismological Society of America* 99, 3217–3233. <https://doi.org/10.1785/0120080298>.
- Bonnefoy-Claudet, S., Cotton, F., Bard, P.Y., **2006**. The nature of noise wavefield and its applications for site effects studies. A literature review. *Earth-Science Reviews* 79, 205–227. <https://doi.org/10.1016/j.earscirev.2006.07.004>.
- Bottelin, P., Jongmans, D., Baillet, L., Lebourg, T., Hantz, D., Levy, C., le Roux, O., Cadet, H., Lorier, L., Rouiller, J.-D., Turpin, J., Darras, L., **2013a**. Spectral Analysis of Prone-to-fall Rock Compartments using Ambient Vibrations. *Journal of Environmental & Engineering Geophysics* 18, 205–217. <https://doi.org/10.2113/JEEG18.4.205>.
- Bottelin, P., Lévy, C., Baillet, L., Jongmans, D., Guéguen, P., **2013b**. Modal and thermal analysis of les arches unstable rock column (vercors massif, french alps). *Geophysical Journal International* 194, 849–858. <https://doi.org/10.1093/gji/ggt046>.
- Bottelin, P., Baillet, L., Larose, E., Jongmans, D., Hantz, D., Brenguier, O., Cadet, H., Helmstetter, A., **2017**. Monitoring rock reinforcement works with ambient vibrations: La Bourne case study (Vercors, France). *Engineering Geology* 226, 136–145. <https://doi.org/10.1016/j.enggeo.2017.06.002>.
- Burjánek, J., Gassner-Stamm, G., Poggi, V., Moore, J.R., Fäh, D., **2010**. Ambient vibration analysis of an unstable mountain slope. *Geophysical Journal International* 180, 820–828. <https://doi.org/10.1111/j.1365-246X.2009.04451.x>.
- Burjánek, J., Moore, J.R., Yugsi Molina, F.X., Fäh, D., **2012**. Instrumental evidence of normal mode rock slope vibration. *Geophysical Journal International* 188, 559–569. <https://doi.org/10.1111/j.1365-246X.2011.05272.x>.

- 
- Burjánek, J., Gischig, V., Moore, J.R., Fäh, D., **2018**. Ambient vibration characterization and monitoring of a rock slope close to collapse. *Geophysical Journal International* 212, 297–310. <https://doi.org/10.1093/gji/ggx424>.
- Cabrelles, M., Galcerá, S., Navarro, S., Lerma, J.L., Akasheh, T., Haddad N., **2009**. Integration of 3D laser scanning, photogrammetry and thermography to record architectural monuments. Proc. of the 22nd CIPA Symposium 9, 3–8.
- Cai, M., Kaiser, P.K., Morioka, H., Minami, M., Maejima, T., Tasaka, Y., Kurose, H., **2007**. FLAC/PFC coupled numerical simulation of AE in large-scale underground excavations. *International Journal of Rock Mechanics and Mining Sciences* 44, 550–564. <https://doi.org/10.1016/j.ijrmms.2006.09.013>.
- Carlà, T., Farina, P., Intrieri, E., Botsialas, K., Casagli, N., **2017**. On the monitoring and early-warning of brittle slope failures in hard rock masses: Examples from an open-pit mine. *Engineering Geology* 228, 71–81. <https://doi.org/10.1016/j.enggeo.2017.08.007>.
- Carslaw, H.S., Jaeger, J.C., **1959**. *Conduction of heat in solids*, Second edition. ed. Clarendon Press, Oxford.
- Chen, Y.L., Ni, J., Jiang, L.H., Liu, M.L., Wang, P., Azzam, R., **2014**. Experimental study on mechanical properties of granite after freeze-thaw cycling. *Environmental Earth Sciences* 71, 3349–3354. <https://doi.org/10.1007/s12665-013-2725-0>.
- Chicco, J.M., Vacha, D., Mandrone, G., **2019**. Thermo-physical and geo-mechanical characterization of faulted carbonate rock masses (Valdieri, Italy). *Remote Sensing* 11. <https://doi.org/10.3390/rs11020179>.
- Chopra, A.K., **2013**. *Dynamics of structures: international edition*. Pearson Education Limited.
- Civitelli, G., Brandano, M., **2005**. Atlante delle litofacies e modello deposizionale dei Calcari a Briozoi e Litotamni nella Piattaforma carbonatica laziale-abruzzese. *Bollettino della Società Geologica Italiana* 124, 611.
-

- Clinton, J.F., Bradford, S.C., Heaton, T.H., Favela, J., **2006**. The observed wander of the natural frequencies in a structure. *Bulletin of the Seismological Society of America* 96, 237–257. <https://doi.org/10.1785/0120050052>.
- Collins, B.D., Stock, G.M., **2016**. Rockfall triggering by cyclic thermal stressing of exfoliation fractures. *Nature Geoscience* 9, 395–400. <https://doi.org/10.1038/ngeo2686>.
- Collins, B.D., Stock, G.M., Eppes, M.C., Lewis, S.W., Corbett, S.C., Smith, J.B., **2018**. Thermal influences on spontaneous rock dome exfoliation. *Nature Communications* 9, 1–12. <https://doi.org/10.1038/s41467-017-02728-1>.
- Collins, B.D., Stock, G.M., Eppes, M.C., **2019**. Relaxation Response of Critically Stressed Macroscale Surficial Rock Sheets. *Rock Mechanics and Rock Engineering* 52, 5013–5023. <https://doi.org/10.1007/s00603-019-01832-6>.
- Colombero, C., **2017**. Microseismic strategies for characterization and monitoring of an unstable rock mass. Ph.D. Thesis. University of Turin, Department of Earth Sciences. Turin.
- Colombero, C., Baillet, L., Comina, C., Jongmans, D., Larose, E., Valentin, J., Vinciguerra, S., **2018a**. Integration of ambient seismic noise monitoring, displacement and meteorological measurements to infer the temperature-controlled long-term evolution of a complex prone-to-fall cliff. *Geophysical Journal International* 213, 1876–1897. <https://doi.org/10.1093/gji/ggy090>.
- Colombero, C., Comina, C., Vinciguerra, S., Benson, P.M., **2018b**. Microseismicity of an Unstable Rock Mass: From Field Monitoring to Laboratory Testing. *Journal of Geophysical Research: Solid Earth* 123, 1673–1693. <https://doi.org/10.1002/2017JB014612>.
- Colombero, C., Godio, A., Jongmans, D., **2021a**. Ambient seismic noise and microseismicity monitoring of a prone-to-fall quartzite tower (Ormea, NW Italy). *Remote Sensing* 13. <https://doi.org/10.3390/rs13091664>.
- Colombero, C., Jongmans, D., Fiolleau, S., Valentin, J., Baillet, L., Bièvre, G., **2021b**. Seismic Noise Parameters as Indicators of Reversible

- 
- Modifications in Slope Stability: A Review, Surveys in Geophysics. Springer Netherlands. <https://doi.org/10.1007/s10712-021-09632-w>.
- Cooley, J.W., Tukey, J.W., **1965**. An algorithm for the machine calculation of complex Fourier series. *Mathematics of computation* 19, 297–301.
- Coratza, P., Gauci, R., Schembri, J., Soldati, M., Tonelli, C., **2016**. Bridging Natural and Cultural Values of Sites with Outstanding Scenery: Evidence from Gozo, Maltese Islands. *Geoheritage* 8, 91–103. <https://doi.org/10.1007/s12371-015-0167-7>.
- Cosentino, D., Cipollari, P., Marsili, P., Scrocca, D., **2010**. Geology of the central Apennines: a regional review. *Journal of the virtual explorer* 36, 1–37.
- Coviello, V., Pogliotti, P., Chiarle, M., Arattana, M., Morra di Cella, U., **2015**. Monitoring Rock Wall Temperatures and Microseismic Activity for Slope Stability Investigation at J.A. Carrel Hut, Matterhorn, in: *Engineering Geology for Society and Territory - Volume 1: Climate Change and Engineering Geology*. Springer International Publishing Switzerland, pp. 305–309. <https://doi.org/10.1007/978-3-319-09300-0>.
- D5731-08, A., **2008**. Standard test method for determination of the point load strength index of rock and application to rock strength classifications. *ASTM Int West Cochohocken, PA* 22, 51–60.
- Dai, F., Li, B., Xu, N., Fan, Y., Zhang, C., **2016**. Deformation forecasting and stability analysis of large-scale underground powerhouse caverns from microseismic monitoring. *International Journal of Rock Mechanics and Mining Sciences* 86, 269–281. <https://doi.org/10.1016/j.ijrmms.2016.05.001>.
- Dai, F., Li, B., Xu, N., Zhu, Y., **2017**. Microseismic early warning of surrounding rock mass deformation in the underground powerhouse of the Houziyan hydropower station, China. *Tunnelling and Underground Space Technology* 62, 64–74. <https://doi.org/10.1016/j.tust.2016.11.009>.
- D'Angiò, D., **2019**. Rheological effects related to neo-fracturing processes in rock masses. Ph.D. Thesis. Sapienza University of Rome, Department of Earth Sciences. Rome.
-

- D'Angiò, D., Fantini, A., Fiorucci, M., Iannucci, R., Lenti, L., Marmoni, G.M., Martino, S., **2021a**. Environmental forcings and micro-seismic monitoring in a rock wall prone to fall during the 2018 Buran winter storm. *Natural Hazards* 106, 2599–2617. <https://doi.org/10.1007/s11069-021-04556-5>.
- D'Angiò, D., Lenti, L., Martino, S., **2021b**. Microseismic monitoring to assess rock mass damaging through a novel damping ratio-based approach. *International Journal of Rock Mechanics and Mining Sciences* 146, 104883. <https://doi.org/https://doi.org/10.1016/j.ijrmms.2021.104883>.
- del Gaudio, V., Muscillo, S., Wasowski, J., **2014**. What we can learn about slope response to earthquakes from ambient noise analysis: An overview. *Engineering Geology* 182, 182–200. <https://doi.org/10.1016/j.enggeo.2014.05.010>.
- Delchiaro, M., Fioramonti, V., della Seta, M., Cavinato, G.P., Mattei, M., **2021**. Fluvial inverse modeling for inferring the timing of Quaternary uplift in the Simbruini range (Central Apennines, Italy). *Transactions in GIS* 1–26. <https://doi.org/10.1111/tgis.12833>.
- Della Seta, M., Esposito, C., Fiorucci, M., Marmoni, G.M., Martino, S., Sottili, G., Belviso, P., Carandente, A., de Vita, S., Marotta, E., Peluso, R., **2021**. Thermal monitoring to infer possible interactions between shallow hydrothermal system and slope-scale gravitational deformation of Mt Epomeo (Ischia Island, Italy). *Geological Society, London, Special Publications* 519, SP519-2020–131. <https://doi.org/10.1144/SP519-2020-131>.
- Deprez, M., de Kock, T., de Schutter, G., Cnudde, V., **2020**. A review on freeze-thaw action and weathering of rocks. *Earth-Science Reviews* 203, 103143. <https://doi.org/10.1016/j.earscirev.2020.103143>.
- Devoto, G., **1970**. Sguardo geologico dei Monti Simbruini (Lazio nord-orientale). *Geologica Romana* 9, 127–136.
- DeWitt, D.P., Nutter, G.D., **1991**. *Theory and practice of radiation thermometry*. John Wiley & Sons.
- Dietze, M., Krautblatter, M., Illien, L., Hovius, N., **2021**. Seismic constraints on rock damaging related to a failing mountain peak: the Hochvogel, Allgäu.



- 
- Earth Surface Processes and Landforms 46, 417–429. <https://doi.org/10.1002/esp.5034>.
- Do Amaral Vargas, E., Velloso, R.Q., Chávez, L.E., Gusmão, L., do Amaral, C.P., **2013**. On the effect of thermally induced stresses in failures of some rock slopes in Rio de Janeiro, Brazil. *Rock Mechanics and Rock Engineering* 46, 123–134. <https://doi.org/10.1007/s00603-012-0247-9>.
- Eppes, M.C., Magi, B., Hallet, B., Delmelle, E., Mackenzie-Helnwein, P., Warren, K., Swami, S., **2016**. Deciphering the role of solar-induced thermal stresses in rock weathering. *Bulletin of the Geological Society of America* 128, 1315–1338. <https://doi.org/10.1130/B31422.1>.
- Fabbi, S., **2018**. Geology of the eastern slopes of the Simbruini Mts. between Verrecchie and Capistrello (Central Apennines – Abruzzo, Italy). *Journal of Maps* 14, 435–446. <https://doi.org/10.1080/17445647.2018.1483843>.
- Fantini, A., Fiorucci, M., Martino, S., **2017**. Rock Falls Impacting Railway Tracks: Detection Analysis through an Artificial Intelligence Camera Prototype. *Wireless Communications and Mobile Computing* 2017. <https://doi.org/10.1155/2017/9386928>.
- Fantini, A., Fiorucci, M., Martino, S., Marino, L., Napoli, G., Prestininzi, A., Salvetti, O., Sarandrea, P., Stedile, L., **2016**. Multi-sensor system designed for monitoring rock falls: the experimental test-site of Acuto (Italy). *Rendiconti Online Societa Geologica Italiana* 41, 147–150.
- Finlayson, B., Statham, I., **1980**. *Hillslope analysis*. Butterworth-Heinemann.
- Fiorucci, M., **2017**. Approaches of data analysis from multi-parametric monitoring systems for landslide risk management. Ph.D. Thesis. Sapienza University of Rome, Department of Earth Sciences. Rome.
- Fiorucci, M., Marmoni, G.M., Martino, S., Mazzanti, P., **2018**. Thermal response of jointed rock masses inferred from infrared thermographic surveying (Acuto test-site, italy). *Sensors (Switzerland)* 18. <https://doi.org/10.3390/s18072221>.
- Fischer, L., Huggel, C., **2008**. Methodical design for stability assessments of permafrost affected high-mountain rock walls. *Ninth International Conference on Permafrost* 1, 439–444.
-

- Foglini, F., Prampolini, M., Micallef, A., Angeletti, L., Vandelli, V., Deidun, A., Soldati, M., Taviani, M., **2016**. Late quaternary coastal landscape morphology and evolution of the Maltese Islands (Mediterranean Sea) reconstructed from high-resolution seafloor data. *Geological Society Special Publication 411*, 77–95. <https://doi.org/10.1144/SP411.12>.
- Francioni, M., Simone, M., Stead, D., Sciarra, N., Mataloni, G., Calamita, F., **2019**. A new fast and low-cost photogrammetry method for the engineering characterization of rock slopes. *Remote Sensing 11*, 1–24. <https://doi.org/10.3390/rs11111267>.
- Franzoni, E., Sassoni, E., Scherer, G.W., Naidu, S., **2013**. Artificial weathering of stone by heating. *Journal of Cultural Heritage 14*, e85–e93. <https://doi.org/10.1016/j.culher.2012.11.026>.
- Frayssines, M., Hantz, D., **2006**. Failure mechanisms and triggering factors in calcareous cliffs of the Subalpine Ranges (French Alps). *Engineering Geology 86*, 256–270. <https://doi.org/10.1016/j.enggeo.2006.05.009>.
- Frodella, W., Elashvili, M., Spizzichino, D., Gigli, G., Adikashvili, L., Vacheishvili, N., Kirkitadze, G., Nadaraia, A., Margottini, C., Casagli, N., **2020**. Combining infrared thermography and UAV digital photogrammetry for the protection and conservation of rupestrian cultural heritage sites in Georgia: A methodological application. *Remote Sensing 12*, 0–25. <https://doi.org/10.3390/rs12050892>.
- Frodella, W., Elashvili, M., Spizzichino, D., Gigli, G., Nadaraia, A., Kirkitadze, G., Adikashvili, L., Margottini, C., Antidze, N., Casagli, N., **2021**. Applying Close Range Non-Destructive Techniques for the Detection of Conservation Problems in Rock-Carved Cultural Heritage Sites. *Remote Sensing 13*. <https://doi.org/10.3390/rs13051040>.
- Galdies, C., **2011**. *The Climate of Malta: statistics, trends and analysis 1951-2010*. Valletta (Malta).
- Galea, P., D'Amico, S., Farrugia, D., **2014**. Dynamic characteristics of an active coastal spreading area using ambient noise measurements-Anchor Bay, Malta. *Geophysical Journal International 199*, 1166–1175. <https://doi.org/10.1093/gji/ggu318>.

- 
- Gasc-Barbier, M., Girma, G., Gendre, V., **2014**. Laboratory analysis of thermal fatigue in limestone. *Rock Engineering and Rock Mechanics: Structures in and on Rock Masses - Proceedings of EUROCK 2014, ISRM European Regional Symposium* 285–290. <https://doi.org/10.1201/b16955-46>.
- Gatt, P., **2013**. Geological and geotechnical report on the Azure Window, Gozo: rock assessment and recommendations on preservation and conservation.
- Gauci, R., Scerri, S., **2019**. A synthesis of different geomorphological landscapes on the Maltese Islands, *World Geomorphological Landscapes*. Springer International Publishing. [https://doi.org/10.1007/978-3-030-15456-1\\_5](https://doi.org/10.1007/978-3-030-15456-1_5).
- Geimer, P.R., Finnegan, R., Moore, J.R., **2020**. Sparse Ambient Resonance Measurements Reveal Dynamic Properties of Freestanding Rock Arches. *Geophysical Research Letters* 47, 1–9. <https://doi.org/10.1029/2020GL087239>.
- Gigli, G., Frodella, W., Mugnai, F., Tapete, D., Cigna, F., Fanti, R., Intrieri, E., Lombardi, L., **2012**. Instability mechanisms affecting cultural heritage sites in the Maltese Archipelago. *Natural Hazards and Earth System Science* 12, 1883–1903. <https://doi.org/10.5194/nhess-12-1883-2012>.
- Girardeau-Montaut, D., **2021**. CloudCompare. <https://www.danielgm.net/cc/>.
- Gischig, V.S., Moore, J.R., Evans, K.F., Amann, F., Loew, S., **2011a**. Thermomechanical forcing of deep rock slope deformation: 1. Conceptual study of a simplified slope. *Journal of Geophysical Research: Earth Surface* 116, 1–18. <https://doi.org/10.1029/2011JF002006>.
- Gischig, V.S., Moore, J.R., Evans, K.F., Amann, F., Loew, S., **2011b**. Thermomechanical forcing of deep rock slope deformation: 2. the Randa rock slope instability. *Journal of Geophysical Research: Earth Surface* 116, 1–17. <https://doi.org/10.1029/2011JF002007>.
- Got, J.L., Mourot, P., Grangeon, J., **2010**. Pre-failure behaviour of an unstable limestone cliff from displacement and seismic data. *Natural Hazards and Earth System Science* 10, 819–829. <https://doi.org/10.5194/nhess-10-819-2010>.
-

- Grechi, G., Fiorucci, M., Marmoni, G.M., Martino, S., **2021**. 3D Thermal Monitoring of Jointed Rock Masses through Infrared Thermography and Photogrammetry. *Remote Sensing* 13. <https://doi.org/10.3390/rs13050957>.
- Greif, V., Brcek, M., Vlcko, J., Varilova, Z., Zvelebil, J., **2017**. Thermomechanical behavior of Pravcicka Brana Rock Arch (Czech Republic). *Landslides* 14, 1441–1455. <https://doi.org/10.1007/s10346-016-0784-5>.
- Grinzato, E., **2012**. IR Thermography Applied to the Cultural Heritage Conservation. 18th World Conference on Nondestructive Testing 2–5.
- Guerin, A., Jaboyedoff, M., Collins, B.D., Derron, M.H., Stock, G.M., Matasci, B., Boesiger, M., Lefeuvre, C., Podladchikov, Y.Y., **2019**. Detection of rock bridges by infrared thermal imaging and modeling. *Scientific Reports* 9, 1–19. <https://doi.org/10.1038/s41598-019-49336-1>.
- Guerin, A., Jaboyedoff, M., Collins, B.D., Stock, G.M., Derron, M.H., Abellán, A., Matasci, B., **2021**. Remote thermal detection of exfoliation sheet deformation. *Landslides* 18, 865–879. <https://doi.org/10.1007/s10346-020-01524-1>.
- Guilbert, V., Antoine, R., Heinkelé, C., Maquaire, O., Costa, S., Gout, C., Davidson, R., Sorin, J.L., Beaucamp, B., Fauchard, C., **2020**. Fusion of thermal and visible point clouds: Application to the Vaches Noires landslide, Normandy, France. *International Archives of the Photogrammetry, Remote Sensing and Spatial Information Sciences - ISPRS Archives* 43, 227–232. <https://doi.org/10.5194/isprs-archives-XLIII-B2-2020-227-2020>.
- Gunzburger, Y., Merrien-Soukatchoff, V., Guglielmi, Y., **2005**. Influence of daily surface temperature fluctuations on rock slope stability: Case study of the Rochers de Valabres slope (France). *International Journal of Rock Mechanics and Mining Sciences* 42, 331–349. <https://doi.org/10.1016/j.ijrmms.2004.11.003>.
- Gutenberg, B., Richter, C.F., **1954**. Seismicity of the earth and associated phenomena, 2nd edition. ed. Princeton University Press.
-

- 
- Hall, K., **1999**. The role of thermal stress fatigue in the breakdown of rock in cold regions. *Geomorphology* 31, 47–63. [https://doi.org/10.1016/S0169-555X\(99\)00072-0](https://doi.org/10.1016/S0169-555X(99)00072-0).
- Hall, K., André, M.F., **2001**. New insights into rock weathering from high-frequency rock temperature data: An Antarctic study of weathering by thermal stress. *Geomorphology* 41, 23–35. [https://doi.org/10.1016/S0169-555X\(01\)00101-5](https://doi.org/10.1016/S0169-555X(01)00101-5).
- Hall, K., Thorn, C.E., **2014**. Thermal fatigue and thermal shock in bedrock: An attempt to unravel the geomorphic processes and products. *Geomorphology* 206, 1–13. <https://doi.org/10.1016/j.geomorph.2013.09.022>.
- Harrison, J.C., Herbst, K., **1977**. Thermoelastic strains and tilts revisited. *Geophys. Res. Lett.* 4, 535–537.
- Hatzor, Y.H., **2003**. Keyblock stability in seismically active rock slopes-snake path cliff, Masada. *Journal of Geotechnical and Geoenvironmental Engineering* 129, 697–710. [https://doi.org/10.1061/\(ASCE\)1090-0241\(2003\)129:8\(697\)](https://doi.org/10.1061/(ASCE)1090-0241(2003)129:8(697)).
- Häusler, M., Michel, C., Burjánek, J., Fäh, D., **2021**. Monitoring the Preonzo Rock Slope Instability Using Resonance Mode Analysis. *Journal of Geophysical Research: Earth Surface* 126. <https://doi.org/10.1029/2020JF005709>.
- Helmstetter, A., Garambois, S., **2010**. Seismic monitoring of Schilienne rockslide (French Alps): Analysis of seismic signals and their correlation with rainfalls. *Journal of Geophysical Research: Earth Surface* 115, 1–15. <https://doi.org/10.1029/2009JF001532>.
- Hibert, C., Mangeney, A., Grandjean, G., Baillard, C., Rivet, D., Shapiro, N.M., Satriano, C., Maggi, A., Boissier, P., Ferrazzini, V., Crawford, W., **2014**. Automated identification, location, and volume estimation of rockfalls at Piton de la Fournaise volcano. *Journal of Geophysical Research: Earth Surface* 119, 1082–1105. <https://doi.org/https://doi.org/10.1002/2013JF002970>.
-

- Hibert, C., Provost, F., Malet, J.P., Maggi, A., Stumpf, A., Ferrazzini, V., **2017**. Automatic identification of rockfalls and volcano-tectonic earthquakes at the Piton de la Fournaise volcano using a Random Forest algorithm. *Journal of Volcanology and Geothermal Research* 340, 130–142. <https://doi.org/10.1016/j.jvolgeores.2017.04.015>.
- Hudyma, M., Potvin, Y.H., **2010**. An engineering approach to seismic risk management in hardrock mines. *Rock Mechanics and Rock Engineering* 43, 891–906. <https://doi.org/10.1007/s00603-009-0070-0>.
- Hyde, H.P.T., **1955**. *The Geology of the Maltese Islands: With Special Reference to Water Supply and the Possibilities of Oil*. Lux Press.
- Iannucci, R., Lenti, L., Martino, S., **2020a**. Seismic monitoring system for landslide hazard assessment and risk management at the drainage plant of the Peschiera Springs (Central Italy). *Engineering Geology* 277, 105787. <https://doi.org/10.1016/j.enggeo.2020.105787>.
- Iannucci, R., Martino, S., Paciello, A., D'Amico, S., Galea, P., **2020b**. Investigation of cliff instability at Għajn Hadid Tower (Selmun Promontory, Malta) by integrated passive seismic techniques. *Journal of Seismology* 24, 897–916. <https://doi.org/10.1007/s10950-019-09898-z>.
- Irikura, K., Kawanaka, T., **1980**. Characteristics of microtremors on ground with discontinuous underground structure. *Bulletin of the Disaster Prevention Research Institute* 30, 81–96.
- Julian, M., Anthony, E., **1996**. Aspects of landslide activity in the Mercantour Massif and the French Riviera, southeastern France. *Geomorphology* 15, 275–289. [https://doi.org/10.1016/0169-555x\(95\)00075-g](https://doi.org/10.1016/0169-555x(95)00075-g).
- Kaya, Y., Ventura, C., **2019**. Seismic structural health monitoring of bridges in british columbia, Canada. *Springer Tracts in Civil Engineering* 31–49. [https://doi.org/10.1007/978-3-030-13976-6\\_2](https://doi.org/10.1007/978-3-030-13976-6_2).
- Kleinbrod, U., Burjáněk, J., Fäh, D., **2017**. On the seismic response of instable rock slopes based on ambient vibration recordings *Seismology. Earth, Planets and Space* 69. <https://doi.org/10.1186/s40623-017-0712-5>.

- 
- Kleinbrod, U., Burjánek, J., Fáh, D., **2019**. Ambient vibration classification of unstable rock slopes: A systematic approach. *Engineering Geology* 249, 198–217. <https://doi.org/10.1016/j.enggeo.2018.12.012>.
- Kylili, A., Fokaides, P.A., Christou, P., Kalogirou, S.A., **2014**. Infrared thermography (IRT) applications for building diagnostics: A review. *Applied Energy* 134, 531–549. <https://doi.org/10.1016/j.apenergy.2014.08.005>.
- Lague, D., Brodu, N., Leroux, J., **2013**. Accurate 3D comparison of complex topography with terrestrial laser scanner: Application to the Rangitikei canyon (N-Z). *ISPRS Journal of Photogrammetry and Remote Sensing* 82, 10–26. <https://doi.org/https://doi.org/10.1016/j.isprsjprs.2013.04.009>.
- Larose, E., Carrière, S., Voisin, C., Bottelin, P., Baillet, L., Guéguen, P., Walter, F., Jongmans, D., Guillier, B., Garambois, S., Gimbert, F., Massey, C., **2015**. Environmental seismology: What can we learn on earth surface processes with ambient noise? *Journal of Applied Geophysics* 116, 62–74. <https://doi.org/10.1016/j.jappgeo.2015.02.001>.
- Lévy, C., Baillet, L., Jongmans, D., Mourot, P., Hantz, D., **2010**. Dynamic response of the Chamousset rock column (Western Alps, France). *Journal of Geophysical Research: Earth Surface* 115, 1–13. <https://doi.org/10.1029/2009JF001606>.
- Lévy, C., Jongmans, D., Baillet, L., **2011**. Analysis of seismic signals recorded on a prone-to-fall rock column (Vercors massif, French Alps). *Geophysical Journal International* 186, 296–310. <https://doi.org/10.1111/j.1365-246X.2011.05046.x>.
- Li, X., Shang, X., Wang, Z., Dong, L., Weng, L., **2016**. Identifying P-phase arrivals with noise: An improved Kurtosis method based on DWT and STA/LTA. *Journal of Applied Geophysics* 133, 50–61. <https://doi.org/10.1016/j.jappgeo.2016.07.022>.
- Liu, H., Shah, S., Jiang, W., **2004**. On-line outlier detection and data cleaning. *Computers & Chemical Engineering* 28, 1635–1647. <https://doi.org/https://doi.org/10.1016/j.compchemeng.2004.01.009>.
-

- Liu, Q.S., Wu, J., Zhang, X.P., Tang, L.X., Bi, C., Li, W.W., Xu, J.L., **2020**. Microseismic Monitoring to Characterize Structure-Type Rockbursts: A Case Study of a TBM-Excavated Tunnel. *Rock Mechanics and Rock Engineering* 53, 2995–3013. <https://doi.org/10.1007/s00603-020-02111-5>.
- Loche, M., Scaringi, G., Blahůt, J., Melis, M.T., Funedda, A., da Pelo, S., Erbi, I., Deiana, G., Meloni, M.A., Cocco, F., **2021**. An Infrared Thermography Approach to Evaluate the Strength of a Rock Cliff. *Remote Sensing* 13. <https://doi.org/10.3390/rs13071265>.
- Ma, J., Guan, J., Duan, J., Huang, L., Liang, Y., **2021**. Stability analysis on tunnels with karst caves using the distinct lattice spring model. *Underground Space (China)* 6, 469–481. <https://doi.org/10.1016/j.undsp.2020.08.002>.
- Magri, O., **2006**. A Geological and Geomorphological Review of the Maltese Islands with Special Reference to the Coastal Zone. *Territoris* 6, 7–26.
- Mahmutoglu, Y., **1998**. Mechanical Behaviour of Cyclically Heated Fine Grained Rock. *Rock Mechanics and Rock Engineering* 31, 169–179. <https://doi.org/10.1007/s006030050017>.
- Mainsant, G., Larose, E., Brnnimann, C., Jongmans, D., Michoud, C., Jaboyedoff, M., **2012**. Ambient seismic noise monitoring of a clay landslide: Toward failure prediction. *Journal of Geophysical Research: Earth Surface* 117, 1–12. <https://doi.org/10.1029/2011JF002159>.
- Marmoni, G.M., Fiorucci, M., Grechi, G., Martino, S., **2020**. Modelling of thermo-mechanical effects in a rock quarry wall induced by near-surface temperature fluctuations. *International Journal of Rock Mechanics and Mining Sciences* 134, 104440. <https://doi.org/10.1016/j.ijrmms.2020.104440>.
- Martino, S., Lenti, L., Delgado, J., Garrido, J., Lopez-Casado, C., **2016**. Application of a characteristic periods-based (CPB) approach to estimate earthquake-induced displacements of landslides through dynamic numerical modelling. *Geophysical Journal International* 206, 85–102. <https://doi.org/10.1093/gji/ggw131>.
-



- 
- Maset, E., Fusiello, A., Crosilla, F., Toldo, R., Zorzetto, D., **2017**. Photogrammetric 3D building reconstruction from thermal images. *ISPRS Annals of the Photogrammetry, Remote Sensing and Spatial Information Sciences* 4, 25–32. <https://doi.org/10.5194/isprs-annals-IV-2-W3-25-2017>.
- Matsuoka, N., Sakai, H., **1999**. Rockfall activity from an alpine cliff during thawing periods. *Geomorphology* 28, 309–328. [https://doi.org/10.1016/S0169-555X\(98\)00116-0](https://doi.org/10.1016/S0169-555X(98)00116-0).
- Matsuoka, N., **2001**. Direct observation of frost wedging in alpine bedrock. *Earth Surface Processes and Landforms* 26, 601–614. <https://doi.org/10.1002/esp.208>
- Matsuoka, N., Murton, J., **2008**. Frost weathering: Recent advances and future directions. *Permafrost and Periglacial Processes*. <https://doi.org/10.1002/ppp.620>.
- Mattei, M., Funicello, R., Parotto, M., **2008**. Rome and recent geodynamic evolution of Central Italy, in: *The Geology of Rome. From the Historical Center to the Outskirts.*, pp. 13–24.
- McNamara, D.E., Buland, R.P., **2004**. Ambiente noise levels in the continental United States. *Bulletin of the Seismological Society of America* 94, 1517–1527. <https://doi.org/10.1785/012003001>.
- Merrien-Soukatchoff, V., Gunzburger, Y., Clement, C., **2010**. Natural thermal strains close to surface of rock slopes Measurement and modelling at the "Rochers de Valabres " site. *Rss* 2010 24–25.
- Meyer, M., Weber, S., Beutel, J., Thiele, L., **2019**. Systematic identification of external influences in multi-year microseismic recordings using convolutional neural networks. *Earth Surface Dynamics* 7, 171–190. <https://doi.org/10.5194/esurf-7-171-2019>.
- Mineo, S., Pappalardo, G., Rapisarda, F., Cubito, A., di Maria, G., **2015**. Integrated geostructural, seismic and infrared thermography surveys for the study of an unstable rock slope in the Peloritani Chain (NE Sicily). *Engineering Geology* 195, 225–235. <https://doi.org/10.1016/j.enggeo.2015.06.010>.
-

- Modanesi, S., **2015**. Suscettibilità al distacco di blocchi da pareti in roccia valutata attraverso analisi di stabilità e metodi di verifica della compatibilità cinematica basata su rilievi geostrutturali con tecniche dirette e da remoto applicata ad un sito sperimentale. M.Sc. Thesis. Sapienza University of Rome, Department of Earth Sciences. Rome.
- Moore, J.R., Gischig, V., Burjanek, J., Loew, S., Fäh, D., **2011a**. Site effects in unstable rock slopes: Dynamic behavior of the Randa instability (Switzerland). *Bulletin of the Seismological Society of America* 101, 3110–3116. <https://doi.org/10.1785/0120110127>.
- Moore, J.R., Gischig, V., Katterbach, M., Loew, S., **2011b**. Air circulation in deep fractures and the temperature field of an alpine rock slope. *Earth Surface Processes and Landforms* 36, 1985–1996. <https://doi.org/10.1002/esp.2217>
- Moore, J.R., Thorne, M.S., Koper, K.D., Wood, J.R., Goddard, K., Burlacu, R., Doyle, S., Stanfield, E., White, B., **2016**. Anthropogenic sources stimulate resonance of a natural rock bridge. *Geophysical Research Letters* 43, 9669–9676. <https://doi.org/10.1002/2016GL070088>
- Moore, J.R., Geimer, P.R., Finnegan, R., Thorne, M.S., **2018**. Use of Seismic Resonance Measurements to Determine the Elastic Modulus of Freestanding Rock Masses. *Rock Mechanics and Rock Engineering* 51, 3937–3944. <https://doi.org/10.1007/s00603-018-1554-6>
- Mufundirwa, A., Fujii, Y., Kodama, N., Kodama, J. ichi, **2011**. Analysis of natural rock slope deformations under temperature variation: A case from a cool temperate region in Japan. *Cold Regions Science and Technology* 65, 488–500. <https://doi.org/10.1016/j.coldregions.2010.11.003>.
- Occhiena, C., Coviello, V., Arattano, M., Chiarle, M., Morra Di Cella, U., Pirulli, M., Pogliotti, P., Scavia, C., **2012**. Analysis of microseismic signals and temperature recordings for rock slope stability investigations in high mountain areas. *Natural Hazards and Earth System Science* 12, 2283–2298. <https://doi.org/10.5194/nhess-12-2283-2012>.
- Occhiena, C., Pirulli, M., **2012**. Analysis of climatic influences on slope microseismic activity and rockfalls: Case Study of the Matterhorn peak (Northwestern Alps). *Journal of Geotechnical and Geoenvironmental*
-

- 
- Engineering 138, 1012–1021. [https://doi.org/10.1061/\(ASCE\)GT.1943-5606.0000662](https://doi.org/10.1061/(ASCE)GT.1943-5606.0000662).
- Pappalardo, G., Mineo, S., Imposa, S., Grassi, S., Leotta, A., la Rosa, F., Salerno, D., **2020**. A quick combined approach for the characterization of a cliff during a post-rockfall emergency. *Landslides* 17, 1063–1081. <https://doi.org/10.1007/s10346-019-01338-w>.
- Pappalardo, G., Mineo, S., Zampelli, S.P., Cubito, A., Calcaterra, D., **2016**. InfraRed Thermography proposed for the estimation of the Cooling Rate Index in the remote survey of rock masses. *International Journal of Rock Mechanics and Mining Sciences* 83, 182–196. <https://doi.org/10.1016/j.ijrmms.2016.01.010>.
- Pedley, H.M., House, M.R., Waugh, B., **1976**. The geology of Malta and Gozo. *Proceedings of the Geologists' Association* 87, 325–341. [https://doi.org/https://doi.org/10.1016/S0016-7878\(76\)80005-3](https://doi.org/https://doi.org/10.1016/S0016-7878(76)80005-3).
- Pedley, M., **2011**. The Calabrian stage, Pleistocene highstand in Malta: A new marker for unravelling the late neogene and quaternary history of the Islands. *Journal of the Geological Society* 168, 913–926. <https://doi.org/10.1144/0016-76492010-080>.
- Peng, P., He, Z., Wang, L., **2019**. Automatic Classification of Microseismic Signals Based on MFCC and GMM-HMM in Underground Mines. *Shock and Vibration* 2019. <https://doi.org/10.1155/2019/5803184>.
- Peterson, J.R., Survey, U.S.G., **1993**. Observations and modeling of seismic background noise, Open-File Report. <https://doi.org/10.3133/ofr93322>.
- Prampolini, M., Gauci, C., Micallef, A.S., Selmi, L., Vandelli, V., Soldati, M., **2018**. Geomorphology of the north-eastern coast of Gozo (Malta, Mediterranean Sea). *Journal of Maps* 14, 402–410. <https://doi.org/10.1080/17445647.2018.1480977>.
- Prendes-Gero, M.B., Suárez-Domínguez, F.J., González-Nicieza, C., Álvarez-Fernández, M.I., **2013**. Infrared thermography methodology applied to detect localized rockfalls in self-supporting underground mines. *ISRM International Symposium - EUROCK 2013* 825–829. <https://doi.org/10.1201/b15683-141>.
-

- Provost, F., Malet, J.P., Hibert, C., Helmstetter, A., Radiguet, M., Amitrano, D., Langet, N., Larose, E., Abancó, C., Hürlimann, M., Lebourg, T., Levy, C., le Roy, G., Ulrich, P., Vidal, M., Vial, B., **2018**. Towards a standard typology of endogenous landslide seismic sources. *Earth Surface Dynamics* 6, 1059–1088. <https://doi.org/10.5194/esurf-6-1059-2018>.
- Qu, S., Verschuur, E., Chen, Y., **2018**. Automatic microseismic-event detection via supervised machine learning, in: *SEG Technical Program Expanded Abstracts 2018*, SEG Technical Program Expanded Abstracts. Society of Exploration Geophysicists, pp. 2287–2291. <https://doi.org/doi:10.1190/segam2018-2998279.1>.
- Regina, M., **2018**. Analisi delle condizioni di stabilità in alcune aree costiere dell'arcipelago maltese attraverso modellazione geologico-tecnica e numerica. M.Sc. Thesis. Sapienza University of Rome, Department of Earth Sciences. Rome.
- Roten, D., Fäh, D., Cornou, C., Giardini, D., **2006**. Two-dimensional resonances in Alpine valleys identified from ambient vibration wavefields. *Geophysical Journal International* 165, 889–905. <https://doi.org/10.1111/j.1365-246X.2006.02935.x>.
- Rusinkiewicz, S., Levoy, M., **2001**. Efficient variants of the ICP algorithm, in: *Proceedings Third International Conference on 3-D Digital Imaging and Modeling*. pp. 145–152. <https://doi.org/10.1109/IM.2001.924423>.
- Sansivero, F., Vilardo, G., **2019**. Processing thermal infrared imagery time-series from volcano permanent ground-based monitoring network. Latest methodological improvements to characterize surface temperatures behavior of thermal anomaly areas. *Remote Sensing* 11. <https://doi.org/10.3390/rs11050553>.
- Satariano, B., Gauci, R., **2019**. Landform loss and its effect on health and well-being: The collapse of the azure window (Gozo) and the resultant reactions of the media and the maltese community, in: *World Geomorphological Landscapes*. Springer, pp. 289–303. [https://doi.org/10.1007/978-3-030-15456-1\\_23](https://doi.org/10.1007/978-3-030-15456-1_23).
- Senfaute, G., Duperret, A., Lawrence, J.A., **2009**. Micro-seismic precursory cracks prior to rock-fall on coastal chalk cliffs: A case study at Mesnil-Val,

- 
- Normandie, NW France. *Natural Hazards and Earth System Science* 9, 1625–1641. <https://doi.org/10.5194/nhess-9-1625-2009>.
- Serridge, M., Licht, T.R., **1987**. *Piezoelectric Accelerometer and Vibration Preamplifier Handbook*. Brüel & Kjær.
- Siegesmund, S., Ullemeyer, K., Weiss, T., Tschegg, E.K., **2000**. Physical weathering of marbles caused by anisotropic thermal expansion. *International Journal of Earth Sciences* 89, 170–182. <https://doi.org/10.1007/s005310050324>.
- Spillmann, T., Maurer, H., Green, A.G., Heincke, B., Willenberg, H., Husen, S., **2007**. Microseismic investigation of an unstable mountain slope in the Swiss Alps. *Journal of Geophysical Research: Solid Earth* 112, 1–25. <https://doi.org/10.1029/2006JB004723>.
- Starr, A.M., Moore, J.R., Thorne, M.S., **2015**. Ambient resonance of Mesa Arch, Canyonlands National Park, Utah. *Geophysical Research Letters* 42, 6696–6702. <https://doi.org/10.1002/2015GL064917>
- Sturzenegger, M., Stead, D., **2009**. Close-range terrestrial digital photogrammetry and terrestrial laser scanning for discontinuity characterization on rock cuts. *Engineering Geology* 106, 163–182. <https://doi.org/10.1016/j.enggeo.2009.03.004>.
- Sunamura, T., **1992**. *Geomorphology of rocky coasts*. J. Wiley, Chichester ; New York.
- Taboada, A., Ginouvez, H., Renouf, M., Azemard, P., **2017**. Landsliding generated by thermomechanical interactions between rock columns and wedging blocks: Study case from the Larzac Plateau (Southern France). *EPJ Web of Conferences* 140, 14012. <https://doi.org/10.1051/epjconf/201714014012>.
- Tang, C., Li, L., Xu, N., Ma, K., **2015**. Microseismic monitoring and numerical simulation on the stability of high-steep rock slopes in hydropower engineering. *Journal of Rock Mechanics and Geotechnical Engineering* 7, 493–508. <https://doi.org/10.1016/j.jrmge.2015.06.010>.
-

- Taruselli, M., Arosio, D., Longoni, L., Papini, M., Zanzi, L., **2021**. Seismic noise monitoring of a small rock block collapse test. *Geophysical Journal International* 224, 207–215. <https://doi.org/10.1093/gji/ggaa447>.
- Teza, G., **2014**. THIMRAN: MATLAB toolbox for thermal image processing aimed at damage recognition in large bodies. *Journal of Computing in Civil Engineering* 28, 1–8. [https://doi.org/10.1061/\(ASCE\)CP.1943-5487.0000368](https://doi.org/10.1061/(ASCE)CP.1943-5487.0000368).
- The MathWorks Inc., **2021**. MATLAB. <https://it.mathworks.com/products/matlab.html>.
- Trnkoczy, A., **2012**. Understanding and parameter setting of STA/LTA trigger algorithm, in: Bormann, P. (Ed.), *New Manual of Seismological Observatory Practice 2 (NMSOP-2)*. Deutsches GeoForschungsZentrum GFZ, Potsdam.
- Ulusay, R., **2014**. *The ISRM suggested methods for rock characterization, testing and monitoring: 2007-2014*. Springer.
- Vaezi, Y., van der Baan, M., **2014**. Analysis of instrument self-noise and microseismic event detection using power spectral density estimates. *Geophysical Journal International* 197, 1076–1089. <https://doi.org/10.1093/gji/ggu036>.
- Valentin, J., Capron, A., Jongmans, D., Baillet, L., Bottelin, P., Donze, F., Larose, E., Mangeney, A., **2017**. The dynamic response of prone-to-fall columns to ambient vibrations: Comparison between measurements and numerical modelling. *Geophysical Journal International* 208, 1058–1076. <https://doi.org/10.1093/gji/ggw440>.
- Vidale, J.E., **1986**. Complex polarization analysis of particle motion. *Bulletin of the Seismological Society of America* 76, 1393–1405. <https://doi.org/10.1785/BSSA0760051393>.
- Vignaroli, G., Mancini, M., Brilli, M., Bucci, F., Cardinali, M., Giustini, F., Voltaggio, M., Yu, T.L., Shen, C.C., **2020**. Spatial-Temporal Evolution of Extensional Faulting and Fluid Circulation in the Amatrice Basin (Central Apennines, Italy) During the Pleistocene. *Frontiers in Earth Science* 8, 1–23. <https://doi.org/10.3389/feart.2020.00130>.

- 
- Villarraga, C.J., Gasc-Barbier, M., Vaunat, J., Darrozes, J., **2018**. The effect of thermal cycles on limestone mechanical degradation. *International Journal of Rock Mechanics and Mining Sciences* 109, 115–123. <https://doi.org/10.1016/j.ijrmms.2018.06.017>.
- Villarraga Diaz, C.J., **2018**. Effect of thermal cycles on rock massif stability. Ph.D. Thesis. Universitat Politècnica de Catalunya, Department of Geotechnical Engineering and Geosciences. Barcelona.
- Vlcko, J., Greif, V., Grof, V., Jezny, M., Petro, L., Brcek, M., **2009**. Rock displacement and thermal expansion study at historic heritage sites in Slovakia. *Environmental Geology* 58, 1727–1740. <https://doi.org/10.1007/s00254-008-1672-7>.
- Voigtländer, A., Leith, K., Krautblatter, M., **2018**. Subcritical Crack Growth and Progressive Failure in Carrara Marble Under Wet and Dry Conditions. *Journal of Geophysical Research: Solid Earth* 123, 3780–3798. <https://doi.org/10.1029/2017JB014956>.
- Vollmer, M., Möllmann, K.-P., **2013**. Infrared thermal imaging: Fundamentals, research and applications, *Infrared thermal imaging: Fundamentals, research and applications*. <https://doi.org/10.1002/9783527693306>.
- Wenner, M., Hibert, C., Meier, L., Walter, F., **2020**. Near Real-Time Automated Classification of Seismic Signals of Slope Failures with Continuous Random Forests. *Natural Hazards and Earth System Sciences* 1–23. <https://doi.org/10.5194/nhess-2020-200>.
- Wesseloo, J., Sweby, G., **2008**. Microseismic Monitoring of Hard Rock Mine Slopes 433–450. [https://doi.org/10.36487/acg\\_repo/808\\_179](https://doi.org/10.36487/acg_repo/808_179).
- Westoby, M.J., Brasington, J., Glasser, N.F., Hambrey, M.J., Reynolds, J.M., **2012**. “Structure-from-Motion” photogrammetry: A low-cost, effective tool for geoscience applications. *Geomorphology* 179, 300–314. <https://doi.org/10.1016/j.geomorph.2012.08.021>.
- Wilson, R.C., **1993**. Relation of Arias intensity to magnitude and distance in California, Open-File Report. <https://doi.org/10.3133/ofr93556>.
- Withers, M., Aster, R., Young, C., Beiriger, J., Harris, M., Moore, S., Trujillo, J., **1998**. A comparison of select trigger algorithms for automated global
-

- seismic phase and event detection. *Bulletin of the Seismological Society of America* 88, 95–106. <https://doi.org/10.1785/bssa0880010095>.
- Xia, Y., Xu, Y.L., Wei, Z.L., Zhu, H.P., Zhou, X.Q., **2011**. Variation of structural vibration characteristics versus non-uniform temperature distribution. *Engineering Structures* 33, 146–153. <https://doi.org/10.1016/j.engstruct.2010.09.027>.
- Xiao, Y.X., Feng, X.T., Hudson, J.A., Chen, B.R., Feng, G.L., Liu, J.P., **2016**. ISRM Suggested Method for In Situ Microseismic Monitoring of the Fracturing Process in Rock Masses. *Rock Mechanics and Rock Engineering* 49, 343–369. <https://doi.org/10.1007/s00603-015-0859-y>.
- Xu, N.W., Li, T.B., Dai, F., Zhang, R., Tang, C.A., Tang, L.X., **2016**. Microseismic Monitoring of Strainburst Activities in Deep Tunnels at the Jinping II Hydropower Station, China. *Rock Mechanics and Rock Engineering* 49, 981–1000. <https://doi.org/10.1007/s00603-015-0784-0>
- Yavuz, H., Demirdag, S., Caran, S., **2010**. Thermal effect on the physical properties of carbonate rocks. *International Journal of Rock Mechanics and Mining Sciences* 47, 94–103. <https://doi.org/10.1016/j.ijrmms.2009.09.014>
- Zhan, Z., **2017**. Gutenberg–Richter law for deep earthquakes revisited: A dual-mechanism hypothesis. *Earth and Planetary Science Letters* 461, 1–7. <https://doi.org/10.1016/j.epsl.2016.12.030>